Non-local Theories of Geomorphic Transport: From Hillslopes to Rivers to Deltas to the Stratigraphic Record

A DISSERTATION
SUBMITTED TO THE FACULTY OF THE GRADUATE SCHOOL
OF THE UNIVERSITY OF MINNESOTA
BY

Naga Vamsi Ganti

IN PARTIAL FULFILLMENT OF THE REQUIREMENTS
FOR THE DEGREE OF
Doctor of Philosophy

Efi Foufoula-Georgiou

August, 2012

Acknowledgements

First and foremost, I would like to thank my adviser, Prof. Efi Foufoula-Georgiou, for her support and kindness through the five years of my graduate life. Efi will always remain to me an inspirational mentor and a great friend. I hope to approach research with the same enthusiasm and motivation as she does. This thesis would have never been possible without her endless patience and unwavering trust in me. I'm also grateful to her for creating a professional and social environment that made me feel at home in an alien country.

I would like to thank my committee members: Profs. Chris Paola, Vaughan Voller and Heinz Stefan. I'm grateful to Chris for always urging me to find a physical, observable meaning of every abstract equation I'd in mind. He was instrumental in shaping my approach towards research over the past few years and it is my pleasure to have had the chance to work with him and, more importantly, to learn from him. The journey of understanding the fractional differential equations would not have been as enjoyable, if not for the discussions with Vaughan. I would like to thank Heinz for his encouragement and support throughout.

There are many people with whom I collaborated during the course of my Ph.D. - Profs. Bill Dietrich, Gary Parker, Mark Meerschaert, Colin Stark, Kyle Straub, Paola Passalacqua, Josh Roering. Interactions with all of them taught me so much and I would like to thank all of them for making this an enjoyable and enriching journey. Many thanks to the members of my research group - both past and present - from whom I learnt more than I could offer to them. Special thanks to Paola for being a dear friend and a constant source of support. I sincerely thank all the students, faculty, and staff at the St. Anthony Falls Laboratory (SAFL) for making the lab a great place for research. Special thanks to everyone at the lab who keep the experiments running -

without whom the lab would not be the place it is!

Many thanks to the Silberman family, the Institute on the Environment, the Graduate School of the University of Minnesota, and the Hydrology Section of the American Geophysical Union for the financial support and for considering me worthy of the honors bestowed upon me. I am grateful to National Science Foundation and National Center for Earth-surface Dynamics (NCED) for providing funding for the work done in this thesis. Special thanks are due to everyone at NCED for creating an interdisciplinary environment, which has greatly contributed to this thesis.

I am deeply indebted to all my friends who have always been a source of support and encouragement. Many of my old friends kept in touch during this long process, so I thank Samarth, Siddarth, Rahul, Vinoop, Gokul, Achal, Karthik, Bala and Anuj. Special thanks to my housemates and friends - Akshanth and Vivek - for making my stay in Minneapolis enjoyable.

I'm grateful to my family members - my mother, father, brother and sister-in-law - for their constant support and affection through the years. I'll always be indebted to my mother, for the sacrifices she made in pursuit of my interests and for inculcating in me the drive for academic excellence; and my father, for his calm and levelheaded support through the years and for teaching me to accept success and failure with humility. I'm grateful to my brother and sister-in-law for being there when I needed them. Special thanks to my wife's parents and sister for bringing much joy and stability in the short period of time that I have known them.

Finally, and most importantly, I would like to thank my wife, Sneha. Her support, encouragement, patience and unwavering love were undeniably the bedrock upon which the past eight years of my life was built upon. No words can do justice to the role she played in making me reach my goals.

Dedication

To my dearest father, who I wish lived to see this day.

Abstract

Landscapes are shaped by the interplay between tectonics and climate. The mass fluxes associated with the physical and chemical processes acting across the landscape involve the production and transport of sediment and solutes from the uplands to the lowlands. The processes operating on the Earth's surface dictate the selective long-term preservation of the history of these processes in the geological record. Acknowledging the stochastic nature of the processes that drive the evolution of the landscapes at various time scales involved is essential for building predictive models of sediment transport on the Earth's surface. However, traditional models often do not acknowledge the high variability of the driving forces, broad scales of motion involved and the heavy-tailed nature of events that shape the landscapes. This thesis research challenges existing thinking and puts forth a new class of macroscopic sediment transport models which take into account the probabilistic structure of the processes that shape the landscapes. A new class of macroscopic sediment flux models that are based on non-local theories, where sediment flux is not only a function of local hydro-geomorphic quantities but is a linear function of the space-time history of the system, are introduced. The unifying goal underlying this work is to develop sediment transport models that capture the extreme heterogeneity of the involved processes over a large range of scales, consider the presence of extreme fluctuations that arise due to the climatic forcing, and the spatial heterogeneity of landscapes that affects sediment production, storage, movement and delivery and to study how these surface dynamics are preserved in the Earth's geological record.

Contents

List of Tables

List of Figures

Chapter 1

Introduction

Accurate models for computing the production of sediment from hillslopes, the transport of this sediment through rivers, and its deposition on floodplains and low relief areas, are essential tools for managing landscapes. Yet these sediment transport models are hard to be derived from first principles and hard to be calibrated in the field due to lack of detailed observations. As land-use changes, e.g., for agricultural or alternative energy purposes, and as watershed management is geared towards a holistic approach to sustainable-ecosystem-services, the need for integrated and accurate environmental transport models spanning the scales of streambed, to hillslope to the whole watershed have become an area of accelerated research. The availability of high resolution digital topography data from laser altimetry (LiDAR data at 0.5 to 1 m scale) and the advancement of sediment dating techniques and smart environmental sensors have contributed to the ability to critically re-examine the existing transport laws in the context of hydro-geomorphology.

The proposed thesis research challenges existing thinking by putting forward a new class of transport models that are able to account for the extreme heterogeneity of the involved processes over a large range of scales (from collective particle motion in streambeds to the large-scale motion of soil due to landslides on hillslopes), consider the presence of extreme fluctuations due to floods and debris flows (which can accelerate the movement of sediment much beyond the expected movement due to an average velocity downstream) and the spatial heterogeneity of landscapes which affects sediment storage, release and delivery. This research extends to both erosional and depositional

landscapes, which are uplift driven and subsidence driven, respectively. The central questions that the proposed thesis research addresses are: (a) How do hydrologic, biologic and geologic processes, which show extreme variability over a broad range of space and time scales, manifest themselves in landscape form?; (b) How much information about the past climate and history of Earth-surface evolution can be deduced from what is preserved in the stratigraphic record? The thesis is structured as follows:

- Chapter 2 briefly presents the background and motivation along with the main results of this thesis research.
- In Chapter 3, a non-local theory of sediment transport on hillslopes is presented.
- Chapter 4 deals with the issues of scale-dependence of local, nonlinear and non-local, linear sediment transport models on hillslopes.
- Chapter 5 presents a theoretical development that describes the dispersion of tracers in gravel-bedded streams under the case that the sediment travel distances follow a thin-tailed or heavy-tailed distribution.
- In Chapter 6, a new stochastic model for sediment transport in rivers is proposed to explain the experimentally observed multi-scale statistics of sediment transport rates.
- In Chapter 7, statistical characterization of the surface dynamics of an experimental deltaic system is presented.
- In Chapter 8, with the aid of numerical simulations, we relate the statistics of surface dynamics to the statistics of 1D preserved stratigraphy.
- In Chapter 9, the kinematic controls on the 2-D geometrical structure of the preserved cross-sets are studied.
- Chapter 10 presents concluding remarks and areas of future research.

Chapter 2

Background and Motivation

Landscapes are shaped by the interplay of hydrologic, biologic and tectonic processes operating over a wide range of space-time scales. These processes leave their signature on intricate patterns of hillslope to valley transitions, meandering and braided rivers, and complex hierarchical tributary and distributary river networks. Over geologic time scales, the space-time history of landscape evolution is preserved in the stratigraphic record whose analysis can give information of the historical floods and droughts and abrupt transitions due to earthquakes or tectonic events, offering, thus, valuable information for the future. In addition to natural processes shaping landscapes, human activities interfere with the course of nature and induce acceleration or deceleration of water and sediment fluxes in watersheds with shorter-term effects on river morphology and longer-term consequences on landscape evolution.

Central to any quantitative understanding of Earth-surface evolution is the Exner equation, which is a statement of mass balance [e.g., 14, 15, 16]:

$$\frac{\partial z}{\partial t} = \sigma - \nabla . q_s \tag{2.1}$$

where z is the elevation of the Earth's surface as measured from a datum, σ is some tectonic forcing, either uplift or subsidence, and q_s is the sediment flux. As it is clear from the above equation, one of the keys to quantitative understanding and prediction of Earth's surface evolution lies in the accurate modeling of sediment flux. Sediment flux models, in essence, should represent a parameterized version of the statement of conservation of momentum. However, this is a monumental task as geomorphic transport

spans a wide range of space and time scales and deriving sediment flux relationships from first principles is almost impossible and also impractical. Thus, sediment flux models or geomorphic transport models should represent an essential abstraction of the physical and statistical structure of the transport processes that shape the Earth's surface. Dietrich et al. [17] define a geomorphic transport model as "a mathematical statement derived from a physical principle or mechanism, which expresses the mass flux or erosion caused by one or more processes in a manner that: 1) can be parameterized from field measurements, 2) can be tested in physical models, and 3) can be applied over geomorphically significant spatial and temporal scales." They also noted that geomorphic transport models are "a compromise between physics-based theory that requires extensive information about materials and their interactions, which may be hard to quantify across real landscapes, and rules-based approaches, which cannot be tested directly but only can be used in models to see if the model outcomes match some expected or observed state". The essential goal of this thesis research is to both highlight the importance and take into account the statistical structure (heterogeneity and variability), along with the physics, of the process and form involved in geomorphic transport.

Current geomorphic transport models for landscape evolution are mathematical formulations framed around the underlying assumption of the existence of a representative elementary control volume (REV) where the mass balance and sediment flux computation can be performed. Inherent to the assumption of a finite REV is the presence of a characteristic space and time scale of transport in the system. This underlying assumption coupled with the assumption of a statistically homogeneous system (i.e., the variability in the system has a linear dependence on scale) facilitates the integration of the processes from micro-scales in time and space to geomorphic model scales. When no characteristic space and/or time scale of transport exists, then the notion of performing mass balance over a characteristic scale (or the notion of flux divergence converging as the volume shrinks to zero) loses its meaning [2]. Further, assumption of a finite REV is inconsistent with the transport processes in which significant amount of total flux comes from events across a broad span of frequency and magnitude (as this would require one to account for the spatiotemporal memory of the system). In many geomorphic systems, the time and length scales of motion vary widely: particles can be

trapped for both short and long periods of time and can travel large or small distances in very short intervals of time. This leaves us with the question: do geomorphic systems exhibit a characteristic space and/or time scale of transport (which depend on the physical parameters, e.g., rainfall rate, streamflows) such that the classical geomorphic transport models can be applied?

To understand this concept better, let us start with the well-known advection-dispersion equation (ADE). This formulation is based on the classical definition of divergence of a vector field. The divergence is defined as the ratio of the total flux through a closed surface to the volume enclosed by the surface when the volume shrinks to zero [e.g., 18, 1]:

$$\nabla . q_s = \lim_{V \to 0} \frac{1}{V} \iint_S q_s . \eta dS \tag{2.2}$$

where q_s is a vector field, V is an arbitrary volume enclosed by surface S, and η is a unit normal vector. Implicit in equation (2.2) is that the limit of the integeral exists, that is, the vector q_s exists and is smooth as $V \to 0$.

The classical notion of divergence maintains that as an arbitrary control volume shrinks, the ratio of total surface flux to volume must converge to a single value. This would hold true for a homogeneous system, where the total surface flux exhibits a linear dependence on the control volume size. However, in many natural systems, heterogeneity and variability across many scales can result in a nonlinear dependence of the total surface flux on control volume size. This would imply that the ratio of the total surface flux to the volume will be scale-dependent. In particular, in systems in which a considerable portion of the mass is contributed from far upstream (e.g., due to a large variability in transport velocities, or due to collective behavior in particle movement), we note that by increasing the control volume the total surface flux increases nonlinearly (see Figure 2.1 left panel). Thus, the ratio of total flux to volume does not remain constant but varies with the size of the volume. As a result, the classical diffusion equation is no longer self-contained with a closed form solution at all scales [e.g., 1, 19, 11, 2].

To adopt the classical theory, the best approximation that can be done is to assume the total flux to volume as piece-wise constant within small ranges of scales (see Figure 2.1 right panel), allowing one to talk about an effective scale-dependent dispersion coefficient. Alternatively, one can consider mass balance over an infinite volume,

or equivalently, consider an integral or convolution Fickian flux. When the flux is expressed as a convolution integral of the hydro-geomorphic attributes of the system, that not only include the local properties, but also the properties of the system that extend away from the point of interest, we call the flux to be non-local in nature. Mathematically, when the convolution kernel takes a form of a power-law decay, then the flux can be concisely expressed as a fractional (noninteger) derivative.

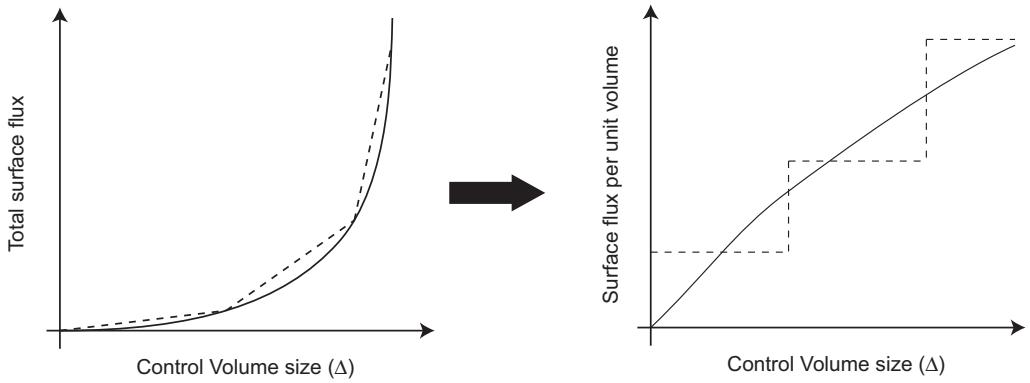

Figure 2.1: Extended definition of divergence of particle flux when the system exhibits heterogeneity over many scales, as expressed in a nonlinear total flux to volume relationship. Linear approximation of total flux to volume in local neighborhoods (dashed lines in left plot) enables the adoption of classical divergence (constant flux per unit volume shown in the right plot) highlighting, however, the emergence of a scale dependence in the dispersivity coefficient. An extended definition of divergence can be achieved by adopting an integral or convolution Fickian flux using fractional derivatives. Figure adapted from [1, 2].

This chapter is structured as follows. In the next section, we probe into the meaning of non-locality of transport and understand it from both a statistical and a physical viewpoint. We present background and motivation for the application of non-local theories of transport, along with a short summary of main results for erosional and depositional landscapes in Sections 2.2 and 2.3, respectively.

2.1 What is non-locality of transport?

Sediment flux on the Earth's surface comprises the transport of sediment particles, for example, transport of solute particles in surface and subsurface water flows, soil

particles undergoing biochemical transport and mixing by bioturbation, transport of sediment particles in turbulent flows. Almost all these examples share a few common features: (i) behavior of a well-defined ensemble of particles, which can be considered as "tracers" whose total mass is conserved or otherwise accounted for if some physical transformations or chemical reactions are involved; (ii) These sediment particles (tracers) typically alternate between states of motion and rest over many time scales, with most of the tracers of interest in Earth surface systems being at rest most of the time; and (iii) when in transport, some sediment particles move faster, and some slower than the average motion due to spatiotemporal variations in the mechanisms inducing their motion [3]. Tracer motions thus may be considered as consisting of quasi-random walks with rest periods.

2.1.1 Space non-locality

Consider an ensemble of tracers in motion in one-dimension. The movement of these tracers can be characterized by the distances that they move, either in the downstream or upstream direction. Consider that tracers are released into a flow at some location x_0 at time $t = 0$ and they remain in motion. Most of the tracer particles will travel a short distance, while some particles can travel a really long distance. The distance traveled by each of these sediment particles in a given time Δt is a random variable, which we call 'the sediment travel distance', which has its own probability density function (pdf). After some time t, the sediment particles will be on an average at $x = x_0 + vt$, where v is the mean speed of the tracer particles and the spread around this mean location, which is characterized by the standard deviation, grows in time as $\sigma \sim \sqrt{t}$. This behavior is called Fickian or Boltzmann scaling and can be characterized as "local" transport phenomenon. This behavior is called local in that the sediment particles on an average travel to nearby positions in a given time or conversely the sediment particles arriving at a given location originate from the neighboring locations (see Figure 2.2 for an Eulerian viewpoint). If $C(x, t)$ denotes the concentration of the tracers at any given space and time, then the evolution of the concentration of tracers is described by the classical advection-dispersion equation. The Green's function solution of the ADE is the Gaussian distribution, which can be arrived at through arguments based on the Central Limit Theorem [e.g., 20, 21, 3].

However, if some of the sediment tracer particles travel a really long distance inducing a large amount of variability in sediment travel distances such that a meaningful or convergent variance (or mean) does not exist for the pdf of sediment travel distances, then the standard advection-dispersion theory is no longer applicable. In such a case, the pdf of the sediment travel distances is said to be heavy-tailed, which signifies that the tails of the distribution are heavier (decay much slower) than their thin-tailed counterparts. Heavy-tailed distributions are characterized by power-law decaying tails with an exponent $-(\alpha+1)$ where $0 < \alpha < 2$. The parameter α is called the tail-index of the distribution. From a statistical viewpoint, the primary reason for the classical theory to break down here is because the Central Limit Theorem is no longer applicable as the sum of independent, identically distributed random numbers converges to an α-stable distribution, instead of a Gaussian distribution [e.g., 20, 3].

Two distinct cases arise here, namely, when $0 < \alpha < 1$ and $1 < \alpha < 2$. In the former case, the sediment travel distances do not have an existing first moment (mean) and second moment (variance). However, in the latter case, the particle travel distances have an existing mean, but a non-existing theoretical second moment (variance). In the case of heavy-tailed travel distances, particles can travel anomalously large distances, albeit with a small (but finite) probability, resulting in a concentration spread around the mean tracer location scaling as $\sigma \sim t^{1/\alpha}$ where $1 < \alpha < 2$. From this scaling relationship, we can notice that the spread grows faster than normal diffusion and thus we call this process 'superdiffusion'. It is also worth noting that $0 < \alpha < 1$ corresponds to the case, which describes a motion that is faster than pure advection ($\alpha = 1$) and is often referred to as 'superadvection'. This behavior is called as "non-local" in space in that during a small time interval, tracers released from position x_0 mostly move to nearby locations, but some move by unusually large distances. Conversely, during the same time interval, tracers arrive at a given location, not only from its neighboring locations but also from points far away from the point of interest (see Figure 2.2). In such cases, the tracer concentration $C(x,t)$ cannot be modeled using the classical ADE, but one has to move into the realms of generalized transport models. These include the fractional ADEs with a non-integer order derivative in space [e.g., 1, 22, 23, 21, 3] and the related continuous time random walk (CTRW) models [see 24, 25, 26, 27].

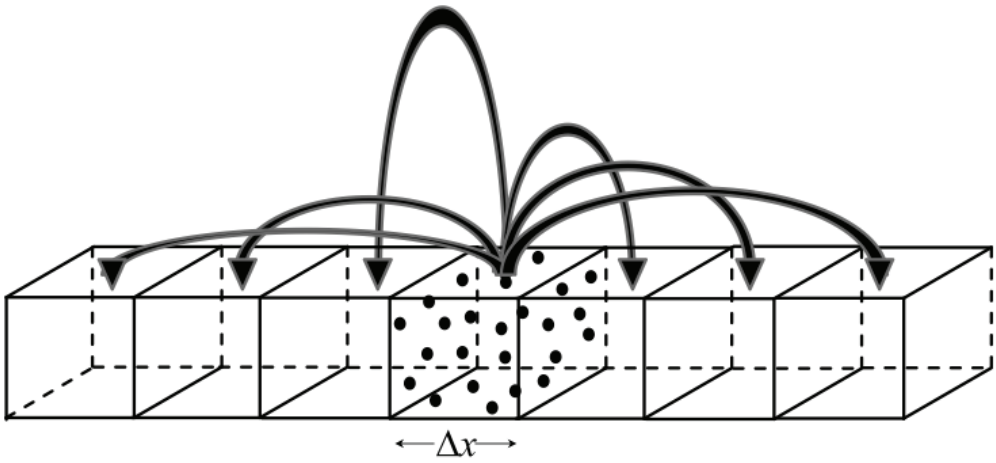

Figure 2.2: Figure reproduced from Schumer et al. [3]. Eulerian viewpoint of space non-locality is shown. If the sediment travel distances have heavy-tailed pdfs, then the particles can travel to a far away cell from a given cell in small intervals of time. Thus, one needs to consider the whole system size while accounting for sediment flux at any given location.

2.1.2 Time non-locality

Consider now an ensemble of sediment particles whose motions include states of rest as well. The rest time or waiting time or residence time can also be considered as a random variable. If the waiting times have an existing mean and are described by a thin-tailed distribution, then the sediment particles motion can be described by a "virtual speed" that includes both periods of rest and motion. The local rate of change in tracer concentration, $\partial C/\partial t$, in the classical ADE accommodates this. However, if the waiting times are described by a pdf that is heavy-tailed with presence of unusually long rest periods for tracers in storage, then this behavior can be described by a fractional-in-time ADE. In this case, the fractional order of differentiation (integration) is in time, where the standard $\partial C/\partial t$ is replaced by $\partial^\gamma C/\partial t^\gamma$ with $0 < \gamma < 1$. The dispersion now scales as $\sigma \sim t^{\gamma/2}$, and since this spread is slower than normal Fickian dispersion, we refer to it as "subdiffusion". Non-locality in time, like the space non-locality, characterizes long memory effect but in time, i.e., one needs to consider the influence from far back in time (see Figure 2.3).

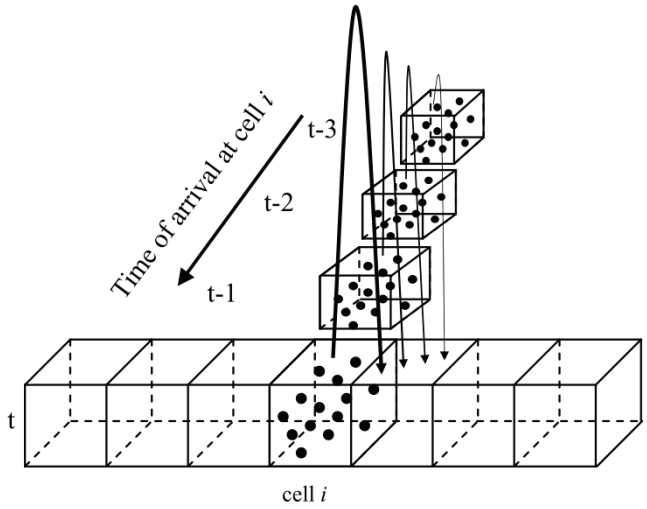

Figure 2.3: Figure reproduced from Schumer et al. [3]. Eulerian viewpoint of time non-locality is shown. If the waiting times have heavy-tailed pdfs, then the sediment flux at a given time can feel the influence from far back in time. This long memory effect is referred to as time non-locality and can be concisely encapsulated in a time-fractional derivative.

An alternate way of understanding time non-locality is through the notion of *operational time*. We can consider the clock (physical) time to be made up of periods of rest and the time for which the sediment particles are in motion, i.e., the time for which the sediment particles are *operated* upon. Consider the situation not as a function of time, but rather as a function of the number of steps that a sediment particle takes. We can easily convince ourselves that the particle's displacement is a function of number of steps and is a discrete time random walk. Now we can consider the number of steps as the internal, operational time governing the system's evolution. The role of the waiting times in this case reduces to the fact that the actual number of steps made up to the time instant t fluctuates, so that the operational time is a random function of the physical time t (see Figure 2.4) [4]. This notion of randomizing the clock time is called *subordination*, and when the randomized time has a heavy-tailed pdf then we move into the realm of non-locality in time.

We note that both super diffusion (or advection) and sub diffusion imply that the behavior at a certain location depends not only on the local condition (nearby locations or

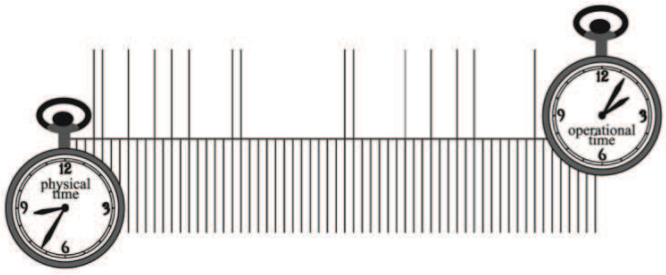

Figure 2.4: Figure reproduced from Sokolov and Klafter [4]. Operational time of a CTRW process with a power-law waiting time distribution between steps. The steps follow very irregularily in physical time, and show step-free intervals on all time scales. On the average, the operational time is in delay compared with the physical one.

present time), but also on the behavior upstream and/or what has happened in the past. The behavior is thus non-local either in space or time or both. If the sediment particle distances and their waiting times have heavy-tailed distributions, then the dispersion scales as $\sim t^{\gamma/\alpha}$, where γ relates to the tail-index of the waiting time distribution and α relates to the tail-index of the sediment travel distances. One important observation that can be readily made is that a particular value of γ/α can result from a non-unique combination of values of α and γ. In this case, additional physical or observational information is needed to differentiate whether this anomalous dispersion has resulted from heavy-tailed sediment travel distances, long waiting times or a combination of both.

2.2 Transport in net erosional landscapes

In this section, we will explore the applicability of the non-local sediment transport models in net erosional systems. Net erosional systems are uplift driven, where there is a balance between the net erosion and the uplift in the system. Some of the examples include hillslopes, channels, rivers, etc. In a source to sink framework, net erosional systems form the convergent part of the landscapes.

2.2.1 Transport on hillslopes

Hillslopes are shaped by varied disturbance-driven processes, ranging from gopher mounds, bioturbation, wood blockage, freezing and thawing cycles, tree throws, landslides, etc.

Each of these processes has its own event-based transport distances over which the sediment particles are mobilized and transported. The frequency of occurrence of these events that shape a given hillslope can vary greatly. Thus, sediment transport on hillslopes is a stochastic process where sediment mobilization and movement happens sporadically over a relatively long period of time. In a general form, we can treat sediment flux on hillslopes as follows [e.g., 28]:

$$q_s = \frac{volume}{event} \times \frac{events}{area} \times \frac{distance}{event} \times \frac{events}{time} \tag{2.3}$$

where q_s is the sediment flux $[L^2T^{-1}]$. The above expression is valid for each disturbance event and also has the ability to encapsulate a whole range of disturbance processes. We can combine the first two terms of equation (2.3) to get $n \times h$, where n is the number of events and h is the active soil depth. Further, identifying the last term in equation (2.3) as the frequency of the events, we can write the expression for sediment flux on hillslopes as:

$$q_s = n \times h \times f \times l \tag{2.4}$$

where f is the frequency of events and l is the sediment travel distance. Several studies have addressed the stochastic nature of the active soil depth and their dependence on the local topographic slope [e.g., 29, 30]. However, the variations in the active soil depth are much smaller than the variations in transport distances, and here we neglect the variations in soil depth by treating it as a deterministic constant (H). This approximation is akin to the active layer approach in modeling sediment transport on river beds [e.g., 31].

The product of the number of events (n) and the frequency of events (f) in equation (2.4) gives us the waiting times (τ), under the assumption that sediment transport on hillslopes happens instantaneously. This assumption is a relatively good approximation of the disturbance-driven processes as the most likely state of the sediment particles is that of rest. Thus, the sediment flux can be expressed now as:

$$q_s = H\frac{l}{\tau} \tag{2.5}$$

The ratio of the sediment travel distance and the waiting times in equation (2.5) is a "pseudo mass velocity", averaged over the stochasticity of the events that shape a given hillslope. We note that the above definition of the sediment flux resembles the standard

continuum definition, which states that q_s is a product of the mass velocity and the depth of active soil mass, i.e., $q_s = v_s h$, which is the starting point for much of the continuum modeling of sediment transport on hillslopes.

The standard models for sediment flux include the linear, local model [e.g., 32, 33, 34] and the nonlinear, local model [e.g., 35, 7], both of which express the sediment flux as a function of some local topographic attributes of the hillslopes. As discussed in Section 2.1, critical to the application of the local vs non-local model for sediment transport is the knowledge of the probability distribution functions of the sediment travel distances and the waiting times. Equation (2.5), though built under certain assumptions (that sediment transport on hillslopes happens instantaneously and the active soil depth is a constant), gives us a means of probing into the (non) locality of transport on the hillslopes. Following equation (2.5), now consider the pdf of the sediment flux, $f(q_s)$, which is given by:

$$f(q_s) = Hf\left(\frac{l}{\tau}\right) \tag{2.6}$$

Equation (2.6) states that the pdf of the sediment flux is directly proportional to the pdf of the pseudo mass velocities. Recalling that heavy-tailed velocities are consistent with non-local transport, while thin-tailed velocities are consistent with local transport, the question arises as to whether one could infer (or get insight on) the pdf of pseudo mass velocities by examining the pdf of sediment flux on hillslopes. To explore this question, we need direct measurements of sediment flux in a given hillslope over a period of time to get a reliable estimate of the pdf of the sediment flux, which are rare at best. Thus, we resort to using sediment flux models to estimate the sediment flux from topographic data of different field sites. The most common and widely accepted form of the sediment flux model that is applicable on the hillslopes is the nonlinear flux model proposed by Roering et al. [7](similar form was also arrived at in [35]):

$$q_s = \frac{-K\nabla z}{1 - \left(|\nabla z|/S_c\right)^2} \tag{2.7}$$

where K is the diffusivity, z is the topographic elevation measured from a datum, and S_c is called as critical gradient, which relates to the angle of repose. The nonlinear flux model has been extensively studied, validated, and the parameters of the model have been calibrated in several field sites.

We used the nonlinear flux model of equation (2.7) on two different landscapes, namely, Gabilan Mesa (GM) and the Oregon Coast Range (OCR) to get insight into the distribution of pseudo mass velocities. The parameters of the nonlinear flux model were calibrated in these two field sites [5]. Figure 2.5 shows the estimated probability of exceedance of the sediment flux, which is a reflection of the pdf of the pseudo mass velocities according to equation (2.6). We note that the pdf of the pseudo mass velocities in GM have an exponential tail, indicative of thin-tailed statistics and local transport. However, the pdf of the pseudo mass velocities in OCR have a power-law tail (tail index of $\alpha = 1.3$), indicative of heavy-tailed statistics and non-local transport. OCR is a steep landscape, which is shaped by varied processes such as debris flow, tree throw, and landslides (processes which can move sediment by an unusually large distances); whereas GM is a less steep landscape, which is shaped by slow rheological creep. Thus, it could be argued that the nature of the transport (local vs non-local) on these hillslopes is dependent on the variability of the external driving forces of sediment transport.

Heavy-tailed velocities and non-local transport can result from various combinations of the nature of sediment travel distance and waiting time pdfs. Under the assumption that sediment travel distance l and waiting time τ are independent, we used numerical simulations to generate pseudo mass velocities (ratio of l/τ) by sampling l and τ from two end-member distributions, namely, exponential pdf (thin-tailed) and Pareto pdf (heavy-tailed). We conclude that the resulting pseudo mass velocities are thin-tailed when the sediment travel distances are thin-tailed, independently of whether the waiting times are thin- or heavy-tailed. Heavy-tailed pseudo mass velocities result when the sediment travel distances are heavy-tailed, with the waiting times being either thin- or heavy-tailed. Thus, it is evident that the nature of the pdf of the pseudo mass velocities is a direct reflection of the nature of the pdf of the sediment travel distances, at least under the assumption of independence of sediment travel distances and waiting times. However, this assumption of independence is a strong one, which might not hold true for real hillslopes. The waiting times and the sediment travel distances are both slaved to the topographic features of the landscape, i.e., larger sediment travel distances that are likely to occur at steep gradients in a landscape can have lesser waiting times and vice versa, thus, indicating the presence of some dependence between the sediment travel distances and waiting times.

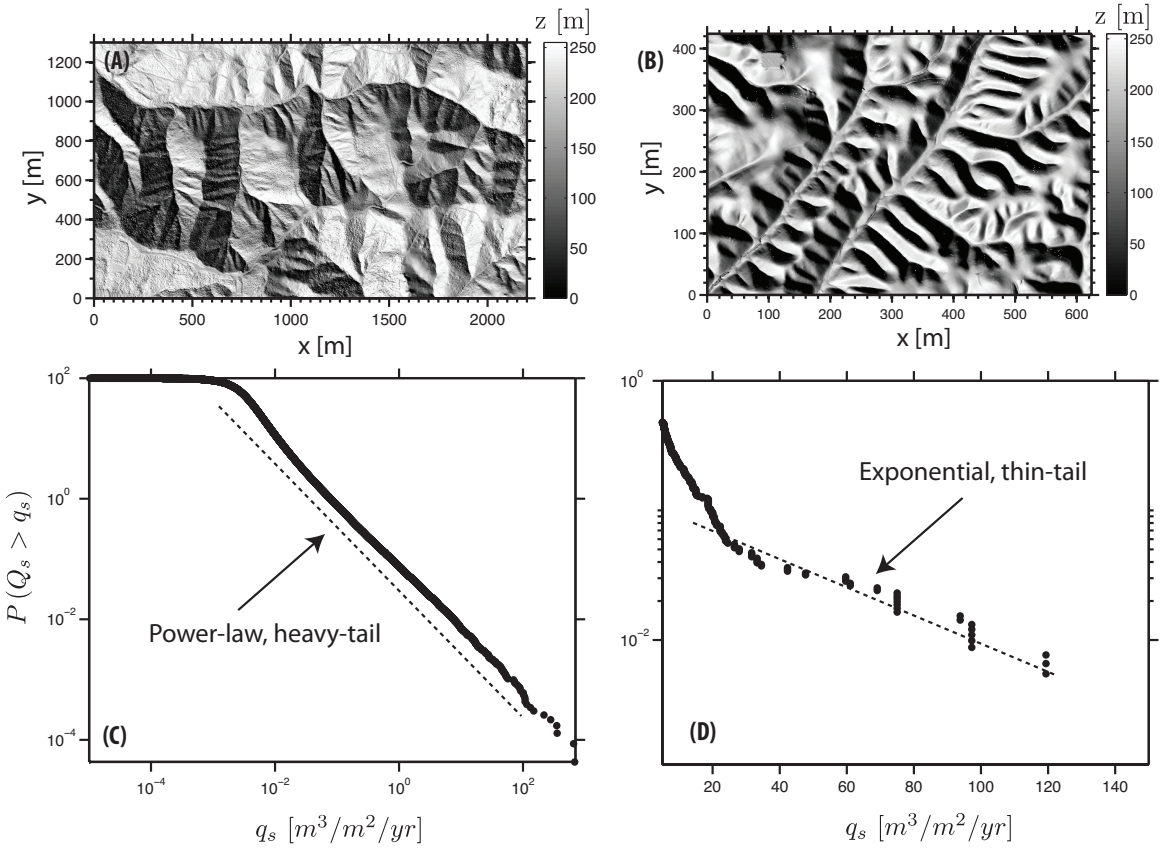

Figure 2.5: High-resolution LiDAR data (resolution of 1 m) of Oregon Coast Range and Gabilan Mesa are shown in (A) and (B), respectively. Plots showing the probability of exceedance of the estimated sediment flux from the hillslope pixels using the nonlinear flux model of equation (2.7) in (C) Oregon Coast Range, and (D) Gabilan Mesa. Using equation (2.6), we note that the pseudo mass velocities in OCR are heavy-tailed (pointing to a non-local model), whereas the pseudo mass velocities are thin-tailed in GM (pointing to a local model). The parameters of the nonlinear flux model used were $K = 0.003\ m^2/yr$ and $S_c = 1.2$ for OCR and $K = 0.038\ m^2/yr$ and $S_c = 1.2$ for GM [5].

In a general case, under no assumption of independence of sediment travel distances and waiting times, we can express the pdf of the ratio of sediment travel distances and waiting times, i.e., of the pseudo mass velocity, in terms of a joint distribution as:

$$f(q_s) = H \int \tau f(l\tau, \tau)\, d\tau \tag{2.8}$$

It is clear from the above equation that we can not decouple sediment travel distances and waiting times without a priori knowledge of their joint distribution and the distribution of their product. However, such detailed field or experimental observations of sediment travel distance and waiting time are seldom available, highlighting the need for extensive field and laboratory observations to probe into the physical origins of non-locality.

The issue of non-locality of transport on hillslopes is explored in depth in this thesis research. In Chapter 3, we hypothesize that the heterogeneity of disturbance-driven processes can lead to a heavy-tailed distribution of sediment travel distances. We proposed that such a behavior calls for a non-local computation of the sediment flux, where the sediment flux at a point is not strictly a function (linear or nonlinear) of the gradient at that point only but is an integral flux taking into account the upslope topography (convolution Fickian flux). We encapsulated this non-local behavior in a simple fractional diffusive model which involves fractional derivatives, with the order of differentiation dictating the degree of non-locality. The model predicts an equilibrium hillslope profile which is parabolic close to the ridgetop and transits, at a short downslope distance, to a power law with an exponent equal to the parameter α (tail-index of sediment travel distance) of the fractional transport model. Hillslope profiles reported in previously studied sites [e.g., 36, 7] support this prediction. Furthermore, we showed that the non-local transport model gives rise to a nonlinear dependence on local slope and that variable upslope topography leads to widely varying rates of sediment flux for a given local hillslope gradient. Both of these results are consistent with available field data and suggest that nonlinearity in hillslope flux relationships may arise in part from non-local transport effects in which sediment travel distances increase with hillslope gradient. The proposed hypothesis of non-local transport implies that field studies and models of sediment fluxes should consider the size and displacement lengths of disturbance events that mobilize hillslope colluvium.

Further, we show that though nonlinear and non-local models of sediment transport on hillslopes lead to similar morphological features at steady-state, they differ in their application and their scale-dependence. Typically, topographic attributes are computed from digital elevation data (DEMs) and thus their estimates depend on the DEM resolution (1 m, 10 m, 90 m, etc.) rendering any sediment flux computation scale-dependent. Often calibration compensates for this scale-dependence resulting in effective parameterizations with limited physical meaning. In Chaper 4, we demonstrate the scale-dependence of local nonlinear hillslope sediment flux models and derive a subgrid scale closure via upscaling. We parameterize the subgrid scale closure in terms of the low resolution, resolved topographic attributes of the landscape, thus allowing the reliable computation of a scale-independent sediment flux from low resolution digital elevation data. We also show that the accuracy of the derived subgrid scale closure model depends on the dimensionless erosion rate and the dimensionless relief of any given basin. Finally, we present theoretical arguments and demonstrate that the non-local sediment flux models are scale-independent. These concepts were demonstrated via an application on a small basin (MR1) of the central Oregon Coast Range using high-resolution LiDAR topographic data.

2.2.2 Sediment transport on river beds

The idea of diffusion or dispersion of bed load particles is central to the understanding of sediment transport on river beds. This idea is at the heart of understanding kinematics of downstream (or cross-stream) diffusion of tracer particles in experimental flumes or natural rivers [37, 38, 39, 40, 41, 42, 43, 44, 45, 46, 47], and also in understanding how particle diffusion contributes to sediment flux under steady and unsteady conditions of transport [e.g., 48, 44, 45]. The stones that make up the bed of gravel bed rivers are transported as bed load during floods. During periods of overall transport, each particle undergoes alternating periods of movement and rest. Movement consists of rolling, sliding or saltation, which continues until a single step length of motion is completed (see Figure 2.6). The particle is at rest when it is deposited, either on the bed or deeper within the deposit.

Despite considerable research over the past several decades, the problem of accurate estimation of bed load sediment transport in rivers remains unsolved. One of the main

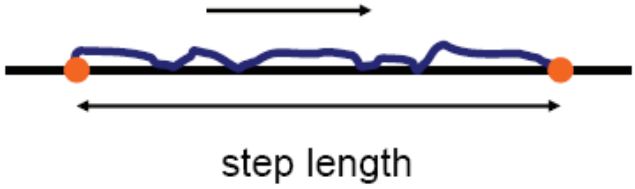

Figure 2.6: Figure reproduced from Gary Parker's e-book. Definition sketch of a step length of a sediment particle (shown as orange solid circle) - distance traveled from when entrained until it is deposited again. The amount of time a sediment particle is at rest before it is entrained again is called as the waiting time. The arrow indicates the direction of flow - from left to right.

challenges lies in the fact that the motions of individual particles happen at random, rendering the process of transport a stochastic process. As discussed in Section 2.1, transport of tracers and their ensemble behavior will heavily depend on the nature of statistics of the step length and waiting time of the sediment particles. A single step length is defined as the distance traveled by a sediment particle once it is entrained into the flow until it is deposited in the bed (see Figure 2.6). Further, the waiting time can be defined as the time between deposition and next (following) entrainment of a sediment particle. The importance of the stochastic nature of the step lengths in bed load transport was recognized as early as the work of Einstein [49] and many stochastic theories of sediment transport followed thereafter. The ensemble behavior of the tracers and their concentration in natural sand-bed rivers was also studied as early as the work of Sayre and Hubble [37]. Nikora et al. [41] have studied the diffusion of bed load particles using the measured motion of individual particles in a canal as the basis for ensemble averaging. They extracted from their data various statistical moments characterizing particle location as a function of time. They delineated three ranges of temporal and spatial scales, each with different regimes of diffusion: ballistic diffusion (at the scale of saltation length), normal/anomalous diffusion (at a scale of step length) and subdiffusion (at global scale). Their study thus represents a pioneering effort in the identification of anomalous diffusion of bed load particles.

In the light of the new developments in characterizing non-local transport, this thesis research re-examines some of our basic modeling approaches to tracer dispersal and minimum complexity models of sediment transport. There is growing experimental

and field evidence that the statistics of sediment transport can be non-local in nature, even under steady, uniform conditions. For example, Bradley et al. [50] revisited the Sayre and Hubble data and showed that the breakthrough curves of the tracers in the sand bed rivers exhibited heavy-tails and Martin et al. [43] probed into the physical basis for the sediment particles to have heavy-tailed step lengths and waiting times under controlled experimental conditions.

One way to study the mechanism of gravel bed load transport is to seed the bed with marked gravel tracer particles within a chosen patch and to follow the pattern of migration and dispersal of particles from this patch. In Chapter 5, we invoke the probabilistic Exner equation for sediment conservation of bed gravel, formulated in terms of the difference between the rate of entrainment of gravel into motion and the rate of deposition from motion. Assuming an active layer formulation, stochasticity in particle motion is introduced by considering the step length as a random variable. For step lengths with a relatively thin (e.g., exponential) tail, the above formulation leads to the standard advection-diffusion equation for tracer dispersal. However, the complexity of rivers, characterized by a broad distribution of particle sizes and extreme flood events, can give rise to a heavy-tailed distribution of step lengths. This consideration leads to an anomalous advection-diffusion equation involving fractional derivatives. By identifying the probabilistic Exner equation as a forward Kolmogorov equation for the location of a randomly selected tracer particle, a stochastic model describing the temporal evolution of the relative concentrations was developed. The normal and anomalous advection-diffusion equations are revealed as its long-time asymptotic solution. Sample numerical results illustrate the large differences that can arise in predicted tracer concentrations under the normal and anomalous diffusion models. They highlight the need for intensive data collection efforts to aid the selection of the appropriate model in real rivers.

Further, several experimental studies showed the presence of non-Gaussian pdfs of the sediment transport rates and also the elevation fluctuations [51, 52, 53]. Recent studies have presented evidence that PDFs of bed elevation and sediment transport rates depend on time scale (sampling time), but this dependence is not accounted for in any previous stochastic models of sediment transport. Motivated by the need to explain this rich multi scale structure of the sediment transport rates, in Chapter 6 we propose an extension of Brownian motion, called fractional Laplace motion, as a

model for sediment transport that acknowledges the fact that the time over which the gravel particles are in motion is in itself a random variable. We show that this model reproduces the multiscale statistics of sediment transport rates as quantified via a large-scale laboratory experiment.

2.3 Transport in net depositional landscapes

In this section, we will explore the applicability of non-local transport models to the net depositional systems. In these systems, the amount of net deposition in the system balances the rate of subsidence. Deltas are formed at the mouth of the rivers owing to the deposition of the sediment that is carried by the rivers. Deltas around the world are recognized to be one of the most vulnerable ecosystems. Understanding delta dynamics and developing predictive models that form the basis of delta restoration are the need of the hour. What are the system dynamics of a delta and how does a delta system self-organize into a dynamical structure that sustains its subaerial structure?

Three distinct time scales were identified in the evolution of deltaic systems [54, 55]. The two end members of the time scales of evolution of the deltaic system are a "short" time scale (time scale of evolution of bed forms and bars) and a "long" time scale (time scales of basin wide deposition), which are deterministic in nature. On the short time scales the channels in the deltaic system behave coherently and deterministically in response to the sediment routing system, and the long time scale represents an upper bound on which autocyclic variability sums to produce the average behavior of the sedimentary system [54]. Sandwiched between these two deterministic time scales is an intermediate time scale, where the deltaic system is driven by the so-called "mesoscale" dynamics.

The mesoscale time range is the domain of stochastic behavior associated with avulsion and reorganization of the fluvial system. This stochastic behavior was acknowledged as early as the work of Leeder [56], in which fluvial basins were filled by channels avulsing at a constant frequency to random locations. Figure 2.7 shows a plan view of an experimental delta basin, which clearly shows the presence of channels of varied range of scales and also the braided structure of the channels. Braided channels have been extensively studied for their statistical structure and it has been documented that

they have a fractal structure [e.g., 57, 58, 59, 60]. Sapozhnikov and Foufoula-Georgiou [58] also showed that the evolution of braided channels exhibit dynamic scaling. Further, channels can be viewed as the fast transport paths (or least resistant) of sediment transport. The heterogeneity in the channel lengths should then reflect in the sediment travel distances. Also evident from Figure 2.7 is the presence of both mobile and immobile phases of transport in the system, i.e., the sediment particle is in motion when its location is occupied by a channel and the sediment particle is at rest when its location is not occupied by a channel. The frequency of the channel visits to a given location should be dependent on the avulsion frequency and the statistics of channel avulsions should reflect in the waiting times of the sediment particles. Some of the basic questions that this thesis research explores are the following: (a) which probability distributions describe the processes that govern the depositional dynamics of the system and (b) what physical mechanisms leave their signature on the pdfs that govern the surface evolution?

Figure 2.7: Plan view of an experiment under near steady state conditions in the Experimental EarthScape (XES) facility located at Saint Anthony Falls Laboratory, University of Minnesota. Figure reproduced from Voller and Paola [6].

Unlike net erosional systems, in net depositional systems the signature of the evolution of the Earth's surface is not only imprinted on its form but also is selectively

preserved in the stratigraphic record. The architecture of the preserved stratigraphy is a function of three characteristics of the depositional system: (a) topography of the actively evolving surface, (b) kinematics of topographic evolution, and (c) rate of net deposition [54, 61, 62]. Quantitative analysis of stratigraphy exposed in outcrops or imaged in seismic data coupled to numerical modeling of sedimentary basin filling has blossomed over the last 30 years, initiating with the pioneering works of Leeder [56] and Allen [63]. The general goal for many of these studies was to develop tools to invert stratigraphic data for paleoenvironmental conditions. Of the many challenges associated with inverting the stratigraphic record one of the greatest is characterizing how large-magnitude but infrequent events (e.g., avulsions, storms, floods) influence the dynamics of depositional systems and how this information gets stored in stratigraphy. Characterizing these large magnitude infrequent events is challenging because many of these events have recurrence intervals with intermediate time scales ($10^1 - 10^4$ years) which make them difficult to study directly or to constrain using dating techniques [55]. One of the goals of this thesis is to make advances in the statistical mapping of the surface dynamics of depositional systems into the architecture of stratigraphy.

Stratigraphy preserved in alluvial basins selectively records information of the associated Earth-surface dynamics and holds important information for reconstructing past environmental conditions. However, erosional events erase part of the space and time record of the Earths surface evolution in the stratigraphic column. In Chapters 7 and 8 we explore, through the use of physical and numerical experiments, the forward problem, that is, how the probabilistic structure of the processes that govern the evolution of depositional systems relates to the probability distributions of the hiatus lengths in time and the preserved bed thicknesses of the stratigraphic column. We show that the extreme variability in the hiatus lengths in time, as evidenced by the heavy-tailed nature of their probability distribution, results in the non-ergodic nature of the stratigraphic column, which in turn leads to the Sadler effect (the apparent dependence of deposition rate on time) [64]. Further, we show that the extremes associated with the erosional and depositional events, caused by the channel dynamics in the depositional system, largely cancel themselves out leaving no distinct imprint of their occurrence in the resulting stratigraphic column. We also show that the variability of surface elevation increments, as measured by the interquartile range of their probability distribution, has a robust

and well-defined relationship with the preserved mean bed thickness, thus providing a means of statistically inverting the stratigraphic record to infer the associated surface dynamics.

Cross-stratified units are one of the most common features preserved in the stratigraphic record formed by migrating ripples and dunes. Their geometry has been understood to depend on the movement, change in shape, and direction of travel of the bed forms. In Chapter 9, we provide theoretical relationships that map the statistics of surface kinematics of bed form evolution into the 2-D geometrical structure of the preserved stratigraphy. The surface kinematics of bed form evolution is characterized by the migration (translation of the waveforms) and deformation (change in shape of the waveforms) of the bed forms. We show that the local slope and curvature of the preserved stratigraphic deposits depend on the competition between migration and deformation of the evolving bed forms. Further, we show that deformation is the sole cause for the formation of curved deposits in cross-stratified units and, for the first time, provide quantitative relationship between curvature of preserved strata and the deformation of the bed forms. The results presented in this study are validated using experimental data of bed form evolution collected under equilibrium, steady-state conditions with no net deposition.

Chapter 3

A nonlocal theory of sediment transport on hillslopes

In absence of overland flow-driven or wind-driven transport, the movement of soil on landscapes requires some kind of disturbance (Figure 3.1). This disturbance arises in many ways leading to a wide range of length scales of displacement. In clay-rich soils mantling sloping landscapes, periodic wetting of the ground may cause swelling and downslope flow, but even as the soils remain wet, progressively increasing grain resistance may halt motion. Drying and cracking then resets the contacts and allows another period of flow in the next wet season [65]. This cycle operates over some length scale of displacement. Simple wetting expansion and drying col- lapse through a season can incrementally shift near surface soils short distances downslope [e.g., 66]. Seasonal cycles of movement by ice-driven processes shift soils and during spring melt can give way as continuously moving solifluction lobes which may carry soil a considerable distance even on gentle slopes [e.g., 67]. Biota work the soil at a wide range of scales, leading to dilation and displacement downslope. Insects and worms may cause minor local displacement but through their persistent and pervasive activity cause significant movement [e.g., 68]. Burrowing animals can make an extensive network of tunnels and push piles of dirt meters downslope. The collapse of large trees may rotate and expose their root system and displace clumps of soil meters downslope [e.g., 69, 28]. The exposed, locally steep, tree throw mound and the smaller annual burrow mounds are sites

of accelerated rain splash, raveling and fine scale biotic disturbance. In effect, the biotic roughening of the ground surface by the local mound formation leads to accelerated soil movement. On sufficiently steep granular soils, fire may suddenly remove particles stored behind fallen woody debris and unleash particles to ravel downslope [e.g., 70], sometimes tens of meters. Shallow landslides may also initiate, mobilize, and redeposit on hillslopes. Soil movement, then, arises through the sum of stochastic processes, influenced by seasonal and biotic cycles, the integral of which is a net flux of soil which tends to increase with increasing hillslope gradient. The individual particle step lengths resulting from disturbances will vary greatly.

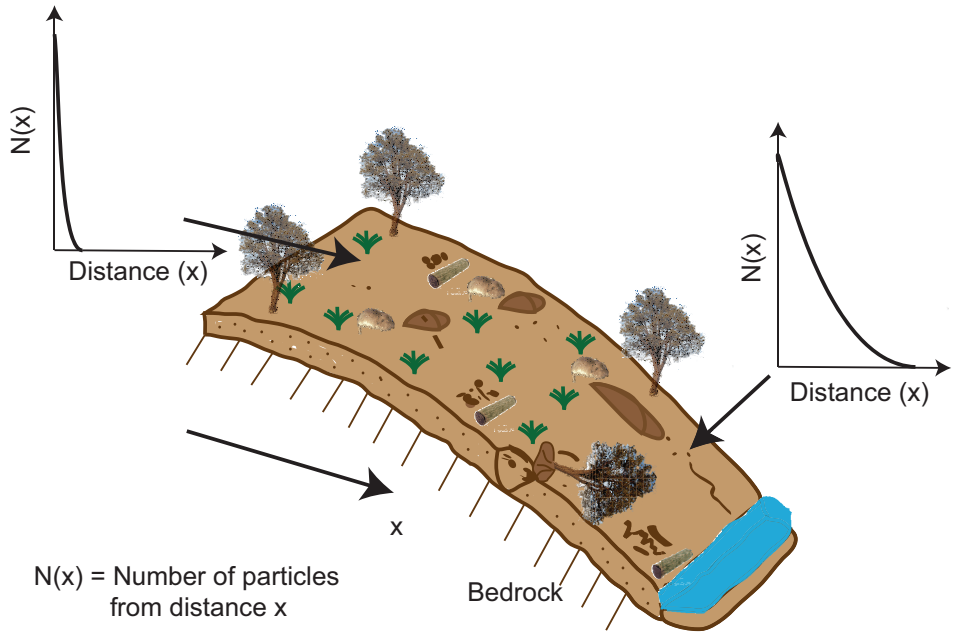

Figure 3.1: Cartoon illustrating processes such as gopher mounds, tree throws, and wood blockage, which contribute to sediment transport on a hillslope. Owing to the varied range of length scales of transport of these processes, the number of sediment particles arriving at a given location downslope is influenced by a region of upslope topography. This can be treated using the notion of a nonlocal flux (equation (3.8)) which is computed by a weighted average of upslope contributions.

On gentle hillslopes there is field evidence [e.g., 8] that the mean soil transport varies linearly with local gradient. On steeper slopes, however, theory and limited

observations suggest that transport increases nonlinearly with slope [e.g., 7]. Increasing field and theoretical evidence indicates that flux also depends on active transport depth [29, 71, 72]. In particular, Furbish et al. [72] show that a diffusivity-like coefficient which takes into account the local slope depth product produces a sediment flux which varies linearly with local gradient. Both linear and nonlinear flux laws assume that transport depends on some "local" slope, although we lack theory for what sets the length scale over which that slope should be determined. The disturbance by biota creates an irregular ground surface, with locally steep piles of loose soil that diffuse downslope across the mean slope (Figure 3.1). Hence, the slope at any point may not represent the actively contributing slope-driving processes, and cannot account for travel distances resulting from disturbances. If we could monitor every particle on a hillslope where these disturbance-driven processes (often placed together under the term "creep") occur, it is possible that long transport events occur with a finite, non-vanishing, non-exponentially decaying probability such that the pdf of transport distances is heavy tailed [e.g., 73]. This conception of soil transport may not be well represented by a transport expression that relates flux to a "local" slope. Moreover, the possibility of heavy-tailed particle travel histories makes selecting a meaningful mean slope for the application of such local laws problematic. To date, empirical fitting procedures (reducing variance by increasing the length scale of averaging while trying to maintain local profile curvature) have been used for the estimation of the local slope; common methods include polynomial fitting and Gaussian filtering [e.g., 7, 9].

Here we propose an alternative formulation of sediment transport on hillslopes which relies on the notion of nonlocal computation of sediment flux, reflecting the fact that mass flux at a point on the hillslope is being influenced by disturbances well upslope and not simply linked to local slope (and soil depth). Our analysis may also explain the variance in flux rate for a given local slope observed in some studies. Our theory, although not derived from physical considerations (e.g., involving balances of forces and resistances), presents a general mathematical framework within which the upslope influences to the sediment flux at a given point can be cast into a continuum constitutive law for sediment transport. Specifically, we propose a nonlocal formulation of transport laws which relies on an integral (non-Fickian) flux computation which explicitly takes into account the upslope topography from any point of interest. The proposed non-

local transport model includes linear diffusive transport as a special case.

This chapter is structured as follows. In section 3.2, we formulate the nonlocal constitutive law for sediment trans- port on hillslopes and in section 3.3 we derive its steady state equilibrium profile under appropriate boundary conditions. In section 3.4 we interpret observed hillslope profiles in the Oregon Coast Range, in the Appalachians of Maryland and Virginia, and east of San Francisco (California) within the nonlocal transport formulation. In section 3.5 we compare the linear, nonlinear and nonlocal transport models in several ways. The most important result is that the linear nonlocal model gives rise to a nonlinear relationship between sediment flux and local slope, akin to that observed on steep slopes. In section 3.6 we demonstrate that applying the non- local flux model to an ensemble of hillslope profiles produces significant variability of sediment flux for a given value of local slope as a result of variations in upslope topography. In section 3.7, we discuss the relationship between the shape of the probability density function of the sediment displacement lengths (which dictate the microscopic behavior of the transport process but which are typically not measured) and the parameter a of the nonlocal transport model (which describes the macroscopic properties of the transport). In section 3.8 we present some preliminary thoughts as to the ability of the nonlocal transport formulations to circumvent the scale dependence of sediment flux computed using local, nonlinear models. We conclude that our model shows the possibility that nonlocal sediment transport processes may be important on hillslopes and warrant more consideration both in field studies and theoretically. Our model anticipates more process-based considerations that would account mechanistically for biotic disturbance and it suggests that models for transport and weathering of colluvial soils and geochronological analysis of particles on steep hillslopes should consider the possible effects of nonlocal transport.

3.1 A Nonlocal Constitutive Law for Hillslope Sediment Transport: Convolution Fickian Flux

The simplest sediment flux law, proposed by Culling [32] in analogy to Fick's law of diffusion, expresses sediment flux as proportional to the topographic gradient:

$$q_s(x) = -K\nabla h \tag{3.1}$$

where q_s is sediment flux (volume per unit time per unit width: $L^3/L/T$) at location x (where x is distance from the ridgetop), K is the diffusivity coefficient (L^2/T), and h is the surface elevation with respect to a datum. It is easy to show [e.g., 74] that substituting (3.1) in the continuity (Exner) equation:

$$\rho_r \frac{\partial h}{\partial t} = \rho_r U - \rho_s \nabla . q_s \tag{3.2}$$

where ρ_s and ρ_r are the bulk densities of sediment and rock, respectively, and U is the rock uplift rate results in the linear diffusion equation:

$$\frac{\partial h}{\partial t} = -U + K\nabla^2 h \tag{3.3}$$

where we have assumed for simplicity that the bulk densities of rock and sediment are the same (which is almost never the case) and have ignored chemical erosion. (Note that equation (3.3) can also be derived using a moving coordinate system of erosion driven by diffusive transport in which the uplift term enters as a lower boundary condition.) If the rate of surface erosion is approximately balanced by the rock uplift, i.e., dynamic equilibrium [75, 76], then $\partial h/\partial t \approx 0$ and the steady state 1D case can be written as

$$\frac{\partial h}{\partial t} = 0 \iff \frac{\partial^2 h}{\partial x^2} = -\frac{U}{K} \tag{3.4}$$

Integrating twice and imposing the boundary conditions

$$h(0) = H_{top} = \frac{U}{2K} L^2 \tag{3.5a}$$

$$\frac{dh}{dx}|_{x=0} = 0 \tag{3.5b}$$

such that $h(L) = 0$ (river edge), the solution is given by

$$h(x) = H_{top} - \frac{U}{2K} x^2 \tag{3.6}$$

for $0 \leq x \leq L$ [e.g., 77]. Furthermore, the properties of the equilibrium hillslope profiles predicted by linear diffusion are (3.1) linear increase of local slope with down- slope distance and (3.2) constant curvature along the hillslope profile.

The underlying assumption of a classical diffusion equation is that the step lengths of sediment particles, defined as the distances traveled by the particles once entrained until

they are deposited again on the surface, have a thin-tailed (e.g., exponential or Gaussian) distribution [e.g, 3, 42]. However, for the reasons discussed in the introduction, the distribution of step lengths of sediment particles may be heavy tailed; that is, they have a small but significant chance of traveling a large distance downslope. In such cases, the sediment flux at a point x has a significant contribution from a large upslope distance and thus a local computation of flux, such as that of equation (3.1), is no longer appropriate. Recently, a particle-based model for sediment transport on hillslopes was developed based on a plausible set of rules capturing disturbance-driven transport processes and it was shown that a heavy-tailed step length distribution can emerge due to the interactions between these disturbances and micro-topography [73]. Here, we develop a continuum constitutive model for such a behavior. Specifically, we propose a notion of nonlocal sediment flux which takes into account the heavy tails in step lengths of sediment particles by expressing the sediment flux at a given point as a weighted average of the upslope topographic attributes:

$$q_s^\star(x) = -K^* \int_0^x g(l) \nabla h(x-l) dl \tag{3.7}$$

where $q_s^\star(x)$ is sediment flux(volume per unit time per unit width: $L^3/L/T$) at location x (where x is distance from the ridgetop), K^* is the diffusivity coefficient, $h(x)$ is the topographic elevation at location x, and $g(l)$ is a kernel performing a weighted average of local gradients upslope of the point of interest x as they contribute to the sediment flux at the point x (Figure 3.1). This is a special case of the more general convolution Fickian flux laws [78, 79]. It has been shown [22] that when the weighting function $g(l)$ has no characteristic length scale, i.e., when $g(l)$ decays as a power law with the lag l, $g(l) \sim l^{1-\alpha}$, (3.7) takes the form of a fractional derivative:

$$q_s^\star(x) = -K^* \nabla^{\alpha-1} h(x) \tag{3.8}$$

where $\alpha \in (1, 2)$. Substituting (3.8) in the continuity equation (3.2) and making the assumption that bulk densities of rock and sediment are equal, leads to a fractional diffusion equation:

$$\frac{\partial h}{\partial t} = U + K^* \nabla^\alpha h \tag{3.9}$$

The order of differentiation, α, directly relates to the heaviness of the distribution of step lengths [21, 80, 81, 3] and $1 < \alpha < 2$ implies a distribution of step lengths

with a finite population mean but infinite population variance (sample variance that diverges unstably as the number of samples increases) [82], resulting in an accelerated diffusion (superdiffusion). It is noted that for $\alpha = 2$, (3.8) becomes the standard Fickian flux (3.1), and (3.9) collapses to the linear diffusion equation (3.3).

The concept of nonlocal transport, implemented via fractional derivatives or Continuous Time Randon Walk (CTRW) models, has been extensively used in other fields of study, such as subsurface transport [e.g., 83, 27], transport of pollutants in rivers [84, 85], hydrodynamics [e.g., 23], statistical mechanics [e.g., 24, 26, 25], molecular biology [e.g., 86] and turbulence [e.g., 87, 88]. Recently, it has been used in geomorphology to encapsulate the nonlocality of bed sediment transport along bedrock channels [89] and to model the anomalous diffusion of tracer particles in gravel streams and sand bed rivers [42, 50]. A review of the application of partial fractional differential equations to the transport of solutes and sediment can be found in the work of [3].

3.2 Equilibrium Hillslope Profiles for Nonlocal Transport

In order to derive the equilibrium hillslope profile for the fractional diffusion equation (3.9) we note that under dynamic equilibrium, the steady state 1-D equation can be written as

$$\frac{\partial h}{\partial t} = 0 \iff \frac{\partial^\alpha h}{\partial x^\alpha} = -\frac{U}{K^*} \tag{3.10}$$

The two most commonly used definitions of a fractional derivative are the Riemann-Liouville and the Caputo forms [90]. These forms differ from each other in that the Riemann-Liouville definition expresses the fractional derivative as an integer order differential of a fractional integral (equation (11a)), whereas the Caputo definition expresses the fractional derivative as a fractional integral of an integer order derivative (equation (11b)):

$$\frac{d^\alpha h}{dx^\alpha} = \frac{d^n}{dx^n}\left(I_x^{n-\alpha} h(x)\right) \tag{3.11a}$$

$$\frac{d^\alpha h}{dx^\alpha} = I_x^{n-\alpha}\left(\frac{d^n h(x)}{dx^n}\right) \tag{3.11b}$$

where n is an integer such that $n-1 < \alpha < n$ and $I_x^{n-\alpha}(.)$ is a fractional integration operator of order $n-\alpha$. This distinction is important in the case of boundary-valued

and initial-valued problems as the Riemann-Liouville definition requires the calculation of the derivatives of the fractional integrals of the function at the initial value, whereas the Caputo definition only requires the calculation of initial values of the function and its integer derivatives (see [6] for a detailed discussion). It is further worth noting that the Caputo fractional derivative (equation (11b)) of a constant is zero, and in this form a fractional integral and a fractional derivative are commutative, whereas the Riemann-Liouville fractional derivative (equation (11a)) of a constant is a power law. Specifically, the α-order fractional integral of a constant c is a power function:

$$I_x^\alpha\{c\} = \frac{c}{\Gamma(1+\alpha)}x^\alpha \tag{3.12}$$

where $I_x^\alpha\{.\}$ is the fractional integral operator of order α, c is a constant and $\Gamma()$ is the gamma function [91]. Implementation of the fractional derivative on a finite domain $0 \leq x \leq L$ with boundary conditions, requires defining the functional value $h(x)$ beyond the left boundary that is for $x < 0$. In a boundary-valued problem, the Caputo form of the fractional derivative assigns the values of the function (in this case $h(x)$) beyond the boundary to be equal to the value of the function at the boundary, i.e., it inherently assumes that $h(?\infty)$ up to $h(0)$ are assigned the value of $h(0) = H_{top}$. This, however, is physically unreasonable as no sediment is supplied at the ridge from any point beyond the ridge. In order to circumvent this issue we numerically evaluate the steady state equilibrium hillslope profiles predicted by equation (3.10).

A fractional derivative can be discretized using the one-shift Grünwald expansion [92]:

$$\frac{\partial^{\alpha-1}h(x)}{\partial x^{\alpha-1}} \simeq \frac{1}{\Delta x^{\alpha-1}}\sum_{k=0}^{N} g_k h\left(x - k\Delta x + \Delta x\right) \tag{3.13}$$

where g_k are the one-shift Grünwald weights, Δx is the spatial grid size in the numerical evaluation, N is the number of node points upslope of the given point and $\partial^{\alpha-1}/\partial x^{\alpha-1}$ is the fractional differentiation operator of order $\alpha - 1$ ($1 < \alpha \leq 2$). The Grünwald weights are given as [93, 92]:

$$g_k = \frac{\Gamma(k-\alpha+1)}{\Gamma(-\alpha+1)\Gamma(k+1)} \tag{3.14}$$

Imposing the boundary conditions

$$h(0) = H_{top} = \frac{U}{\Gamma(1+\alpha)K^*}L^\alpha \tag{3.15a}$$

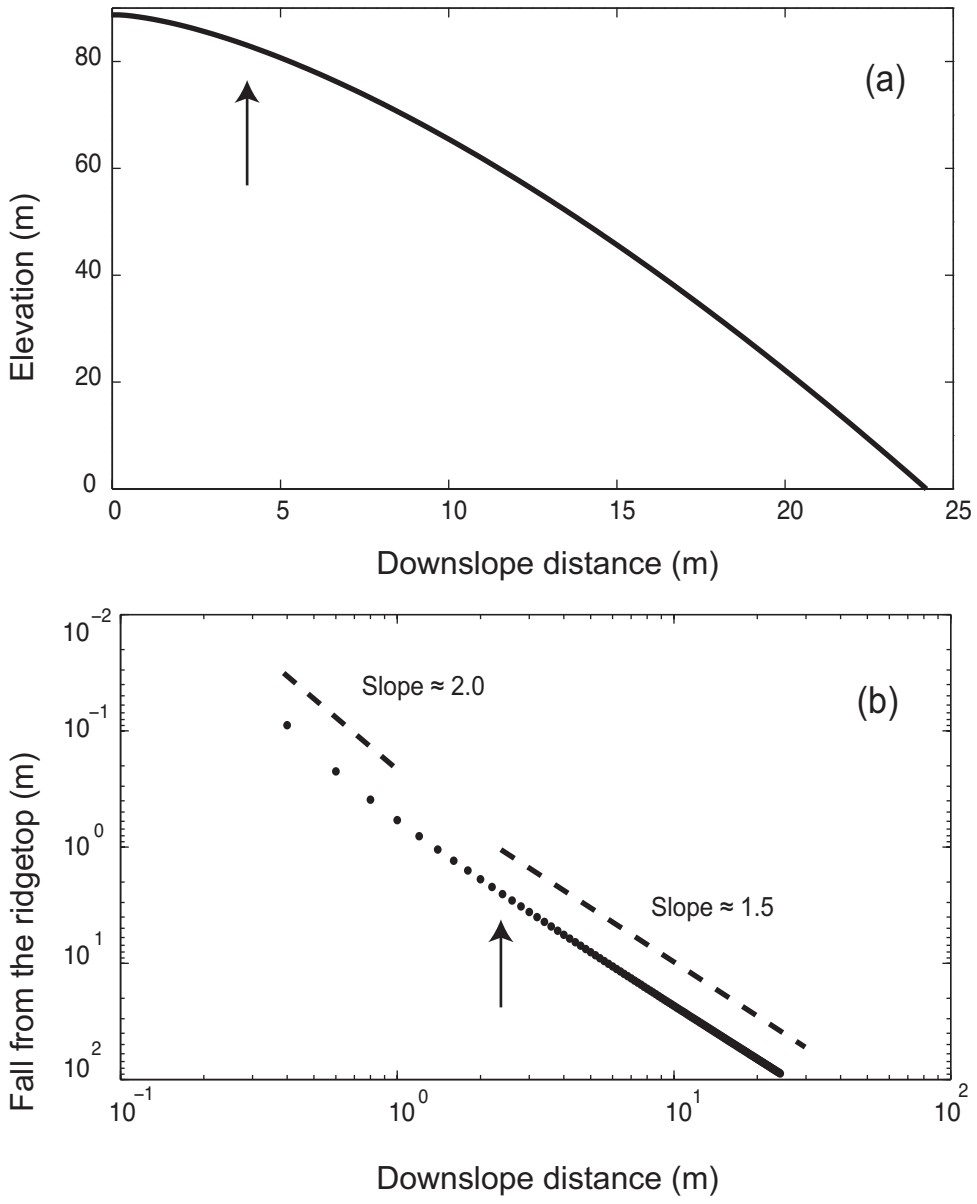

Figure 3.2: Steady state hillslope equilibrium profile predicted from fractional diffusive transport (equation (3.9)) with $\alpha = 1.5$ and boundary conditions of zero slope at the ridge and zero elevation at the most downslope point. The parameter of the model K^* was chosen to be 1.0 $m^{1.5}/yr$ and the rock uplift rate was set to unity $[m/yr]$ (Note that a different value of rock uplift rate would not change the shape of the profile but only its absolute elevation would differ). (a) Profile shape and (b) log-log plot of vertical drop from the ridge top versus downslope distance. Notice the transition to a power law profile with exponent $\alpha = 1.5$ at a distance of approximately 3 m from the ridgetop (arrow).

$$\frac{dh}{dx}|_{x=0} = 0 \tag{3.15b}$$

such that $h(L) = 0$ at the river edge, and imposing an additional condition that $h(x) = 0$ for $x < 0$ (since there is no sediment supply to the domain from any point beyond the ridge), one can solve numerically for the steady state equilibrium hillslope profiles predicted by equation (3.10). Figure 3.2(a) shows the hillslope equilibrium profile for fractional transport with degree of nonlocality $\alpha = 1.5$. It is noted that the hillslope profile is parabolic close to the ridge and transitions to a power law with an exponent of α.

It is worth noting that under the Caputo form of the fractional derivative (which assumes that the values of $h(x) = H_{top}$ for $x < 0$), equation (3.10) can be solved analytically. The analytical solution of equation (3.10) with the boundary conditions (3.15) and $h(x) = H_{top}$ for $x < 0$ is given as

$$h(x) = H_{top} - \frac{U}{\Gamma(1+\alpha) K^*} x^{\alpha} \tag{3.16}$$

where x is the horizontal distance from the ridgetop, and H_{top} is the elevation of the ridgetop. As shown in Figure 3.2(b), this solution is reached in the numerically evaluated profile (which assumes $h(x) = 0$ for $x < 0$) only at a finite distance downslope of the ridge when enough upslope topographic distance exists for the nonlocal contribution to substantially contribute to the sediment flux at a given point. Hence overall, the steady state hillslope equilibrium profile is parabolic near the ridgetop and becomes, shortly after, a power law profile with an exponent α (given by equation (3.16)). Further, we note that the steady state solution to the fractional diffusion equation predicts power law relationships of local gradient and curvature with downslope distance given by

$$-\nabla h \sim x^{\alpha-1} \tag{3.17}$$

$$\nabla^2 h \sim x^{\alpha-2} \tag{3.18}$$

That is, the fractional flux law predicts that curvature downslope of the ridge is not constant but decreases with downslope distance in a manner dictated by the exponent α (such a decrease has been documented, for example, in field observations in the work of

Roering et al. [7]). For $\alpha = 2$ the nonlocal transport model reproduces the linear profile in gradient and constant curvature with downslope distance, as expected for linear diffusive transport, while values of a between 1 and 2 give the flexibility of reproducing a suite of observed hillslope profiles. In section 4, we analyze field data from several real hillslopes and show that they are consistent with the nonlocal hypothesis of sediment flux.

3.3 Observed Hillslope Profiles Interpreted Within the Nonlocal Transport Theory

The one-dimensional nonlocal theory presented here applies to hillslope profiles in which transport is assumed to be only along that profile, i.e., a one-dimensional approximation. Hillslopes, however, typically have significant contour (planform) curvature (i.e., ridges and hollows) and at steady state such curvature can accommodate the increasing soil production that must be carried downslope such that a single profile along the hillslope can be straight even in the case of linear flux-dependent transport and spatially constant erosion rates. Only a few detailed studies of hillslope form and process have been reported on hillslopes without significant planform curvature. Here we reexamine three well-known study sites (one clearly lacking planform curvature) and interpret them within the proposed nonlocal flux theory.

Roering et al. [7] motivate their work on non-linear flux laws by reporting hillslope profiles in the Oregon Coast Range that clearly deviate from parabolic shape or constant curvature. Their study site experiences large scale disturbances due to massive tree throw mounds [29], mammal burrowing and periodic fire [70] and there is evidence for approximate steady state with considerable local variation over time scales of hillslope soil adjustment and development [7, 29, 94]. One of their profiles is shown in Figure 3.3(a) and the log-log plot of elevation fall versus horizontal distance (Figure 3.3(b)) suggests a slope of 1.3 for distances beyond 10 m downslope of the ridgetop and a slope of 2 close to the ridge (only 3 points are shown in Figure 3.3(b) at distance 0 to 10 m, but the slope of 2 is supported by more points obtained from the interpolated profile shown by the dashed line in Figure 3.3(a)). This profile is consistent with the nonlocal flux hypothesis and suggests that the nonlocal transport model proposed

herein might be an alternative to the nonlinear model of Roering et al. [7]. The conceptual bases of these two models are fundamentally different as they hypothesize different mechanisms of erosion and transport. This profile will be further analyzed in section 5.

In their seminal paper on the geomorphology and forest ecology of the Shenandoah River area of Virginia, Hack and Goodlett [36] report the result of plotting fall against distance for both their intensely surveyed study site and for a broad survey of 27 hillslopes in the Appalachians in Maryland and Virginia. They propose that the many regularities of the landforms and soils in the studied regions suggest steady state landscape adjustment. Ignoring the data points close to the divide, they report log-log linear profiles with a slope of 1.23 for the survey site and values ranging from close to 1 up to 1.7 for Maryland and Virginia. It is not clear how the broad survey data were collected (in the field versus from available topographic maps), nor whether they avoided slopes with planform curvature, but it is worth noting that the profiles do not include data points near the divide. They conclude that steeper hillslopes are generally straight (a values close to 1) and gentle ones more curved (a values closer to 2). Within our theory, this would suggest nonlocal transport on steeper hillslopes and local transport (linear diffusion) on gentle slopes. Hack and Goodlett [36] describe soil transport as being driven by "growing roots, burrowing animals, falling raindrops, frost, tree blowdowns and the like" (p. 58). These processes would create a wide range of transport distances for a given slope. Specific localities and erosion rates for the hillslope profiles are not reported, so we must consider this suggestion as only a possibility, not an established condition.

McKean et al. [8] selected a hillslope transect with minimal planform curvature in the grasslands east of San Francisco, CA underlain by marine shales and documented soil transport rates using 10Be concentrations in the clay-rich soils (Figure 3.4). From analysis of three soil pits within the first 35 m of hillslope length (from the ridge) they found evidence for a linear flux law and quantified the diffusive rate constant K (i.e., equation (3.1)). The soil transport occurs by seasonal creep of the high-plastic clay with biogenic transport being of some importance near the divide. Soil thickness varies inversely with curvature, consistent with a balance between soil production and linear transport [95, 96]. The thickness is about 40 cm near the ridge and then increases downslope. Boundary conditions (channel incision rate and history) strongly influence

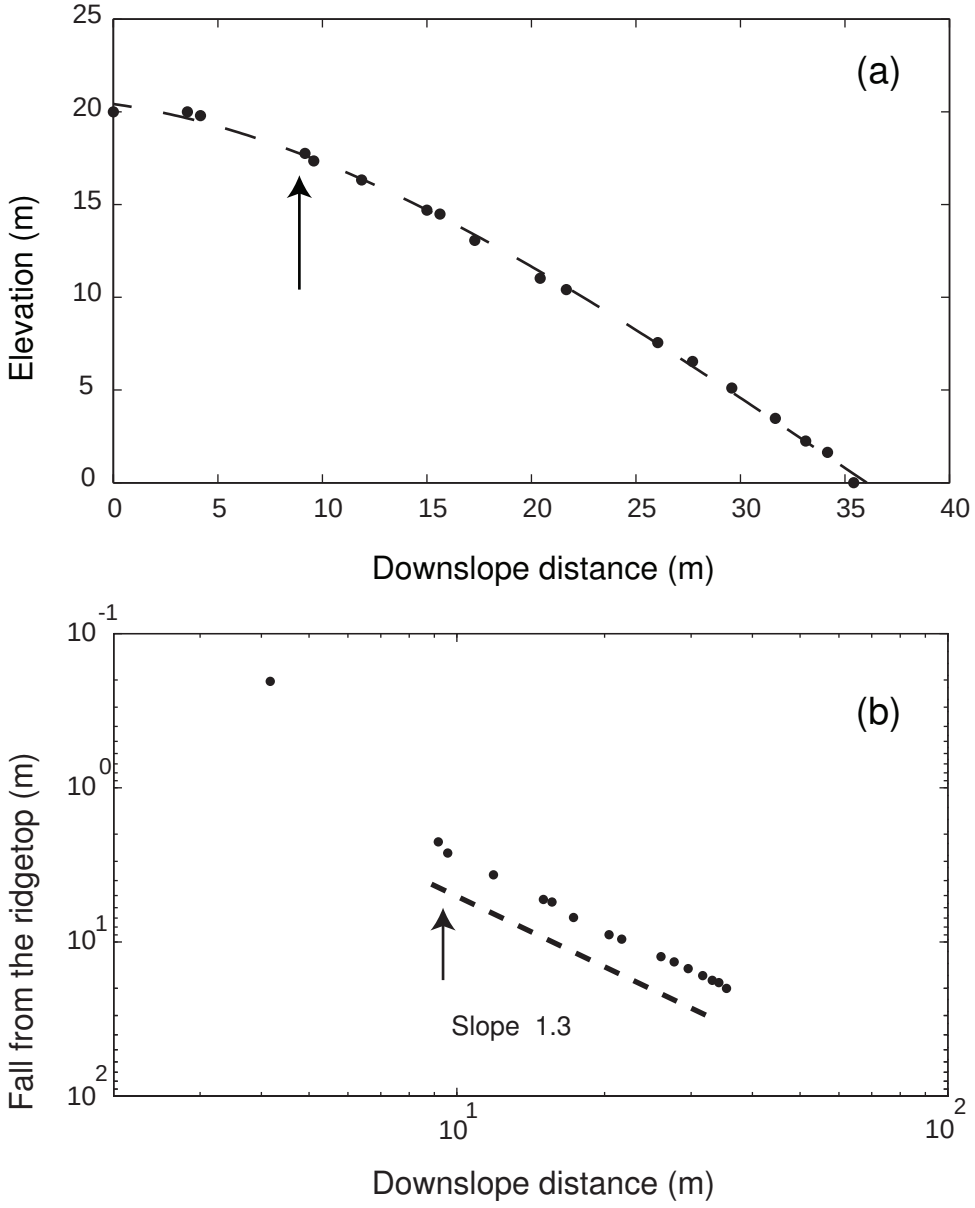

Figure 3.3: (a) A hillslope profile in the Oregon Coast Range. Solid circles represent the observed data points (reproduced from [7]) and the dashed line indicates a spline fit to the observations. (b) Log-log plot of the fall from the hilltop versus horizontal distance for the above profile. Notice the power law profile with exponent 1.3 starting at a distance of 9 m from the ridgetop (arrow) consistent with a nonlocal transport law with parameter $\alpha = 1.3$.

hillslope profiles and at this study site the hillslope terminates in a broad, aggraded valley, which has led to a break in slope at the base of the hillslope and progressive thickening of soil toward the valley axis [95]. Both Yoo et al. [95] and McKean et al. [8] suggest that the upper smoothly convex hillslope could be at approximate steady state erosion, that is, the effect of stabilization of the lower boundary has not reached to the divide.

We used the survey data collected by McKean et al. [8] to construct the longitudinal profile reported in Figure 3.4(a). By plotting on a log-log scale the elevation fall versus horizontal distance from the ridge (Figure 3.4(b)) we observe a slope of ≈ 1.8 from a distance of 8 m from the ridgetop up to approximately 25 m downslope; in the first 8 m from the ridgetop one would expect a parabolic profile (slope of 2). The hillslope rapidly flattens upslope from 8 m and the available survey data do not provide adequate constraint on the profile shape. The gentle hillslope gradient and high clay content (which favors creep) and the dry, grassy, relatively low biota mantle on the convex hilltop all would favor an almost local transport, and the slope value of 1.8 extending for the first 25 m is consistent with this expectation. Downslope of 50 m to the lowest portion of the hillslope surveyed the slope of the power law plot of elevation against distance is ≈ 1.2. This transition is not consistent with the nonlocal flux law of $\alpha = 1.8$ discussed above; rather the bottom part of the hillslope is interpreted as experiencing a change from net erosion to progressive soil accumulation (due to lower boundary conditions) and field observations support this interpretation. This example illustrates that the nonlocal flux theory can also be used as a diagnostic tool for inferring process from form and further motivate data collection to test alternative hypotheses.

3.4 Nonlocal Versus Nonlinear Flux: Same Behavior for Different Reasons

3.4.1 Nonlinear Transport Model as an Emulator of Superdiffusivity

Deviation from purely diffusive behavior in many hillslopes has prompted the development of more complex transport laws which have a nonlinear dependence on topographic gradient. A review of several of these laws can be found in the work of Dietrich et al.

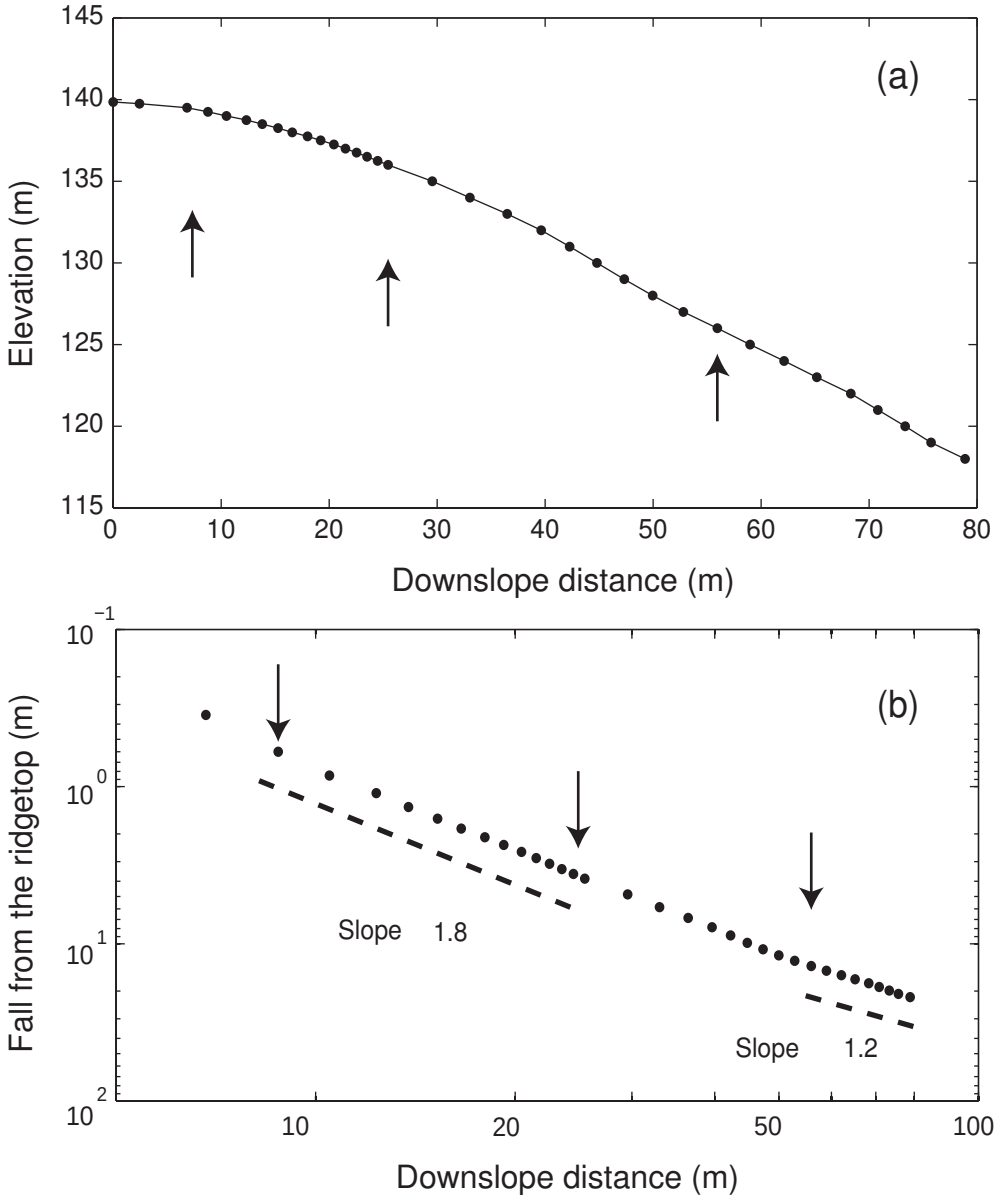

Figure 3.4: (a) Longitudinal profile of a hillslope reproduced from the survey data collected by McKean et al. [8]. (b) Log-log plot of the fall from the hilltop versus horizontal distance. Notice the power law regime with exponent 1.8 starting at approximately 8 m from the ridgetop until 25 m downslope. This profile is consistent with a nonlocal flux hypothesis with exponent $\alpha = 1.8$. The abrupt transition to a slope of 1.2 on the lower portion of the hillslope is indicative that this part is still experiencing changes from net erosion to progressive soil accumulation.

[17]. For example, for soil mantled hillslopes, Roering et al. [7] proposed the following flux equation (see also [35, 74]):

$$q_s' = \frac{-K\nabla h}{1-(|\nabla h|/S_c)^2} \tag{3.19}$$

where q_s' is the sediment flux calculated at a point via the nonlinear flux law, K is the diffusivity coefficient, and S_c is called the "critical gradient". It is noted that the above equation imitates a superdiffusive behavior, that is, close to linear diffusion at low slopes and accelerated diffusion at high slopes. Although this can be directly seen from (3.19), it is interesting to see it from a different perspective. By substituting (3.19) in (3.2) and performing a Taylor series expansion we obtain

$$\frac{\partial h}{\partial t} = K\nabla^2 h + K\frac{\nabla^2 h}{S_c^2}\left(|\nabla h|\right)^2 + \dots \tag{3.20}$$

The second term in the RHS of (3.20) shows that the nonlinear transport law of (3.19) captures the superdiffusive behavior at high slopes by enhancing the regular diffusion with the addition of a term that has an explicit nonlinear dependence on gradient. The gradient in the above equation is "local". We propose that such superdiffusive behavior in steep hillslopes can be addressed using nonlocal transport laws, which are linear (i.e., they involve only linear combinations of local gradients) but take into account that disturbances contributing to sediment flux at a point of interest have an origin far upslope of that point. It is interesting to note that the proposed nonlocal flux law gives rise to a nonlinear dependence of sediment flux on the local gradient at any point (this will be presented in section 5.2) but for reasons different than the explicit quadratic dependence of flux on local gradient as in equation (3.20).

3.4.2 Nonlocality Gives Rise to a Nonlinear Dependence of Flux on Local Gradient

We use the hillslope profile from the Oregon Coast Range [7] to illustrate the computation of the sediment flux from the nonlocal transport model of (3.8) and compare it to those of the linear (3.1) and nonlinear (3.19) models. In order to have a continuous set of elevation data points over the domain of interest, the observations were interpolated using a spline as shown in Figure 3.3(a) with dashed lines.

The computation of the fractional flux was performed on a discrete grid of size Δx by the Grünwald-Letnikov discrete approximation of the fractional integral operator given as [93, 97]

$$\nabla^{\alpha-1}h(x) = I_x^{2-\alpha}\{\nabla h(x)\} = \lim_{\Delta x\to 0}(\Delta x)^{2-\alpha}\sum_{k=0}^{x/\Delta x}\frac{\Gamma(2-\alpha+k)}{k!\Gamma(2-\alpha)}\nabla h(x-k\Delta x) \quad (3.21)$$

It is noted that writing the fractional flux as a fractional integral of the local slopes (first equality in the above equation) is enabled by use of the Caputo definition of the fractional derivative (equation (3.11b)).

The parameters chosen for the three flux laws (linear, nonlinear and nonlocal) are $K = 0.0015\ m^2/yr$, $S_c = 1.4$, $\alpha = 1.5$ and $K^* = 0.0007\ m^\alpha/yr$. The model parameters for the nonlinear flux law are chosen from the ones calibrated for Oregon Coast Range in the work of Roering et al. [7]. For the nonlocal flux law, α is set to 1.5 and K^* is chosen such that all the three flux laws show a similar increase in sediment flux with slope at lower gradients. This is done in order to study the effect of the three flux laws at the higher gradients. Figure 3.5 shows the sediment flux computed using the three different flux laws. The sediment flux computed from the nonlocal transport law (3.8) shows a similar behavior as the nonlinear, local transport law (equation (3.19)), with enhanced diffusion at higher gradients. Hence, a nonlinear relationship between sediment flux and local gradient can also arise from a nonlocal, linear flux model. It is emphasized that in a real hillslope, the parameters K for the non-linear model and K^* for the nonlocal model are obtained via calibration; the unfamiliar units of K^* (L^α/T) are not an issue and simply reflect that the quantity $(K^*t)^{1/\alpha}$ maintains the units of length (length scale of diffusion) in analogy to the quantity $(Kt)^{1/2}$ for standard diffusion [e.g., 1].

3.4.3 Nonlocality and Upslope "Region of Influence"

The nonlocal transport law differs from any local transport law (linear or nonlinear) in that in the former, the sediment flux contribution to a given point on the hillslope is computed from a weighted average of the topographic gradients upslope of that point. Therefore, unlike the local transport laws, the nonlocal transport law has a "memory" of the upslope topography. Although the power law kernel $g(l)$ of the nonlocal integral flux (equation (3.7)) implies lack of characteristic scale over which the averaged gradient

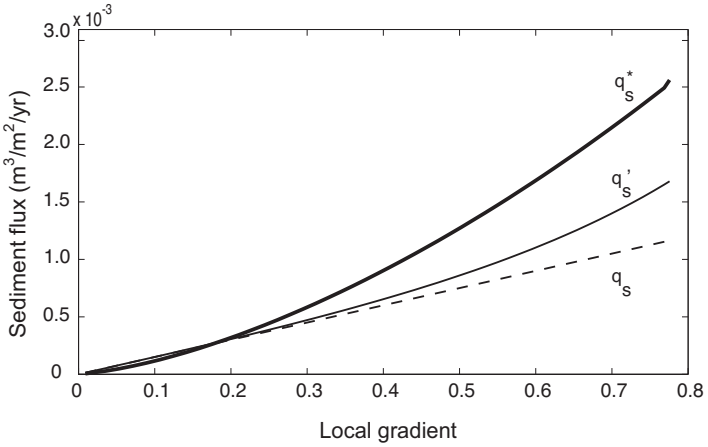

Figure 3.5: Comparison of the three flux laws. The dashed line shows the sediment flux predicted by linear, local flux law (equation (3.1)). The thick line shows the sediment flux predicted by the linear, non-local law (equation (3.8)), and the thin line shows the sediment flux predicted by local, non-linear law (equation (3.19)). The parameters for q_s' are chosen to be $K = 0.0015\ m^2/yr$ and $S_c = 1.4$ (from [7]). The parameters for the calculation of $q_s^\star$ are chosen to be $\alpha = 1.5$ and $K^* = 0.0007\ m^{1.5}/yr$.

is computed, we take the liberty below to introduce a cutoff scale in order to illustrate this upslope influence effect. Specifically, we introduce a physically tangible measure of nonlocality for the computation of sediment flux by defining an influence length, La, as the distance upslope from a given point, beyond which the contribution of the sediment flux is less than 10% of the total; that is, L_α is defined by the equation

$$K^* \int_0^{L_\alpha} g(l) \nabla h\,(x - l)\, dl \approx 0.9 q_s^\star(x) \tag{3.22}$$

where $g(l) \sim l^{1-\alpha}$ $(1 < \alpha < 2)$ are the weights given to the gradients uplsope and $q_s^\star$ is the nonlocal flux calculated by (3.8). The cutoff of 10% is chosen here arbitrarily to illustrate the behavior of nonlocal flux and it can be chosen to be lower or higher depending on the problem at hand.

The influence length was calculated for the Roering [7] profile from equation (3.22) for three different values of a and is shown in Figure 3.6. The degree of non-locality increases with a decrease in α; that is, the closer the value of α is to 1.0 the more nonlocal the transport is compared to a value of α closer to 2. As expected, a higher degree of nonlocality results in a larger value of L_α as seen in Figure 3.6. For $\alpha = 2$,

equation (3.22) is not applicable for computation of the influence length. In this case, the step lengths have a thin-tailed distribution whose characteristic scale (standard deviation) can be used to define the influence length.

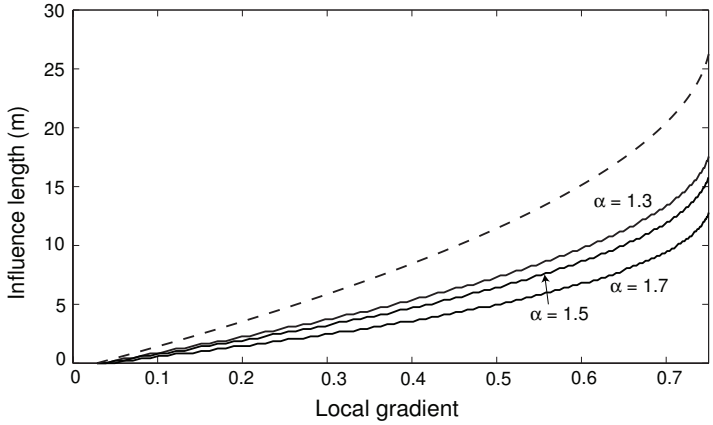

Figure 3.6: Plot showing the upslope influence length La (see text for definition) as a function of local gradient and degree of non-locality for the hillslope of Roering et al. [7]. The dashed line indicates the distance to the ridgetop, in other words, the maximum available distance to take part in the transport.

3.5 Nonlocality Naturally Reproduces Spatial Variability of Sediment Flux

In section 5, all the flux laws were discussed in the context of a single hillslope profile. However, even in a small hillslope, there exists considerable variability in the form of hillslope profiles which results in a considerable variability in the observed sediment flux. This flux variability was documented by Roering et al. [7] for the MR1 basin of Oregon Coast Range. They computed the sediment flux using

$$q_s = U\frac{\rho_r}{\rho_s}\frac{a}{b} \tag{3.23}$$

where U is the constant rock uplift rate, ρ_r and ρ_s are bulk densities of rock and sediment, respectively, and a/b is the drainage area per unit contour length, and compared it against the flux computed from their nonlinear transport model. Figure 3.7 (reproduced from [7]) shows the spread of the computed sediment flux as a function of gradient.

Notice that for a given gradient, say for a gradient of 0.8 there is an order of magnitude variability in the computed flux. To describe this variability with the nonlinear law, equation (3.19), the calibrated parameters of the model had to vary considerably: $K = 0.0015\ m^2/yr$ to $0.0045\ m^2/yr$ and $S_c = 1.0$ to 1.4 as reported by Roering et al. [7]. We note that S_c is a calibration parameter which was attached a physical meaning of a critical slope and was related to the angle of repose in the work of Roering et al. [7]; later in the work of Roering and Gerber [70] it was proposed that K increased and S_c decreased in response to forest fire.

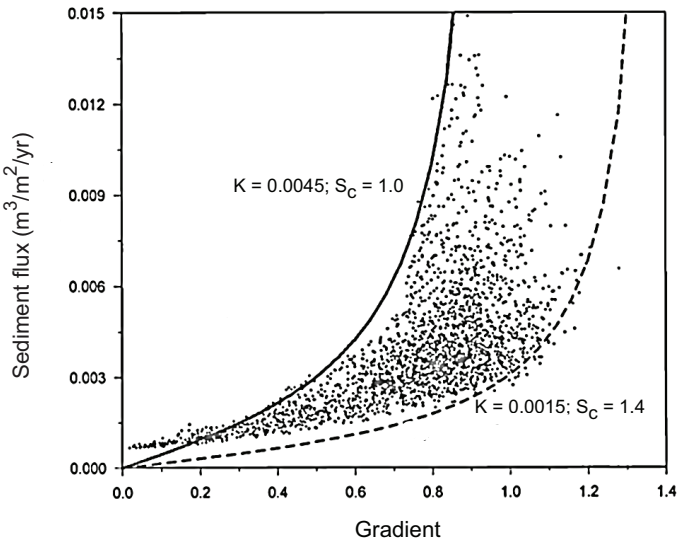

Figure 3.7: Reproduced from [7] to illustrate the large natural variability of calculated sediment flux (dots) even in a small hillslope (MR1 basin in Oregon Coast Range; sediment flux calculated using equation (3.23)) and the wide range of fitted parameters K (m^2/yr) and S_c that would be needed to reproduce the observed variability under the assumption of a nonlinear local transport law.

Here we pose the hypothesis that a non-local transport model can capture the observed variability of sediment flux within a given hillslope by a single or very narrow range of parameters, unlike any local transport law. To test the hypothesis, we generated a set of hillslope profiles using different cubic polynomials (see Figure 3.8) to imitate the natural variability of hillslope profiles within a small basin. Along those profiles the sediment flux was computed using the nonlocal, linear flux model (equation (3.8)) and local, nonlinear flux model (equation (3.19)). Figure 3.9 shows the computed sediment

flux as a function of the local gradient.

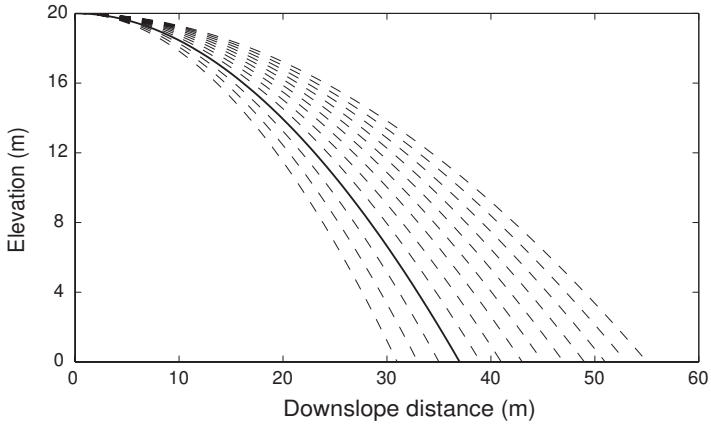

Figure 3.8: Plot showing the suite of generated hillslope profiles to imitate the natural variability of profiles (flow paths perpendicular to contour lines) in a zero-order basin. The thick line indicates the profile reproduced from [7].

The nonlocal transport law with a single set of parameters K^* and a produces a variability of sediment flux for a given gradient comparable to that observed in real hillslopes (Figure 3.7). However, the local transport law cannot reproduce this variability with a single set of parameters K and S_c but requires a considerable range of parameter values as indicated by the envelope curves in Figure 3.9. This is simply because two points with the same local slope would result in the same flux from any local transport law but different fluxes from a nonlocal law, due to different upslope topography. Having the need for such a wide range of parameters to reproduce the sediment flux variability in a small hillslope makes physical interpretation of those parameters difficult. Apart from the upslope hillslope profile variability considered here, there are other factors contributing to the sediment flux/local gradient variability, such as, for example, the dependence of K on soil depth [e.g., 71].

3.6 Probability Distribution of Particle Displacement and Fractional Transport

Sediment transport on hillslopes can be thought of as disturbance driven, in which soil is mobilized en masse or as individual particles. A single disturbance event may move the

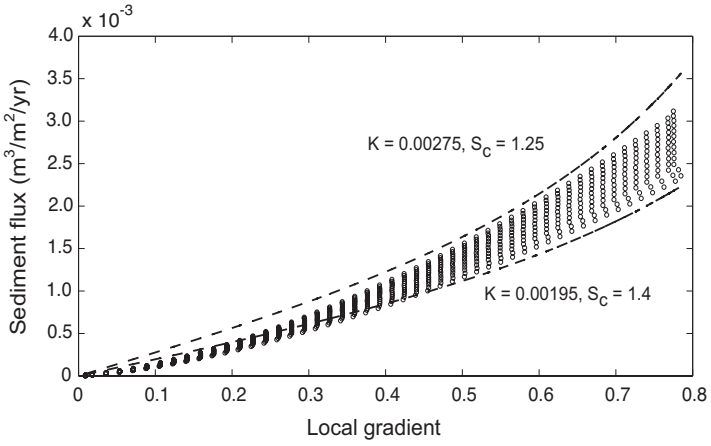

Figure 3.9: Sediment flux computed on the suite of hillslope profiles (shown in Figure 3.8) using the linear, nonlocal transport law (equation (3.8)) with parameters $\alpha = 1.5$ and $K^* = 0.0007\ m^\alpha/yr$ (open circles). Note that while these parameters are kept constant, a large variability of the sediment flux is produced due to the variability in the ensemble of profiles. In order to reproduce this variability with the nonlinear transport law (equation (3.19)), the range of fitted parameters required (concentrating on the higher gradients where the nonlinear transport law is more pertinent; see also Figure 3.7) is $K = 0.00195\ m^2/yr$ and $S_c = 1.4$ and $K = 0.00275\ m^2/yr$ and $S_c = 1.25$ (broken lines).

mobilized sediment a considerable distance (e.g., raveling after a fire). Disturbed piles of sediment (e.g., tree throw mounds) will create sustained local areas of elevated flux and increased downslope delivery. For simplicity we can think of event-based transport as a kind of "hopping" process, where the sediment moves downslope in a series of steps resulting from local disturbances. Here a single hop can be thought of as the distance covered by a grain of sediment from where disturbance has displaced it into an active flux state to where it comes to transient rest (until next disturbance). It can also be thought of as a package of sediment made significantly more active due to local mounding and exposure, say during a tree throw, which results in rapid flux compared to what would happen under mean slope conditions. As discussed in the introduction, many processes generate slope-dependent transport and operate over a wide range of distances. These processes may result in a heavy-tailed PDF of the sediment "hops" or displacement distance [see also 73], which means that there is a relatively small but significant possibility that sediment grains will move a great distance downslope in a

single hop. In other words, these distances do not have a characteristic length scale and may assume values comparable to the size of the hillslope itself.

If the PDF of hopping distances were thin-tailed, e.g., Gaussian or exponential with an e-folding distance small relative to the size of the hillslope, then the continuum equation describing the evolution of the hillslope would be the diffusion equation [20, 3]. However, if the probability distribution of hopping distances is broad tailed as argued above, then a faster than linear diffusion is expected. It turns out that, since a sum of broad-tailed pdfs results in an a stable distribution for the hopping process [20], then the governing equation of elevation change consistent with this distribution is the fractional diffusion equation (3.9) [21, 80, 3]. That is, the corresponding macroscopic process of sediment transport can be described using a modified diffusion equation where the ∇^2 operator is replaced with a nonlocal operator ∇^α. The degree of nonlocality is governed by the order of differentiation, α. The lower the value of α, the greater is the degree of non-locality. This is a manifestation of the fact that an α-stable PDF has a heavier tail for lower values of α.

3.7 Locality and Scale Dependence of Computed Flux

In this section we discuss some preliminary ideas related to the potential of nonlocal transport laws to circumvent the problem of scale dependence of sediment flux computations. We start with the classical divergence theorem and elementary control volume which is of little use when there is no characteristic scale in particle displacement distances. Then, we allude to the fact that local transport laws suffer from scale dependencies which would require closures [see, e.g., 98] and which can be naturally taken care of by the nonlocal transport laws.

The advection-dispersion equation (ADE) is based on the classical definition of divergence of a vector field. The divergence is defined as the ratio of total flux through a closed surface to the volume enclosed by the surface when the volume shrinks to zero [e.g., 18](see also [1] for an exposition relevant to subsurface transport):

$$\nabla . q_s = \lim_{V \to 0} \frac{1}{V} \iint_S q_s . \eta dS \tag{3.24}$$

where q_s is a vector field, V is an arbitrary volume enclosed by surface S, and η is a

unit normal vector. Implicit in this equation is that the limit of the integral exists; that is, the vector q_s exists and is smooth as $V \to 0$.

The classical notion of divergence maintains that, as an arbitrary control volume V shrinks to zero, the ratio of total surface flux to volume must converge to a single value. However, when a heavy-tailed distribution of displacement lengths exists, this notion of convergence is challenged. In fact, due to the lack of a characteristic scale of the displacement distances, no convergence is guaranteed when the size of the control volume changes. As a result, the classical diffusion equation is no longer self-contained with a closed form solution at all scales. To adopt the classical theory, the best approximation that can be done is to assume that the total flux to volume ratio can be assumed piecewise constant within small ranges of scales, allowing one to talk about an "effective" scale-dependent dispersion coefficient [see, e.g., 1]. Several techniques have been proposed in the subsurface transport literature to tackle the problem of scale-dependent dispersivity. These vary from small perturbation approaches and effective parameterizations [e.g., 99, 100], to power law dependence of D on scale [e.g., 101], to volume statistical averaging [e.g., 78, 79] and to fractional advection-dispersion equations (fADE) [e.g., 1, 102, 103, 81, 3].

Any sediment transport law that directly involves a "local" gradient or curvature in the computation of flux, will be scale dependent as gradients and curvatures depend on the scale at which they are computed [see, e.g., 9]. For example, this was demonstrated by Passalacqua et al. [98] using a local nonlinear flux law (a Langevin model which has square dependence on local slope). In that study, the development of a closure term, akin to the Large Eddy Simulation (LES) turbulence closures, was proposed to handle this scale dependence and the closure term was shown to have a power law dependence on scale (grid size). The proposed nonlocal fractional diffusive model has in principle the ability to remove this scale dependency as it is free of any "representative" or "control volume" concept and the power law integration of local gradients (see equation (3.21)) eliminates the need for the aforementioned power law closure [see, e.g., 19]. This issue requires further study.

3.8 Discussion and Conclusions

Most geomorphic transport laws proposed to date are local in character; that is, they express the sediment flux or erosion at a point as a function of the elevation gradient, contributing drainage area, or other geomorphic quantities at that point only. For the case of soil-mantled landscapes, it is reasonable to propose that disturbance processes inducing transport have widely varying transport distances and this gives rise to a non-locality of sediment transport, as proposed here. As summarized below, we see several advantages to the nonlocal transport law.

1. The proposed nonlocal transport model with boundary conditions of zero slope at the ridgetop and constant elevation at the ridge bottom predicts a steady state profile which is parabolic very close to the ridgetop and changes, after a short distance downslope to a power law with exponent equal to the parameter α (order of differentiation) in the fractional transport law. This prediction is supported by data in three study sites and provides useful insight for one of the sites which may still experience transition from net erosion to soil accumulation.

2. The non-local linear model gives rise to a non-linear relationship between the sediment flux at a point and the local slope. Hence, non-locality of sediment flux is an alternative hypothesis that can explain the observed hillslope profiles and the nonlinear flux dependence on slope.

3. In a practical implementation of a local sediment flux law (linear or nonlinear), the "local" slope is always assigned a "scale" over which some smoothing or averaging is done, without however a theory as to how to select this scale. The nonlocal flux law is scale free (it lacks a characteristic scale of upstream particle displacement distance); rather it uses a "power law weighted average slope" stating that upslope hillslope gradients matter to local flux, but with diminishing influence as a function of upslope distance.

4. The proposed nonlocal model produces significant variability of sediment flux for a given local slope, as it explicitly takes into account variations in upslope topography. In this case, transport parameters, such as K^*, can remain constant,

and retain, perhaps, a stronger physical meaning while reproducing the variability observed in real hillslopes.

5. The nonlocal model has the potential to eliminate scale dependency. The usefulness of nonlocal fractional models to address issues of scale dependence in subsurface transport (e.g., scale-dependent dispersivity in porous media with multiple scales of heterogeneity) has been amply demonstrated and needs to be explored for similar problems on the Earth's surface.

Chapter 4

A sub-grid scale closure for nonlinear hillslope sediment transport models

4.1 Introduction

The generation and movement of sediment on hillslopes has been the subject of continuous theoretical and field work since the pioneering conceptualizations of Gilbert [104, 75] and the mathematical formalisms introduced later by Culling [32, 33, 34]. Culling [33] proposed that the magnitude of the average rate of downslope sediment flux depends linearly on the magnitude of the local gradient:

$$q_{s,L} = K_L |\nabla z| \tag{4.1}$$

where $q_{s,L}$ is the volumetric sediment transport rate per unit contour length, z is local hillslope elevation, $|\nabla z|$ is the magnitude of the local hillslope gradient, and K_L is the proportionality constant (a diffusion-like coefficient) which depends on climate and material. The value of K_L has been estimated from a variety of approaches including field and experimental tests (e.g., see [105] and [106] for reviews) and process-specific derived models [e.g., 107, 108, 109]. Excellent reviews and further references can be found in [17] and [110].

The linear slope-dependent sediment transport model of equation (4.1) has been found inadequate to explain the observed sediment flux on steep slopes (slopes in excess of 20%) and nonlinear sediment transport models have been proposed [e.g., 111, 112, 113, 114, 115, 35, 116, 117, 74, 7, 108]. A nonlinear sediment transport model widely used is of the form:

$$q_s = \frac{K|\nabla z|}{1 - (|\nabla z|/S_c)^2} \tag{4.2}$$

where q_s is the magnitude of the nonlinear sediment flux, K is a diffusivity, and S_c is the so-called critical gradient. The above equation has been derived from different assumptions and theories and has been verified by field and experimental studies [35, 7, 118, 71]. From equation (4.2) one observes that at small gradients, the nonlinear flux model imitates linear diffusive transport. However, as local gradients approach a critical threshold gradient (S_c), the nonlinear flux model depicts an accelerated diffusion on hillslopes and the magnitude of the nonlinear sediment flux approaches infinity. The diffusivity and the critical gradient (K and S_c) are calibrated parameters [e.g., 7, 30]. Both equations (4.1) and (4.2) use the magnitude of the local gradient at every pixel to compute the sediment flux at that location. We will call both these transport models as "local", linear and nonlinear, respectively. The local sediment transport models inherently assume the existence of a representative elementary volume (that incorporates the heterogeneities of the landscape) where the model can be applied.

Recently, a new approach has emerged motivated by the observation that the scales of transport or particle displacement on hillslopes span a wide range as a result of very heterogeneous disturbance processes (such as gopher mounds, rain splash, wood blockage, tree throw, etc) [11, 119]. Thus, there is no separation between the scales of transport and the scale of the system itself, putting in question the standard local gradient theory formulations [e.g., see review in 2]. Non-local theories of sediment transport on hillslopes have been proposed using discrete particle-based models [73] or a fractional diffusion continuum formulation [11]. The continuum non-local model takes the general form:

$$q_s^\star(x) = K^\star \int_0^x g(l) |\frac{\partial z(x-l)}{\partial x}| dl \tag{4.3}$$

where $q_s^\star$ is the magnitude of the non-local flux, $K^\star$ is the measure of the diffusivity, $g(l)$ is a weighting function which takes into account the upslope history of the system, and

x is the distance from the ridgetop along the hillslope flow path. When the weighting function takes a power-law form, $g(l) \sim l^{1-\alpha}$ where $1 < \alpha \leq 2$, then the above equation can be cast into a fractional diffusive flux model for sediment transport on hillslopes [11]. The non-local transport models are inherently scale-free and do not assume the existence of a representative elementary volume.

It has been discussed in the literature that the computation of local gradients and many of the geomorphic and hydrologic quantities (e.g., width function, channel initiation threshold, topographic index, etc.) of a catchment are strongly dependent on the resolution of the digital elevation models (DEMs) used [e.g., 120, 121, 122, 123, 124, 125, 126, 17, 127, 98, 128, 19] and even on the gridding methods used in building the DEM [e.g., 129, 130]. Hence, any local sediment transport model (linear or nonlinear) that is a function of the local gradients will be scale-dependent. For example, using 90 m or 30 m DEMs will result in different local gradients than those computed from a 1 m DEM. How then is the scale-dependence of gradients to be handled in computing the sediment flux from equations (4.1) or (4.2)? One can argue that this can be handled by appropriate calibration of the flux equation to local data to yield an effective (scale-dependent) parameter K [117]. This is unsatisfying in the long-run as this parameter loses its physical meaning. At the same time both equations (4.1) and (4.2) physically apply at some scale that is assumed to the representative elementary control volume for the application of the local sediment transport models (e.g., determined to be the scale which averages over biotic processes [131]). For example equation (4.2) has been derived from ballistic particle transport considerations [35] or from the balance of frictional and gravitational forces at a scale below which topography is dominated by biotic processes [7, 131]. Thus, in principle if equations (4.1) and (4.2) were to be applied at length scales greater than the scale of the pre-defined representative elementary volume, new mean field equations would need to be derived via upscaling. These mean field equations will not only involve the same model formulation evaluated at the larger scale, but would also involve additional terms which take into account the variability that lies within the scale of application. The additional terms are called the sub-grid scale closure terms as they account for the sub-grid variability of the landscape and need to be taken into account while applying flux models at larger scales. In simple words, applying flux models at a larger scale would not simply involve keeping the model equation intact

and tuning the parameter K, but it would instead involve the addition of a closure term to incorporate the variability of gradients within the scale of averaging.

The scope of this study is to put forward in a formal way the scale-dependence of the local, nonlinear sediment flux models (Section 4.2), and to derive the closure term for the nonlinear sediment flux model of equation (4.2) (Section 4.3). The parameterization and the applicability of the proposed sub-grid scale closure model are discussed in Sections 4.4 and 4.5, respectively. Finally, we present preliminary analysis that points in the direction that the non-local transport model of equation (4.3) can be scale-independent (Section 4.6). To demonstrate the above concepts we use the 2 m lidar topography of a small basin within the Oregon Coast Range. Conclusions and recommendations for further work are given in Section 4.7.

4.2 Scale-dependence of local nonlinear transport models

In this section we demonstrate via an example the scale-dependence of the magnitudes of local gradients and the computed sediment flux using DEMs at different resolutions. We used lidar data from a small watershed (MR1) within the Oregon Coast Range, near Coos Bay, Oregon, collected at a resolution of approximately 2 m (see Figure 4.1). Details about this site can be found in [7].

Computation of local gradients and curvatures at different scales requires a "smoothing" and a corresponding "differencing" filtering of the landscapes. The simplest smoothing filter is the arithmetic averaging in which local gradients and curvatures are the first and second order differences of the smoothed landscape at the corresponding scale. A much more efficient way of implementing both the smoothing and differencing filtering in a single operation is the wavelet-based methodology proposed by Lashermes et al. [9]. A nonlinear filtering framework for smoothing landscapes that enhances the geomorphic features present in the landscape was proposed by Passalacqua et al. [132] (comparison of the performance of the nonlinear filtering framework and the wavelet-based methodology was shown in [133]). To be consistent with the upscaling framework used here to derive the sub-grid scale closure (Section 4.3), a simple moving averaging of the landscape in boxes of size $\Delta \times \Delta$ m^2 has been used as the smoothing filter and first and second order differencing operations have been performed to compute the local

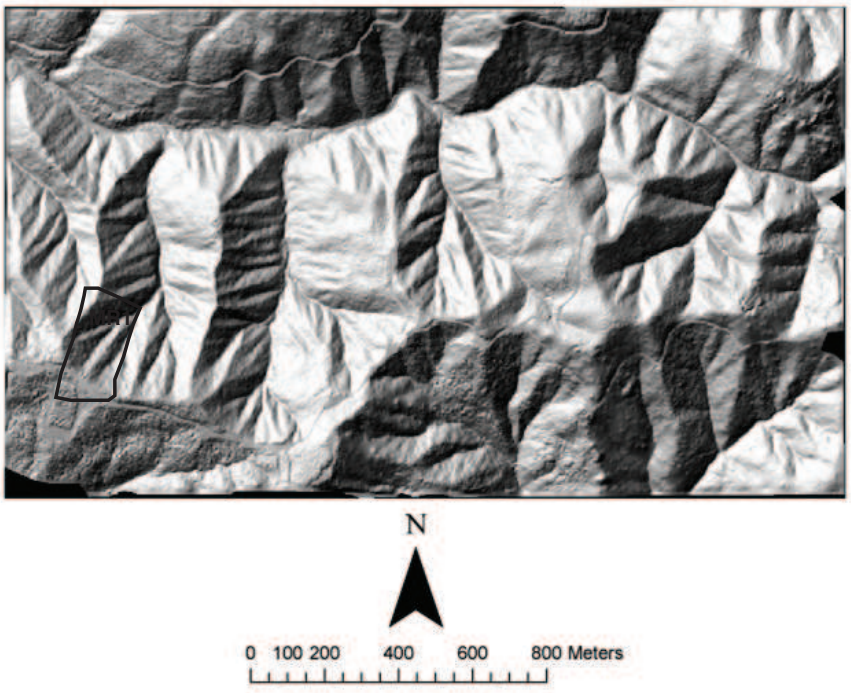

Figure 4.1: High resolution topographic data of a 2.8 km^2 area in the Oregon Coast Range near Coos Bay, Oregon. The MR1 basin used in this study to demonstrate the scale-dependence of nonlinear hillslope flux model is indicated. The resolution of the data is approximately 2 m.

gradients and curvatures at that scale Δ. The results reported here are not sensitive to the choice of the smoothing and differencing filter and similar results were obtained using the wavelet-based methodology.

To evaluate the sediment flux q_s from the hillslope pixels of the study site, one needs to first remove the pixels corresponding to the fluvial or channelized parts of the landscape. For this purpose we use the methodology proposed in [9] that is based on the curvature quantile-quantile plot, where any pixel with curvature above a critical threshold value (equal to the curvature value corresponding to the standard normal deviate of 1), which inherently emerges from this quantile plot, corresponds to channelized parts of the landscape (as discussed in [132] these pixels correspond to the pixels around the centerline of the channels). Figure 4.2(b) displays the quantile-quantile plot of the

curvatures and determines the threshold value of 0.1 as the one that delineates hillslope pixels from valleys and channels. Excluding all the pixels for which $\nabla^2 z > 0.1$ yields the pixels of the study site over which the nonlinear hillslope sediment flux model of equation (4.2) was applied (see Figure 4.2(c)). The model parameters used for the computation of the nonlinear sediment flux from the MR1 basin were $K = 0.0032\ m^2/yr$ and $S_c = 1.25$ (see Table 1 in [7] for calibrated values of the parameters for the Oregon Coast Range). The scales over which the above computations were performed ranged from 2 m (resolution of the data) to 30 m (which is the measure of the length scale of hillslopes obtained from the wavelength corresponding to the scaling break in the power spectral density of lateral elevation transects, taken perpendicular to the trunk stream, of the MR1 basin shown in Figure 4.2(d)). For scales larger than 30 m, valley-forming processes dominate the landscape that would require a different transport model.

For the hillslope pixels of the MR1 basin, Figure 4.3(a) shows the probability density function (pdf) of the magnitude of the local gradients at different scales Δ. It is observed that the pdfs change with scale not only in shape but also in terms of the mean value $|\overline{\nabla z}|$. Figure 4.3(b) shows the numerically evaluated pdf of q_s, $f(q_s)$, using equation (4.2) on the hillslope pixels of MR1 and for scales $\Delta = 2, 10$ and 30 m. To gain more insight into how the pdf of slopes projects via the nonlinear relationship (4.2) into the pdf of sediment fluxes q_s we show in Figure 4.4 a detailed example of the numerical evaluation for $\Delta = 2$ m. It is observed from Figure 4.4 that the nonlinear shape of the q_s vs $|\nabla z|$ relationship changes the shape of the pdf of $|\nabla z|$ to a more skewed pdf for q_s (since high values of $|\nabla z|$ produce disproportionately large amount of sediment flux). This change of shape of the pdf via the transformation of $|\nabla z|$ to q_s implies that plugging the average local gradient value into equation (4.2) at a given scale will not result in a good approximation for the average sediment flux at that scale (in fact, it severely underestimates the average sediment flux). This is because the nonlinear relationship in equation (4.2) implies that $\overline{N(x)} \neq N(\bar{x})$ (where $N(\cdot)$ is some nonlinear function of x), that is:

$$\overline{q_s} = \overline{\frac{K|\nabla z|}{1 - (|\nabla z|/S_c)^2}} \neq \frac{K|\overline{\nabla z}|}{1 - \left(|\overline{\nabla z}|/S_c\right)^2} \tag{4.4}$$

where the overbar indicates the expected value of the quantity. To get a better approximation of the average flux $\overline{q_s}$ at scale Δ one needs to consider not only the mean

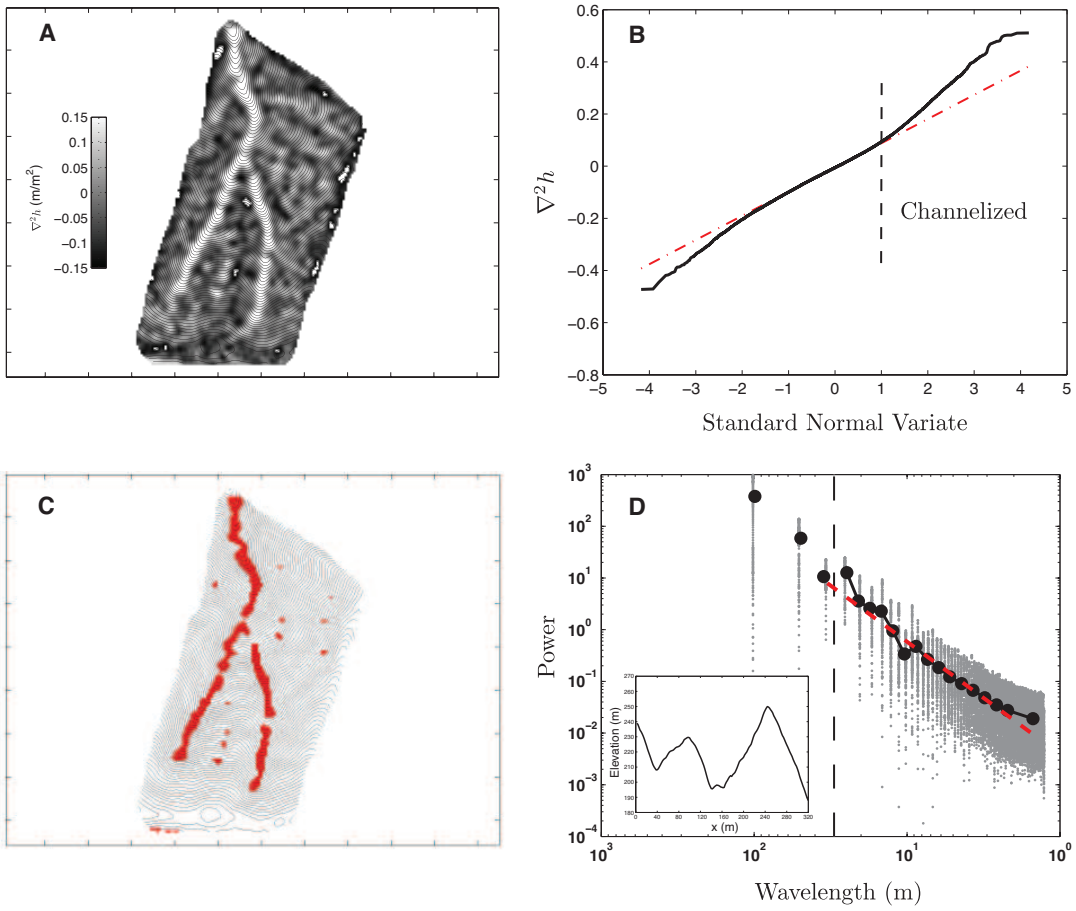

Figure 4.2: (A) Curvature map of the MR1 basin with the 2 m contour lines overlaid. (B) Quantile-quantile plot of the Laplacian curvatures in the MR1 basin. The deviation of the positive curvature from normality (a straight line in this plot) can be used to identify the channelized pixels as shown by Lashermes et al. [9]. The threshold on curvature for delineating the channelized pixels was found to be $\simeq 0.1$. (C) Extracted likely channelized pixels of the MR1 basin (marked in red) using the curvature threshold of 0.1. The computation of the nonlinear hillslope sediment flux was performed on all the pixels of the MR1 basin except for the ones marked in red. (D) Power spectral density of the lateral elevation transects (taken perpendicular to the trunk stream every 2 m) of the MR1 basin. The change in the scaling regime of the power spectral density marks the length scale of hillslopes here considered approximately 30 m as shown with the vertical broken line. The inset plot shows an example elevation transect of the MR1 basin.

value of the local gradients within a box of size $\Delta \times \Delta$ but also their variability. On the contrary, the average flux $\overline{q}_{s,L}$ for the linear local relationship (4.1) can be exactly computed by evaluating equation (4.1) at the box-average slope. This is because for linear relationships: $\overline{L(x)} = L(\bar{x})$. In the next section, we derive the sub-grid scale closure for the nonlinear flux model of equation (4.2).

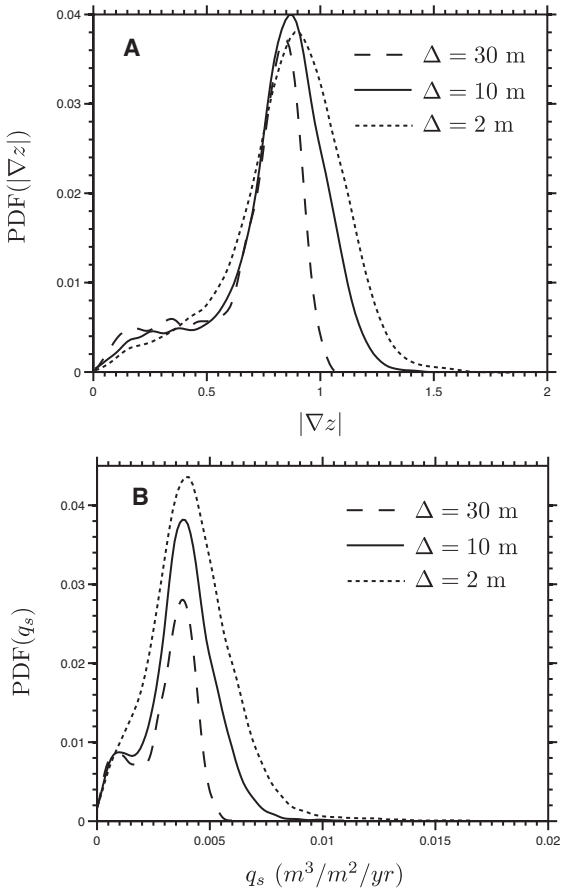

Figure 4.3: Change of probability density functions of (a) the magnitude of local gradients and (b) the magnitude of the nonlinear sediment flux (equation (4.2)) with scale Δ computed at the hillslope pixels in the MR1 basin (see Figure 4.4 for further discussion).

4.3 Derivation of closure for the local nonlinear transport model

The motivation for deriving the sub-grid scale flux for the nonlinear transport model of equation (4.2) is two-fold. Firstly, DEMs at the resolution of 1 m or 2 m are often unavailable thus forcing the application of the flux models at larger scales. Secondly, even when the high-resolution DEMs are available, the local gradients are computed at scales larger than 1 m to ensure robustness, remove noise, and to average over some stochastic processes such as biotic processes, frost action, etc., that shape the hillslope. Thus, the chosen scale for this computation often introduces unforeseen scale-dependent effects in the computation of sediment flux.

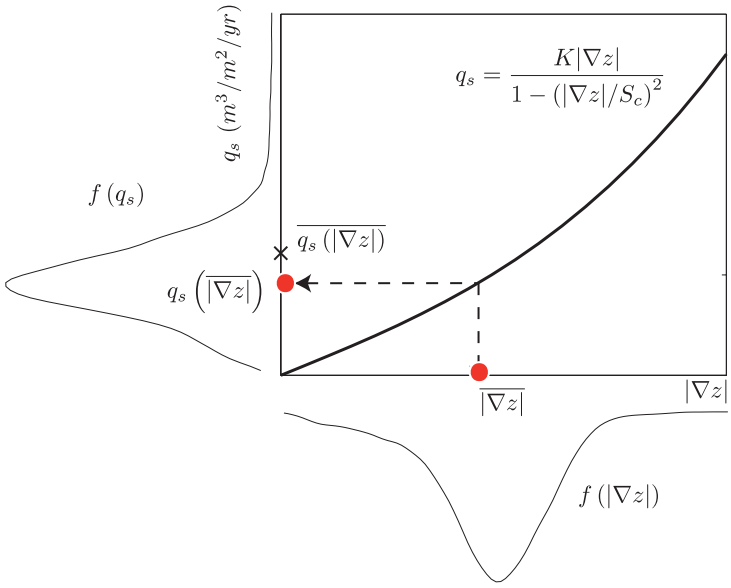

Figure 4.4: Using the nonlinear flux model of (4.2), we evaluate how the probability distribution of local slopes $|\nabla z|$ projects into a (derived) probability distribution of sediment flux q_s. We note that the nonlinearity of the functional relationship between $|\nabla z|$ and q_s implies that $\overline{q_s\left(|\nabla z|\right)} \neq q_s\left(|\overline{\nabla z}|\right)$. That is, computing the flux in a box of size $\Delta \times \Delta$ using the box-average gradient in the nonlinear flux model, $q_s\left(|\overline{\nabla z}|\right)$, is not the same as the arithmetic average of the sub-pixel fluxes $\overline{q_s\left(|\nabla z|\right)}$. This is due to the nonlinear relationship and the variability of gradients within the box of size $\Delta \times \Delta$. The values of the parameters used here are $K = 0.0032\ m^2/yr$ and $S_c = 1.25$ as reported in [7].

Consider the nonlinear sediment flux model of equation (4.2). For simplicity of notation, let us denote by S the absolute value of slopes $|\nabla z|$ at the smallest scale, i.e., the scale for which the model of equation (4.2) is theoretically derived. One can write the nonlinear flux model of equation (4.2) using Taylor series expansion as:

$$q_s = KS\left(1 + \left(\frac{S}{S_c}\right)^2 + \left(\frac{S}{S_c}\right)^4 + \cdots\right) \tag{4.5}$$

Since the local slopes are smaller than the critical gradient S_c, the ratio of S to S_c is always less than one and we can neglect the fourth and higher order terms in the series expansion as the contribution to the sediment flux from those terms is negligible (see Section 4.5 for a discussion of the effect of Taylor series approximation on the computed sediment flux). This simplification yields a simple polynomial relation of sediment flux which involves the first and the third powers of the local slope given by:

$$q_s \simeq KS + \frac{K}{S_c^2}S^3 \tag{4.6}$$

The computed sediment flux using equation (4.6) from all the hillslope pixels of the MR1 basin shows a strong dependence on scale, as seen from Figure 4.5 (open circles). The parameters of the nonlinear model used for the computation were $K = 0.0032\ m^2/yr$ and $S_c = 1.25$ [7]. Starting with equation (4.6), which applies at some pre-defined scale of the representative elementary volume, we derive the sub-grid scale closure, i.e., the term that needs to be added to this equation to account for the variability of local slopes within a box of size $\Delta \times \Delta$. We approach this derivation from two different viewpoints: (a) a physical consideration of upscaling the flux to derive a new mean field equation at larger scales, and (b) a statistical viewpoint where upscaling is considered as taking an expectation of the probability distributions of slopes at a given scale.

4.3.1 Subgrid scale closure: Physical viewpoint

Let us denote the upscaled flux at a given scale Δ as $\widetilde{q}_{s_\Delta}$. This flux can be computed by a filtering or upscaling of the right hand side of equation (4.6) as:

$$\widetilde{q}_{s_\Delta} \simeq \widetilde{KS + \frac{K}{S_c^2}S^3} \tag{4.7}$$

At every pixel of the landscape, the magnitude of the gradient, S, can be decomposed into its filtered component at scale Δ, $\widetilde{S}_\Delta$, and its fluctuation around the filtered component, S'_Δ, i.e., $S = \widetilde{S}_\Delta + S'_\Delta$. This operation is akin to the Reynolds decomposition or the Large Eddy Simulation approach used extensively in modeling turbulence [e.g., 134, 135, 136, 137, 138, 139, 140, 141, 142, 98].

Replacing in equation (4.7) the local slopes, S, by the sum of their filtered components, $\widetilde{S}_\Delta$, and their fluctuations, S'_Δ, and expanding the right hand side results in:

$$\widetilde{q}_{s_\Delta} \simeq K\widetilde{S}_\Delta + \frac{K}{S_c^2}\left((\widetilde{S}_\Delta)^3 + \widetilde{S'^3_\Delta} + 3\widetilde{S}_\Delta\widetilde{S'^2_\Delta} + 3\widetilde{S'_\Delta}(\widetilde{S}_\Delta)^2\right) \tag{4.8}$$

Noting that $\widetilde{S'_\Delta} = 0$ at any scale Δ (i.e., the average of the fluctuations around the mean is zero) the above equation after rearrangement simplifies to:

$$\widetilde{q}_{s_\Delta} \simeq K\widetilde{S}_\Delta + \frac{K}{S_c^2}(\widetilde{S}_\Delta)^3 + \frac{K}{S_c^2}\left(3\widetilde{S}_\Delta\widetilde{S'^2_\Delta} + \widetilde{S'^3_\Delta}\right) \tag{4.9}$$

By comparing equation (4.6) with the filtered equation (4.9), it is observed that they have the same form except for the additional term in the right hand side of equation (4.9). This term is the so-called sub-grid scale closure which needs to be added to the flux model of equation (4.6) if one uses the filtered slope, $\widetilde{S}_\Delta$, instead of the local slope S in equation (4.7) to guarantee scale-independence. The terms $\widetilde{S'^2_\Delta}$ and $\widetilde{S'^3_\Delta}$ in the closure represent the second and the third central moments of the slope fluctuations at the given scale Δ. Depending on the statistical nature of the landscape, the contributions of the second-order term (which contains $\widetilde{S'^2_\Delta}$) and the third-order term (which contains $\widetilde{S'^3_\Delta}$) will vary. Our goal is to demonstrate the effect that the variability of the slope fluctuations has on the computed sediment flux at different scales. Thus, we neglect the third order moment in the closure term and approximate the sub-grid scale closure term as:

$$\sigma_{sg}(\Delta) \simeq \frac{3K}{S_c^2}\widetilde{S}_\Delta Var(S'_\Delta) \tag{4.10}$$

where $\sigma_{sg}(\Delta)$ denotes the sub-grid scale flux at a scale Δ, and $Var\,(S'_\Delta) = \widetilde{S'^2_\Delta}$ denotes the variance of slope fluctuations within a box of size $\Delta\times\Delta$. From a geometrical point of view, smoothing the landscape is equivalent to piecewise linearization of the landscape in boxes of size $\Delta\times\Delta$ m^2 (i.e., fitting a plane to the landscape in boxes of size $\Delta\times\Delta$). The normalized slope fluctuations S'_Δ are a measure of the local curvature of the landscape.

Thus, the derived sub-grid scale closure, which is dependent on the slope fluctuations at that scale, S'_Δ, accounts for the deviation from the linearization approximation of smoothing (or the deviation of the landscape shape from the fitted plane in boxes of size $\Delta \times \Delta$). The nature of the sub-grid scale flux and its parameterization are discussed in section 4.4. In the next subsection 4.3.2 we derive the sub-grid scale flux from a statistical viewpoint.

4.3.2 Subgrid scale closure: Statistical viewpoint

Since the upscaling filter using arithmetic averaging is a linear operator, equation (4.7) can be broken down as:

$$\widetilde{q}_{s_\Delta} \simeq K\widetilde{S}_\Delta + \frac{K}{S_c^2}\widetilde{S^3_\Delta} \tag{4.11}$$

i.e., the sum of a linear and a nonlinear term: $q_s = L(S) + N(S)$. The nonlinear term involves the filtering of the third power of S which is not the same as the third power of the filtered term, i.e., $\widetilde{S^3_\Delta} \neq \left(\widetilde{S_\Delta}\right)^3$. The nonlinear term $\widetilde{S^3_\Delta}$ in the right hand side of equation (6.4) can be written in terms of the slopes at the resolved scale $\widetilde{S}_\Delta$ using the Taylor expansion which is given by:

$$\widetilde{N(S)} = N(\widetilde{S}_\Delta) + \frac{N''(\widetilde{S}_\Delta)}{2}Var(S'_\Delta) + \ldots = \frac{K}{S_c^2}(\widetilde{S}_\Delta)^3 + \frac{3K}{S_c^2}\widetilde{S}_\Delta Var(S'_\Delta) + \ldots \tag{4.12}$$

Neglecting the higher order terms in equation (5.29) and substituting it in equation (6.4) the sub-grid scale closure, which is given by $\sigma_{sg} = \widetilde{N(S)} - N(\widetilde{S})$, is the same as that in section 4.3.1 (equation (4.10)).

4.4 Parameterization of the sub-grid scale flux

The sub-grid scale flux (equation (4.10)) is dependent on the filtered components of the slopes at the given scale Δ, $\widetilde{S}_\Delta$, the variance of the slope fluctuations S'_Δ within boxes of scale Δ, $Var\,(S'_\Delta)$, and the parameters of the nonlinear flux model, namely, K and S_c. The filtered components of the slopes, $\widetilde{S}_\Delta$, were computed through a simple moving averaging filter (as detailed in Section 4.2) and the slope fluctuations were then determined by taking the differences of the filtered slopes and the slopes computed at the finest resolution of the landscape. By performing this computation over a range

of scales Δ, we gained access to the variance of the slope fluctuations and how this variance changes across the landscape. For a given scale Δ, the sub-grid scale variance $Var\left(S'_\Delta\right)$ depends on the location of the box of size $\Delta \times \Delta$ within the landscape. When high-resolution data are available, say at a scale of 1 m or 2 m, then the sub-grid scale closure term can be computed locally for each box of size $\Delta \times \Delta$ m^2 by estimating the variance of slope fluctuations within each box ($Var\left(S'_\Delta\right)$). The resulting sub-grid scale closure, which corrects for the sub-grid scale variability of slopes specific to each $\Delta \times \Delta$ box, is referred to here as the local sub-grid scale closure. Figure 4.5 (solid black circles) shows the sediment flux computed using the nonlinear flux model of equation (4.6) with the proposed locally-computed sub-grid scale closure. Figure 4.5 demonstrates that the proposed sub-grid scale term alleviates the scale-dependence that the nonlinear flux model suffers from (see open circles in Figure 4.5). The largest scale to which the computations were performed is equal to the scale of the hillslope, $\Delta = 30$ m (see Figure 4.2(d)), as beyond this scale the landscape is shaped by valley-forming processes.

The variance of the slope fluctuations, $Var\left(S'_\Delta\right)$, within boxes of size $\Delta \times \Delta$ needed in equation (4.10) requires data at scales smaller than Δ. In the absence of data at resolution higher than Δ, this quantity is unknown and we need to parameterize it in terms of the resolved quantities of the topographic data at scales larger than Δ (say 2Δ). This can be achieved by investigating the relationship between the variance of slope fluctuations within a given scale and the scale Δ. This parameterization can be done locally (for each pixel of the landscape) or globally for the whole landscape. In global parameterization we use the spatially averaged variance of slope fluctuations over the whole landscape ($\langle Var\left(S'_\Delta\right)\rangle$) as a first-order estimate of $Var\left(S'_\Delta\right)$ for each pixel at the given scale Δ. The standard error of this estimate for each pixel is quantified by the standard deviation of the variance of slope fluctuations, which quantifies the pixel-to-pixel variability of $Var\left(S'_\Delta\right)$ across the landscape. Figure 4.6 shows the functional dependence of these two quantities ($\langle Var\left(S'_\Delta\right)\rangle$ and $std\left(Var\left(S'_\Delta\right)\right)$) on scale for the hillslope pixels of the MR1 basin. A power-law relationship was found to provide a very good approximation of the functional dependence of the first two central moments of $Var\left(S'_\Delta\right)$ on scale, given by:

$$\langle Var\left(S'_\Delta\right)\rangle \sim \Delta^\beta \tag{4.13a}$$

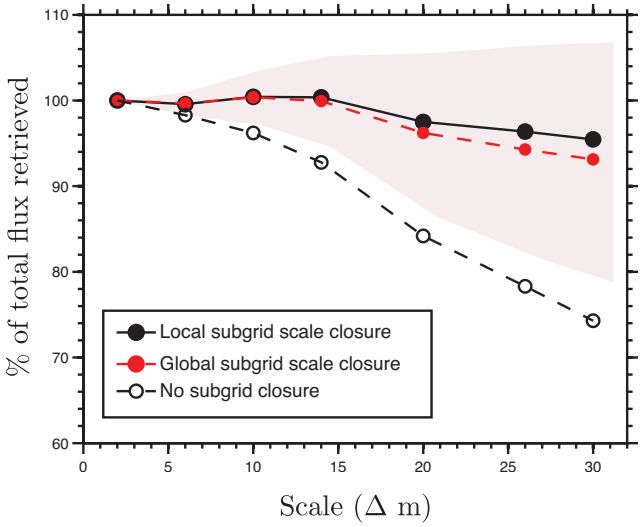

Figure 4.5: Plot showing the percentage of the total sediment flux computed from the hillslope pixels of MR1 basin that is retrieved at scales larger than $\Delta = 2$ m when compared with the flux computed at scale $\Delta = 2$ m ($\widetilde{q}_{s_\Delta}/q_s$). The open circles denote the sediment flux computed using the nonlinear flux model of equation (4.6) and the solid circles denote the sediment flux computed using the nonlinear flux model with the proposed second-order closure (equation (4.10)). The black solid circles indicate sub-grid scale closure term added locally for each box $\Delta \times \Delta$ across the landscape. The solid red circles indicate the flux calculated using the sub-grid scale closure parameterized using the global statistics of slope fluctuations across the basin. The shaded area denotes the standard error (evaluated from equation (4.10) by replacing $Var\left(S'_\Delta\right)$ with $std\left(Var\left(S'_{\lambda\Delta}\right)\right)$) in the estimate of the nonlinear flux with the global sub-grid scale closure parameterization. The values of the parameters used were $K = 0.0032\ m^2/yr$ and $S_c = 1.25$ (same as the values calibrated in [7]).

$$std\left(Var\left(S'_\Delta\right)\right) \sim \Delta^\gamma \tag{4.13b}$$

where $\langle\cdot\rangle$ denotes the expectation operator and $std(\cdot)$ denotes the standard deviation of the quantity in the parenthesis. This functional dependence provides us with a means of parameterizing the sub-grid scale flux in terms of the known quantities of the landscape. For instance, if one were attempting to compute the sediment flux from the nonlinear flux model at a scale Δ, an averaging (or filtering) operation would need to be performed on the DEM to compute the slopes at some larger scale $\lambda\Delta$ ($\lambda > 1$). Then the power law form that has been established in Figure 4.6 can be invoked to estimate the exponents,

β and γ, using:

$$\frac{\langle Var\left(S'_{\lambda\Delta}\right)\rangle}{\langle Var\left(S'_{\Delta}\right)\rangle} = \lambda^{\beta} \tag{4.14a}$$

$$\frac{std\left(Var\left(S'_{\lambda\Delta}\right)\right)}{std\left(Var\left(S'_{\Delta}\right)\right)} = \lambda^{\gamma} \tag{4.14b}$$

Once the power law exponents are estimated, the mean and standard deviation of the variance of slope fluctuations at the scale of interest can be extrapolated by using the computed mean and standard deviation of $Var(S'_{\lambda\Delta})$. This operation provides a "global" correction for the computed sediment flux over the whole landscape and thus this sub-grid scale term computed using global statistics is referred to here as the "global sub-grid scale closure". This can be viewed as informing the flux model with the information about the landscape statistics at higher scales to downscale the variability to an unknown smaller scale. This is a common approach to sub-grid scale parameterization in large-eddy simulation [e.g., 138] as well as in precipitation [e.g., 143] and soil moisture [e.g., 144] applications. Practically, the implication of this result is that if one were to have DEM data that is too coarse to get reasonable estimates of the sediment flux (e.g., ASTER or SRTM data), then one can quantify the sub-grid scale variance of the slope fluctuations within a given scale using the power-law relationships shown in Figure 4.6 and arrive at a reasonable estimate of the sediment flux by applying the sub-grid scale closure correction at each pixel of the landscape.

Figure 4.5 (solid red circles) shows the computed nonlinear sediment flux with the proposed global sub-grid scale correction from all the hillslope pixels of the MR1 basin (using the global average $\langle Var\left(S'_{\Delta}\right)\rangle$ value instead of the box-specific values of $Var\left(S'_{\Delta}\right)$ in equation (4.10)). The model parameters used were $K = 0.0032\ m^2/yr$ and $S_c = 1.25$. As seen in Figure 4.5, the global subgrid-scale correction performs only slightly worse than the local correction model even for scales larger than 20 m. In order to explicitly account for the uncertainty introduced by substituting the local variance of slope fluctuations by their spatially average value, the standard error of estimate was also computed (using the standard deviation of the variance of slope fluctuations available at any scale Δ and the power-law relationship established in Figure 4.6). This standard error of estimate is shown as the shaded area in Figure 4.5.

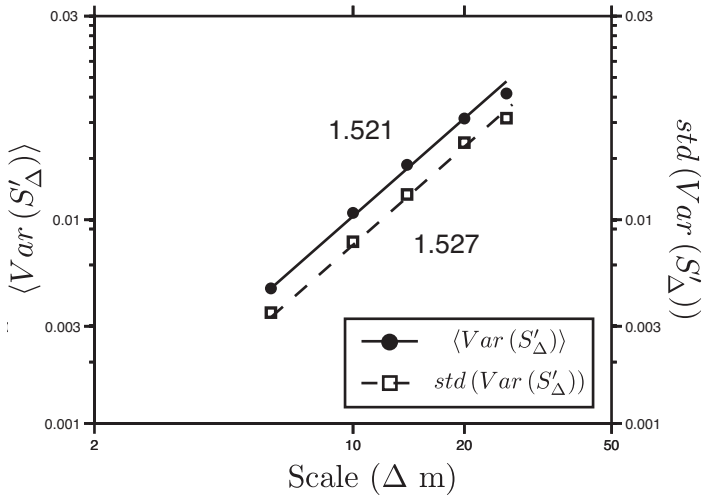

Figure 4.6: Plot showing the functional dependence of the mean and standard deviation of the variability of slope fluctuations, S'_Δ, on scale Δ in the MR1 basin. The power-law dependence on scale of the first two moments of the variance of slope fluctuations within the given scale, $(Var\,(S'_\Delta))$, allows one to parameterize the sub-grid scale closure of equation (4.10).

4.5 Applicability of the sub-grid scale closure model

As shown in Section 4.4, the proposed sub-grid scale closure model of equation (4.10), when applied to the MR1 sub basin of the Oregon Coast Range, alleviates much of the scale-dependence that the nonlinear hillslope sediment transport model suffers from. The natural question that arises then is: how general is this result and what attributes of a given landscape control the performance of the proposed sub-grid scale closure model? Critical to the derivation of the sub-grid scale closure is the Taylor series approximation of equation (4.2) and its truncation (neglecting the higher order terms in equation (4.5)). The Taylor series expansion of equation (4.5) does not capture the steep nonlinearity of the functional form of the nonlinear sediment flux model as the average slope of a hillslope approaches the critical value of S_c ($\overline{S}/S_c \rightarrow 1$) and, therefore, for such values of slopes equation (4.5) becomes an increasingly less accurate approximation of equation (4.2) . Thus, this polynomial approximation of the nonlinear sediment transport model would have a direct effect on the performance of the proposed sub-grid scale closure model. In this section, we will explore the applicability of the

proposed sub-grid scale closure model to real landscapes and highlight the primary physical controls on the accuracy of the proposed model.

Morphologic characteristics of hillslopes (e.g., average slope, hillslope relief) are known to depend on the interplay between tectonic forcings and the climate-dependent erosional processes, and several studies have quantified the dependence of different measures of topographic inclination on denudation rates (see [5] and references therein). To study the linkage between the hillslope morphology and denudation, one can combine the nonlinear sediment flux model with the one-dimensional, continuity equation given by:

$$\rho_s \frac{\partial z}{\partial t} = -\rho_s \frac{\partial q_s}{\partial x} + \rho_r U \tag{4.15}$$

where q_s is the nonlinear sediment flux, U is the rock uplift rate, t is time, x is the horizontal hillslope distance, and ρ_r and ρ_s are densities of rock and soil, respectively. Under the assumption of steady-state denudation $\partial z/\partial t \rightarrow 0$ (where the rate of bedrock erosion, E, is equal to the rate of rock uplift, U), Roering et al. [5] derived the one-dimensional, functional forms of the magnitude of local gradient ($S = |\partial z/\partial x|$) and hillslope elevation profiles predicted by the nonlinear sediment flux model in terms of the transport parameters (K and S_c), erosion rate (E), and material properties (ρ_r and ρ_s). Further, they showed that in dimensionless form, the magnitudes of local gradients (S^*) and the hillslope relief (R^*) can be expressed as [5]:

$$S^* = \frac{S}{S_c} = \frac{1}{(E^* x^*)} \left(1 - \sqrt{1 + (E^* x^*)^2} \right) \tag{4.16a}$$

$$R^* = \frac{\overline{S}}{S_c} = \frac{1}{(E^*)} \left(\sqrt{1 + (E^*)^2} - ln \left(\frac{1}{2} \left(1 + \sqrt{1 + (E^*)^2} \right) \right) - 1 \right) \tag{4.16b}$$

where E^* and x^* are independent dimensionless variables, and $\overline{S}$ is the average slope of the hillslope. The expressions for the dimensionless hillslope distance and dimensionless erosion rate were given by:

$$x^* = \frac{x}{L_H} \tag{4.17a}$$

$$E^* = \frac{E}{E_R} \tag{4.17b}$$

where L_H is the hillslope length (measured horizontally from the hilltop to the channel margin) and E_R is a reference erosion rate given by $E_R = KS_c/\left(2L_H\left(\rho_r/\rho_s\right)\right)$. As

seen from the above equations, the average slope and dimensionless hillslope relief of a hillslope are primarily controlled by the dimensionless erosion rate, E^*.

To quantify the accuracy of the Taylor series approximation of the nonlinear hillslope sediment flux model, we evaluated the steady-state magnitudes of the local gradients predicted by the nonlinear sediment flux model for various values of the dimensionless erosion rates. We then computed the total sediment flux from the hillslope profiles (whose magnitudes of local gradients are given by equation (4.16a)) using equations (4.2) and (4.6). The accuracy of the Taylor series approximation of the nonlinear sediment flux model can then be defined as the ratio of the total flux from the hillslope profile computed using equation (4.6) to the total sediment flux computed using equation (4.2). Figure 4.7 shows the functional dependence of the accuracy of the Taylor series approximation of the nonlinear sediment flux model as a function of the dimensionless erosion rate. The functional dependence of the dimensionless hillslope relief R^* on the dimensionless erosion rate E^* is also shown in this plot. As seen in Figure 4.7, the accuracy of the Taylor series approximation and thus the proposed sub-grid scale closure model reduces with an increase in the dimensionless erosion rate. For values of $E^* > 10$, the decrease in the accuracy of the Taylor series approximation of the nonlinear sediment flux is significant, as the polynomial approximation of the nonlinear sediment flux model does not capture the threshold behavior of the nonlinear sediment flux model (i.e., the sediment flux does not approach infinity, as the local slope approaches the critical value of S_c). This observation is a manifestation of the fact that hillslope profiles become increasingly planar with an increase in the dimensionless erosion rate and their average slope approaches the critical threshold value ($\overline{S} \rightarrow S_c$). Thus, the ratio of $\overline{S}$ to S_c approaches a value of 1 for higher values of E^* (see Figure 4.7) and the Taylor series approximation (given by equation (4.6)) does not adequately describe the nonlinear sediment flux model of equation (4.2). This result has a direct effect on the performance of the proposed sub-grid scale closure, as the derivation of the closure is built upon the polynomial approximation of the nonlinear sediment flux model of equation (4.2).

The reported values of the dimensionless variables for the Oregon Coast Range (of which MR1 is a sub basin) were $E^* \sim 6.33$ and $R^* \sim 0.64$ [5] and thus, from the theoretical relation in Figure 4.7, we note that the Taylor series approximation provides an adequate representation of the nonlinear sediment flux model of equation (4.2) for

this basin. This results in the good performance of the proposed sub-grid scale closure model as shown in Section 4.4. We plotted the dimensionless erosion rates and the dimensionless relief from the Oregon Coast Range, Gabilan Mesa (see Table 1 from [5]), and several catchments of the San Gabriel mountains (calculated from Table 1 of [10]) in Figure 4.7. The dimensionless relief for the catchments in San Gabriel mountains were computed (equation (4.16a)) using the values of average slope ($\overline{S}$) and the magnitude of the critical gradient (S_c) and the dimensionless erosion rates were computed (equation (4.17b)) using the reported values of the erosion rates (E), K, S_c, L_H, ρ_r and ρ_s in Table 1 of [10]. As seen in Figure 4.7, the Oregon Coast Range, Gabilan Mesa and some catchments of the San Gabriel Mountains have a low dimensionless erosion rate ($E^* < 10$), which enables one to apply the proposed sub-grid scale closure model to these field sites. We conclude that both the dimensionless erosion rate and the dimensionless hillslope relief are non-parametric measures of the accuracy of the proposed sub-grid scale closure and can be used to determine whether the proposed closure provides an accurate representation of the sub-grid scale fluxes for a given landscape.

4.6 Scale-independence of non-local flux model

In this section we put forth the hypothesis that the non-local sediment transport model is scale-independent and test this hypothesis using an example computation on a hillslope profile of the MR1 basin. The non-local flux model of equation (4.3) uses a linear combination of slopes along the flow path on the hillslope. Unlike the nonlinear flux model where the flux computation is performed at each pixel of the landscape, the non-local flux model takes into account the magnitude of local gradients of the upslope topography along the flow path. As shown in Foufoula-Georgiou et al. [11], when the convolution kernel, $g(l)$, in equation (4.3) takes a power-law form the non-local flux model can be cast into a fractional derivative form, given by:

$$q_s^\star(x) = K^\star \left| \frac{\partial^{\alpha-1} z}{\partial x^{\alpha-1}} \right| \tag{4.18}$$

where $q_s^\star(x)$ is the magnitude of the non-local sediment flux, $K^\star$ is a diffusion-like coefficient, $\partial^{\alpha-1}/\partial x^{\alpha-1}$ denotes the fractional derivative operator and x is the distance from the ridgetop along the flow path. The fractional derivative can be computed using

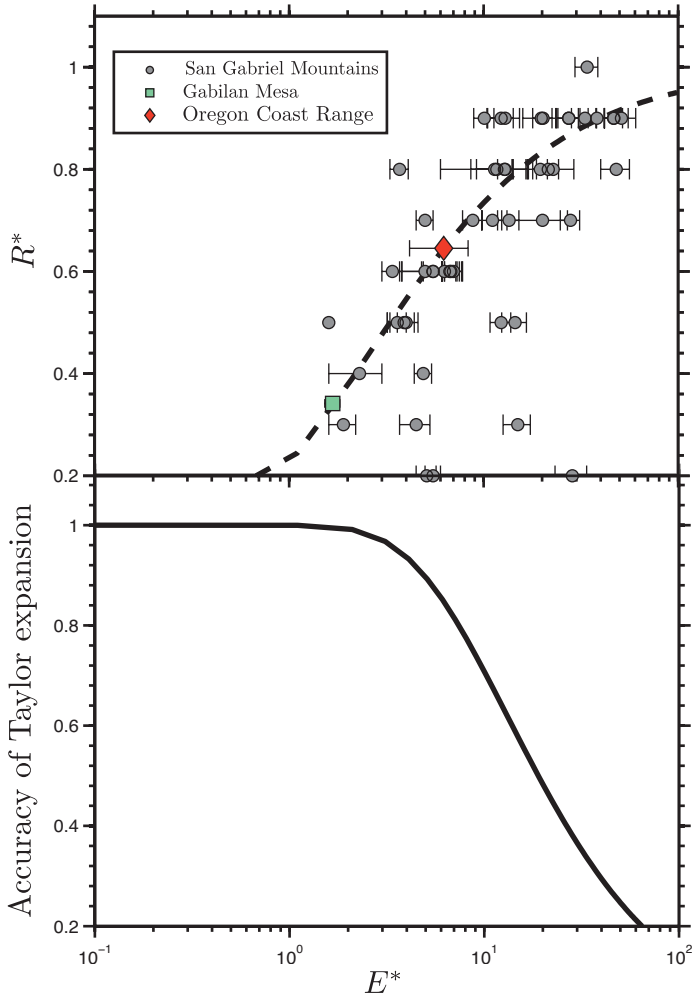

Figure 4.7: Functional dependence of the accuracy of the Taylor series approximation of the nonlinear sediment flux model on the dimensionless erosion rate, E^* (bottom panel). The accuracy of Taylor series approximation is defined as the ratio of the total sediment flux computed from the predicted steady-state, equilibrium hillslope profile of the nonlinear sediment transport model using equation (4.6) to that computed using equation (4.2). The top panel (broken line) shows the theoretical relationship between the dimensionless relief R^* and the dimensionless erosion rate E^* derived from the nonlinear sediment flux model of equation (4.2). Data points from the Oregon Coast Range, the Gabilan Mesa and several catchments from the San Gabriel mountains (as reported in [5] and [10]) are also shown on this plot. The above plot can be used to determine whether the proposed closure provides an accurate representation of the sub-grid scale fluxes for a given landscape.

the one-shift Grünwald expansion [92]:

$$\frac{\partial^{\alpha-1} z(x)}{\partial x^{\alpha-1}} \simeq \frac{1}{\Delta x^{\alpha-1}} \sum_{k=0}^{N} g_k z\left(x - k\Delta x + \Delta x\right) \tag{4.19}$$

where g_k are the one-shift Grünwald weights, Δx is the spatial grid size in the numerical evaluation, N is the number of node points upslope of the given point and $\partial^{\alpha-1}/\partial x^{\alpha-1}$ is the fractional differentiation operator of order $\alpha - 1$ $(1 < \alpha \leq 2)$. The Grünwald weights are given as [93, 92]:

$$g_k = \frac{\Gamma(k - \alpha + 1)}{\Gamma(-\alpha + 1)\Gamma(k + 1)} \tag{4.20}$$

where $\Gamma(.)$ is the gamma function. It is readily observed from equations (4.18) and (4.19) that computation of the non-local flux, $q_s^\star(x)$, at a location x involves not only the gradient at that location but also gradients upslope of that location.

One can write the fractional derivative operator on elevation in equation (4.18) as a fractional integration on the slopes and thus the non-local flux model becomes:

$$q_s^\star(x) = K^\star I_x^{1-\alpha}\left(S\right) \tag{4.21}$$

where $I_x^{1-\alpha}\left(\cdot\right)$ is a fractional integration operation of order $1 - \alpha$ [91]. Filtering the above equation yields the following relation:

$$\widetilde{q_{s_\Delta}^\star}(x) = K^\star \widetilde{I_x^{1-\alpha}\left(S\right)} \tag{4.22}$$

In the above equation, we are performing an averaging of the fractional integral of the slopes, S, which can be decomposed into the sum of their filtered components at a given scale, $\widetilde{S}_\Delta$, and their fluctuations component, S'_Δ. Noting that the fractional integration is a linear operator, the above equation would amount to the sum of the fractional integral of the filtered slope $(\widetilde{S}_\Delta)$ and the fractional integral of the average of the fluctuating component of the slopes (S'_Δ). Noting that the latter term is zero $(\widetilde{S'_\Delta} = 0)$, equation (4.22) can be written as:

$$\widetilde{q_{s_\Delta}^\star}(x) = K^\star I_x^{1-\alpha}\left(\widetilde{S}_\Delta\right) \tag{4.23}$$

denoting that the filtered flux is equal to the value of the flux calculated by plugging the value of the filtered slope in its original functional form of equation (4.21). This result

demonstrates theoretically that the non-local sediment transport model of equation (4.3) is scale-independent.

We investigate the scale-independence of the non-local transport model by computing the sediment flux on a hillslope profile of the MR1 basin at various scales. The hillslope profile chosen was one from the MR1 basin (Figure 4.8(a)) that was reported in [7] and later shown by Foufoula-Georgiou et al. [11] to be consistent with the steady-state prediction from a non-local flux model. Figure 4.8(b) shows the total computed sediment flux from this single hillslope profile using both the non-local flux model (equation (4.21)) and the nonlinear flux model (equation (4.2)). The parameters of the nonlinear model used were $K = 0.0032\ m^2/yr$ and $S_c = 1.25$ and $K^\star$ was calibrated such that the total computed sediment flux from the hillslope profile was equal for both the models at the smallest scale (2 m). The value of $\alpha = 1.3$ was chosen, which was estimated from the form of the hillslope profile in [11]. As shown in Figure 4.8(b), the scale-dependence of the non-local flux model is minimal when compared with the nonlinear flux model. This difference, when added up over all the hillslope profiles of the MR1 basin, amounts to considerable scale-dependence in the case of the nonlinear flux model, whereas the negligible scale-dependence of the non-local flux model promises to alleviate the issue of scale-dependence when applied to the whole of MR1 sub basin.

The above demonstration was performed on a single hillslope profile only rather than on the whole MR1 basin, as done in Section 4.4. This is because, to the best of our knowledge, the numerical implementation of fractional derivatives on a $2-D$ field along directed flow paths that possess a tree-like structure is not known. Testing the scale-independence of the non-local flux model on a $2-D$ elevation field is the subject of future research.

4.7 Conclusions

In this chapter, theoretical analysis and high-resolution lidar data were used to demonstrate the scale-dependence of local nonlinear geomorphic transport models of sediment transport on hillslopes. The following conclusions were drawn:

1. The magnitude of local gradients and consequently the computed sediment flux

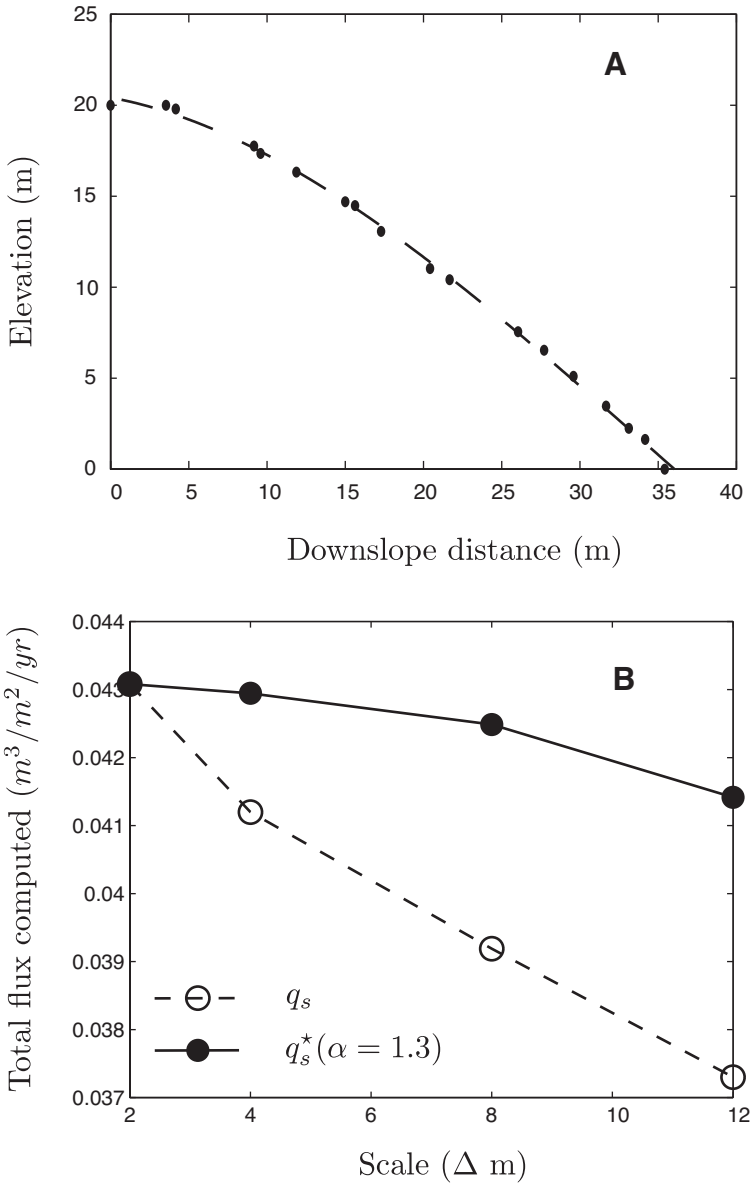

Figure 4.8: (A) Hillslope profile in the MR1 basin of the Coos Bay region. This profile was reported in Roering et al. [7] and later shown by Foufoula-Georgiou et al. [11] to be consistent with the fractional flux model with the parameter of $\alpha = 1.3$. (B) Flux computed at four different scales along a single profile of the MR1 basin in the Coos bay region. As seen above the nonlinear flux model suffers from scale-dependence of the total flux computed from the hillslope profile, whereas the non-local flux model shows very little dependence on scale. The parameters used for the nonlinear flux model were $K = 0.0032\ m^2/yr$ and $S_c = 1.25$. The diffusivity of the fractional flux model, $K^\star$ was calibrated such that the fluxes computed from non-local and nonlinear flux models are equal at the smallest scale.

from a local nonlinear sediment transport model were shown to be strongly dependent on the scale at which the gradients were computed. A simple moving averaging method was used for the purpose of smoothing the 2 m high-resolution lidar data of the MR1 basin in the Oregon Coast Range to create landscapes at lower resolutions. Other smoothing filters have been tested with little difference in the results.

2. A sub-grid scale closure was derived via upscaling of the nonlinear sediment flux model for sediment transport on hillslopes. It is noted that the local nonlinear flux model inherently suffers from scale-dependence owing to the scale-dependent nature of the local gradients and the nonlinear relationship of the sediment flux and local gradients.

3. The proposed sub-grid scale closure that accounts for the variability at scales smaller than the scale Δ at which the model is applied was shown to depend on the model parameters (diffusivity and critical gradient, K and S_c, respectively), the filtered component of the local gradients ($\widetilde{S}_\Delta$), and the variance of the slope fluctuations within the scale Δ ($Var\left(S'_\Delta\right)$). The mean and standard deviation of the within-box (of scale Δ) variability of the slope fluctuations were shown to have a power-law dependence on scale, thus enabling one to effectively parameterize the unknown variability at a given scale by using statistical information of the landscape from larger scales. It was shown that both the local sub-grid scale closure (each box of scale Δ has its own correction derived from its immediate larger-scale neighborhood) and the global sub-grid scale closure (same closure for all boxes based on the statistics of the whole landscape) alleviate the scale-dependence that the nonlinear sediment flux model suffers from.

4. The accuracy of the proposed sub-grid scale model was shown to be directly related to the dimensionless erosion rate (E^*) and the dimensionless hillslope relief (R^*) of a given landscape. It was shown that for large value of the dimensionless erosion rate ($E^* > 10$ and $\overline{S} \to S_c$) the proposed sub-grid scale closure will not perform well as the Taylor series approximation of the nonlinear sediment transport model, on which the proposed sub-grid scale closure derivation relies, breaks down.

5. Finally, the recently proposed non-local flux model for sediment transport on hillslopes [11] was shown theoretically to be scale-independent owing to its inherent scale-free nature and the fact that it does not assume the existence of a representative elementary control volume. It was demonstrated that the non-local flux model shows negligible scale-dependence compared to the nonlinear flux model, when applied to a single hillslope profile of the MR1 basin of the Oregon Coast Range.

The conceptual framework for deriving the sub-grid scale closure presented in this chapter (Section 4.3) is general and can be applied to any nonlinear sediment transport model. The most notable examples in geomorphic transport are the stream power model for bedrock erosion ($\xi \sim A^m S^n$, where ξ is the rate of bedrock erosion, A is the upstream drainage area and S is the local slope) and the bed load sediment transport models ($q_{bl} \sim \tau^a$, where q_{bl} is the bed load sediment flux and τ is the instantaneous shear stress at the bed). The investigation and derivation of the sub-grid scale closure models for these nonlinear sediment transport models is a subject of future study.

Chapter 5

Normal and Anomalous Diffusion of Gravel Tracer Particles in Rivers

The stones that make up the bed of gravel-bed rivers are transported as bedload during floods. During periods of overall transport, each particle undergoes alternating periods of movement and rest. Movement consists of rolling, sliding or saltation, which continues until a single step length of motion is completed. The particle is at rest when it is deposited, either on the bed or deeper within the deposit. One way to study the mechanism of bedload transport in gravel bed rivers is to seed the bed with marked tracer particles within some small area of the bed (patch), and to follow the pattern of migration and dispersal of particles from that patch [39, 145, 146, 40, 147, 148]. Tracers provide a way of characterizing not only mean parameters pertaining to transport, but also the stochasticity of particle motion itself.

This stochasticity was first elaborated by Einstein [149]. Einstein based his analysis on experimental observations of painted tracer particles. He noted that: "The results demonstrated clearly that even under the same experimental conditions stones having essentially identical characteristics were transported to widely varying distances ... Consequently, it seemed reasonable to approach the subject of particle movement as a probability problem." Einstein considered a particle that moves in discrete steps

punctuated by periods of inactivity. He quantified the problem in terms of the statistics of step length and resting period (waiting time). Einstein [49] went on to explain how these quantities enter into the delineation of macroscopic relations of bedload transport (i.e., relations that represent averages over the stochasticity of sediment motion). More specifically, Einstein [49] showed that the bedload transport rate is proportional to the step length and inversely proportional to the resting period. Following the seminal work of Einstein [49], many stochastic theories for sediment transport have been proposed which account for the aforementioned stochasticity (see for example, [150, 151, 152, 153, 154, 155, 156, 157, 158], [159, 160]; [161]; [72],[162] and references therein).

Two macroscopic quantities that can be captured by means of statistical analyses of tracer motion are the overall tendencies of ensembles of tracers to be advected downstream, and to disperse, or diffuse. (Various authors use the terms "dispersion" or "diffusion" of tracers to describe the same process: here we rather arbitrarily use the term "diffusion".) Both advection and diffusion are governed by a wide range of factors.

Bedload particles may roll, slide or saltate over the bed. In the case of grains of uniform size, mean saltation length may be on the order of ten diameters [163]; whereas mean step length may be on the order of 100 grain diameters [164, 165, 166]. Einstein [164] suggested that mean step length can be approximated as a constant multiple of grain diameters, whereas Wong et al. [166] indicate a weak variation with Shields number, which is a proxy for flow strength. Step length is known, however, to vary stochastically [165]. As illustrated below, this stochasticity is one source of diffusion.

When a particle comes to rest, it may deposit so as to be exposed at the bed surface, or it may become buried at depth [167]. From a statistical point of view, deeper burial in general implies a longer resting time before exhumation and re-entrainment. This effect can influence both diffusion and advection [147]. Most natural gravels consist of a mixture of grain sizes, each of which undergoes steps and resting periods according to size-specific probabilities. For example, Tsujimoto [165] has shown that larger grains in a mixture have longer step lengths, but also longer resting times. As these different sizes move downstream, their motion is affected by the presence of bedforms such as dunes [168], bars and bends associated with channel meandering/braiding [148], and large-scale variations in channel width. In addition, the bed may be undergoing aggradation, which enhances the capture of bedload particles, or degradation, which causes

the exhumation of grains that have undergone long-term storage [147]. Grains can also enter floodplain storage for long periods of time, and then be exhumed as the channel migrates into the relevant deposit [169, 170, 171]. Again, all these effects can influence the advection/diffusion of tracer particles.

The macroscopic transport of grains undergoing steps and rest periods governed by statistical laws can be most simply characterized in terms of the classical advection-diffusion model, according to which the particles spread downstream with a constant diffusivity. When step lengths and rest periods are governed by a multiplicity of mechanisms over a very wide range of spatial and temporal scales, however, the advection/diffusion of tracer particles may no longer be characterizable in terms of the classical model. It is widely known in the groundwater literature that a multiplicity of scales over which transport takes place can lead to "anomalous diffusion", for which the advection/diffusion equation can be characterized by fractional derivatives [1, 27, 22, 172].

Nikora et al. [41] have studied the diffusion of bedload particles using the measured motion of individual particles in a canal as the basis for ensemble averaging. They extracted from their data various moments characterizing particle location as a function of time. They delineated three ranges of temporal and spatial scales, each with different regimes of diffusion: ballistic diffusion (at the scale of saltation length), normal/anomalous diffusion (at a scale of step length) and sub-diffusion (at global scale). Their study thus represents a pioneering effort in the identification of anomalous diffusion of bedload particles.

We develop here a theoretical model for the study of anomalous diffusion of tracer particles moving as bedload. The present model is not intended to be comprehensive, in that it covers only a restricted set of phenomena that might lead to anomalous diffusion. It is our desire, however, that this first model should serve as an example illustrating the pathway to more general models of anomalous diffusion.

The chapter is structured as follows. In Section 5.1, a straightforward formulation of the Exner equation for sediment conservation is presented which incorporates the probability density function (pdf) for step lengths, i.e., the distances traveled by particles once they are entrained to when they are deposited again on the river bed. In Section 7.2 we show that the assumption of step lengths having a distribution with thin

tails (e.g., exponential, normal, log-normal distributions) leads to a classical advection-diffusion equation for tracer dispersal. However, in real rivers the complexity resulting from broad distributions of particle sizes and flood events can lead to a heavy tail in the pdf of step lengths (arising, for example, from the combination of an exponential distribution for step length conditional on a particle size and a gamma distribution of particle sizes). In Section 6.2, we show that this consideration leads to an anomalous advection-diffusion formulation which includes fractional derivatives. That model was introduced earlier in the context of other problems, such as groundwater dispersion. Section 5.4 shows how a heavy-tailed step length distribution can arise from a thin-tailed (exponential) pdf of step length for particles of a given size, together with a thin-tailed grain size distribution. In Section 6.4, we build a stochastic model to describe the time evolution of the relative concentration of the tracers in the active layer, and show that the approximate solutions obtained in Sections 7.2 and 6.2 are long-time asymptotic solutions of the derived model. Finally, in section 6.5, numerical results are presented showing the difference between normal and anomalous advection-diffusion of gravel tracer particles.

5.1 Formulation

The starting point for our analysis is the entrainment-based one-dimensional Exner equation for sediment balance [165, 31, 173];

$$(1-\lambda_p)\,\frac{\partial \eta(x,t)}{\partial t} = D_b\,(x,t) - E_b\,(x,t) \tag{5.1}$$

where η denotes local mean bed elevation, t denotes time, x denotes the downstream co-ordinate, D_b denotes the volume rate per unit area of deposition of bedload particles onto the bed, E_b denotes the volume rate per unit area of entrainment of bed particles into bedload, and λ_p is the porosity of bed sediment. We assume that, once entrained, a particle undergoes a step with length r before depositing. We further assume that this step length is probabilistic, with a probability density $f_s(r)$ (pdf of step length). The deposition rate of tracers $D_b(x,t)$ is then given as:

$$D_b\,(x,t) = \int_0^\infty E_b\,(x-r,t)\,f_s(r)dr \tag{5.2}$$

In the above formulation E_b is a macroscopically determined parameter, which can be shown to vary inversely with the mean resting time of a particle. The formulation thus includes the effect of stochasticity in step length, but not in resting time.

A model formulation for tracers that simplifies the above-mentioned model of entrainment and deposition is the active layer formulation. According to this formulation, grains in an active bed layer of thickness L_a below the local mean bed surface exchange directly with bedload grains. Grains below the active layer, i.e., grains in the substrate, exchange with the active layer only by means of bed aggradation (when active layer grains are transferred to the substrate) and degradation (when substrate grains are transferred to the active layer). In such a model, substrate grains do not directly exchange with the bedload grains.

Let $f_a(x,t)$ denote the fraction of tracer particles in the active layer at any location x and time t. In addition, let $f_I(x,t)$ denote the fraction of tracer particles in the sediment that is exchanged across the interface between the active layer and the substrate as the bed aggrades or degrades. The equation of mass conservation of tracers can then be written as:

$$\begin{aligned}(1-\lambda_p)\left(f_I(x,t)\frac{\partial\eta(x,t)}{\partial t}+L_a\frac{\partial f_a(x,t)}{\partial t}\right)\\ =D_{bT}(x,t)-E_{bT}(x,t)\end{aligned} \tag{5.3}$$

where E_{bT} denotes the volume entrainment rate of tracers and D_{bT} denotes the corresponding deposition rate, which are given as [31]:

$$E_{bT}(x,t)=E_b(x,t)f_a(x,t) \tag{5.4}$$

and

$$D_{bT}(x,t)=\int_0^\infty E_b\left(x-r,t\right)f_a\left(x-r,t\right)f_s(r)dr \tag{5.5}$$

Here we exclude the complication induced by bedforms such as dunes [e.g., 168] by considering conditions of lower regime plane-bed transport, such as those investigated by Wong et al. [166].

The fraction f_I of tracers exchanged at the interface as the mean bed elevation fluctuates can be expected to differ depending upon whether or not the bed is aggrading or degrading. Hoey and Ferguson [174] and Toro-Escobar et al. [175] have suggested

forms for interfacial exchange fractions which can be adapted to the problem of tracers. Here we restrict consideration to the case for which the bed elevation is at equilibrium, so that L_a, E_b, η and the pdf $f_s(r)$ are all constant in x and t. Under this condition, equations (5.3), (5.4) and (5.5) reduce to:

$$\begin{aligned}(1-\lambda_p)\frac{L_a}{E_b}\frac{\partial f_a(x,t)}{\partial t} \\ = \int_0^\infty f_a\left(x-r,t\right) f_s(r) dr - f_a(x,t)\end{aligned} \tag{5.6}$$

The nature of the pattern of tracer diffusion predicted by equation (5.6) depends on the nature of the pdf $f_s(r)$ of step lengths. As shown in Sections 7.2 and 6.2, a thin-tailed pdf, i.e., one for which all moments of $f_s(r)$ exist, leads to a classical Fickian advection-diffusion equation, while a heavy-tailed pdf, i.e., one for which moments larger than a given order do not exist, can lead to an anomalous advection-diffusion equation.

5.2 Tracer transport with thin-tailed step length distribution

In this section, we show that a thin-tailed pdf for the step length distribution, $f_s(r)$, in equation (5.6) leads to a classical Fickian (normal) advection-diffusion equation. For simplicity, we assume the porosity to be zero, i.e., $\lambda_p = 0$. The simplest way to solve the integral equation (5.6) is to use Fourier transforms, since the convolution becomes a product in Fourier space. The Fourier transform of a function $f_a(x,t)$ is given by:

$$\hat{f}_a(k,t) = \int_{-\infty}^{\infty} e^{-ikx} f_a(x,t)\,\mathrm{d}x \tag{5.7}$$

Taking the Fourier transforms in equation (5.6) and manipulating yields:

$$\frac{L_a}{E_b}\frac{\partial \hat{f}_a(k,t)}{\partial t} = \left(\hat{f}_s(k) - 1\right)\hat{f}_a(k,t) \tag{5.8}$$

Expanding the Fourier transform of $f_s(r)$ as a Taylor series gives:

$$\hat{f}_s(k) = 1 - ik\mu_1 + \frac{1}{2}(ik)^2\mu_2 + \cdots \tag{5.9}$$

where $\mu_n = \int r^n f_s(r)\mathrm{d}r$ denotes the n^{th} order moment of the step length distribution. The above expansion is valid provided that the moments μ_n exist and are finite, and the

series converges uniformly in a neighborhood of $k = 0$ [176]. Substituting equation (5.9) into (5.8) we obtain:

$$\frac{L_a}{E_b}\frac{\partial \hat{f}_a(k,t)}{\partial t} = \left(-ik\mu_1 + \frac{1}{2}(ik)^2\mu_2 + \cdots\right)\hat{f}_a(k,t) \tag{5.10}$$

Recall that $(ik)\hat{f}_a(k,t)$ is the Fourier transform of $\partial f_a(x,t)/\partial x$. By making the approximation that higher order terms can be neglected (which will be shown equivalent, in Section 6.4, to considering a long-time asymptotic solution), and by setting $v = \mu_1$ and $2D_d = \mu_2$, it follows by an inverse Fourier transform that the function $f_a(x,t)$ is the approximate solution to the advection-diffusion equation:

$$\frac{L_a}{E_b}\frac{\partial f_a}{\partial t} = -v\frac{\partial f_a}{\partial x} + D_d\frac{\partial^2 f_a}{\partial x^2} \tag{5.11}$$

This is the standard form of the advection-diffusion equation for tracer dispersal, and applies under equilibrium bedload conditions where v and D_d can be considered constant. The associated Green's function, i.e., the solution to the above equation with a pulse as the initial condition at $t = 0$, is the Gaussian distribution, which describes the tracer concentration at any given time $t > 0$. If the source is distributed in space and/or time, the solution to equation (5.11) is the convolution of the Green's function with the source.

5.3 Tracer transport with heavy-tailed step length distribution

As detailed in the next section, a heavy-tailed, power-law distribution for step lengths in gravel bed rivers can result from a thin-tailed pdf of step length for particles of a given size, together with a thin-tailed pdf of grain sizes. In this section, we develop a formalism that incorporates heavy tails for the step length distribution into the probabilistic Exner equation. In equation (5.6), consider $f_s(r)$ to be a step length distribution with power-law decaying tail, i.e., $f_s(r) \approx C\alpha r^{-\alpha-1}$ for $r > 0$ sufficiently large, some constant $C > 0$, and some power law index $1 < \alpha < 2$. In this case, the Fourier transform expansion (5.9) in terms of statistical moments of $f_s(r)$ is not valid, as the integrals $\mu_n = \int r^n f_s(r)\mathrm{d}r$ do not converge for $n > 1$ [82]. Instead, we may use a fractional

Taylor expansion to write [177, 178]:

$$\hat{f}_s(k) = 1 - ik\mu_1 + c_\alpha (ik)^\alpha + \cdots \tag{5.12}$$

where c_α is a constant that depends only on C and α. Substituting back into equation (5.8) we obtain:

$$\frac{L_a}{E_b}\frac{\partial \hat{f}_a(k,t)}{\partial t} = \left(-ik\mu_1 + c_\alpha (ik)^\alpha + \cdots\right) \hat{f}_a(k,t) \tag{5.13}$$

This equation (6.1) can be understood in terms of fractional derivatives. Fractional derivatives are close cousins of their integer order counterparts. The fractional derivative $\partial^\alpha f_a(x,t)/\partial x^\alpha$ can be defined simply as the function whose Fourier transform is $(ik)^\alpha \hat{f}_a(k,t)$. As in the normal advection-diffusion case, we make an approximation by including the first two terms in the expansion and neglecting the higher order terms. Then by setting $v = \mu_1$ and $D_d = c_\alpha$, it follows from (6.1) that the function $f_a(x,t)$ is approximately the solution of the fractional advection-diffusion equation:

$$\frac{L_a}{E_b}\frac{\partial f_a}{\partial t} = -v\frac{\partial f_a}{\partial x} + D_d\frac{\partial^\alpha f_a}{\partial x^\alpha} \tag{5.14}$$

Fractional advection-diffusion has been extensively used in modeling the dispersal of tracers or pollutants in porous media which exhibit multiple scales of variability, as in subsurface transport [83, 102, 27] and pollutant transport in rivers [84, 85]. However, to the best of our knowledge, its application has not yet been explored in the context of river transport, apart from a recent study which uses fractional advection for transporting sediment in buffered bedrock rivers [89].

In most natural rivers, the distribution of step lengths holds in the near field, but eventually transport steps become limited by river features (e.g., bars) that change the intermediate and far field distributions. The application of the governing equations (5.11) and (6.3) depends on the natural truncation of the step length distributions. If the truncation occurs at a very small threshold, then the Central Limit Theorem applies and a standard advection-diffusion equation will be the governing equation for the fraction of tracers in the active layer. However, if the truncation occurs at a large threshold, then the distribution can still be approximated by a power-law in the intermediate field and the governing equation for the fraction of tracers in the active layer is the fractional advection-diffusion equation. It is worth noting that equation (6.3) is

the governing equation on scales where the power-law approximation of the step length distribution is accurate. In the next section, we explain how a power-law distribution for step lengths could emerge by combining a thin-tailed pdf of step length for particles of a given size with a thin-tailed pdf of grain sizes. Then in Section 6.4 we describe the stochastic model underlying the probabilistic Exner equation (5.6), and we show how equations (5.11) and (6.3) represent long-time asymptotic solutions.

5.4 Transport of sediment mixtures

5.4.1 Generalized Exner equation

A generalization of equation (5.6) for a range of grain sizes D can be expressed as follows. Let $f_{ad}\,(x,t,D)$ denote the fraction of tracers in the active layer with grain size D, so that,

$$f_a(x,t) = \int_0^\infty f_{ad}(x,t,D)dD \tag{5.15}$$

In addition, let $E_{bu}(D)$ denote the entrainment rate per unit bed content of size D. The generalization of equation (5.6) is then [179],

$$\begin{aligned}(1-\lambda_p)L_a\frac{\partial f_a\,(x,t,D)}{\partial t}&\\ = E_{bu}(D)\Big(\int_0^\infty f_{ad}\,(x-r,t,D)\,f_s(r|D)dr&\\ - f_{ad}\,(x,t,D)\Big)&\end{aligned} \tag{5.16}$$

In the above formulation, the conditional pdf of step length f_s is specified as a function of grain size, but the thickness of the active layer L_a is taken to be a constant for all grain sizes. The form corresponding to equation (5.6) is obtained by integrating over all grain sizes,

$$\begin{aligned}\big(1-\lambda_p\big)L_a\frac{\partial f_a\,(x,t)}{\partial t}&\\ = \int_0^\infty E_{bu}(D)\Big(\int_0^\infty f_{ad}\,(x-r,t,D)\,f_s(r|D)dr&\\ - f_{ad}\,(x,t,D)\Big)dD&\end{aligned} \tag{5.17}$$

In general, E_{bu} and f_{ad} can both be expected to vary significantly with D. Closure of equation (5.17) requires specification of forms for E_{bu} and f_{ad} as functions of, among

other parameters, grain size D. Such forms are available in the literature [165].

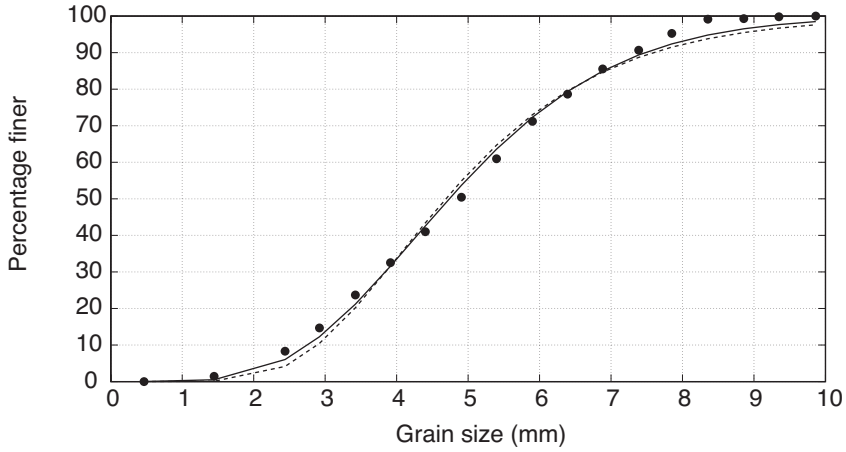

Figure 5.1: Plot showing fitted log-normal (dashed line) and gamma (solid line) distributions, to a grain-size distribution (solid points) reproduced from [12].

The goal of the present analysis is, however, to study the role of heavy-tailed pdfs for step lengths in driving the diffusion of tracer particles. With this in mind, the problem is simplified for the purposes of illustration to one in which f_{ad} varies in D but E_{bu} does not. More specifically, by assuming independence of grain size D on space-time location (x, t), one can write $f_{ad}(x, t, D) = f_a(x, t)f(D)$. Then unconditioning of $f_s(r|D)$ with respect to the grain size pdf $f(D)$ in equation (5.17) is used to develop the Exner equation for a grain size mixture. In the next subsection, we show that a heavy-tailed pdf for step lengths in a mixture of particles can emerge, under certain conditions, from two thin-tailed pdfs.

5.4.2 Power laws emerging from thin tails

A typical finding in sediment transport is that step lengths r are exponentially distributed for a given grain size D [180, 181], i. e.,

$$\mathbb{P}(R > r \,|\, D) = e^{-r/\mu_r(D)} \tag{5.18}$$

where $\mu_r(D)$ is the mean step length as a function of grain size D. If we let f denote the pdf of grain sizes, then the unconditional distribution of step length can be derived

from:

$$\mathbb{P}(R > r) = \int_0^\infty e^{-r/\mu_r(D)}\, f(D)\, dD. \tag{5.19}$$

The resulting pdf for step length, relating to a mixture of particle sizes, depends on both the mean step length $\mu_r(D)$ for grains of size D, and the pdf of grain sizes.

In this study we explore two distinct cases, one in which $\mu_r(D)$ increases with grain size, and another for which $\mu_r(D)$ decreases with grain size. The true dependence of mean step length on grain size in sediment mixtures remains somewhat ambiguous. In the case of uniform sediment, Nino and Garcia [163] found that grain saltation length decreases with increasing grain size. One step length, however, typically consists of around 10 saltation lengths. Hassan and Church [182] have studied the travel distance of size mixtures of stones in gravel-bed rivers, and have found a marked tendency for travel distance to decrease with increasing grain size. This result must be qualified in light of the fact that the distance traveled by a grain during a flood can be expected to be associated with multiple step lengths. This qualification notwithstanding, the data suggest a range of conditions under which the dependence between grain size and mean travel distance can be approximated by the simplified model:

$$\mu_r(D) = \kappa/D \tag{5.20}$$

where κ is a constant. A lognormal pdf of grain sizes

$$f(D) = \frac{1}{D\sigma\sqrt{2\pi}} e^{-\frac{1}{2}\frac{(\ln D - \mu)^2}{\sigma^2}} \tag{5.21}$$

was invoked by [12, 173, 183, 179], where μ, σ are the mean and standard deviation of the sedimentological scale $\psi = \ln D$. The overall (unconditional) step length distribution can then be obtained, in principle, by substituting equations (5.20) and (5.21) into equation (5.19) and computing the integral. However, this integral is difficult to compute analytically with a log-normal form for $f(D)$. Figure 5.1 shows the grain size data from [12] along with a lognormal fit, as well as an alternative gamma distribution fit to the same data. The gamma pdf

$$f(D) = \frac{\nu^\nu}{\Gamma(\nu) {D_\mathrm{m}}^\nu} D^{\nu-1} \exp\left(-\nu \frac{D}{D_\mathrm{m}}\right) \tag{5.22}$$

with mean D_m and shape parameter ν provides a convenient alternative to the lognormal distribution that makes it possible to analytically evaluate the integral (5.19). Following

the argument of Stark et al. [89], we substitute equations (5.20) and (5.22) into equation (5.19) and evaluate the integral to obtain the unconditional probability distribution of step length:

$$\mathbb{P}(R > r) = \left(1 + \left(\frac{D_{\mathrm{m}}}{\nu\kappa}\right) r\right)^{-\nu} \tag{5.23}$$

The above equation (5.23) represents a heavy-tailed power-law pdf for the step length distribution arising from a thin-tailed pdf of step length combined with a thin-tailed pdf of grain sizes. The distribution in equation (5.23) is known as the Generalized Pareto distribution, and its variance exists only when the shape parameter $\nu > 2$ [20]. The Generalized Pareto distribution also arises from exceedances over a fixed high threshold, and has consequently been used in modeling extreme floods and other hydrological phenomena [184].

The relationship (5.20) between mean step length and grain size may not be applicable in all situations. Depending upon the grain size distribution and the flow conditions, large particles may roll over holes that trap smaller particles, so that step length increases with grain size. Such a tendency has been reported in the experiments of Tsujimoto [165]. Also Wong et al. [166] observed that, in the case of uniform sediment subject to the same bed shear stress, step length increases with grain size. Such an increase in step length does not directly translate into a higher bedload transport rate for coarser grains, because the entrainment rate $E_{bu}(D)$ in equation (5.17) may decline with increasing grain sizes. In the present simplified analysis, where E_{bu} is assumed to be independent of grain size, the tendency for step length to increase with grain size can be captured in terms of the following simple form:

$$\mu_r(D) = \kappa D \tag{5.24}$$

where κ is a constant.

If D has an inverse gamma pdf with mean D_{m} and shape parameter ν, also similar in shape to the lognormal,

$$f(D) = \frac{(\nu-1)^{\nu} {D_{\mathrm{m}}}^{\nu}}{\Gamma(\nu)} D^{-\nu-1} \exp\left(-\frac{(\nu-1)D_{\mathrm{m}}}{D}\right) \tag{5.25}$$

then a change of variables $y = 1/D$ in (5.19) leads to another generalized Pareto:

$$\mathbb{P}(R > r) = \left(1 + \left(\frac{1}{(\nu-1)D_{\mathrm{m}}\kappa}\right) r\right)^{-\nu} \tag{5.26}$$

as shown in [185], so that again the step length distribution averaged over all particle sizes has a heavy tail.

Note that in both cases considered above, whether mean step length increases or decreases with grain size, a heavy-tailed distribution for step lengths can emerge from a combination of two thin-tailed distributions. The gamma and inverse gamma distributions are used for particle sizes, as opposed to the more typical log-normal distribution, in order to derive analytically the heavy-tail pdf of the resulting step length distribution for a mixture of grain sizes. The alternative pdf assumption should be considered reasonable if the reader accepts that the fitted log-normal and gamma distributions for the grain size data from [12] in Figure 5.1 are practically indistinguishable. We hasten to emphasize, however, that the finding of a possible heavy-tailed pdf for step length is by no means universal. Many different choices of the grain size pdf $f(D)$ would certainly lead to a thin-tailed pdf of step length. Our point is simply that both thin-tail and heavy-tail models are reasonable, and hence it becomes very important to investigate the grain size distributions more exhaustively, to determine which type of overall step length pdf applies in a given situation.

5.5 Stochastic model for gravel transport in rivers

In this section, we develop a stochastic model to describe the time evolution of the relative concentration of gravel tracer particles in rivers. We derive an exact solution for $f_a(x,t)$ and show that, in the long-time asymptotic limit, a thin tail for the step length distribution leads to classical advection-diffusion, whereas heavy tails for the step length distribution leads to anomalous advection-diffusion. We start by rewriting (5.6) in the equivalent form:

$$\frac{\partial f_a(x,t)}{\partial t} = -\lambda f_a(x,t) + \lambda \int_0^\infty f_a(x-r,t) f_s(r)\,\mathrm{d}r \tag{5.27}$$

where $\lambda = E_b/L_a$ is the rate at which particles are entrained. The Fourier transform of the above equation is given by:

$$\frac{\partial \hat{f}_a(k,t)}{\partial t} = -\lambda \hat{f}_a(k,t)\left(1-\hat{f}_s(k)\right) \tag{5.28}$$

Equation (6.4) describes the time evolution of the pdf $f_a(x,t)$ and can be regarded as a Kolmogorov forward equation for some Markov process $X(t)$, where $X(t)$ represents the

location of a randomly selected gravel particle at time $t > 0$ [see 20]. In this context, $f_a(x,t)$ is the pdf of the random variable $X(t)$. In this Markov process, the waiting time between entrainments has an exponential distribution with a rate parameter λ, and the number of entrainment events, $N(t)$, by any time $t > 0$ has a Poisson distribution with mean λt [20], i.e.,

$$P[N(t) = n] = e^{-\lambda t}\frac{(\lambda t)^n}{n!} \tag{5.29}$$

Let Y_n denote the travel distance during the n^{th} entrainment period. Since there are $N(t)$ entrainment periods by time $t > 0$, the particle location at some time $t > 0$ is given by the random sum:

$$X(t) = Y_1 + \cdots + Y_{N(t)} = \sum_{i=1}^{N(t)} Y_i \tag{5.30}$$

This random sum is a compound Poisson process [e.g., 20]. Its pdf can be derived directly from equation (5.28) whose point source solution is:

$$\hat{f}_a(k,t) = \exp\left(-\lambda t\left(1 - \hat{f}_s(k)\right)\right) \tag{5.31}$$

As a result, the fraction of tracers in the active layer, $f_a(x,t)$, can be obtained by taking the inverse Fourier transform of (5.31) and is given by:

$$f_a(x,t) = e^{-\lambda t}\sum_{n=0}^{\infty}\frac{(\lambda n)^n}{n!}f_s^{n^*}(x) \tag{5.32}$$

where $f_s^{n^*}(x)$ is the n-fold convolution of the density function $f_s(x)$ (recall that $f_s^{n^*}(x)$ is the inverse Fourier transform of $\hat{f}_s(k)^n$), which is also the pdf of $Y_1 + \cdots + Y_n$. One way to understand this formula for $f_a(x,t)$ is that it randomizes the density of the sum of the particle movements according to the pdf of the number of jumps $N(t)$. The random sum, equation (5.30), is a special case of a continuous time random walk (CTRW) [186, 187, 188]. It is important to note that the connection of the probabilistic Exner equation with CTRWs allows one to obtain the exact solution of equation (6.4) via simulation of the tracer particle motion. For example, a forward Kolmogorov equation of a Markov process can be solved by simulating a CTRW with an exponential waiting time distribution and step length distribution $f_s(r)$ [e.g., 189, 190]. Even if the complete shape of the pdf of step lengths is not known, the behavior of the stochastic process $X(t)$ is well defined in the long-time limit as shown below.

Consider the standardized particle location:

$$Z(t) = \frac{X(t) - \lambda\mu_1 t}{\sqrt{\lambda\mu_2 t}} \tag{5.33}$$

This random process has a mean 0 and variance 1 at every time $t > 0$. An easy calculation shows that the pdf of $Z(t)$ has Fourier transform:

$$\hat{f}_a\left(\frac{k}{\sqrt{\lambda\mu_2 t}}, t\right) \exp\left(\frac{ik\lambda\mu_1 t}{\sqrt{\lambda\mu_2 t}}\right) \tag{5.34}$$

Combining this equation with:

$$\hat{f}_a(k,t) = \exp\left(-\lambda t\left(ik\mu_1 - \frac{1}{2}(ik)^2\mu_2 + \cdots\right)\right) \tag{5.35}$$

which is obtained by substituting equation (5.9) into equation (5.31) results in the Fourier transform of the pdf of $Z(t)$ taking the form:

$$\exp\left(-\lambda t\left(-\frac{1}{2}\frac{(ik)^2}{\lambda\mu_2 t}\mu_2 + \frac{1}{3!}\frac{(ik)^3}{(\lambda\mu_3 t)^{\frac{3}{2}}}\mu_3 + \cdots\right)\right) \tag{5.36}$$

As $t \to \infty$, (5.36) tends to $\exp\left(-\frac{1}{2}k^2\right)$ which is the Fourier transform of a standard normal density. This shows that $Z(t)$ tends to a standard normal deviate, Z, for large times t. Substituting into equation (5.33) and solving, we see that the long-time asymptotic solution for the particle location is:

$$X(t) \approx \lambda\mu_1 t + \sqrt{\lambda\mu_2 t}Z \tag{5.37}$$

By taking the Fourier transforms of the corresponding pdfs we obtain:

$$\hat{f}_a(k,t) = \exp\left(-\lambda\mu_1 t(ik) + \frac{1}{2}\lambda\mu_2 t(ik)^2\right) \tag{5.38}$$

which is the point source solution to the differential equation:

$$\frac{\partial \hat{f}_a(x,t)}{\partial t} \approx \left(-\lambda\mu_1(ik) + \frac{1}{2}\lambda\mu_2(ik)^2\right)\hat{f}_a(k,t) \tag{5.39}$$

Inverting this Fourier transform yields the advection-diffusion equation (5.11) with $v = \lambda\mu_1$ and $2D_d = \lambda\mu_2$, as in Section 7.2. In summary, equation (5.11) governs the asymptotic particle density in the long-time limit.

Now consider the case of a particle jump length density with a heavy tail. A similar argument shows that equation (6.3) governs the asymptotic particle density in the long-time limit, when the particle jump length density $f_s(r)$ has a heavy tail with a power-law decay, i.e., $f_s(r) \approx C\alpha r^{-\alpha-1}$ for $r > 0$ sufficiently large, some constant $C > 0$, and some power law index $1 < \alpha < 2$. In this case, we note that the governing equation in the long-time asymptotic limit for $\hat{f}_a(k,t)$ is given by:

$$\frac{\partial \hat{f}_a(k,t)}{\partial t} \approx \left(-\lambda\mu_1(ik) + \lambda c_\alpha (ik)^\alpha\right) \hat{f}_a(k,t) \tag{5.40}$$

Inverting the Fourier transform yields the fractional advection-diffusion equation (6.3) with $v = \lambda\mu_1$ and $D_d = \lambda c_\alpha$, as in Section 6.2. We remark that, while the derivation in this section is new in the context of stone tracer dispersion, a similar approach was taken to derive the fractional advection-diffusion equation for tracers in ground water, under a different set of assumptions [81]. The next section provides a numerical demonstration to illustrate how a source of tracers will disperse over time under normal or anomalous diffusion.

The standardized particle location cannot be expressed using equation (5.33) when the step length distribution has a heavy tail, because the second moment μ_2 of the distribution $f_s(r)$ does not exist, i.e., the population variance is infinite while the sample variance diverges unstably as the number of samples increases [82]. Instead, we consider the normalized process:

$$S(t) = \frac{X(t) - \lambda\mu_1 t}{(\lambda c_\alpha t)^{\frac{1}{\alpha}}} \tag{5.41}$$

The pdf of $S(t)$ has the Fourier transform:

$$\hat{f}_a\left(\frac{k}{(\lambda c_\alpha t)^{\frac{1}{\alpha}}}, t\right) \exp\left(\frac{ik\lambda\mu_1 t}{(\lambda c_\alpha t)^{\frac{1}{\alpha}}}\right) \tag{5.42}$$

Substitution of equation (6.2) into equation (5.31) results in:

$$\hat{f}_a(k,t) = \exp\left(-\lambda t\left(ik\mu_1 - c_\alpha(ik)^\alpha - d_\alpha(ik)^{2\alpha} + \cdots\right)\right) \tag{5.43}$$

which combined with (5.42) gives the left-hand side of the equation (5.44) for the Fourier transform of the PDF of $S(t)$. In the long-time limit, i.e., as $t \to \infty$ this tends to the limit in the right-hand side below, i.e.,

$$\exp\left(\lambda t\left(c_\alpha \frac{(ik)^\alpha}{\lambda c_\alpha t} + d_\alpha \frac{(ik)^{2\alpha}}{(\lambda c_\alpha t)^2} + \cdots\right)\right) \to \exp\left((ik)^\alpha\right) \tag{5.44}$$

since the higher order terms tend to zero as $t \to \infty$. This limit is the Fourier transform of a standard stable density, and the limit argument is closely related to the convergence criterion for compound Poisson random variables (see Chapter 3 in [80] for more details and extensions). Hence, $S(t) \approx S$ is standard stable for large times t. Substituting into equation (5.41) and solving, we see that the long-time asymptotic approximation for the particle location is:

$$X(t) \approx \lambda \mu_1 t + (\lambda c_\alpha t)^{\frac{1}{\alpha}} S \tag{5.45}$$

Taking the Fourier transforms of the corresponding pdfs, we obtain:

$$\hat{f}_a(k,t) \approx \exp\left(-\lambda \mu_1 t(ik) + \lambda c_\alpha t(ik)^\alpha\right) \tag{5.46}$$

This is the Fourier transform of $f_a(x,t)$ with the higher order terms removed, as well as the point source solution to the differential equation:

$$\frac{\partial f_a(\hat{k},t)}{\partial t} \approx \left(-\lambda \mu_1 (ik) + \lambda c_\alpha (ik)^\alpha\right) \hat{f}_a(k,t) \tag{5.47}$$

Inverting this Fourier transform results in the fractional advection-diffusion equation (6.3).

5.6 Tracer dispersal under normal and anomalous diffusion

Consider a patch of tracers entrained instantaneously in the flow at a location x_0 and initial time t_0. This patch will advect and diffuse on the gravel bed over time. It is useful to track the time evolution of the fraction of tracers $f_a(x,t)$ in the active layer at any location x and time t. As was shown in Sections 7.2 and 6.2, the probabilistic Exner equation can be approximated at late time by a normal or anomalous diffusion, equations (5.11) and (6.3) respectively, depending on the pdf of step length. In this section we illustrate the time evolution of a patch of tracers under normal and anomalous advection-diffusion. We know from theory that the Green's function solution to the normal advection-diffusion equation is the Gaussian distribution, and the Green's function solution to the fractional advection-diffusion is the α-stable distribution [102]. The α-stable distributions are also known as Lévy distributions. Specifically, in our case, the Green's function solution to the fractional advection-diffusion equation is an

α-stable distribution with a skewness parameter $\beta = 1$, owing to the fact that step lengths are positive, so that the stable pdf has a heavy leading tail (see Appendix B for a description of stable distributions). Figure 5.2(a) shows the evolution of $f_a(x,t)$ under normal advection-diffusion from a pulse at $t = 0$ and $x = 0$, i.e., $f_a(0,0) = 1$. Figure 5.2(b) shows the evolution of $f_a(x,t)$ under anomalous advection-diffusion with $\alpha = 1.5$ from a pulse at $x = 0$. The α-stable densities in Figures 5.2(a) and 5.2(b) were simulated using the method of Nolan [191]. In this hypothetical experiment, we chose the parameter values of the normal and anomalous diffusion equations to be unity, i.e., $v = 1$ m/day and $D_d = 1$ m$^\alpha$/day. Note that the units of the diffusion coefficient, D_d, is $[L^\alpha/T]$. As can be seen by comparing Figures 5.2(a) and 5.2(b), anomalous advection-diffusion predicts a faster spreading of tracers downstream (heavy leading tails). For example, the leading tails of the fraction of tracers at $t = 100$ reaches a near-zero value at ~ 50 m downstream of its mean in normal advection-diffusion, whereas it reaches this value at ~ 200 m downstream of its mean in fractional advection-diffusion with $\alpha = 1.5$. The mean of $f_a(x,t)$ in both cases is the same. It is worth noting that both the Gaussian pdf, and the skewed stable pdf, assign some extremely small but mathematically nonzero probability to the interval left of the particle source, while the probabilistic Exner equation assigns zero probability to that interval. This illustrates the fact that both the Gaussian and skewed stable pdfs are only approximations to the relative concentration of tracer particles. However, the probability assigned to to the interval left of the particle source is exceedingly small, since both the Gaussian and skewed stable pdfs fall off at a super-exponential rate on the left tail [192], and this approximation is perfectly reasonable in practice.

As seen in the previous section, under equilibrium bedload transport conditions, the long-time asymptotic solutions of the probabilistic Exner equation converge to the normal and anomalous advection-diffusion equation depending on the pdf of the step length. Therefore, long-time asymptotic solutions of the probabilistic Exner equation are the Gaussian and α-stable distributions in the respective cases of thin or heavy tailed pdfs for step length. In Figure 5.3 we compare the long-time asymptotic solutions for several values of α, starting from $\alpha = 2$ (Gaussian corresponding to the solution of normal advection-diffusion equation) to $\alpha = 1.1$. One can easily see the marked

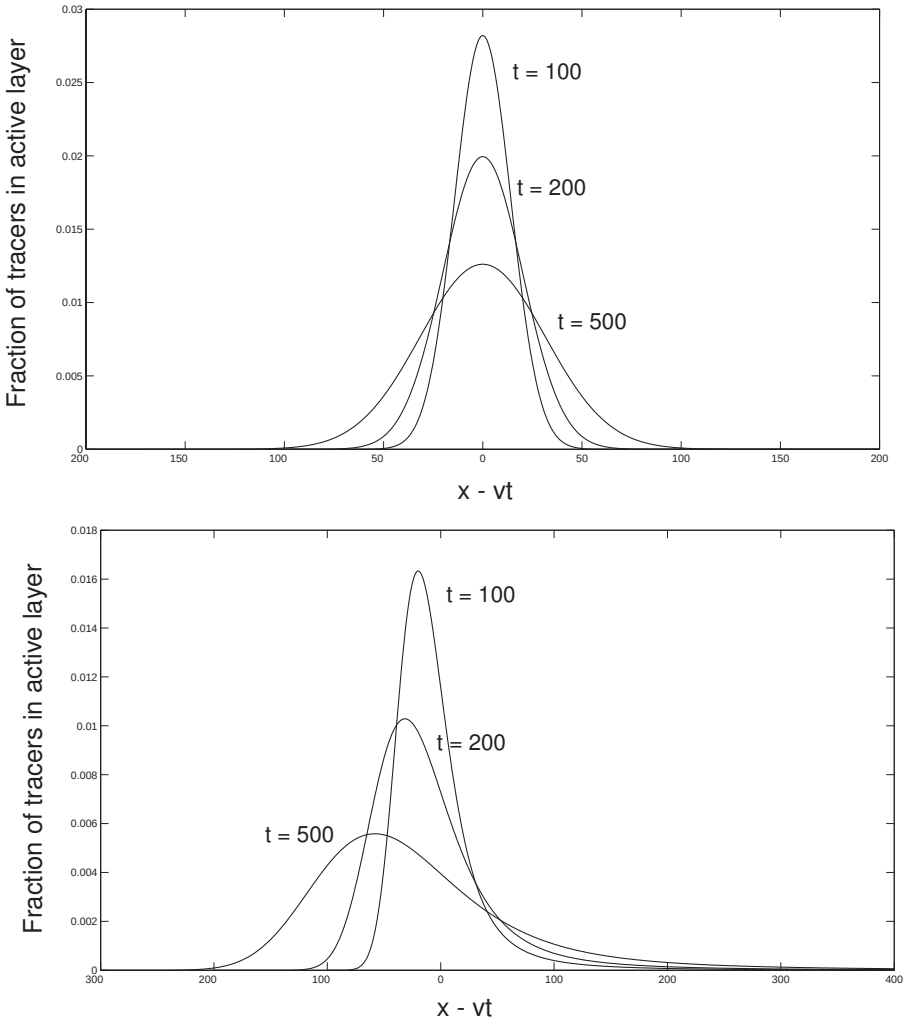

Figure 5.2: Time evolution of the fraction of tracers in the active layer, $f_a(x,t)$, by (a) normal advection-diffusion ($\alpha = 2$), and (b) anomalous advection-diffusion with $\alpha = 1.5$. Note that the advection term has been removed to facilitate comparison of the dispersion of the tracers at different times. The initial condition is a pulse at $x = 0$. The solutions are obtained with parameters $v = 1$ m/day and $D_d = 1$ m$^\alpha$/day. The times (in days) at which the solutions are obtained are labeled in the figure.

difference in the dispersal of tracers downstream in normal and anomalous advection-diffusion. For example, after 500 days, only $\sim 5\%$ of the tracers have been recovered at ~ 550 m in standard advection-diffusion, whereas $\sim 8\%$ and $\sim 18\%$ of tracers are recovered at the same distance in fractional advection-diffusion for $\alpha = 1.5$ and $\alpha = 1.1$, respectively. In the case of $\alpha = 1.1$ the gravel tracer particles are transported very long distances downstream when compared with the normal advection-diffusion case ($\alpha = 2$). The parameter α of the fractional advection-diffusion relates to the heaviness of the tail of the pdf of particle step lengths, in effect determining how far downstream the tracers disperse from the source. In practice, the parameter α will have to be estimated from observations which typically will not be in the form of step lengths but in the form of "breakthrough curves" or pdfs of particle concentration at a given location downstream of the source. Tracer experiments in a large experimental flume are currently under development to document the possibility of faster-than-normal diffusion of tracers and the estimation of the parameter α.

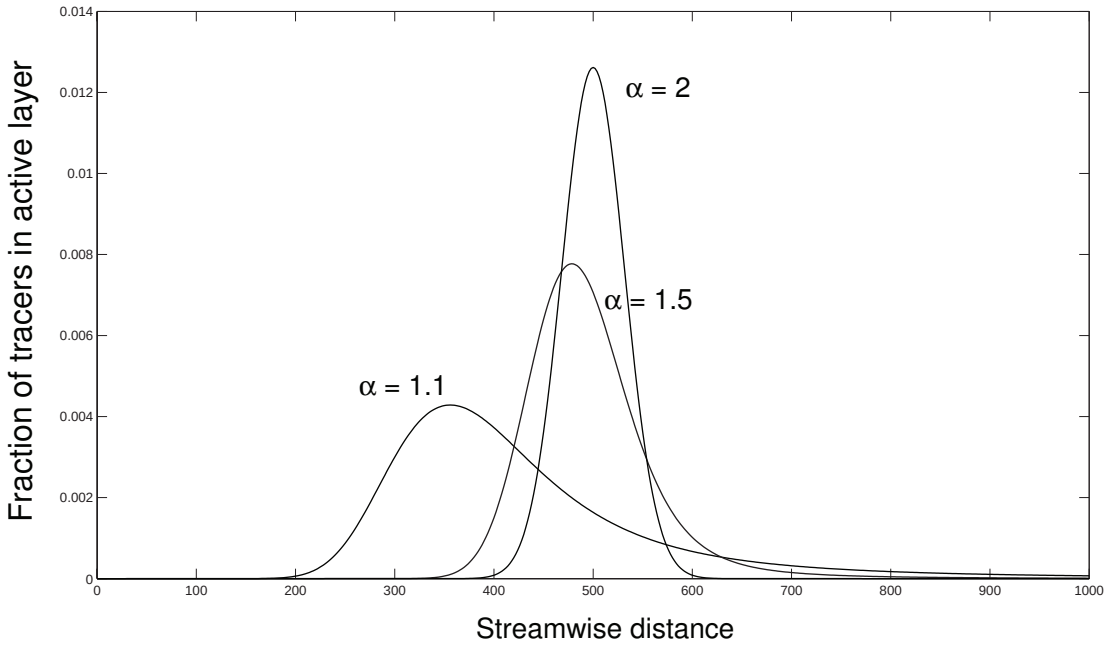

Figure 5.3: Long-time asymptotic solutions of the anomalous advection-diffusion equation for three different values of α. The solutions shown above are for 500 days after a patch of tracers is entrained into the flow. Normal advection-diffusion corresponds to $\alpha = 2$.

5.7 Conclusions

In this work, a mathematical framework for the continuum treatment of tracer particle dispersal in rivers has been proposed, based on the probabilistic Exner equation. We have shown that when the step length distribution is thin-tailed, the governing equation for the tracer dispersal in the long-time limit is given by the standard advection-diffusion equation. However, the step length distributions can be heavy-tailed with power-law decay arising from heterogeneity in grain sizes and other complexities in real gravel bed rivers. It was shown that these heavy tails can be modeled using fractional derivatives, akin to contaminant transport in subsurface hydrology [1, 83, 102, 27]. For a simplified active layer formulation, the probabilistic Exner equation was shown to be governed by a Markov process that describes the tracer dispersal problem. Further, it was shown that the classical (normal) advection-diffusion and fractional (anomalous) advection-diffusion equations arise as long-time asymptotic solutions of that stochastic model. A numerical example was then provided to illustrate the profound effect of fractional diffusion on the leading edge of the particle distribution.

The material presented here is intended to serve as an introduction to the problem of anomalous diffusion in the context of transport in gravel-bed rivers. The full power of the techniques introduced here remains to be realized through future research. For example, the innate variability of rivers is such that the entrainment rate E_b and bed elevation η are unlikely to be constant in x and t. This variability can lead to long-term sequestration, and subsequent long-delayed exhumation of tracers. Parker et al. [31] and Blom et al. [168] have shown how the fractional Exner equation (5.1) can be generalized to a formulation that assigns a probabilistic structure not only to step length, but also to the probabilities of entrainment and deposition as continuously varying functions of vertical position within the bed deposit. These complications can lead to anomalous sub-diffusion if particle resting times have a heavy, power-law tail. A model that can explain the deposition and exhumation of particles at arbitrary depth, including variability in entrainment rate and bed elevation as well as grain size, has the potential to explain at least part of the tendency for a decrease in advection velocity over time described by Ferguson and Hoey[147]. One possible approach to modeling anomalous sub-diffusion caused by power law waiting times between particle movements is by using fractional

time derivatives, as discussed in the paper of Schumer and Jerolmack [193] in the context of interpreting geological deposition records. The anomalous advection-diffusion model proposed herein, as well as further extensions to accommodate additional stochastic elements of transport as discussed above, will require extensive experiments and data collection to directly verify the nature of the distribution of step lenghts, waiting times and entrainment rates of particles in order to select the most appropriate model for transport.

Chapter 6

Subordinated Brownian Motion Model for Sediment Transport

Stochastic theories of sediment transport were initiated with the seminal work of Einstein [194], who introduced a Brownian motion model for particle motion. Since then, these theories were advanced by the need to reproduce the observed statistics of sediment transport rates or particle movement. In [164], a birth-death process was proposed for sediment transport, which was later shown, in [159], to be inadequate as it failed to predict the heavy tails found in the PDFs of the number of moving particles in a given observation window. In [160], the birth-death model was extended to a birth-death-immigration-emigration model to reproduce the experimentally observed negative binomial distributions for the number of moving sediment particles. The stochastic nature of sediment particle entrainment has been widely recognized and considerable efforts have been invested in modeling this behavior [164, 195, 181, 196]. The underlying assumption of these models is that the shear stress, which is the initiator for sediment entrainment, follows a Gaussian distribution. However, many experimental studies have shown that the shear stress fluctuations do not follow a Gaussian distribution and in particular it has been shown that they follow a Gamma distribution [e.g., 197, 198]. The role of near-bed turbulence in sediment transport has also been recognized to play an important role [199, 200]. However, turbulence is well-known to exhibit variability over a range of scales and it is reasonable to ask whether this multi-scale variability shows

its effect on sediment transport series and bed elevation fluctuations.

In a recent study [51], the dependence of the statistics of sediment transport on time-scale (sampling time) akin to the scale-dependent statistics of fully-developed turbulence [201] was documented. Specifically, it was shown that the PDF of sediment transport rates at small sampling times exhibits a heavy tailed distribution which however approaches a Gaussian distribution as the sampling time increases. To the best of our knowledge, no stochastic model of sediment transport exists which reproduces this observed multi-scale statistical structure of sediment transport series. It is the scope of this study to present such a model, discuss its mathematical properties and its physical relevance to modeling sediment transport.

The chapter is structured as follows. In the following section a brief review of multi-scale statistics of sediment transport series observed in a large-scale laboratory experiment is given. In Section 6.2 the application of a stochastic model, called the fractional Laplace motion, is proposed to characterize the sediment transport series and is shown that it is able to reproduce the observed statistics. In Section 6.3 the proposed model is validated against the sediment transport series obtained from a large-scale laboratory experiment. Finally, discussion and conclusions are given in Sections 6.4 and 6.5.

6.1 Multi-scale statistics of sediment transport series

A large-scale laboratory experiment was recently conducted in the Main Channel facility at the St. Anthony Falls Laboratory, University of Minnesota, in order to study sediment transport dynamics in gravel and sand-bed rivers. The details of the experimental facility can be found in [51, 52, 202]. Here we briefly describe one of the experiments from which data was used in this study. The flume is 2.74 m wide and 55 m long, with a maximum depth of 1.8 m (see Figure 6.1). Gravel with a median particle size (D50) of 11.3 mm was placed in a 20 m long mobile-bed section of the 55 m long channel. A constant discharge of water at 4300 liters per second was released into the flume. At the downstream end of the test section was located a bedload trap, consisting of 5 weighing pans of equal size that spanned the width of the channel. Any bedload sediment transported to the end of the test-section of the channel would fall into the

pans, which automatically recorded the weight of the accumulated sediment every 1.1 seconds. Data were collected over a period of 30 hrs once a state of statistical equilibrium was reached [see 202, 51]. The original series of 1.1 s sampling interval were converted to 2 mins sediment accumulations via moving averaging in order to remove mechanical (due to vibration) noise present in the raw data [see 202, 51]. Let us denote by $S(t)$ the 2 mins sediment accumulation series which is shown in Figure 6.2. In this section, we present the multi-scale analysis performed on this sediment transport series.

Figure 6.1: Experimental flume facility at the St. Anthony Falls Laboratory, University of Minnesota.

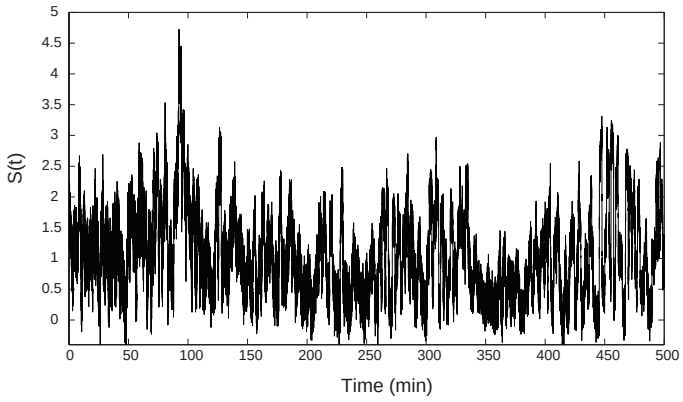

Figure 6.2: Sediment transport series S(t) (in kgs) at a sampling interval of 2 minutes, i.e., series of 2 minutes sediment accumulation.

The goal of a multi-scale analysis is to quantify the manner in which the statistics of the local fluctuations, or variability in a series, changes with scale. In order to investigate

the multi-scale structure of $S(t)$ over a range of scales, differences (or increments) were computed at different scales (lags) r, denoted by $\delta S(t,r)$, as:

$$\delta S(t,r) = S(t + r\Delta t) - S(t) \tag{6.1}$$

i.e., $\delta S(t,r)$ is the incremental sediment accumulation within a time interval $r\Delta t$, where $\Delta t = 2$ mins. In [51], "generalized fluctuations" were used defined via wavelet transforms (acting as a differencing filter). Notice that while $S(t)$ can only be positive, the fluctuation series $\delta S(t,r)$ will have zero mean and can be both positive and negative. The estimates of the q^{th} order statistical moments of the absolute values of sediment transport increments at scale r, also called the partition functions or structure functions, $M(q,r)$ are defined as:

$$M(q,r) = \frac{1}{N_r} \sum_{t=1}^{N_r} |\delta S(t,r)|^q \tag{6.2}$$

where N_r is the number of data points of sediment transport increments at a scale r. The statistical moments $M(q,r)$ for all q completely describe the shape of the PDFs as the scale r changes. Statistical scaling, or scale invariance, requires that $M(q,r)$ is a power law function of the scale, that is:

$$M(q,r) \sim r^{\tau(q)} \tag{6.3}$$

where $\tau(q)$ is the so-called scaling exponent function. For a scale-invariant series, it has been shown that the function $\tau(q)$ completely determines how the PDF of the variable changes with scale [e.g., 203, 204]. The simplest form of scaling, known as simple scaling or mono-scaling, is when the scaling exponents are a linear function of the moment order i.e., when $\tau(q) = Hq$. In this case, the shape of the PDF remains the same over scales apart from a rescaling by a deterministic function which depends on the single parameter H. If $\tau(q)$ is nonlinear, the shape of the PDF changes over scales and more than one parameter is required to describe this change [e.g., 203, 204]. In this case, the series is called a multi-fractal. For most processes the non-linear relationship of $\tau(q)$ with q can be parameterized as a polynomial, and the simplest form is a quadratic approximation:

$$\tau(q) = c_1 q - \frac{c_2}{2} q^2 \tag{6.4}$$

The multi-scale analysis in this framework provides a compact way, using two parameters c_1 and c_2, of parameterizing the change of the PDF over a range of scales. In

parallel to the statistical interpretation of these parameters, there is also a geometrical interpretation. Specifically, the parameter c_1 is a measure of the average "roughness" of the series and c_2, the so-called intermittency coefficient, is a measure of the temporal heterogeneity of the abrupt local fluctuations in the series (in fact, it relates to the variance of the so-called local Hölder exponent which measures the local degree of non-differentiability of the series [e.g., 204]). It is noted that using a higher than second degree polynomial approximation of $\tau(q)$, say a third degree polynomial, introduces a third parameter c_3, which is a measure of the third moment of the local differentiability of the series and it might be hard to accurately estimate from a limited sample size of data. Thus, in most practical applications the approximation of $\tau(q)$ curve is restricted to a quadratic function which is parameterized by c_1 and c_2. Estimation of the multifractal parameters, c_1 and c_2, can be performed in various ways. For example, one can use a quadratic fit to the whole $\tau(q)$ curve (estimated for several values of q from the slopes of $M(q,r)$ vs r in log-log space) or use the first two scaling exponents only, $\tau(1)$ and $\tau(2)$, or use the cumulant analysis method [e.g., [204] and references therein]. In this study, we use the quadratic fit to the $\tau(q)$ curve for the estimation of the parameters c_1 and c_2.

The multi-scale analysis described above was performed on the sediment transport series shown in Figure 6.2. Figure 6.3(a) shows the scaling of the moments of the sediment transport increment series $\delta S(t,r)$ with scale r. It is to note that the structure functions follow a power-law relation in r over a range of scales from $r = 4$ to 64 (8 mins to 128 mins). The scaling exponents of the structure functions, $M(q,r)$ are plotted as a function of the order of moments q in Figure 6.3(b) for $q = 0.5, 1, 1.5, \ldots, 3$. We observe that $\tau(q)$ has a nonlinear dependence on q, which is an indication of the presence of multi-fractality and the fact that the shape of the PDF changes with scale. Figure 6.3(c) displays the PDFs of sediment transport increments at two scales, $r = 10$ and $r = 60$ (i.e., 20 and 120 min sediment accumulations, respectively). It is noted that at smaller scales the PDF of the sediment increments deviates from a Gaussian distribution and is close to a double-exponential. The PDF, eventually, becomes Gaussian at larger scales. The PDFs reported in Figure 6.3(c) are for scales that fall within the scaling regime of the sediment data series (see Figure 6.3(a)). The dependence of the statistics of the sediment transport rates on scale has also been documented in field observations (see

[205] and a discussion in [51]). As discussed above, we estimated the parameters of multifractality by approximating the $\tau(q)$ curve in Figure 6.3(b) as a quadratic function in q and the estimates obtained together with their 95% standard errors were $c_1 = 0.41 \pm 0.005$ and $c_2 = 0.04 \pm 0.004$. It is noted for comparison that the c_2 estimate of velocity fluctuations in fully developed turbulence is of the order of 0.03 [201]. We emphasize that no existing stochastic model for sediment transport addresses the issue of statistical scale-dependence documented in experimental and field observations. In the following section, we propose a new stochastic model for sediment transport which exhibits the observed change in PDFs of sediment transport increments over scales, reproduces the multi-fractal behavior of the experimental data series and provides the potential for relating the observed macro-scale statistics to the micro-scale dynamics of sediment particle movement.

6.2 Proposed model: Fractional Laplace motion

6.2.1 Brownian motion

Brownian motion is widely recognized to be a special case of a Continuous Time Random Walk (CTRW). In general, CTRWs specify the particle location x_i at a time t_i by the iterative discrete equations [e.g., 190, 206]:

$$x_{i+1} = x_i + \eta_i \tag{6.5a}$$

$$t_{i+1} = t_i + \tau_i \tag{6.5b}$$

where (η_i, τ_i) is a set of random numbers drawn from a PDF $\Psi(\eta, \tau)$. One can recast the above equations in the following form:

$$t_n = \sum_{i=1}^{n} \tau_i \tag{6.6a}$$

$$x(t) = \sum_{i=1}^{n} \eta_i \tag{6.6b}$$

where $t \in [t_n, t_{n+1})$. The CTRW is said to be decoupled when the random variables η_i and τ_i are mutually independent. Brownian motion is a special case of a decoupled

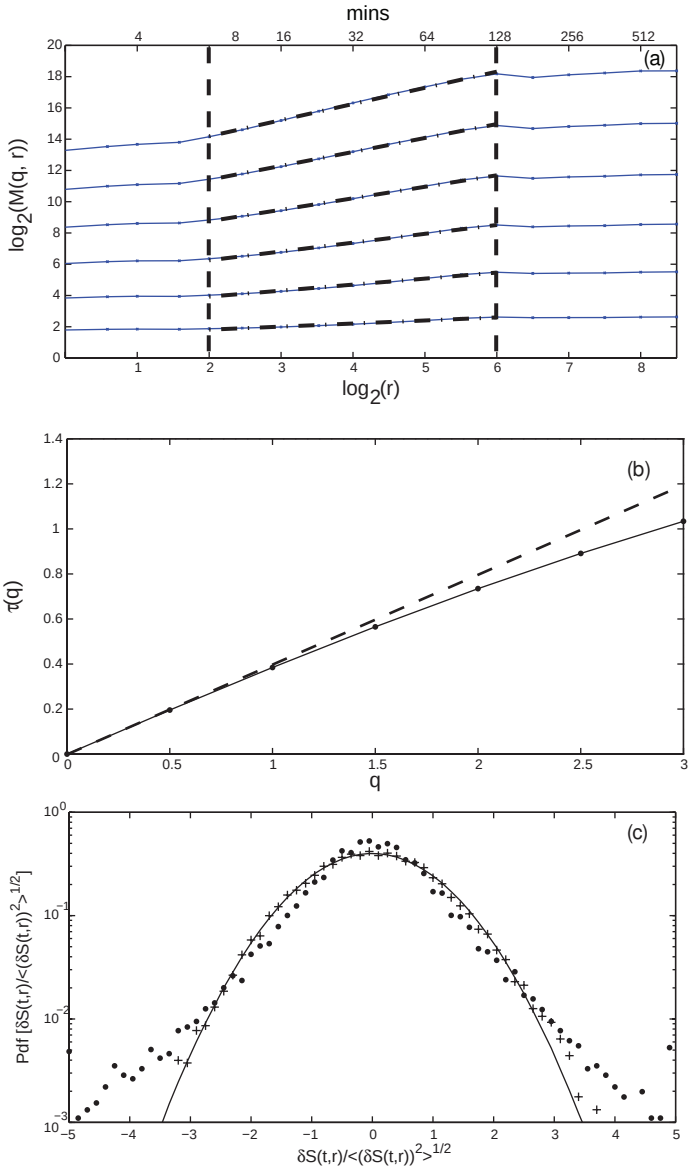

Figure 6.3: (a) Structure functions of sediment transport series. Vertical lines delineate the scaling regime which is between 8 mins and 128 mins (see top horizontal axis). (b) Estimated $\tau(q)$ curve (solid points) from the slopes of structure functions and a quadratic fit (solid line). Deviation from the the straight line establishes the presence of multi-fractality (see text for parameter values). (c) Change in PDF of sediment transport increments with scale. The solid dots correspond to PDF at increments of $r = 10$ (20 mins)and + to increments at $r = 60$ (120 mins). The solid line indicates a Gaussian PDF.

CTRW where η_i are independent, identically distributed (i. i. d) random variables drawn from a Gaussian distribution and τ_i are i. i. d random variables sampled from an exponential distribution. It is to note that the increments of Brownian motion follow a Gaussian distribution. However, the increments of most natural phenomena often show deviation from Gaussian PDFs and this has prompted the introduction of other stochastic processes such as Lévy walks and continuous-time Lévy flights, where the random variables η_i and/or τ_i are sampled from heavy tailed PDFs. However, such processes do not have all of their statistical moments convergent. For example, Lévy walks and Lévy flights do not have convergent second-moments [82]. It is also noted that modeling real data with such processes typically requires an exponential truncation of the algebraic decays [207], or sometimes an even milder than algebraic decay [208]. Correlation and long-range dependence in the observed data can be modeled by relaxing the independence assumption in sampling η_i and/or τ_i or by relaxing the independence assumption of a decoupled CTRW. Fractional Brownian motion, denoted by $B_H(t)$, is a decoupled CTRW starting at zero and has the following correlation function:

$$E\left(B_H(t)B_H(s)\right) = \frac{1}{2}\left(|t|^{2H} + |s|^{2H} - |t-s|^{2H}\right) \tag{6.7}$$

where $E(.)$ denotes the expectation operator and H is a parameter of fractional Brownian motion called the Hurst exponent. For $H = 0.5$, the fractional Brownian motion reduces to the standard Brownian motion with independent increments. For other values of $0 < H < 1$, $B_H(t)$ is called the fractional Brownian motion and its increments are positively correlated for $H > 0.5$ and negatively correlated for $H < 0.5$.

An extension of Brownian motion, or fractional Brownian motion, can be obtained via subordination. The notion of subordination was originated by Bochner [209]. One can obtain a subordinated stochastic process $Y(t) = X\left(T(t)\right)$ by randomizing the clock time of a stochastic process $X(t)$ using a new time $t_* = T(t)$. The resulting process $Y(t)$ is said to be subordinated to the so-called *parent process* $X(t_*)$, and t_* is commonly referred to as the *operational time* [210]. We propose the application of subordination of fractional Brownian motion (called fractional Laplace motion) as an extension to the Brownian motion model proposed by Einstein for sediment transport [164]. In the following subsection, we describe the properties of subordinated fractional Brownian motion.

6.2.2 Fractional Laplace motion

Fractional Laplace motion is a subordinated stochastic process, whose *parent process* is fractional Brownian motion and the *operational time* is a Gamma process [211]:

$$L(t) = B_H(\Gamma_t) \tag{6.8}$$

where $B_H(t)$ is fractional Brownian motion with Hurst exponent $0 < H < 1$ and Γ_t represents a Gamma process for any $t \geq 0$. The increments of the Gamma process $(\Gamma_{t+s} - \Gamma_t)$ have a gamma distribution with shape parameter $\nu = s$ and scale parameter $\beta = 1$, i.e.,

$$f(x) = \frac{1}{\beta^\nu \Gamma(\nu)} x^{\nu-1} e^{-x} \tag{6.9}$$

For $H = 0.5$ the subordinated process $L(t) = B_H(\Gamma_t)$ is called the Laplace motion.

Increments of the fractional Laplace motion defined by $Y(t,r) = L(t+r) - L(t)$, called the fractional Laplace noise, form a stationary process. Fractional Laplace noise has three parameters, namely, the Hurst exponent of the parent process H, the variance of the parent process $B_H(t)$ at the smallest scale $t = 1$, i.e., $\sigma^2 = Var(B_H(1))$, and the shape parameter of the Gamma process (Γ_t), ν. The variance of the fractional Laplace noise can be expressed as a function of the scale r and its parameters as [211]:

$$Var(Y(t,r)) = \sigma^2 \frac{\Gamma(2H + r/\nu)}{\Gamma(r/\nu)} \tag{6.10}$$

The covariance function of the fractional Laplace noise at a given scale r, defined as $\rho(n) = E(Y(t,r)Y(t+n,r))$, can be expressed in terms of its parameters for any $n \geq 1$ as:

$$\rho(n) = \frac{\sigma^2}{2}\left(\frac{\Gamma(2H + (n+1)r/\nu)}{\Gamma((n+1)r/\nu)} + \frac{\Gamma(2H + (n-1)r/\nu)}{\Gamma((n-1)r/\nu)} - 2\frac{\Gamma(2H + nr/\nu)}{\Gamma(\Gamma(nr/\nu))}\right) \tag{6.11}$$

Fractional Laplace noise is positively correlated for $H > 0.5$ and is negatively correlated for $H < 0.5$. In particular, fractional Laplace noise exhibits long-range dependence for $H > 0.5$.

The fundamental difference between fractional Laplace motion and other similar stochastic processes such as fractional Brownian motion and Lévy motion is that in the latter two cases the PDFs of the increments remain Gaussian and Lévy-stable, respectively, at all scales. In fractional Laplace motion, the PDFs of the increments

are variable with scale with Laplace PDFs at small scales and as the scale increases the PDFs approach Gaussian. In particular, fractional Laplace motion deviates from the classical self-similarity and shows stochastic self-similarity [211]. The Laplace PDF emerges from a different and less well-known central limit theorem called the Geometric Central Limit Theorem which states that the sum of a random number of independent, identically distributed variates with finite variance is asymptotically Laplace if the random count is geometrically distributed [188]. In fact, the Laplace PDF can be considered as a Gaussian PDF with a random variance or spread [212]. Given the stochastic self-similarity extensively documented in sediment transport series (in [51] and also in Section 7.2 of this chapter), the subordination of the fractional Brownian motion model proposed herein offers an attractive and simple extension to Brownian motion for particle movement, as demonstrated in more detail in the next section.

6.3 Fractional Laplace motion model for sediment transport

The physical relevance of the fractional Laplace motion to model sediment transport is argued on the basis that the notion of operational time acknowledges the randomness in the entrainment time experienced by sediment particles which are subject to a varied range of velocities in turbulent flows. It is known that turbulent velocity fluctuations themselves exhibit intermittency and possess a multi-fractal behavior [e.g., [201]]. Turbulent velocity "sweeps" and "bursts" are expected to influence particle motion and introduce a multi-scale variability in the fluctuations of the resulting sediment transport series. In groundwater hydrology, the notion of operational time has been used to acknowledge the fact that time passes faster for particles in higher velocity zones [103, 213]. Along these lines, a subordinated Brownian motion model has been proposed to model hydraulic conductivity [188] and connections between turbulent velocities and heterogeneous sediment properties have been proposed [214].

In the following subsections we study the multi-scale properties of fractional Laplace motion and show that fractional Laplace motion reproduces the intricate stochastic structure shown by the sediment transport series. Further, we elaborate on the model parameter fitting to the sediment transport series.

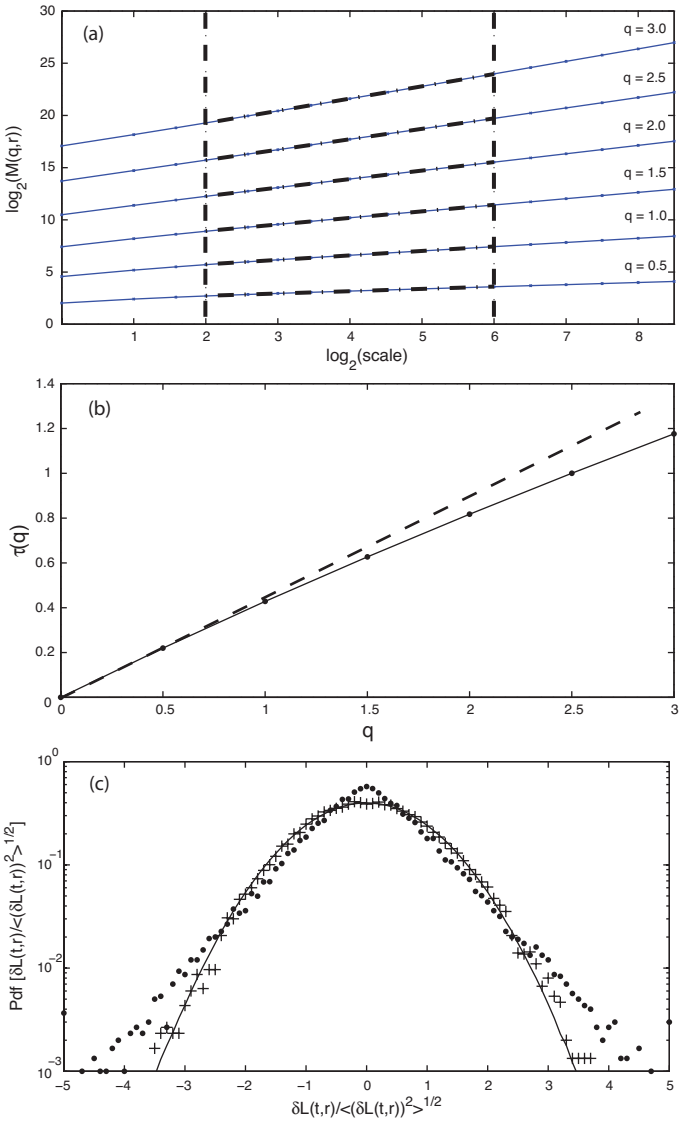

Figure 6.4: (a) Structure functions of fractional Laplace motion for a set of chosen parameters $H = 0.4$, $\nu = 3.0$ and $\sigma = 1$ computed from equation (6.12). The vertical lines correspond to the scaling regime of the sediment transport series which is from scales of $r = 4$ to $r = 64$. (b) Estimated $\tau(q)$ curve (solid points) from the fitted slopes of the structure functions. The solid line indicates a quadratic fit and the non-linear dependence of $\tau(q)$ on q establishes that fractional Laplace motion shows a multi-fractal behavior in the scales under consideration. (c) Change of PDF of increments of simulated fractional Laplace motion series. Solid dots correspond to PDF of increments at $r = 10$ and $+$ to $r = 60$. Solid line indicates a Gaussian PDF.

6.3.1 Multi-fractal properties of fractional Laplace motion

In order to study the self-similar behavior of fractional Laplace motion, we first study the analytical behavior of the structure functions of fractional Laplace motion. The structure functions of fractional Laplace motion for $\sigma = 1$ can be written in terms of its parameters H and ν as [211]:

$$M(q,r) = \sqrt{\frac{2^q}{\pi}}\Gamma(\frac{1+q}{2})\frac{\Gamma(Hq + r/\nu)}{\Gamma(r/\nu)} \tag{6.12}$$

Statistical scaling or self-similar behavior requires that the structure functions follow a power-law relationship in scales. Figure 6.4(a) shows the structure function dependence on scales in log-log space for an arbitrary choice of the parameter values, $H = 0.4$ and $\nu = 3.0$. (These values of H and ν are used for illustration of the model properties and the estimation of these parameters is discussed more thoroughly in the next subsection). It is to note that from Figure 6.4(a) that although (6.12) does not analytically accept a power law expression on r, for all practical purposes, fractional Laplace motion can be approximated by a self-similar process, i.e., the structure functions show a power-law relationship in scales at least for the range of scales which coincide with the scaling regime of sediment transport series (scales or lags of $r = 4$ to $r = 64$). Plotting the $\tau(q)$ curve (estimated from the slopes of $M(q,r)$ vs r in log-log space within the above scaling regime) one can see that the scaling exponents, $\tau(q)$, show a non-linear dependence on the order of moments q (see Figure 6.4(b)). It is to note that the scaling exponents $\tau(q)$ are independent of the variance of the parent process σ^2. The change in PDF of the increments of fractional Laplace motion with scale is shown in Figure 6.4(c), where the PDF at small scales ($r = 10$ in Figure 6.4(a)) shows a double-exponential behavior and it eventually tends to a Gaussian distribution for large scales ($r = 60$ in Figure 6.4(a)). The above results document that fractional Laplace motion can be approximated by a stochastic self-similar process in an intermediate range of scales and within those scales it exhibits a multi-fractal behavior. At the limit of very large time-scales, i.e., as $r \to \infty$, fractional Laplace motion tends to a fractional Brownian motion with $\tau(q)$ a linear function of q (i.e., mono-fractal behavior).

It is interesting to note from equation (6.12) that the second-order structure function of Laplace motion ($H = 0.5$ and $q = 2$) obeys a power law relationship in scales and in

particular it shows a linear dependence on scales:

$$M(2,r) = [\frac{2}{\nu\sqrt{\pi}}\Gamma(1.5)]r \tag{6.13}$$

yielding an exponent of $\tau(2) = 1$. This implies that Laplace motion has self-similar second-order moments, i.e., it shows a log-log linear power spectrum (although higher order moments are not exact power laws). In the next subsection we elaborate on the parameter estimation of the fractional Laplace motion from the sediment transport series.

6.3.2 Model fitting

As seen in the previous section, fractional Laplace motion has three parameters H, ν and σ. The scale parameter of the operational time PDF, β, is 1 by the definition of fractional Laplace motion [211]. Estimation of the parameters H and ν from the sediment transport series is performed by minimizing the mean squared error between the empirical and theoretical $\tau(q)$ curves. The mean squared error, denoted by MSE, is a function of H and ν and is independent of σ:

$$MSE(H,\nu) = \sum_{q} \left(\tau_m(q) - \hat{\tau}(q)\right)^2 \tag{6.14}$$

where $\hat{\tau}(q)$ are the estimated scaling exponents of the sediment transport series (see Figure

refmfexperiment(b)) and $\tau_m(q)$ are the scaling exponents of the fractional Laplace motion model which are computed from the slopes of the theoretical $M(q,r)$ versus r within the scaling regime of the sediment transport series ($4 < r < 64$) in the log-log space (see Figure 6.4(b)). Minimization of the mean squared error for the sediment transport series yields a Hurst exponent of $H = 0.39$ and a shape parameter of $\nu = 6.8$. It is to note that the multi-scale structure of fractional Laplace motion model is determined by the parameters H and ν. Further, we estimate the parameter σ by minimizing the mean squared error between the variance of the increments of sediment transport series and the fractional Laplace noise for $H = 0.39$ and $\nu = 6.8$ over the scaling regime ($4 < r < 64$):

$$\sigma = Min \sum_{r=4}^{r=64} \left(Var(\delta S(t,r)) - Var(Y(t,r))\right)^2 \tag{6.15}$$

where $Var(\delta S(t,r))$ is the variance of the increments of sediment transport series and $Var(Y(t,r))$ is the variance of fractional Laplace noise at the scale r, given by (6.10). The value of σ estimated using (6.15) was $\sigma = 0.296$. The multi-fractal parameters of the fractional Laplace motion model computed with the estimated parameters of $H = 0.39$ and $\nu = 6.8$ were $c_1 = 0.41$ and $c_2 = 0.041$ which compare very well to the values estimated from the sediment transport data of $c_1 = 0.41$ and $c_2 = 0.04$. (Note that c_1 and c_2 were not used directly in the model fitting which was done via (6.14) on the whole $\tau(q)$ curve). As a result the model and the data-estimated $\tau(q)$ curves are indistinguishable. Figure 6.5(a) shows the increments of sediment transport series at a scale of $r = 20$ or 40 mins (note that this scale lies within the scaling regime of the sediment transport series). For visual comparison, the fractional Laplace noise simulated series with the estimated parameters $H = 0.39$, $\nu = 6.8$ and $\sigma = 0.296$ at the same scale is shown in Figure 6.5(b).

As noted in the previous section, fractional Laplace noise is negatively correlated for $H < 0.5$. Figure 6.6(a) shows the autocorrelation function of the increments of sediment transport series at the scale $r = 20$ (40 mins). The data show a negative correlation in the scaling regime of the sediment transport series for small lags. This is qualitatively consistent with the fractional Laplace noise model which shows a negative correlation for the estimated parameter values (see Figure 6.6(b)). The increments of fractional Laplace motion at small scales follow a Laplace PDF which eventually becomes Gaussian at larger scales. Figure 6.7(a) shows the PDF of sediment transport increments at a scale of $r = 4$ which is the beginning of the scaling regime of the sediment transport series. A Laplace PDF provides a good fit to the increments at that scale. As noted in Figure 6.7(b), the PDF of sediment transport increments at a scale of $r = 64$ (128 mins) tends to a Gaussian PDF. Thus, one can see that the sediment transport series are consistent with the properties of fractional Laplace motion within the scaling regime.

6.4 Discussion

In the previous section we established the fact that the fractional Laplace motion model is able to reproduce the intricate stochastic structure of the observed sediment transport

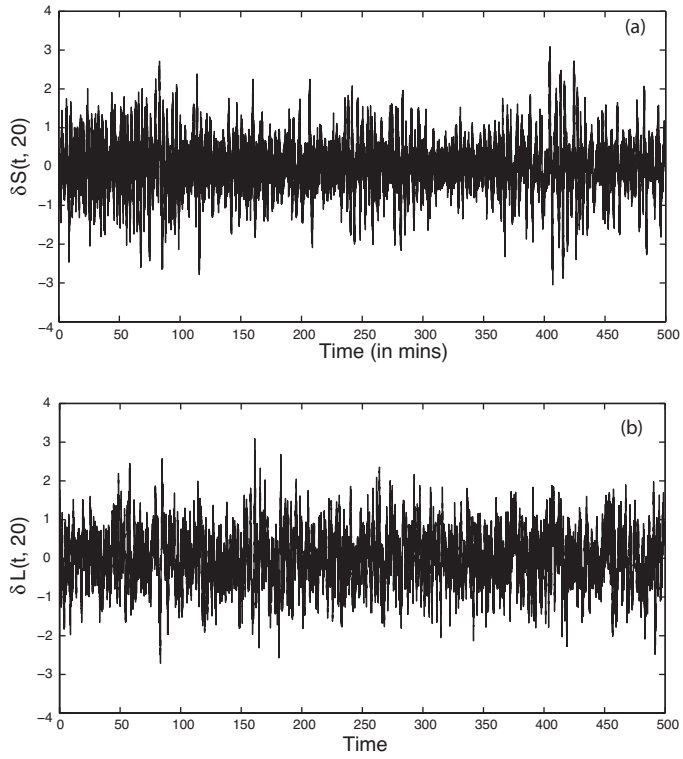

Figure 6.5: Comparison of the increments of the sediment transport series in kgs at scale $r = 20$ (40 mins) (top) and the same scale increments of simulated fractional Laplace motion series with $H = 0.39$, $\nu = 6.8$ and $\sigma = 0.3$ (bottom). The values of H and ν were obtained by minimizing the mean squared error defined in equation (6.14). The value of σ was obtained using (6.15). The scale of $r = 20$ was chosen for comparison as it lies within the scaling regime of the sediment transport series.

series over a range of scales and also reproduce the change of the PDFs of increments of sediment transport series in the scaling regime. In this section, we discuss the physical significance of the notion of operational time in sediment transport series. Near-bed turbulence is known to play an important role in sediment transport [199]. Turbulent velocity fluctuations pick up sediment particles and transport them over long distances. However, since the turbulent velocities themselves are known to exhibit variability over a large range of scales, the entrainment time experienced by the sediment particles is also expected to carry some of this variability. This consideration leads to a randomization of time over which a sediment particle is operated upon, as sediment particles in different

velocity zones experience time to move faster or slower depending on whether they are in a high or low velocity zone, respectively. Thus, the notion of operational time can arise due to the stochastic nature of sediment particle entrainment. It is interesting to note that the turbulent velocity fluctuations themselves exhibit Laplace and stretched Laplace distributions at small scales and their PDFs become Gaussian at larger scales [215]. It is also interesting to note that the rate of sediment particle entrainments, which are proportional to the shear stress fluctuations at the bed, have been reported to follow a Gamma distribution [197]. Both these observations are qualitatively consistent with the fractional Laplace motion model for sediment transport proposed in this study.

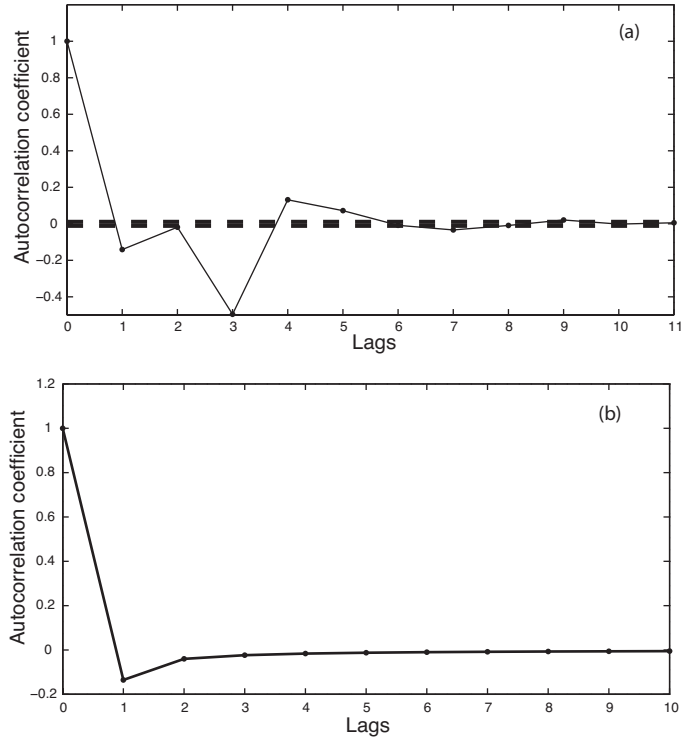

Figure 6.6: (a) The autocorrelation function of the increments of sediment transport series at a scale of $r = 20$ (40 mins). The dashed lines indicate the 95% confidence intervals (approximated as $\pm 1.96/\sqrt{N}$, $N = 30293$ points) on the autocorrelation coefficients. (b) The autocorrelation function of generated fractional Laplace noise series at the same scale with parameters $H = 0.39$ and $\nu = 6.8$ fitted to the data. The autocorrelation of the fractional Laplace noise is computed from equations (6.10) and (6.11).

The observed multi-scaling and intermittency in sediment transport series (macro-scale behavior) was shown to arise by the introduction of the notion of operational time in Brownian-type particle movement (micro-scale behavior). Thus, while the model parameters H and ν relate to the (unobserved) particle movement statistics, they are estimated from the (observed) sediment transport statistics, and specifically from their multi-scale behavior concisely parameterized via the parameters c_1 and c_2. It is of interest to study how the parameter space of (H, ν) relates to that of (c_1, c_2) in order to gain insight on model sensitivity and the physical meaning of the parameter ν which characterizes the variability of the particle motion. We compute the multi-fractal parameters c_1 and c_2 for different values of the model parameters H and ν by evaluating $M(q, r)$ from (6.12), estimating $\tau(q)$ in the range $4 \leq r \leq 64$, and approximating the $\tau(q)$ curve as a quadratic function in q (equation (6.4)). Figure fig:modelspace shows the contour plots of c_1 and c_2 for different values of H and ν. It is to note that the average "roughness" of the sediment series, quantified by the parameter c_1, is strongly dependent on the Hurst exponent of the fractional Brownian motion H (see Figure fig:modelspace(a)) and not as much on the parameter ν of the operational time. On the other hand, from Figure 6.8(b), one can see that the intermittency coefficient c_2 is strongly dependent on the shape parameter ν of the distribution of operational time for a given value of H. In particular, for a given value of H, the value of c_2 is higher for a higher value of ν. One way to understand this is to note that for higher values of ν the Gamma distribution has a higher variance. Thus, for higher values of ν the operational time is sampled from a distribution with higher variance and this variability in the operational time shows up as a higher intermittency coefficient in the sediment transport series (larger degree of temporal heterogeneity in bursts of sediment transport increments). It is emphasized that estimation of the parameter values of the fractional Laplace motion, H and ν, was performed through the scaling exponents of the structure functions of the sediment transport series (equation (6.14)). Direct estimation of the parameters H and ν, or for that matter direct assessment of the whole statistical structure of operational time from observations, would require access to series of particle entrainment which are difficult to make and are not available in the experimental setting studied here. Rather, the present study attempted a physical insight via relating the macro-scale statistics of the sediment series to the micro-scale dynamics of particle movement.

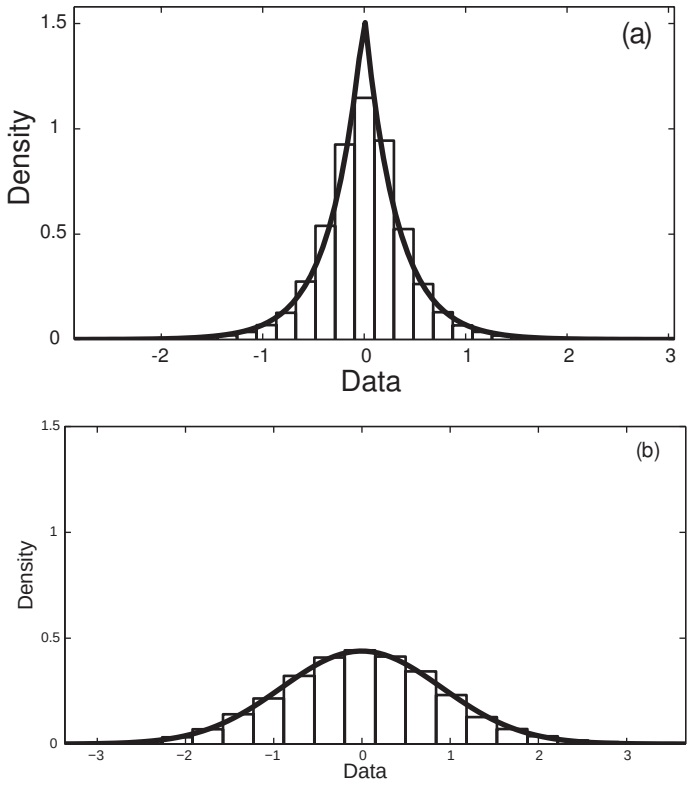

Figure 6.7: Change in PDF of sediment transport increments in the scaling regime. (a) Laplace PDF (solid line) provides a good fit to the PDF of sediment transport increments at $r = 4$ (8 mins; beginning of the scaling regime) and (b) the PDF of sediment transport increments becomes Gaussian (solid line) at $r = 64$ (128 mins; ending of the scaling regime).

6.5 Concluding remarks

In this work we proposed the adaptation of fractional Laplace motion as a stochastic model for sediment transport. Fractional Laplace motion arises from randomization of the clock time in fractional Brownian motion, and introduces the notion of operational time. The physical significance of operational time in the context of sediment transport was reasoned on the basis that the stochastic nature of turbulent velocity fluctuations near the bed induces stochasticity in particle entrainment and, therefore, the time over which particles are in motion. The proposed model was shown able to reproduce the multi-scale statistics of sediment transport series and was validated against a data set

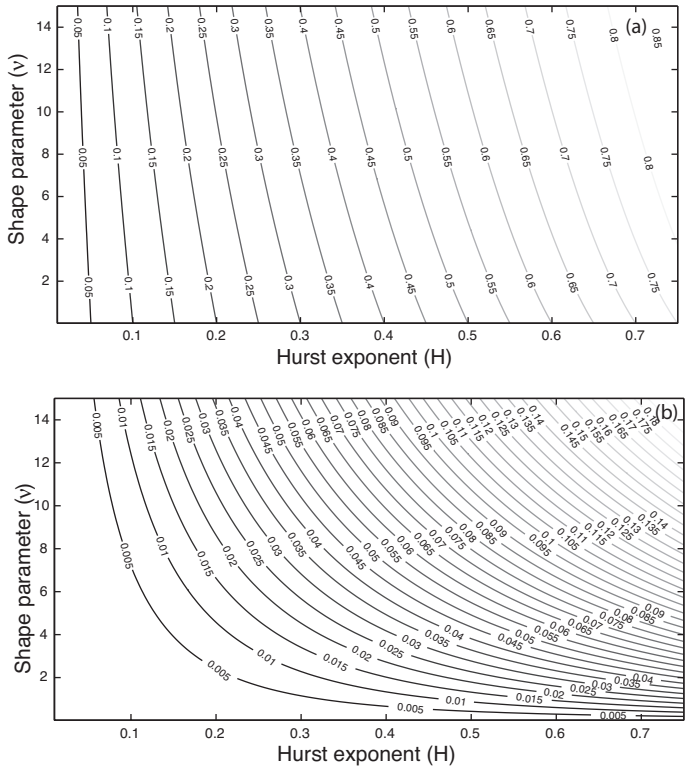

Figure 6.8: Contour plots of the multi-fractal parameters, c_1 (top) and c_2 (bottom), for different values of the fractional Laplace motion model parameters H and ν.

from a large-scale laboratory experiment. The effect of the model parameters on the multi-fractal parameters of sediment transport series was also discussed. Although direct estimation of the model parameters would require particle-scale observations, it was shown here that an indirect estimation based on the statistics of sediment transport series is possible. We see this work as a step towards relating the micro-scale dynamics of particle movement to the macro-scale statistics of sediment transport via minimum complexity stochastic models.

Chapter 7

Statistical Characterization of Surface Dynamics of the Depositional Systems

The architecture of stratigraphy is a function of three characteristics of depositional systems: 1) the topography of an actively deforming surface, 2) the dynamics of the deforming surface, and 3) the rate of net deposition [216, 55, 217, 62]. As all three of these properties are influenced by environmental conditions (e.g., climate and tectonics) the architecture of stratigraphy in sedimentary basins contains a vast amount of data that could be used to quantitatively reconstruct paleolandscape dynamics across many time scales [218, 54, 219]. Quantitative analysis of stratigraphy exposed in outcrops or imaged in seismic data coupled to numerical modeling of sedimentary basin filling has blossomed over the last thirty years, initiating with the pioneering works by Leeder [56] and Allen [63]. The general goal for many of these studies was to develop tools to invert stratigraphic data for paleo-environmental conditions. This exercise has proved to be a difficult venture. Of the many challenges associated with inverting the stratigraphic record one of the greatest is characterizing how large magnitude, but infrequent events (e.g., avulsions, storms, floods) influence the dynamics of depositional systems and how this information gets stored in stratigraphy. Characterizing these large magnitude infrequent events is challenging because many of these events have recurrence

intervals with intermediate time-scales ($10^1 - 10^4$ years) which make them difficult to study directly or to constrain using dating techniques [55]. In this study we used data from a physical experiment on a fluvial system in an experimental basin experiencing relative subsidence to characterize statistics associated with the fluvial dynamics that are dominant in these intermediate time-scales (referred to as "mesoscale" dynamics by Sheets et al. [55]) of depositional systems.

As discussed in [54] and [55] the time-scales associated with mesoscale dynamics lie between two deterministic end members. Sheets et al. [55] provide a heuristic definition for the mesoscale time range as one which has a lower bound given by the 'short' time-scale (time-scales of evolution of bedforms and bars) on which channels behave coherently and deterministically in response to the sediment routing system, and an upper bound given by the 'long' time-scale (time-scales of basinwide deposition) on which autocyclic variability sums to produce the average behavior represented in stratigraphic models [54]. In many cases, the mesoscale time range is the domain of stochastic behavior associated with avulsion and reorganization of the fluvial system. This has been recognized at least since the work of Leeder [56] who developed the first physically based quantitative model for alluvial architecture. In this model, fluvial basins were filled by channels avulsing at a constant frequency to random locations. Since the publication of this model many additional alluvial architecture models have been proposed which characterize various properties of the stochastic depositional dynamics (avulsion frequency, avulsion jump length, etc) through random numbers generated from probability density functions of various shapes [220, 221, 222]. These models have in part been motivated by field observations of stratigraphy in which depositional elements are at least partially organized in a stochastic fashion [223, 224, 225]. However, at present few time-series of depositional dynamics exist to aid the identification of the type and shape of probability distributions which should be used for modeling the mesoscale dynamics that result in stochastic stratigraphy.

The focus of this study is to characterize the probability distributions that describe the dynamics of depositional systems using a time series of elevation recorded at several spatial transects during a physical experiment on delta evolution in a net aggradation setting. During this experiment, elevation was monitored at a temporal frequency comparable to the time-scale of the system's mesoscale dynamics and over a duration long

enough to generate reliable statistics on the magnitude of elevation increments. In particular, this study addresses two issues: 1) which probability distributions describe the processes that govern the depositional dynamics of the system, and 2) to what degree do physical mechanisms constrain the occurrence of extremes and how are these constraints reflected in the probability distributions of the processes? Answering these two questions will not only improve our ability to characterize the statistics of depositional systems but will also aid the community in filtering environmental signals preserved in stratigraphy.

The chapter is structured as follows. In the next section, we give a brief outline of the experimental data analyzed in this study. In Section 7.2, the variables whose statistical characteristics are studied are defined along with their notation. In Sections 7.3 and 7.4, a statistical analysis of the random variables which govern the surface dynamics and preserved stratigraphic record in the experimental delta are presented. Having established the non-Gaussian form of the probability distributions of the processes involved, in Section 7.5 the self-similar structure of surface evolution is characterized using higher-order statistical structure function analysis. In Section 7.6, we address the question of what physical mechanisms constrain the occurrence of extremes in depositional systems and how these constraints reflect in the probability distributions of the random variables studied. Preliminary thoughts on continuum models for surface evolution of depositional systems consistent with the documented probability distributions for erosional, depositional and inactivity events are presented in Section 7.7. Finally, conclusions are drawn in Section 7.8.

7.1 Experimental Setting

The experiment discussed in this study (DB-03) was performed and originally documented by Sheets et al. [217]. The main focus of the work of Sheets et al. [217] was documenting the creation and preservation of channel-form sand bodies in alluvial systems. Since this initial publication, data from the DB-03 experiment have been utilized in studies on compensational stacking of sedimentary deposits [224] and clustering of sand bodies in fluvial stratigraphy [223]. In this section we provide a short description of the experimental setup. For a more detailed description see [217].

The motivation for the DB-03 experiment was to obtain detailed records of fluvial processes, topographic evolution and stratigraphy, with sufficient spatial and temporal resolution to observe and quantify the deposition of channel sand bodies. The experiment was performed in the Delta Basin at St. Anthony Falls Laboratory at the University of Minnesota. This basin is 5 m by 5 m and 0.61 m deep (Figure 7.1(A)). Accommodation is created in the Delta Basin by slowly increasing the base level by way of a siphon-based ocean controller. This system allows for the control of base level with millimeter resolution [217].

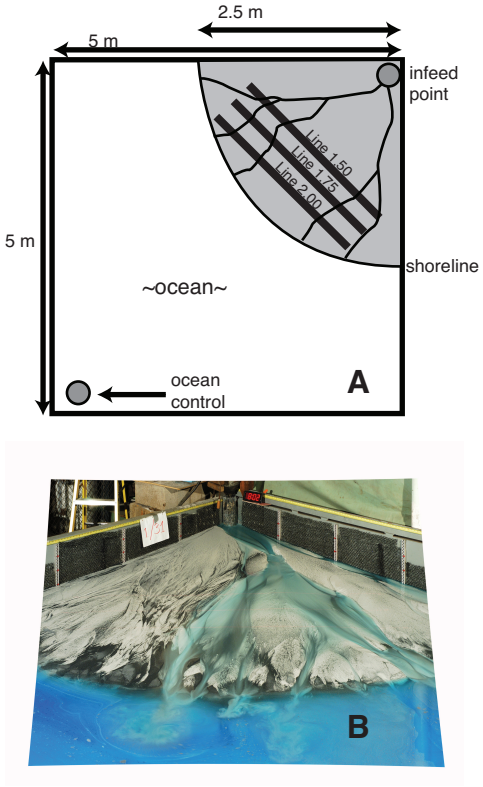

Figure 7.1: (A) Schematic of the experimental arrangement. The data used in this study is of the transect labelled Line 1.75. This transect is located at a perpendicular distance of 1.75 m from the sediment infeed point. (B) A photograph of the DB-03 experiment at a run-time of approximately 11 hrs.

The experiment included an initial buildout phase in which sediment and water were mixed in a funnel and fed into one corner of the basin while base level remained constant.

The delta was allowed to prograde into the basin and produced an approximately radially symmetrical fluvial system. After the system prograded 2.5 m from source to shoreline a base level rise was initiated. Subsidence in the Delta Basin was simulated via a gradual rise in base level, at a rate equal to the total sediment discharge (Q_s) divided by the desired fluvial system area. This sediment feed rate allowed the shoreline to be maintained at an approximately constant location through the course of the experiment. A photograph of the experimental deposit, including the topographic measurement lines is shown in Figure 7.1. Sheets et al. [217] used a sediment mixture of 70% 120 μm silica sand and 30% bimodal (190 μm and 460 μm) anthracite coal.

Topography was measured with a subaerial laser topography scanning system, similar to the system used in the Experimental Earthscape Basin (XES) [55]. Unlike the XES system, however, where the topography of the entire fluvial surface is mapped periodically, topography was monitored at 2 minute intervals along three flow-perpendicular transects, located 1.50 m, 1.75 m, and 2.00 m from the infeed point. To measure a full cross-section of topography, including areas inundated by water, the experiment was stopped every two minutes and water was allowed to drain off the fluvial surface prior to collecting measurements. The time series of deposition along the transect located 1.75 m from the infeed is shown in Figure 7.2 . With this system, we obtained measurements with a sampling interval of 0.8 mm in the horizontal and measurement precision of 0.9 mm in the vertical. This experiment lasted for 30 hours and produced an average of 15 cm of stratigraphy.

No attempt was made to formally up-scale the results from this experiment to field-scale. In addition, parameters associated with this experiment were not set to produce an analogue to any particular field fan-delta system. As such, specific geometric data associated with this experiment cannot strictly be utilized to estimate the field scale deposit geometries or dynamics of a specific system. Rather, the goal of the experiment was to create a self-organized, distributary depositional system in which many of the processes characteristic of larger fan-delta systems could be monitored in detail over spatial and temporal scales which are impossible to obtain in the field. This experimental technique is similar to the 'similarity of process' philosophy outlined in [226]. As such the focus in this chapter is on identifying the general class of distributions (i.e., heavy vs. thin tail) which characterize the dynamics of topography in the DB-03 experiment

and their relation to the architecture of the preserved stratigraphy.

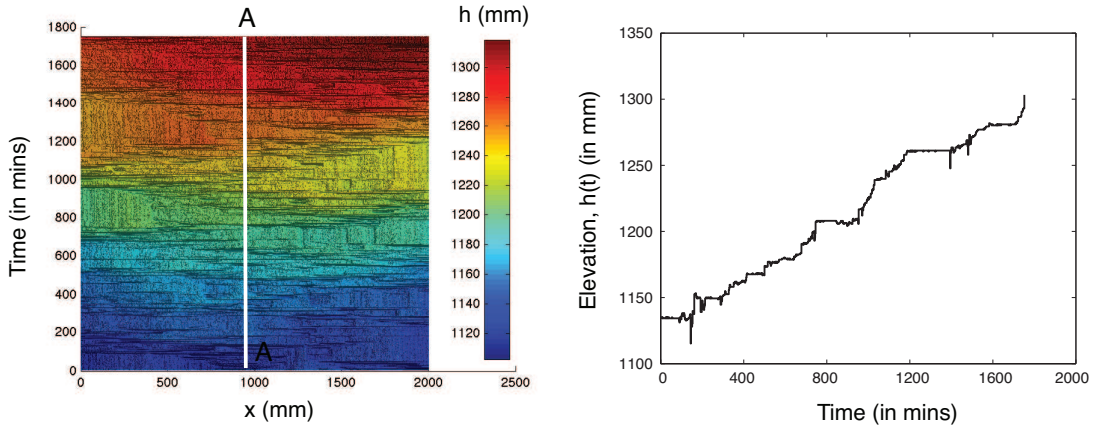

Figure 7.2: Temporal evolution of the transect Line 1.75. The temporal resolution of the data available is 2 mins and the duration for which the data was recorded is 30 hrs. A time transect of elevation is marked as A-A and the plot of that transect is shown in the lower panel.

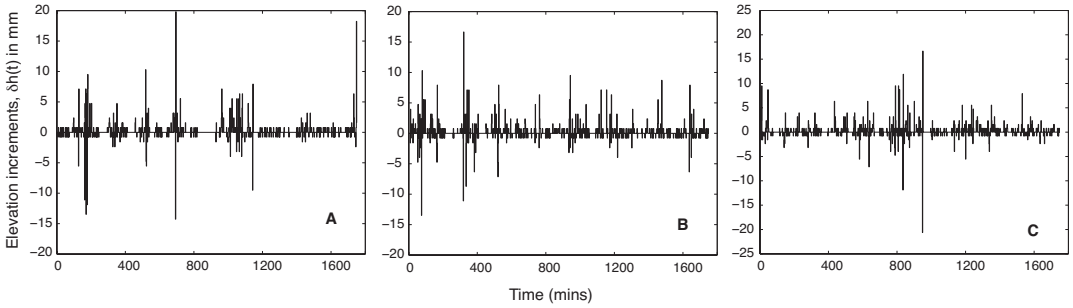

Figure 7.3: Elevation increments in time along three different transects, (A) corresponds to transect A-A, of Figure 7.2. The positive values indicate magnitude of depositions, negative values indicate magnitude of erosions and the zero values indicate periods of inactivity.

7.2 Terminology

The experimental data used in this study consists of a 30 hrs temporal evolution of an elevation transect (Line 1.75 in Figure 7.1) with a temporal resolution of 2 mins

(as described in Section 9.2). At any spatial location along the Line 1.75, we define elevation increments in time as,

$$\delta h(t) = h(t + \Delta t) - h(t) \tag{7.1}$$

where $h(t)$ is the elevation at time t at a given location and Δt is the temporal resolution of the experimental data. Figure 7.3 shows the elevation increments at three different locations along Line 1.75. Positive values of elevation increments correspond to deposition, negative values to erosion and were denoted as,

$$D_i = \delta h(t) > 0 \tag{7.2a}$$

$$E_i = \delta h(t) < 0 \tag{7.2b}$$

while $\delta h(t) = 0$ corresponds to inactivity at that given location. Each of these three processes, deposition, erosion and inactivity, has a characteristic time-scale of operation. Periods of inactivity, τ_i, are defined as continuous periods during which neither deposition nor erosion occurs in the system, i.e., $\delta h(t) = 0$. Similarly, durations of depositional events, τ_d, are defined as the periods during which continuous deposition occurs in the system, i.e., the uninterrupted periods for which $\delta h(t) > 0$, while durations of erosional events, τ_e, are defined as the periods during which continuous erosion occurs, the uninterrupted periods for which $\delta h(t) < 0$. Further, the magnitudes of a single depositional event (D_e) or an erosional event (E_e) are defined as the sum of all the elevation increments during the duration of a single depositional event (τ_d) or an erosional event (τ_e), respectively,

$$D_e = \sum_{i=1}^{\tau_d} D_i \tag{7.3a}$$

$$E_e = \sum_{i=1}^{\tau_e} E_i. \tag{7.3b}$$

It is easy to see that these magnitudes of depositional and erosional events are random sums of random variables. The schematic of Figure 7.4 shows the random variables defined which characterize the surface evolution of the depositional system. The statistical characteristics of this set of random variables $(\delta h(t), D_i, E_i, D_e, E_e, \tau_d, \tau_e, \tau_i)$ are studied in Section 7.3.

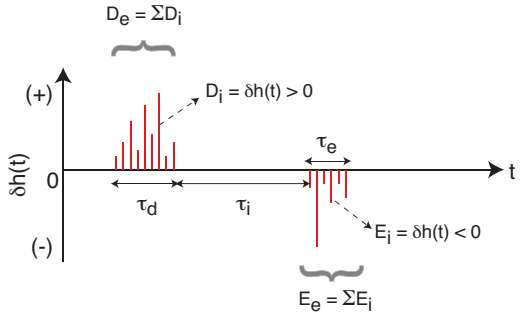

Figure 7.4: A schematic showing the elevation increments in time, and the definitions of the random variables studied in Section 7.3. Magnitudes and durations of erosional and depositional events, along with the periods of inactivity are shown.

The stratigraphic column that results from such an erosional-depositional process can be formed from the elevation time series as shown in the schematic of Figure 7.5. Stratigraphic deposits are depositional bodies bound between two erosional boundaries. The thickness of any deposit is denoted by D_{st}. The time interval demarcating the boundaries of the stratigraphic deposit D_{st} is denoted by τ_{st}. The preserved stratigraphy is completely described by these two random variables (D_{st} and τ_{st}) whose statistical properties are studied in Section 7.4.

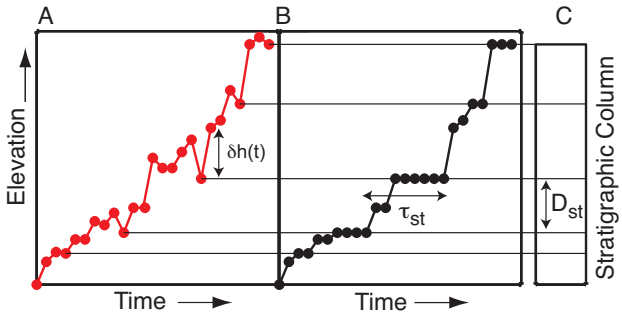

Figure 7.5: A schematic showing the building of a stratigraphic column from the elevation time series. Stratigraphic deposits are depositional bodies bound between two erosional events. Elevation increments ($\delta h(t)$), duration between stratigraphic deposits (τ_{st}) and thickness of stratigraphic deposits (D_{st}) are shown above.

7.3 Statistical characteristics of surface evolution

In this section, we present statistical analysis of random variables that govern the surface dynamics of delta evolution, namely, surface elevation increments (D_i, E_i), the magnitudes of erosional and depositional events (D_e, E_e) and durations of erosional and depositional events (τ_d, τ_e), as well as the periods of inactivity, τ_i. All the statistics presented in the following subsections were computed on the ensemble of time transects along the horizontal line (as shown in Figure 7.2) and the total number of time transects available was 2502, each for a duration of 30 hrs.

7.3.1 Statistics of erosional and depositional magnitudes

Consider the elevation increments, $\delta h(t)$, as defined in equation (7.1). Figure 7.6 shows the probability density function (pdf) of the elevation increments normalized by their standard deviation in semi-log scale. It is noted that the pdf of increments exhibits a concave-up decay in the tails of the pdf indicating a heavy-tail behavior and considerably deviates from a Gaussian pdf (shown as the solid parabola in Figure 7.6). The log-log linear decay (see Figures 7.7(A) and (C)) in the left and right tails of the elevation increments establishes that the positive and negative increments (deposition and erosion, respectively) are heavy-tailed. In contrast to thin-tailed pdfs, where the chance of occurrence of an extreme event is vanishingly zero, in heavy-tailed pdfs an extreme event has a small, but significant chance of occurrence. Heavy-tailed pdfs often have a power-law decay, which is a slower decay than exponential (e.g., exponential pdf) and super-exponential decays (e.g, Gaussian pdf), thus, assigning a relatively higher probability for the occurrence of extremes. In this subsection we characterize the pdfs of both erosional ($E_i = \delta h(t) < 0$) and depositional ($D_i = \delta h(t) > 0$) magnitudes.

A common pdf with power-law decay is a Pareto distribution. The density of a Pareto distribution is given by:

$$f(x) = \alpha \frac{\gamma^\alpha}{x^{\alpha+1}} \tag{7.4}$$

where α is the tail index, γ is the minimum possible value of the random variable and the density is defined for $x \geq \gamma$. The probability of exceedance of a Pareto distribution is given by:

$$P(X > x) = \left(\frac{\gamma}{x}\right)^\alpha \tag{7.5}$$

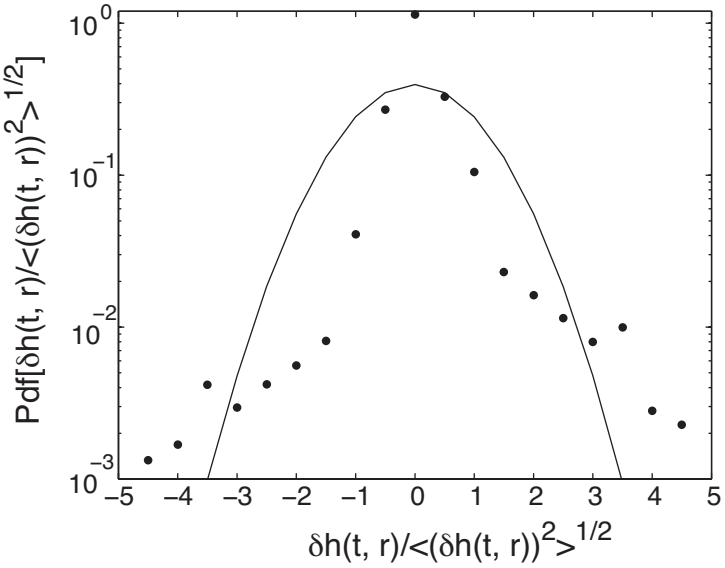

Figure 7.6: Relative frequency of elevation increments $\delta h(t)$ in semi-log scale (solid circles); the solid line indicates a Gaussian density. The concave-up shape of the tails indicate the presence of heavy-tailed behavior (a linear decay corresponds to exponential decay of tails) and show that elevation increments deviate considerably from Gaussian behavior.

It is easy to see that a Pareto distribution assigns a finite probability for the occurrence of very large magnitude events (no upper limit), which do not typically occur in natural systems owing to constraints set by physical mechanisms that govern the evolution of the system (for example, see [227] and [228] for upper bounds reported on probability distributions of other systems). One common truncated heavy-tailed, power-law pdf is the truncated Pareto distribution. The density of the truncated Pareto distribution is given by:

$$f(x) = \frac{\alpha \gamma^{\alpha} x^{-\alpha-1}}{1-(\gamma/\nu)^{\alpha}} \tag{7.6}$$

and its probability of exceedance is given by:

$$P(X > x) = \frac{\gamma^{\alpha}\left(x^{-\alpha} - \nu^{-\alpha}\right)}{1-(\gamma/\nu)^{\alpha}} \tag{7.7}$$

where ν is the truncation parameter or the upper bound on the random variable, α is the tail index and γ is the lower bound on the random variable X. We fitted Pareto

and truncated Pareto distributions to both the depositional and erosional magnitudes, as shown in Figures 7.7(B) and (D), respectively.

In [229], a maximum likelihood estimation (MLE) method was proposed to estimate the parameters α and γ of the Pareto distribution and that method is adopted in this study. In [230], a MLE method was proposed to estimate the parameters of the truncated Pareto distribution and this method is adopted in our study. The estimation involves the conditional MLE based on the $(k+1)$ largest-order statistics representing only the portion of the tail where the truncated Pareto approximation holds. Let $X_1, X_2, \cdots, X_n$ denote a random sample from a truncated Pareto distribution, and $X_{(1)} \geq X_{(2)} \geq \cdots \geq X_{(n)}$ denote its order statistics, where $X_{(k)}$ is the k^{th} largest observation. The conditional MLE for the parameters of the truncated Pareto distribution based on the $(k+1)$ largest-order statistics is given by: $\hat{\nu} = X_{(1)}$, $\hat{\gamma} = k^{1/\hat{\alpha}} \left(X_{(k+1)}\right) [n - (n-k)(X_{(k+1)}/X_{(1)})^{\hat{\alpha}}]^{-1/\hat{\alpha}}$, and $\hat{\alpha}$ is obtained by solving,

$$\frac{k}{\hat{\alpha}} + \frac{k(X_{(k+1)}/X_{(1)})^{\hat{\alpha}} ln\left(X_{(k+1)}/X_{(1)}\right)}{1 - \left(X_{(k+1)}/X_{(1)}\right)^{\hat{\alpha}}} - \sum_{i=1}^{k} [lnX_{(i)} - lnX_{(k+1)}] = 0. \tag{7.8}$$

Aban et al. [230] proposed an asymptotic level-q test $(0 < q < 1)$ which rejects the null hypothesis $H_0 : \nu = \infty$ (Pareto distribution) when $X_{(1)} < [(nC)/(-lnq)]^{1/\alpha}$, where $C = \gamma^{\alpha}$. The corresponding p-value of this test is given by $p = exp\left(-nCX_{(1)}^{-\alpha}\right)$. In practice, they proposed the use of the Hill's estimator,

$$\hat{\alpha}_H = \left(k^{-1} \sum_{i=1}^{k} \left(lnX_{(i)} - lnX_{(k+1)}\right) \right)^{-1} \tag{7.9a}$$

$$\hat{C} = \frac{k}{n} \left(X_{(k+1)}\right)^{\hat{\alpha}_H} \tag{7.9b}$$

for the estimation of parameters C and α. A small value of $p < 0.1$ (suggested by Clauset et al. [229] as a conservative estimate) in this case indicates that the Pareto distribution does not provide a good fit to the data. A detailed description of the proofs and method for estimating the parameters of the distribution can be found in [230].

Using the above test, we rejected the Pareto distribution for D_i and E_i as the estimated p-values (0.0022 and 0.0048) were less than 0.1. However, the truncated Pareto distributions provided an acceptable fit to the data for the magnitudes of D_i and E_i (see

Figure 7.7). The estimated tail indices of the best fit truncated Pareto distributions for positive elevation increments, D_i, and negative elevation increments, E_i, are $\hat{\alpha}_1 = 2.41$ and $\hat{\alpha}_2 = 1.1$, respectively (see Table 7.1 for a summary of the parameters of the fitted distributions and the lengths of the series available for computing the statistics). Aban et al. [230] suggested that goodness of fit of the truncated Pareto distribution is a graphical check of the data tail. The upper bound on both these pdfs was found to be 35 mm. These findings lend strong support for the use of heavy-tailed distributions for the modeling of dynamics of surface evolution in a deltaic system.

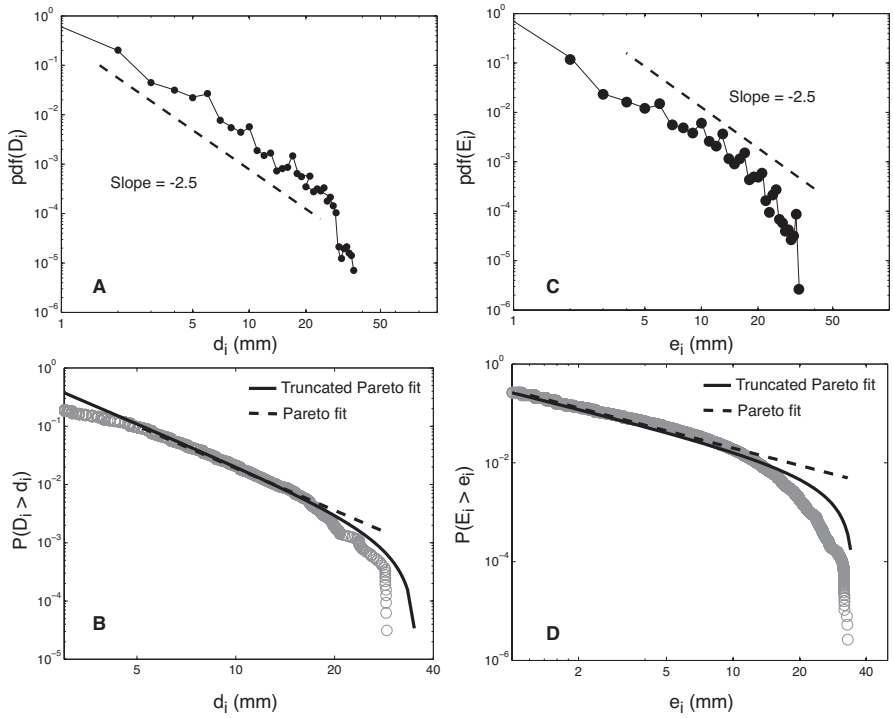

Figure 7.7: Log-log plot of probability density function of (A) positive elevation increments (D_i), and (C) negative elevation increments (E_i). An indicative slope of -2.5 is shown for reference to establish a power-law decay of this distribution. Log-log plot of probability of exceedance for (B) positive elevation increments and (D) magnitudes of negative elevation increments (empty circles) along with the best fit truncated Pareto distribution (solid black line) and best fit Pareto distribution (dashed line). The estimated parameters of these distributions are summarized in Table 7.1.

Further, we defined the magnitude of a depositional event as the sum of the elevation

increments over the duration of that deposition (equation (7.3a)). These random sums of elevation increments, as defined by Kolmogorov [231], are the thickness of a stratum before any further erosion occurs. Erosional events were defined as the random sum of magnitudes of negative increments over the duration of erosional events. It is important to note that the depositional and erosional events are the random variables which finally define the thickness of the preserved stratigraphic column [231]. Figure 7.8 shows the probability of exceedance of D_e and E_e along with their best fit Pareto and truncated Pareto distributions. The Pareto distribution does not provide a good fit to the data of D_e and E_e and the estimated p-values of the fits were 4.05×10^{-4} and 1.63×10^{-6}, respectively. The tail indices of the best fit truncated Pareto distributions for D_e and E_e are $\hat{\alpha}_1' = 3.31$ and $\hat{\alpha}_2' = 3.03$, respectively. The distributions of the depositional and erosional events have a faster decay of tails than their parent distributions of D_i and E_i ($\hat{\alpha}_1' > \hat{\alpha}_1$ and $\hat{\alpha}_2' > \hat{\alpha}_2$), indicating that heavy-tailed surface statistics need not always be preserved in the stratigraphic column thicknesses as the random variables which govern the thickness of deposits have thinner tails than their parent distributions. In the next subsection, we present the analysis of the time statistics of surface evolution, i.e., the durations of erosional and depositional events and periods of inactivity.

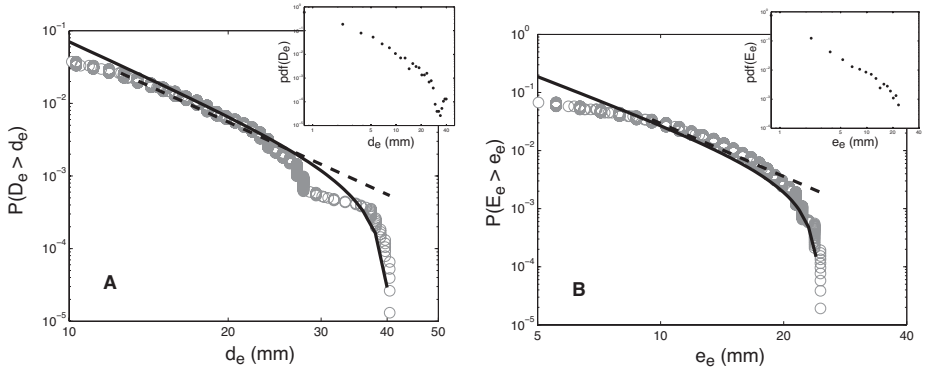

Figure 7.8: Log-log plot of probability of exceedance of (A) depositional events (D_e) and (B) erosional events (E_e). The inset figures show the log-log plots of the probability density functions of depositional and erosional events, respectively. Best fit truncated Pareto distributions are shown in solid black lines and the best fit Pareto distributions are shown in dashed lines. Note that in both cases, a random sum of the elevation increments results in a distribution with a thinner tail than the parent distribution (see Table 7.1 for estimated parameters).

7.3.2 Statistics of periods of inactivity

The relative frequencies computed from the experimental data of the durations of depositional and erosional events, as well as the periods of inactivity, are shown in Figures 7.9(A), 7.9(B) and 7.9(C), respectively. It was found that the mean and standard deviations of the durations of depositional and erosional events were $\hat{\mu}_{\tau_d} = 2.64$ mins, $\hat{\sigma}_{\tau_d} = 1.41$ mins and $\hat{\mu}_{\tau_e} = 2.23$ mins, $\hat{\sigma}_{\tau_e} = 0.781$ mins, respectively, while the mean and standard deviation of the periods of inactivity was $\hat{\mu}_{\tau_i} = 20.4$ mins and $\hat{\sigma}_{\tau_i} = 30.52$ mins. It is noted that the mean and standard deviations of τ_d and τ_e are an order of magnitude less than that of τ_i, indicating that the dominant temporal scale of the system is that of inactivity. The durations of erosion and deposition events have a mean approximately equal to the temporal resolution of the data with a very small standard deviation and it was found that an exponential distribution adequately describes these random variables.

The periods of inactivity, τ_i, were found to have a heavy-tailed distribution characterized by a log-log linear decay of pdf as shown in inset plot of Figure 7.10. Figure 7.10 shows the probability of exceedance and the best fit Pareto and truncated Pareto distributions to the data of periods of inactivity. The Pareto distribution does not provide a good fit to the data of periods of inactivity and the estimated p-value of the fit was 0.056. The truncated Pareto distribution (equation 7.7), fitted using the method proposed by Aban et al. [230] (which is briefly outlined in Section 7.3.1), was found to provide a good fit to the experimental data. The parameters of the fitted distribution were tail index, $\hat{\beta} = 1.14$, lower bound, $\hat{\gamma} = 8$ mins and upper bound, $\hat{\nu} = 240$ mins. The truncation parameter $\hat{\nu}$ is equal to 4 hrs and is expected to be governed by some physical forcing (autogenic dynamics) of the depositional system, and specifically to the characteristic avulsion time scale of the channels, as will be discussed in Section 7.6. Thus, we conclude that the random variables which govern the dynamics of surface evolution, namely, D_i, E_i, D_e, E_e, and τ_i, all exhibit heavy-tailed statistics.

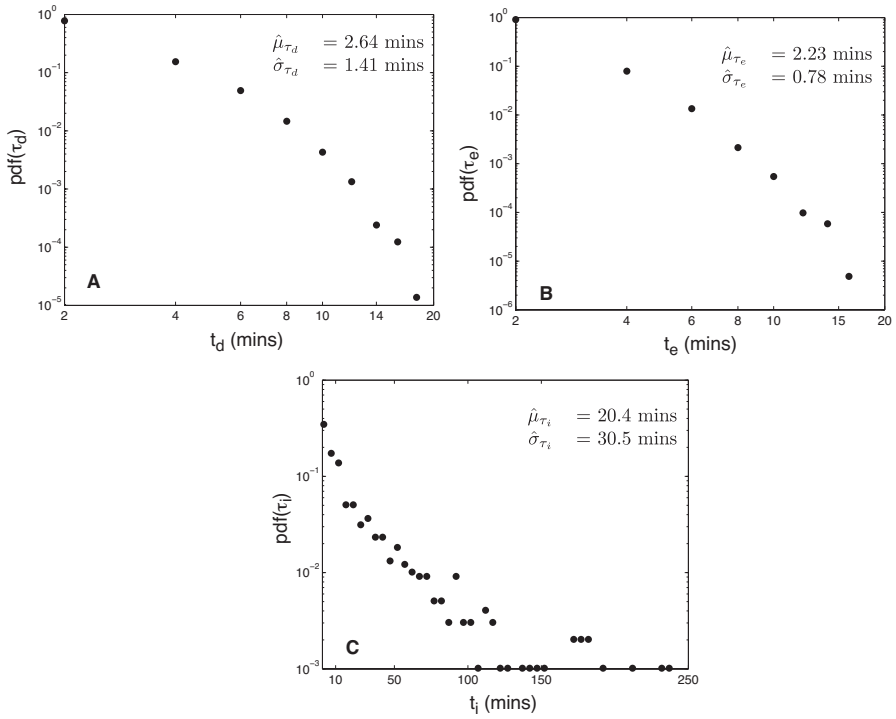

Figure 7.9: Probability density functions of (A) the duration of depositional events (τ_d), (B) the duration of erosional events (τ_e) on a log-log plot, and (C) the periods of inactivity (τ_i) on a semi-log plot. The bin size has been selected equal to 2 mins which is the temporal resolution of the series. It is noted that the dominant time scale in the system is that of inactivity.

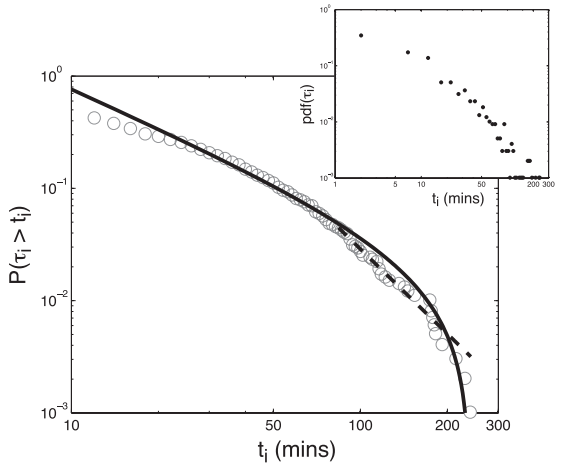

Figure 7.10: Probability of exceedance plot of the periods of inactivity τ_i plotted on a log-log scale. The empty circles indicate the empirical density of the data, the thick solid line shows the best fit truncated Pareto distribution and the dashed line shows the best fit Pareto distribution. The parameters of the truncated Pareto distribution are: tail index $\hat{\beta} = 1.14$ and truncation parameter $\hat{\nu} = 240$ (4 hrs). The truncation parameter $\hat{\nu}$ was found to correspond to the avulsion time scale of the mean channel depth which is around 2 cms in the system. The inset plot shows the pdf of τ_i on a log-log scale. Notice the power-law decay of the distribution, indicating a heavy-tailed behavior.

Random variable	Sample size	Truncated Pareto fit			Pareto fit	
		Tail index	Upper bound	Lower bound	Lower bound	Tail index
D_i (mm)	565237	2.41	35 mm	2 mm	5.2 mm	2.41
E_i (mm)	379931	1.1	35 mm	0.3 mm	1.2 mm	1.16
D_e (mm)	76220	3.31	40 mm	4.5 mm	12.5 mm	3.31
E_e (mm)	52064	3.03	25 mm	2.7 mm	9.5 mm	3.03
τ_i (mins)	186172	1.14	240 mins	8 mins	84 mins	2.44
τ_{st} (mins)	133888	0.7	320 mins	4 mins	10 mins	0.88

Table 7.1: Estimated parameters of fitted truncated Pareto and Pareto distributions. The standard error of estimate for the all parameters is of the order of 10^{-3} in view of the large sample size.

7.4 Statistics of preserved stratigraphy

Stratigraphic columns can be built from the elevation time series (see Figure 7.5) and in this section we analyze the statistics of the stratigraphic deposit thickness (D_{st}) and the time interval demarcating the boundaries of the stratigraphic deposits, τ_{st} (called "hiatuses" in [193]).

The inset plot of Figure 7.11(A) shows the pdf of the time interval demarcating the stratigraphic column in a log-log plot. It is noted that τ_{st} shows a heavy-tailed behavior which can be seen from the power-law decay of the pdf. Figure 7.11(A) shows the probability of exceedance of τ_{st} along with its best fit Pareto and truncated Pareto distributions (see Table 7.1 for a summary of estimated parameters of these distributions). The Pareto distribution does not provide a good fit to the data of τ_{st} and the estimated p-value from equation (7.9) was found to be 0.0017. The truncated Pareto distribution provides a better fit than the Pareto distribution to the experimental data with estimated parameters: tail index $\hat{\beta}' = 0.7$, upper bound $\hat{\nu}' = 320$ mins, and a lower bound 10 mins. The time interval demarcating the stratigraphic deposits is a random sum of durations of erosional and depositional events (τ_d and τ_e) as well as the periods of inactivity (τ_i). Since the dominant time scale is given by the periods of inactivity, τ_{st} is in effect a random sum of the periods of inactivity. The tail index of τ_{st} is lower, $\hat{\beta}' = 0.7$, indicating a heavier tail for τ_{st} than its parent distribution of τ_i ($\hat{\beta} = 1.1$). The implications of the tail index of τ_{st} being less than 1 and the mechanisms that set the scales of truncation on this pdf are discussed in Section 7.6.

The thickness of beds preserved in the stratigraphic columns was calculated in two different ways: 1) constructed from the topographic data collected during the experiment (termed D^e_{st}), and 2) directly measured from the the digital images of the preserved stratigraphy available after sectioning the final deposit (termed D^s_{st}). A comparison of the statistics of these two independently estimated variables tests the degree to which our definition of a bed as a package of sediment bounded by erosional surfaces translates to features readily identifiable by textural changes in the deposit.

Bed thicknesses, D^e_{st} , were constructed from the elevation measurements as outlined schematically in Figure 7.5. At each spatial location, the elevations of all preserved erosional boundaries were first identified and then the thicknesses of sediment bounded

by those preserved erosional surfaces were calculated. The probability density function of the preserved bed thickness, D^e_{st}, is shown in Figure 7.11(B). Unlike the increments of deposition and erosion discussed above, the thickness of beds exhibits a thin-tailed PDF. Figure 7.11(B) shows that an exponential distribution with mean $\langle D^e_{st} \rangle$ provides a good fit to the calculated bed thicknesses.

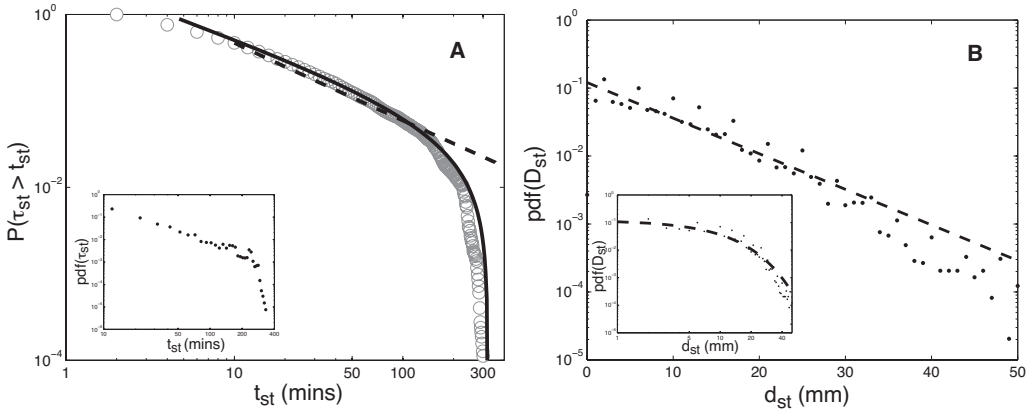

Figure 7.11: (A) Probability of exceedance of the time interval demarcating the stratigraphic deposit (τ_{st}), along with its best fit truncated Pareto (solid line) and Pareto distributions (dashed line). The inset plot shows the pdf of τ_{st} on a log-log scale. (B) Semi-log plot of the pdf of bed thickness (D_{st}) along with the best fit exponential distribution (dashed line). The estimated mean of the fitted exponential distribution is 8.3 mm. The inset figure shows the exponential fit on a log-log scale.

Bed thicknesses, D^s_{st}, were computed from the images of preserved stratigraphy using the high optical contrast between the white quartz grains and black anthracite grains. The difference in density (quartz: 2650 kg/m^3 versus anthracite: 1700kg/m^3) results in differences in their relative mobility, that is, the lighter anthracite particles tend to be more mobile than the quartz grains and are therefore a proxy for fine sediment. This difference in mobility is recorded in the deposit where the coal and quartz often form distinct depositional bodies, such as channel fills and lobes [217], and develop textural boundaries between white and black sediment which can be used as bed boundaries. Using undistorted images of the physical stratigraphy (Figure 7.12(A)) we generated stratigraphic panels with a binary identification scheme. Using a threshold luminosity value we separated anthracite deposits from quartz deposits. The threshold value used for this operation was picked by identifying a value that on visual inspection appeared

to correctly separate the deposit types. Using these binary images (Figure 7.12(B)) we measured bed thicknesses from the stratigraphy, D^s_{st}, as uninterrupted vertical sequences of pixels of a single grain type (i.e., either only white or only black). The probability density function of preserved bed thickness, D^s_{st}, is shown in semi-log space in Figure 7.12(C). Similar to the PDF of D^e_{st} estimated from the surface elevation measurements, the PDF of D^s_{st} estimated from the physical stratigraphy is close to exponential with an estimated mean, $\langle D^s_{st} \rangle$, of 9.5 mm. Importantly, we note that the two distributions of bed thickness, one theoretical, and one measured, both demonstrate that the heavy-tailed statistics of deposition and erosion that characterize the surface evolution are not preserved in the stratigraphy.

We emphasize that the theory of Kolmogorov [231] used the surface elevation time series to construct the preserved bed thicknesses. This is not the same as extracting bed thicknesses from physical stratigraphy as the observable stratal boundaries are not exactly equivalent to the definition of bed boundaries as defined by Kolmogorov [231]: not all visible stratal boundaries are erosional, and not all erosional boundaries result in a change of sediment type. Rather, the boundaries we mapped represent a straightforward class of bed boundaries one might map in the field. A pleasing result of our analysis is the agreement between the constructed and physical stratigraphy statistics giving more confidence in applying the analytical results of Kolmogorov [231] and other studies which use elevation series to define preserved bed thickness. In the next section, we characterize the self-similar fractal structure of the temporal evolution of the surface elevations.

7.5 Multifractality of surface evolution

Surface elevation increments are found to exhibit variability at all scales. For example, Figure 7.13 shows the temporal evolution of a given transect (transect A-A in Figure 7.2) that possesses a devil's staircase-like structure. Notice that visually, the structure of evolution when viewed at different time scales (shown as inset plots in Figure 7.13) looks statistically similar. One common way of documenting the self-similar structure of a given time series is to look at the power spectral density of the time series. Figure 7.14

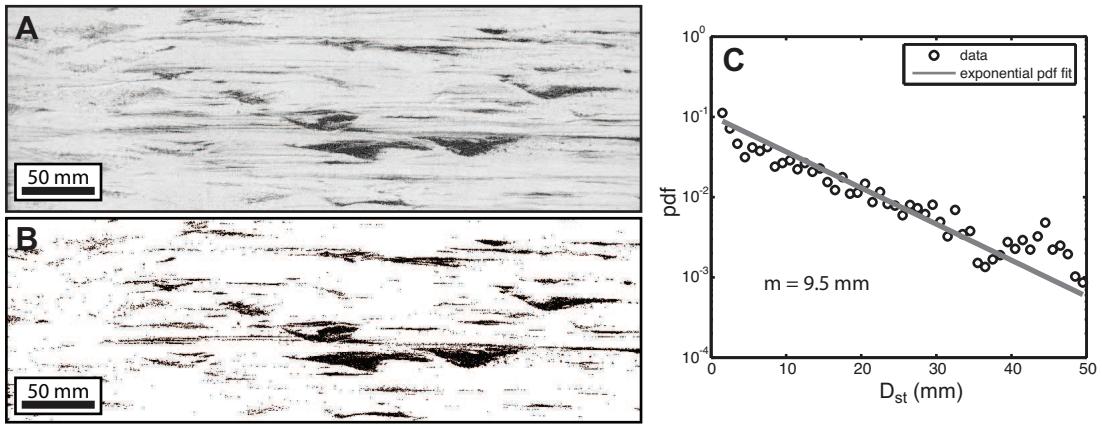

Figure 7.12: Information defining distribution of bed thicknesses for DB-03 experiment generated from images of physical stratigraphy. (a) Photograph of approximately 0.14 m of stratigraphy generated during DB-03 experiment. Stratigraphic section is located approximately 1.75 m from source. (b) Facies map of stratigraphy where white pixels represent quartz deposits and black pixels represent coal deposits. Quartz and coal deposits were identified through threshold luminosity analysis. (c) PDF of D^s_{st} shown in semi-log space generated from deposit facies map. Linear decay of bed thicknesses in semi-log space suggests exponential distribution.

shows the power spectral density as a function of wavelength for the ensemble of temporal transects along Line 1.75. A power-law decay, with an exponent of $\phi = -2.1$ documents the presence of statistical scaling in the temporal evolution of elevation time series. The Hurst exponent (H) which is a measure of the "roughness" of the time series is related to the spectral density's power law decay exponent as $-\phi = 2H + 1$ [232] resulting thus in $H = 0.55$. The fractal dimension D_0 and the Hurst exponent relate as $D_0 = 2 - H$ [232], leading to an estimated fractal dimension for the elevation time series of $D_0 = 1.49$.

The power spectral density expresses the scaling of the second order moment (variance) of the series and completely characterizes the scaling of Gaussian random variables. Since the pdf of elevation increments was documented to significantly deviate from the Gaussian form, it is important to test for scaling in higher-order statistical moments. We performed higher-order structure function analysis of the elevation time series to characterize the statistical scaling of the temporal evolution of the deltaic surface. Elevation increments in time were computed at different scales r, denoted by

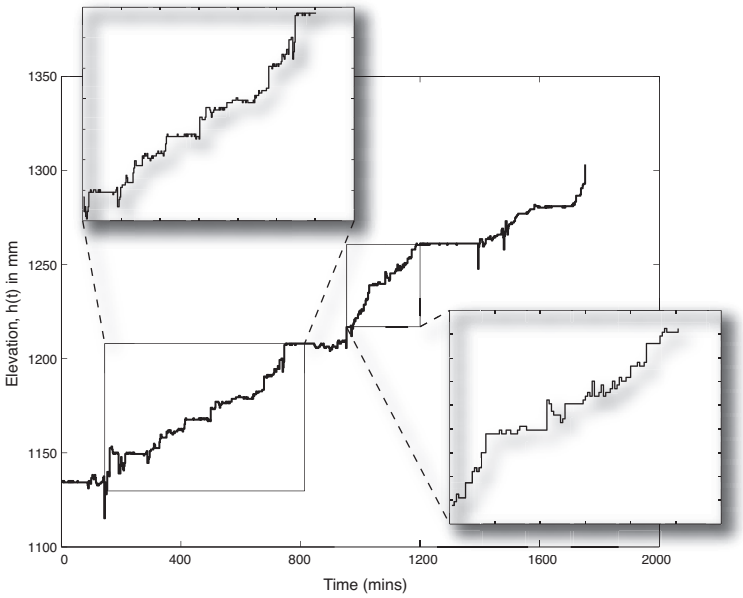

Figure 7.13: Time transect of elevation surface (A-A transect in Figure 7.2). The Devil's staircase like structure is shown in the plot by magnifying small portions of the elevation transect over time. The flat periods in the above plot show the periods of inactivity in the system.

$\delta h(t,r)$, as

$$\delta h(t,r) = h(t + r\Delta t) - h(t) \tag{7.10}$$

where Δt is the temporal resolution of the experimental data. The estimates of the q^{th}-order statistical moments of the absolute values of elevation increments at scale r, also called structure functions, $M(q,r)$, are defined as

$$M(q,r) = \frac{1}{N_r} \sum_{t=1}^{N_r} |\delta h(t,r)|^q \tag{7.11}$$

where N_r is the number of data points of elevation increments at a scale r. Statistical scaling, or scale invariance, requires that $M(q,r)$ is a power-law function of the scale,

$$M(q,r) \sim r^{\zeta(q)} \tag{7.12}$$

where $\zeta(q)$ is the scaling exponent function. When the scaling exponent function has a linear dependence on the order of the statistical moments, i.e., $\zeta(q) = qH$, the series

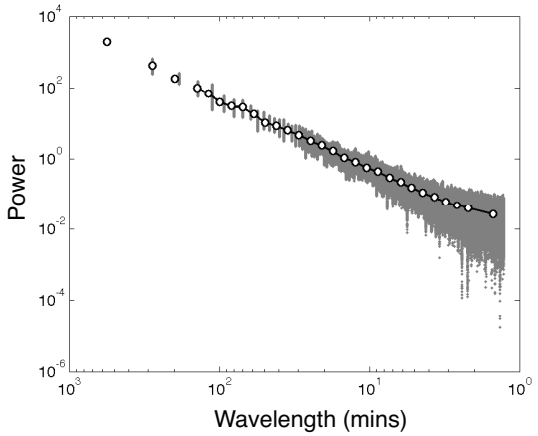

Figure 7.14: Power spectral density of elevation time transects on a log-log plot. The gray dots correspond to the power spectral density of each of the time transects and the solid white circles indicate the log-binned average of the power spectral density. The log-log linear decay with an exponent of $\phi = -2.1$ establishes the self-similar structure of the elevation time series.

is called mono-fractal and H is the so-called Hurst exponent. If the scaling exponent function has a non-linear dependence on the order of statistical moments then the series is called a multi-fractal. The simplest way to characterize the nonlinear dependence of $\zeta(q)$ on q is by using a quadratic approximation,

$$\zeta(q) = c_1 q - \frac{c_2}{2} q^2 \tag{7.13}$$

where c_1 and c_2 are constants parameterizing the scale-invariance of the series over a range of scales (see [233] and [204]). Note that from equation (7.11) that the zero-order structure function $M(0, r)$ is trivially equal to 1 and thus (from equation (7.12)) scale independent. This approach therefore, does not allow us to characterize the possible fractality of the "sparseness" of the data series. However, as seen in Section 7.3.2, the periods of inactivity exhibit a heavy-tailed distribution implying the existence of flat regions of all scales in the evolution of the elevation time series (see Figure 7.13) or sequences of zeroes of all scales in the time series of elevation increments (see Figure 7.3). Quantifying the non-trivial scaling of the zeroth order moment of a data series would require relaxing the $\zeta(0) = 0$ assumption in equation (7.13) and introducing a positive

constant c_0 in the characterization of the nonlinear dependence of the scaling exponents,

$$\zeta(q) = c_0 + c_1 q - \frac{c_2}{2} q^2 \tag{7.14}$$

Figure 7.15(A) shows the estimated higher-order structure functions, $M(q,r)$, as a function of scale r. The log-log linear relationship of $M(q,r)$ on r over the range of scales $2-256$ mins (2^1-2^8 in log scale) for the moments of order $q = 0.1, 0.25, 0.5, 0.75, 1.0, \ldots, 3.0$ documents the scale-invariance of the elevation increments. In Figure 7.15(B), the scaling exponent function $\zeta(q)$ is plotted against the order of moments. The nonlinear dependence of $\zeta(q)$ on q documents the multi-fractal behavior of the elevation increments. Fitting the quadratic function of equation (7.14) to $\zeta(q)$ results in $c_0 = 0.192$, $c_1 = 0.58$ and $c_2 = 0.171$. These three parameters c_0, c_1 and c_2 fully characterize the scaling of all statistical moments and thus the way the pdfs of elevation increments change over scales [204].

The analysis presented above provides a way of quantifying the multi-fractality of a signal via the scaling of its statistical moments. This statistical approach admits an interesting geometrical interpretation in terms of characterizing the "roughness" of a signal or its local singularity (degree of differentiability). A quantitative measure of local singularity is given by the so-called Hölder exponent $\mathcal{H}$ (see equation (A.1) in Appendix A). When more than one singularity is present in the signal, the spectrum of singularities $D(\mathcal{H})$ quantifies the range of singularities and the fractal (Hausdorff) dimension of the support of these singularities. This spectrum of singularities $D(\mathcal{H})$ directly relates to the scaling exponent function $\zeta(q)$ via a Legendre transform (see Appendix A).

Figure 7.15(C) shows the estimated $D(\mathcal{H})$ curve for surface elevation increments. Several observations are made from this figure. First, the most prevailing singularity (peak of the D($\mathcal{H}$) curve) is equal to $< \mathcal{H} >= 0.55$, which is almost identical to the single Hurst exponent computed from the power spectral analysis. Second, the $D(\mathcal{H})$ curve indicates the presence of a wide spectrum of singularities from 0.1 to 0.9 (the spectrum of Figure 7.15(C) is the left part of the full spectrum and due to the quadratic form of $\zeta(q)$ the spectrum is symmetrical around the mean value of $< \mathcal{H} >$). Recall that regions in the elevation series where $\mathcal{H} \approx 0.1$ correspond to regions of abrupt changes in elevation series (large spikes in elevation increments in Figure 7.3) while

$\mathcal{H} \approx 0.9$ corresponds to regions of a gradual change in the elevation series (smaller spikes in elevation increments). These spikes (local singularities) are interwoven in the signal and $D(\mathcal{H})$ characterizes their distribution. Third, it is observed that the fractal dimension of the most prevailing singularity is $D(< \mathcal{H} >) = 0.8$ implying a sparseness in the surface elevation series consistent with the presence of periods of inactivity and the non-zero estimated value of c_0 in equation (7.14).

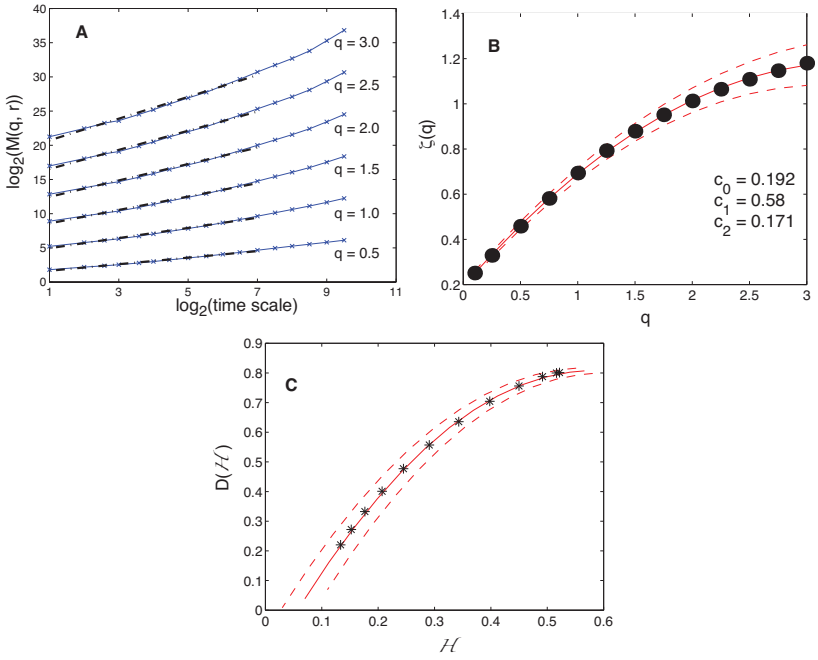

Figure 7.15: (A) Log-log plots of higher-order structure functions $M(q, r)$ vs r. The power-law dependence documents the presence of scale-invariance in the elevation time series $h(t)$. (B) The dependence of scaling exponent function, $\zeta(q)$, on the order of moments. The nonlinear dependence documents the presence of multifractal behavior with $c_0 \approx 0.192$, $c_1 \approx 0.58$ (the most prevailing Hurst exponent in the series) and $c_2 \approx 0.171$ (intermittency parameter). (C) Spectrum of Hölder exponents calculated from the scaling exponent function using equation (A.4). The spread indicates the variability in the singularity exponents found in the elevation time series.

As a final remark, we note that the scaling characterization presented above (via

statistical moments or singularity spectrum) holds within a range of scales (see Figure 7.15(A)) whose upper bound coincides with the truncation parameter of the dominant time scale of the system, i.e., periods of inactivity ($\hat{\nu} = 240$ mins), providing thus a much desired physical interpretation of the upper bound of the scaling regime.

7.6 Channel depths as a first-order control on depositional systems

In this section, we interpret the results on the truncation scales of the fitted distributions to the random variables that govern the surface evolution of depositional systems and show that channel depths act as a first-order control in setting the truncation scales (see Table 7.1 for a summary of parameters of fitted distributions). The observed mean channel depth in the DB-03 experiment was reported to be of the order of 2 cm, while the maximum channel depth was reported to be about 3 cm [217]. Specifically, the maximum channel depth calculated from the topographic cross-sections (see Figure 7.16) was 35 mm, which is equal to the estimated upper bound of both the magnitudes of erosion and deposition (E_i and D_i). This indicates that the maximum channel depth acts as a first-order control on the truncation scale of pdfs of D_i and E_i. Physically, the maximum amount of deposition is governed by the maximum accommodation space available, which in this experiment corresponds to the maximum channel depths. Thus, we note that the maximum channel depths of the actively deforming surface provides an indicative measure of the truncation parameter or the upper bound on the pdfs of D_i and E_i.

The time statistics are expected to be governed by the the time scale of avulsion of the channels in the depositional systems. Mohrig et al. [234] define the characteristic avulsion time scale T_A in a depositional system as:

$$T_A = \frac{\eta}{\sigma_A}, \tag{7.15}$$

where η is the average depth of the channels and σ_A is the vertical aggradation rate in the system. Substituting $\eta = 2$ cm and $\sigma_A = 5$ mm/hr [217], one can easily see that the time scale that sets the scale of truncation of τ_i ($\hat{\nu}_i = 240$ mins) is roughly governed by the mean avulsion rate T_A. One way to think about this result is to consider

the processes that set the periods of inactivity in a depositional system. The smaller values of τ_i arise in the system when that given location is occupied by a channel that is not depositing or eroding sediment. However, longer periods of inactivity arise from abandoning of a previously occupied channel location which leads to long periods of neither deposition nor erosion happening at that location. Indeed, the results from the best fit truncated Pareto distribution to the data of τ_i suggest that the larger values of τ_i have an upper bound which is governed by the mean avulsion rate of the system. However, in real systems this upper bound can be greater than the time scales of avulsion of the mean channel depths owing to climatic/environmental forcing, as the statistics of the experiment only reflect the autogenic effects on the periods of inactivity. It is also interesting to note that Straub et al. [224] show that channel depths act as a first order control on the stratigraphic architecture of channelized sediment transport systems. Straub et al. [224] found that the degree of compensation present in alluvial basins scales with the depths of the channels constructing the stratigraphy. Taken together, our study and the study of Straub et al. [224] illustrate that channel depth is a fundamental length scale for both the surface dynamics of deltas and the architecture of deltaic stratigraphy.

The time interval demarcating the stratigraphic deposits was documented to have a truncated Pareto distribution (see Section 7.4). The best fit truncation parameter was found to be $\hat{\nu}' = 320$ mins with a tail index of $\hat{\beta}' = 0.7$. The time scale of truncation corresponds to the avulsion time scale of a 2.7 cm deep channel (using equation (7.15)), which corresponds roughly to the deepest channels encountered during the experimental run. A heavy-tailed distribution for τ_{st} with a tail index less than 1, introduces a bias into the estimated deposition rates and leads to the so-called "Sadler" effect [64, 193]. Figure 7.17 shows the growth of the sediment surface elevation of the stratigraphic column with respect to time. As discussed in [193], the heavy-tailed behavior of "hiatuses" or the time interval demarcating the stratigraphic columns causes a sub-linear growth of the sediment surface elevation for time scales lesser than the truncation in the pdf of τ_{st} with the scaling exponent equal to the tail index of τ_{st} ($\hat{\beta}' = 0.7$). For time scales larger than $\hat{\nu}'$, the sediment surface elevation grows linearly in time, indicating that there is no bias in the estimated deposition rates. Normalizing the sediment surface elevation increments with the time scale at which the process is observed leads to the estimated

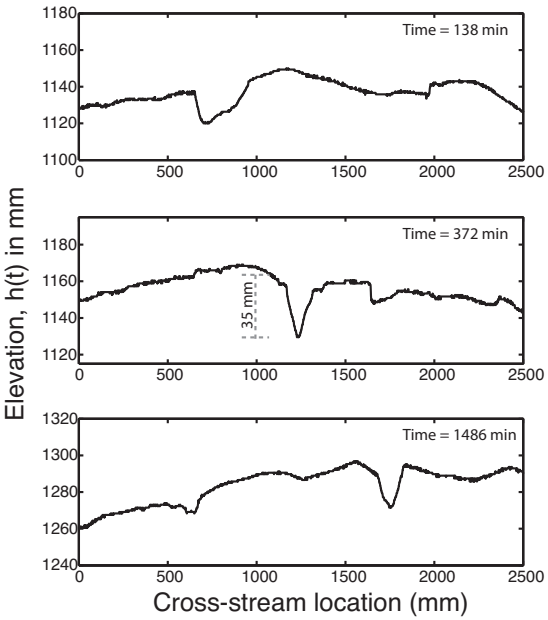

Figure 7.16: Elevation cross-sections showing the deepest channels in the system at three different time steps during the experimental run. The 35 mm deep channel highlighted in the middle panel was the deepest channel that appeared during the experimental run.

depositional rates' dependence on time. It is easy to see that the scaling of the observed deposition rates depends on the tail index of the distribution of τ_{st}, where the estimated deposition rates decay with a power law exponent of $\hat{\beta}' - 1 = -0.3$ until the time scale of truncation of τ_{st} and beyond the the truncation scale $\hat{\nu}'$, the estimated deposition rates do not depend on the time scale of observation. Our experimental data confirm the hypothesis of Schumer and Jerolmack[193] that the bias in estimated deposition rates does indeed arise from heavy-tailed "hiatuses". In the case when the heavy-tailed hiatuses (τ_{st}) arise from heavy-tailed periods of inactivity (τ_i), our analysis shows that the degree of bias in the estimated deposition rates (which can be calculated by the degree to which sediment surface elevation deviates from linear growth) can lead to the estimation of the tail-index of the hiatuses. Moreover, the truncation scale of the pdf of hiatuses can be estimated from the avulsion time scale of the deepest channel in the system.

The scaling regime of the multi-fractal behavior reported in Section 7.5 was from 2 mins to 256 mins. The lower bound on this scaling regime corresponds to the temporal

resolution of the data collected while the upper bound on this regime corresponds to the truncation parameter of the periods of inactivity (τ_i). This indicates that the scaling regime of the surface elevation time series can be derived from the physical controls of the system as the upper bound on the scaling regime is set by the time scale of avulsion of the mean channel depth.

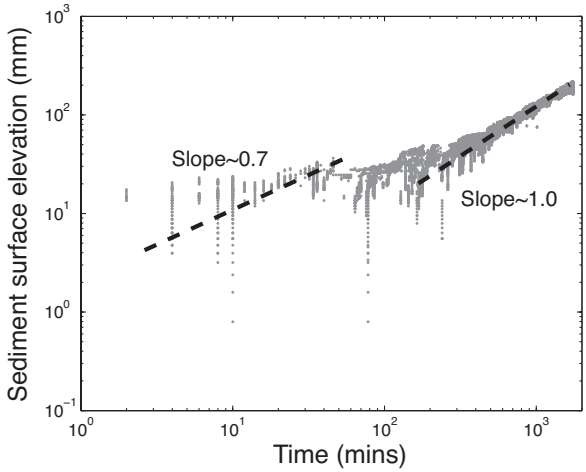

Figure 7.17: Plot showing the sediment surface elevation of the recorded bed thickness as a function of time on log-log scale. The scaling of the sediment surface elevation shows the effect of heavy-tailed "hiatuses" with a slope of $\beta' = 0.7$ until around the time scale of truncation of pdf of τ_{st}. For times larger than the scale of truncation, the sediment surface elevation scales linearly with time. The above plot when normalized with the time scales of observation leads to the estimated deposition rate dependence on time (Sadler effect).

7.7 Modeling of surface evolution and sediment surface elevation of stratigraphic column

In this section, we present some preliminary thoughts on modeling depositional systems using continuum models which are consistent with the heavy-tailed statistics documented in the previous sections. Recently, modeling earth-surface processes that possess variability over a large range of space-time scales and exhibit heavy-tailed statistics has received considerable attention [89, 162, 42, 11, 3, 235, 50, 236]. In a recent study, Voller and Paola [6] acknowledged the deviation of fluvial profiles from ones predicted

by classical diffusion and proposed the exploration of fractional diffusive model to describe the observed steady-state fluvial profiles in a depositional system. However, it is important to note that the underlying assumption of the fractional diffusive model is that the transport distances of sediment particles along the flow paths in depositional systems is heavy-tailed (see [42], [50] and [11] where the heavy-tailed nature of sediment transport distances are shown to result in a fractional diffusive model), for which we do not have direct experimental evidence. However, our results do indicate that the periods of inactivity are heavy-tailed and this needs to be taken into account while modeling the surface dynamics of depositional systems.

The classical diffusion equation has been used to model the surface dynamics of depositional systems [237, 16, 225]. The underlying assumptions of the classical diffusion equation are thin-tailed periods of inactivity and thin-tailed transport distances for sediment particles and the governing equation for the elevation evolution at any point is given by [21]:

$$\frac{\partial h}{\partial t} = D\frac{\partial^2 h}{\partial x^2} - \sigma_A \tag{7.16}$$

where h is the surface elevation, D is the diffusivity coefficient, σ_A is the net aggradation rate and x is the distance along a flow path. A pure power-law, heavy-tailed pdf for the periods of inactivity without any truncation leads to a time-fractional diffusion equation which describes the evolution of surface elevation in time [172, 188]. However, our experimental results indicate that the periods of inactivity are heavy-tailed with an upper bound equal to the avulsion time scale of the mean channel depth. Truncated power-law pdfs of periods of inactivity can be modeled using "tempered anomalous diffusion" equations where the power law pdf of periods of inactivity is described by tempered stable pdfs [238]. Tempered stable pdfs were proposed in [239] and [240] as a smoother alternative to the truncated heavy-tailed pdfs which have a sharp cutoff. In this case, the truncation is not assumed to be a fixed threshold but is assigned an exponential tempering of rate λ where the pdf has a power-law decay till a particular value and beyond that given truncation value the pdf decays exponentially. Assuming tempered stable pdfs of periods of inactivity and thin-tailed pdfs of transport distances of sediment particles, the governing equation that describes the evolution of the surface

elevation can be shown [238] to be given by:

$$\frac{\partial h}{\partial t} + e^{-\lambda t}\frac{\partial^{\beta}}{\partial t^{\beta}}\left(e^{\lambda t}h\right) - \lambda^{\beta}h = D\frac{\partial^2 h}{\partial x^2} - \sigma_A \tag{7.17}$$

where x is the distance along the flow path, $\beta < 1$ is the tail index of periods of inactivity, D is diffusivity and λ is the rate of exponential tempering. The rate of exponential tempering, λ, is equal to the inverse of the mean of the truncation parameter which is governed by the avulsion time scale of the mean channel depth in systems whose dynamics are set by purely autogenic processes (like the experimental arrangement studied here). However, it is important to note that the above equation is valid only when the tail index β of periods of inactivity is less than 1. In the experimental arrangement, the estimated tail index is $\beta = 1.14$ and the thin-tailed assumption of transport distances withstanding, equation (7.16), and not equation (7.17), will describe the dynamics of delta evolution. In systems which have tail index of the periods of inactivity less than 1, equation (7.17) describes the dynamics of evolution of the deltaic surface. Note that all the parameters of equation (7.17) are set by physical processes that govern the evolution of the deltaic surface: β is the tail index of the periods of inactivity, λ is set by the avulsion time scale of mean channel depths of the system, and D is a measure of the spread of the transport distances of sediment particles. In the case that the transport distances of sediment particles are heavy-tailed with a tail index of $\kappa < 2$, the governing equation for surface elevation needs to be modified by replacing the $\partial^2/\partial x^2$ operator with a fractional $\partial^{\kappa}/\partial x^{\kappa}$ operator. The nature of the distribution of transport distances of sediment particles in a fan-delta system is a subject that needs further study.

Let us denote by $S(t)$ the sediment surface elevation of the stratigraphic column, i.e., the summation of all bed thicknesses recorded until clock time t has elapsed, given by [193]:

$$S(t) = \sum_{i=0}^{N_t} d_{st}(i) \tag{7.18}$$

where $d_{st}(i)$ is the bed thickness recorded and N_t is the number of stratigraphic strata recorded in a given time interval $[0, t]$. [193] derive and describe the governing equation for the location of the sediment surface elevation, $S(t)$, of the stratigraphic column in the case when heavy-tailed hiatuses are present in the system. In Section 7.4 we provided evidence for the existence of heavy-tailed hiatuses (τ_{st}) and the exponential

distribution of the bed thickness (D_{st}). These two findings together lead us to the following governing equation for the location of sediment surface elevation:

$$\frac{\partial S}{\partial t} + e^{-\lambda' t} \frac{\partial^{\beta'}}{\partial t^{\beta'}} \left(e^{\lambda' t} S \right) - \lambda'^{\beta'} S = -V \frac{\partial S}{\partial z} + D' \frac{\partial^2 S}{\partial z^2} \tag{7.19}$$

where S is the sediment surface elevation, β' is the tail index and λ' is rate of the exponential tempering of the hiatuses τ_{st}, V is the average rate of accumulation, D' is the diffusivity coefficient which describes the spread of accumulation rate around its mean and z is the vertical coordinate measured in the direction of the stratigraphic column. The tail index of τ_{st} which was found to be less than 1 and the exponential bed thickness distribution call for a tempered anomalous diffusion equation to describe the evolution of sediment surface elevation of the stratigraphic column. The governing equations in the case of constant accumulation rates and power-law, heavy-tailed pdfs without truncation are discussed in [193].

7.8 Conclusions

In this chapter, we used high resolution temporal data collected from a Delta Basin experiment conducted at the St. Anthony Falls Laboratory, University of Minnesota to fully characterize the statistics of surface elevation dynamics in depositional systems. The following conclusions were drawn from the present study:

1. We showed that the magnitudes of surface elevation increments, deposition (D_i) and erosion (E_i), are well approximated by truncated Pareto distributions where the upper bounds in both cases are governed by the maximum depths of the channels on the actively deforming surface of the system.

2. The magnitudes of depositional events (D_e) and erosional events (E_e), which were defined as the random sum of the magnitudes of elevation increments over their respective durations of deposition (τ_d) and erosion (τ_e), were found to be well described by a truncated Pareto distribution with a thinner tail than that of D_i and E_i, indicating that the random variables which govern the stratigraphic column thickness need not always reflect the heavy-tailed nature of surface elevation dynamics.

3. The periods of inactivity (τ_i), which were shown to be the dominant time scale of the system, were found to be well approximated by a truncated Pareto distribution whose upper bound coincides with the avulsion time scale of the mean channel depth, thus allowing for a physical interpretation of the fitted parameters.

4. The hiatus lengths (τ_{st}) or the time intervals demarcating the stratigraphic deposits were shown to carry the signature of the heavy-tailed periods of inactivity and were found to be well approximated by a truncated Pareto distribution with a tail index of $\hat{\beta}' = 0.7$ and upper bound which corresponds to the avulsion time scale of the deepest channels in the system. The implications of heavy-tailed hiatuses for the estimated rate of deposition and sediment surface elevation were discussed and experimental evidence for the hypothesis of Schumer and Jerolmack [193], that the bias in the estimated deposition rates arise from heavy-tailed hiatus lengths, was provided.

5. It was shown that the bed thickness or the thickness of the preserved stratigraphy (D_{st}) is well approximated by an exponential distribution, indicating that the heavy-tailed nature of surface dynamics is apparently not preserved in the stratigraphic column.

6. Preliminary thoughts on modeling surface dynamics using non-local theories using fractional calculus were presented. It was shown that the governing equations for the surface elevation ($h(t)$) and sediment surface elevation ($S(t)$) of the stratigraphic column can be described by tempered anomalous diffusion equations [238] where the time-fractional derivative captures the heavy-tailed nature of the periods of inactivity and the hiatus lengths, respectively.

7. Finally, it was shown that all the truncation scales on the random variables studied are set either by the channel depths (space statistics) or the characteristic avulsion time scales of the channels (time statistics), indicating that channel depths act as a first-order control on the structure of surface dynamics and preserved stratigraphy in depositional systems.

Chapter 8

Relating Earth-surface dynamics to the preserved stratigraphy: Is the tale in the tails?

The accumulation of sediment, even in strongly net depositional environments, is an unsteady process [218] and in most environments, sedimentation and erosion rates vary over a wide range of temporal and spatial scales [241, 54, 64]. Changes in sedimentation/erosion rates, and in particular transitions between erosion and deposition, are often associated with lateral and vertical changes in the texture of sedimentary deposits. This texture in turn results from spatial changes in grain size of deposited particles and typically marks stratal boundaries. In one (vertical) dimension, the intervals between these boundaries define bed thickness, i.e., the thicknesses of individual strata. In the common case where change between erosion and deposition is associated with migrating topography, one would expect some relation between the statistical properties of the topography and those of the preserved beds. The purpose of this study is to investigate this relationship.

Over the past thirty years studies related to the generation of stratigraphy in one dimension have primarily focused on quantifying the "completeness of time" preserved in the stratigraphic record. This line of research initiated with a paper by Sadler [64] who found that the deposition rate decreases as a power law function of the interval of

time over which deposition rate is measured. This simple yet powerful observation motivated several studies on the statistical structure of surface elevation increments as they pertain to the construction of 1D stratigraphic columns [242, 225, 243, 244, 193], mainly using 1D stochastic diffusion models of sedimentation. While these studies produced significant advances in our understanding of how time is recorded within stratigraphy, questions about the distribution of preserved bed thickness remain: what dictates the distribution of bed thicknesses preserved in stratigraphy and how do measurements of bed thickness (simple to obtain in comparison to measurements of deposit age) relate to the nature of the surfaces that created them?

Several recent studies suggest that the shape, extent, and distribution of stratal boundaries are not merely functions of instantaneous paleo-topography, but can be quantified as functions of three characteristics of the geomorphological system: 1) the statistics describing the time-variant topography of an actively changing surface, 2) the kinematics by which the surface is changing, and 3) the rate of net deposition [61, 216, 62]. While this formulation for quantifying the architecture of stratigraphy is becoming increasingly accepted, we still lack predictive methods to reconstruct surface topography from preserved stratigraphy, with only a few notable exceptions [245, 246, 247]. The construction of such inverse predictive methods has the potential to unlock paleo-surface history stored in the stratigraphic record.

The seminal work by Kolmogorov [231] on the relationship between preserved bed thicknesses and the distributions of the erosional and depositional events that form them remains one of the most complete quantitative theories in stratigraphy. In this work, Kolmogorov presented an analytical derivation of the distribution of bed thicknesses and showed that it is a truncated distribution whose shape relates to the distribution of depositional and erosional events in a given setting. In the Kolmogorov model, the construction of stratigraphy is attributed to the summation of depositional and erosional events. A stratigraphic section can be sub-divided into a series of beds, where a bed is described as a package of sediment bounded above and below by surfaces of erosion (Figure 8.1). This stochastic sequence of depositional ($\delta h_e > 0$) and erosional events ($\delta h_e < 0$) produces a set of beds with varying degrees of stratigraphic completeness. The frequency distribution of the depositional and erosional events, $f(\delta h_e)$, which was assumed to be Gaussian in shape by Kolmogorov [231], spans over a range of positive

and negative values with occasional extreme events on either side. As erosion removes material from the stratigraphic record, the distribution of the preserved sequence of beds, D_{st}, is truncated at zero leaving only positive values (Figure 8.2). Kolmogorov showed that the probability density of preserved bed thickness, $f(D_{st})$, can be related to the distribution of depositional and erosional events, $f(\delta h_e)$, by $f(D_{st}) = f(\delta h_e)/K_c$, where K_c is termed the Kolmogorov coefficient that takes a value between 0 and 1. The dimensionless Kolmogorov coefficient represents the long-term fraction of depositional events preserved in a given alluvial basin. Following this work, Dacey [248] proposed a derivation relating the thickness of beds to incremental elevation changes. In this work, Dacey provided a derivation for an exponential distribution of bed thicknesses from exponentially distributed depositional and erosional increments.

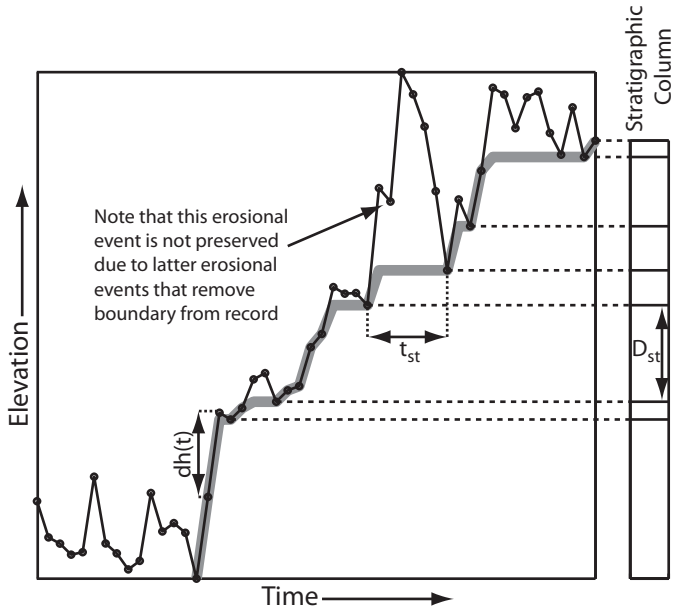

Figure 8.1: Schematic diagram illustrating the construction of a stratigraphic column from elevation increments. Preserved stratigraphic beds occur in environments where the long-term mean of the elevation increments, $\delta h_i(t)$, is positive. Beds in this study are defined as depositional bodies bounded above and below by preserved erosional surfaces.

As elegant as Kolmogorov's [231] theory is, it is based on the statistics of erosional and depositional events, not on the statistics of topography itself. Hence Paola and

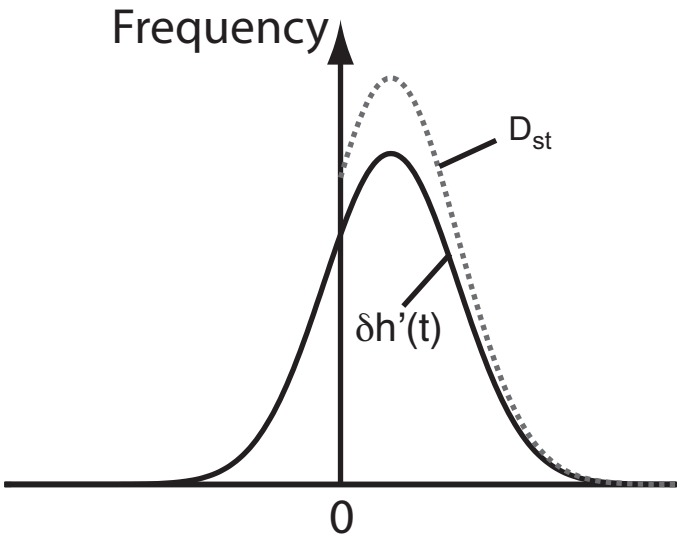

Figure 8.2: Kolmogorov's model of truncated bed thickness distributions. In Kolmogorov's model the frequency distribution, $f(\delta h_e)$, of both depositional and erosional events spans a negative (erosion) to positive (deposition) range. Because erosion removes material from the stratigraphic record, the resulting distribution of bed thicknesses spans only positive values and is thus a left-side truncated frequency distribution, $f(D_{st})$ of bed thicknesses, and has a form that is related through the Kolmogorov coefficient to the positive-value side of $f(\delta h_e)$.

Borgman [13] proposed a method that directly linked preserved bed thickness to topography. Their method yielded an analytical relation between the variance of topography and the probability density function (PDF) of bed thickness, but only in the case when net rate of deposition was zero, and only for exponential-type topographic PDFs. Our specific goal in this chapter is to extend this line of work to the full range of topographic PDFs and rates of net deposition, as a step toward advancing our quantitative ability of inverting bed thickness statistics for information about paleotopography.

While only a few studies examine quantitatively the link between surface elevation increments and bed thickness statistics, several field studies have examined the statistical distribution of preserved bed thickness. For example, Rothman et al. [249] presented measurements of turbidite bed thicknesses and reported that these are well described by a power law distribution, while data presented in [250] and [251] were best fit by lognormal distributions. Critical to the discussion of bed thickness distributions is the

definition of a bed itself. Spatial changes in the texture of sedimentary sections can result from a range of processes. For example, in environments with frequent alternation between erosion and deposition, textural horizons bounding deposits are often associated with unconformities (i.e., erosional boundaries) and the boundaries result from alternation of erosion and deposition. We term these beds "unconformity-bounded beds". In comparison, textural horizons bounding deposits of purely depositional flows are also possible; for example, in purely depositional turbidity currents, beds are primarily associated with the stacking of coarse sediment from deposition by the body of one flow on top of fine grain sediment deposited by the tail of a preceding turbidity current [e.g., 252, 253, 254, 249, 255]. The differences between the two bed definitions above have implications for how one inverts bed thickness distributions for paleo-surface dynamics. The latter case, for convenience termed a "paraconformity-bounded bed", bed thicknesses can easily be mapped to the elevation increments that formed them as the full time sequence of elevations is preserved in the depositional record. The PDF of bed thickness in the paraconformity-bounded case cannot differ from the PDF of elevation fluctuations, so for instance a power law distribution of purely depositional turbidite bed thicknesses implies a power law distribution of the size/duration of individual turbidity current events. Other settings prone to the production of paraconformity-bounded beds include regions with rapid lithification and high resistance to erosion, such as peritidal carbonate settings [256]. The relationship between unconformity bounded beds and the elevation fluctuations that formed them is more difficult to assess due to the removal of sediment during incision. Several studies that define beds as deposits bounded by erosional surfaces report exponential distributions for bed thicknesses in a range of environmental settings and for a range of spatial scales [257, 258, 259, 260]. In the remainder of this chapter we will explore only the unconformity-bounded beds and their relationship to surface elevation increments.

While bed thickness measurements from stratigraphic records are ample and can be used to characterize their probability distribution, measurements of the elevation increments or surface morphodynamics that created those bed thicknesses are rare at best. This is in part due to the difficulty of obtaining time series of elevations long enough to characterize large-magnitude, low-frequency events (e.g., avulsions). As such, we lack

enough data from natural systems to determine even the general family (e.g., exponential, power law, etc.) of distributions that best describe elevation increments in alluvial basins and other environments. It is noted that the Kolmogorov [231] model uses a Gaussian distribution while the work of Dacey [248] uses an exponential distribution for elevation increments to derive the distribution of the preserved bed thickness. However, several recent sediment transport studies have reported heavy-tailed distributions for sediment transport and elevation fluctuations both in river morphodynamics and in hillslope and coupled river-hillslope systems [11, 42, 89]. In this chapter we use data from a physical experiment on a fluvial system in an experimental basin experiencing relative subsidence to characterize the statistics associated with the fluvial dynamics occurring over a range of time-scales and relate these surface statistics to the resulting bed thickness distributions. During this experiment, elevation was monitored at a temporal frequency comparable to the time-scale of the system's "meso-scale dynamics" [54, 217] and over a duration long enough to generate reliable statistics on the magnitude of elevation increments. As shown in Chapter 7, the surface dynamics of aggrading deltas are governed by heavy-tailed statistics. That study raised the question as to why so many observations from field scale stratigraphy show exponential PDFs for bed thickness despite the possible heavy-tailed statistics of surface topography. In this chapter we further probe into this question and demonstrate via analysis of the experimental data and extensive numerical simulations the reasons and conditions under which extreme fluctuations in bed elevation series (e.g., abrupt and large erosional and depositional events) do not get recorded in the stratigraphic record. We also provide a relationship between the preserved mean bed thickness and the variability of the bed elevation increments and show that this relationship remains robust under different probabilistic structures of the alluvial surface dynamics. We propose the interquartile range (defined as the difference between the 75^{th} and 25^{th} quartile of the bed elevation fluctuations) as the proper measure of variability since the heavy-tailed power law distribution of elevation increments suggests theoretical distributions for which the standard variance (second moment around the mean) might not always be properly defined.

8.1 Results from stochastic sedimentation models

8.1.1 Stochastic models for surface elevation evolution

The analysis of surface morphodynamics and the preserved stratigraphy statistics presented in the previous chapter suggest that heavy-tailed distributions of surface evolution do not necessarily translate to heavy-tailed distributions of bed thickness in strata. How general is this result, and are there conditions in which heavy-tails in surface elevation increments can be transferred into the stratigraphic record? We explore these questions using a series of stratigraphic columns constructed from stochastically gen- erated surfaces of sedimentation and erosion (referred to as "synthetic stratigraphic columns"). Several studies have explored the relationship between stochastic models for surface evolution and the synthetic stratigraphy that they generate [261, 260, 225, 262, 243], but no study, to the best of our knowledge, has quantified the effect of heavy-tailed surface elevation increments on the preserved stratigraphy. The advantages of constructing preserved stratigraphic columns from stochastically generated surface elevation series include the ability to explore many physical scenarios for which data are not available and the ability to produce long time series where the shapes of resulting distributions can be confidently interpreted. Such analyses allow us to examine the generality and validity of inferences made from our experimental discretely sampled elevation time series.

We use a 1D model of erosion and sedimentation based on a random-walk formulation that assumes independent magnitudes of erosion and deposition. The magnitudes of erosion and deposition, $\delta h_i(t)$, are assumed to be sampled from a symmetric distribution with thin-or heavy-tails. Specifically, given the concentrated mass at zero (significant chance of having zero or close to zero magnitudes) found from the analysis of experimental data [263] we assume that the surface elevation increments, δh_i, come from either a Laplace distribution (in the case of thin-tails) or a double Pareto distribution (in the case of heavy-tails). The Laplace distribution, also called a double exponential distribution, is given by:

$$f\left(\delta h_i\right) = \frac{1}{2b} exp\left(-\frac{|\delta h_i - \mu|}{b}\right) \tag{8.1}$$

where b is the scale parameter of the distribution and μ is the location parameter (or

the mean of the distribution). The double Pareto distribution is given by:

$$f(\delta h_i) = \begin{cases} \alpha \frac{\mu^\alpha}{\delta h_i^{\alpha+1}} & \text{when } \delta h_i \geq \mu \\ \alpha \frac{\mu^\alpha}{2(2\mu - \delta h_i)^{\alpha+1}} & \text{when } \delta h_i < \mu \end{cases} \tag{8.2}$$

where μ is the mean of the distribution and α is the tail-index.

After generating time series of elevation increments resulting from the above two 1D random-walk models, local preserved minima can be identified and bed thicknesses calculated. A summary of the statistics of preserved stratigraphic columns constructed from the stochastically generated surface elevation series is presented in the next subsection.

8.1.2 Statistics of the Constructed Stratigraphic Columns

As a first step in quantifying the relationship between a parent distribution of elevation increments, $\delta h_i(t)$, and preserved bed thicknesses, D_{st}, we compare the distribution of beds constructed from symmetric, positive mean, thin-tailed distributions of elevation increments (equation (8.1)) to those constructed from symmetric, positive mean, heavy-tailed distributions of elevation increments (equation (8.2)) for a range of parameters of these distributions. Examples of the distributions of $\delta h_i(t)$, D_{st}, τ_d, τ_e, $\delta h_e(t)$ associated with our thin-tailed and heavy-tailed elevation increments are shown in Figures 8.3 and 8.4. For all scenarios explored, we find that: (1) the distribution of Kolmogorov events, $\delta h_e(t)$, show an exponential-type of decay in their tails (thin-tailed) irrespective of the nature of the distribution of elevation increments, $\delta h_i(t)$ (Figures 8.4(B) and 8.4(D)), (2) the distributions of durations of depositional and erosional events (τ_d and τ_e) are always well approximated by thin-tailed distributions, and (3) the resulting bed thicknesses, D_{st}, are best described by exponential distributions (Figures 8.4(B) and 8.4(D)). The outcome of our numerical experiments shows specifically how the process of constructing stratigraphic beds from elevation fluctuations in net depositional settings is associated with a filtering of the information contained within the tails of elevation increments distributions.

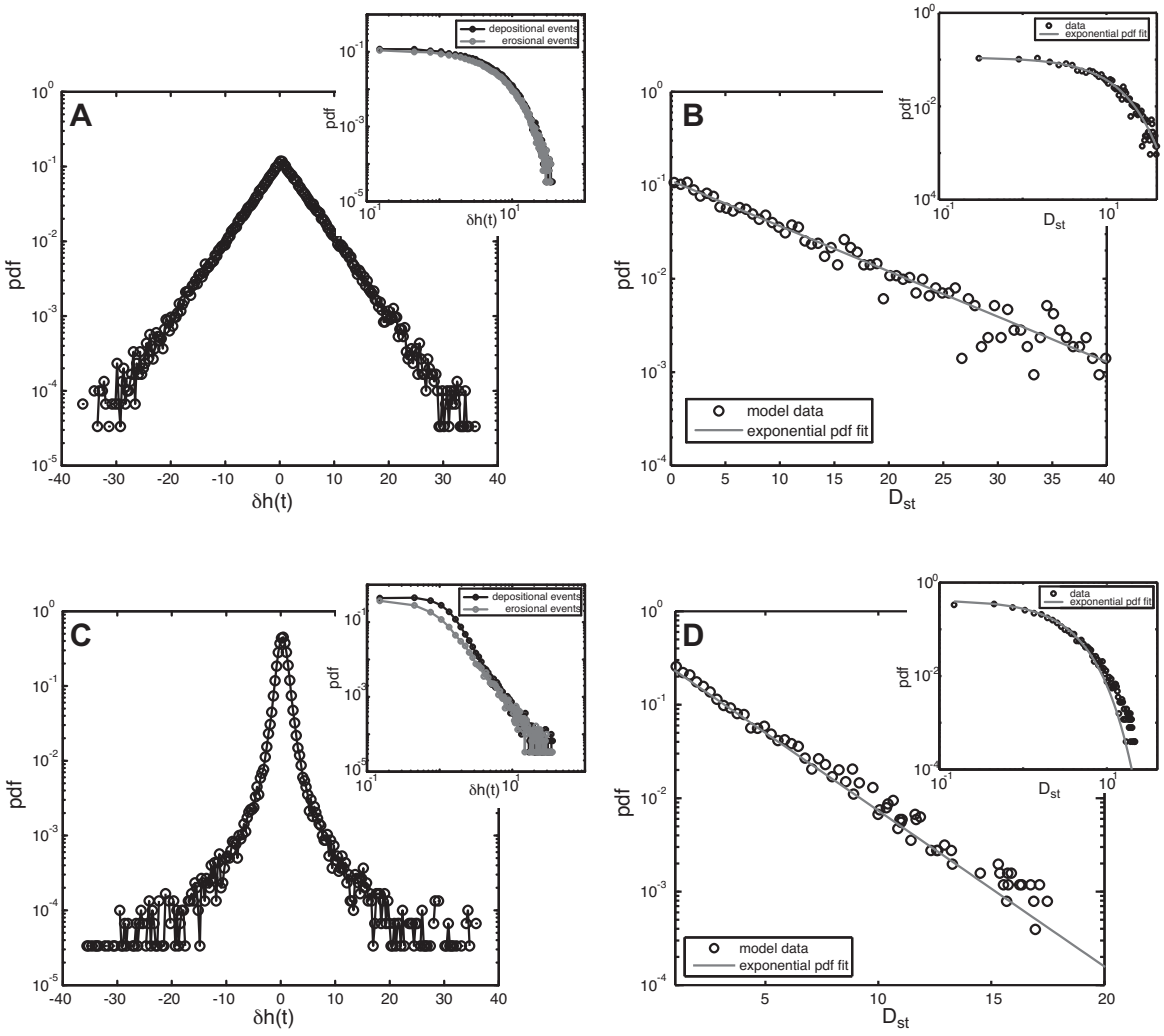

Figure 8.3: Comparison of results from (a, b) 1D numerical models of surface evolution and resulting stratigraphy associated with exponentially distributed elevation fluctuations and (c, d) power law distributed elevation fluctuations. (A) Input PDF of $\delta h_i(t)$ generated from a Laplace distribution of elevation fluctuations with $b = 4.1$ and $\mu = 0.3$. (B) PDF of D^e_{st} shown in both semi-log and log-log plots. Linear decay of bed thicknesses in semi-log space suggests exponential distribution. (C) Input PDF of $\delta h_i(t)$ generated from a double Pareto distribution of mean = 0.3 and $\alpha = 1.5$. (D) PDF of D^e_{st} shown in both semi-log and log-log plots. Linear decay of bed thicknesses in semi-log space suggests exponential distribution. Distributions for both scenarios were generated from model time series with 100,000 elevation increments.

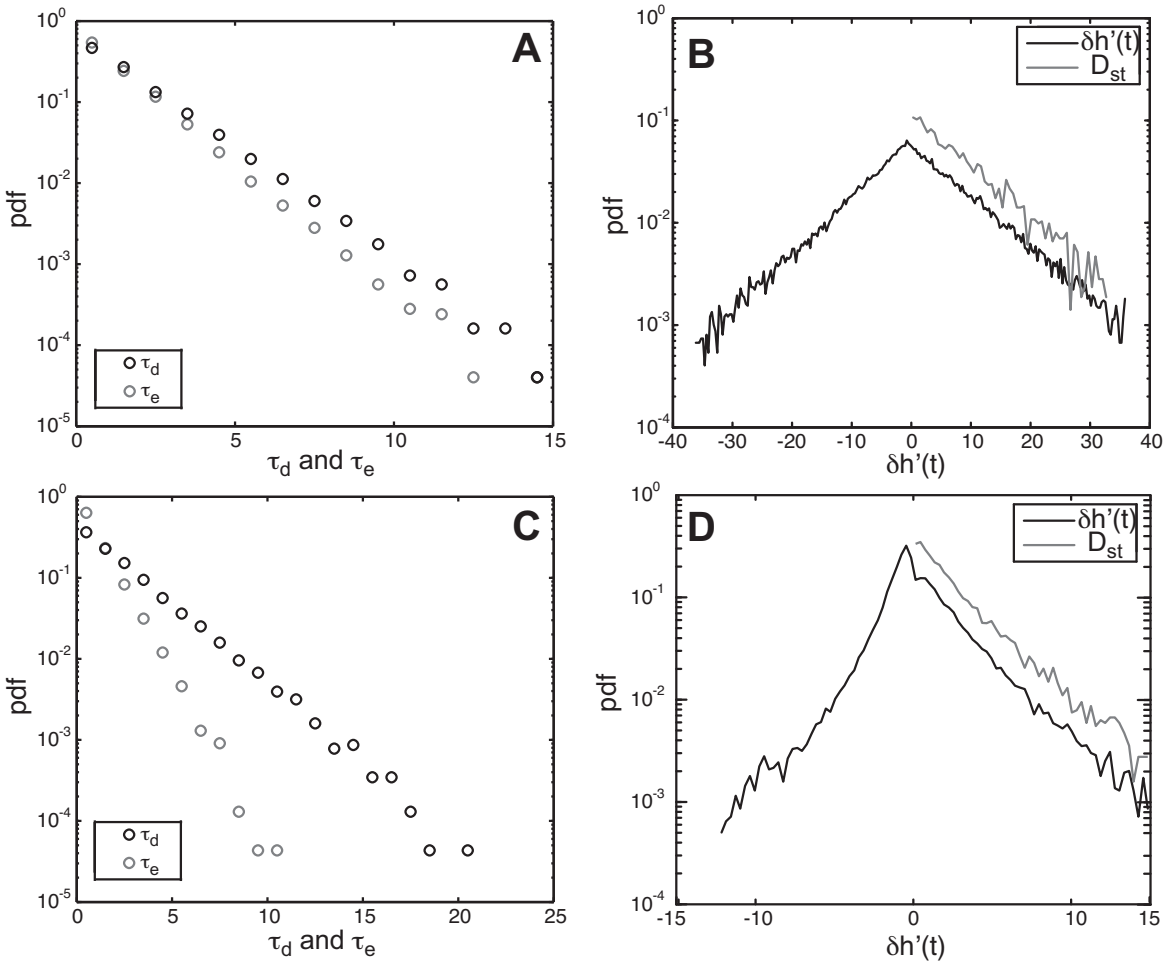

Figure 8.4: Comparison of results from (a, b) 1D numerical models of surface evolution and resulting stratigraphy associated with exponentially distributed elevation fluctuations and (c, d) power law distributed elevation fluctuations. (A) PDF of τ_d and τ_e shown in semi-log space and generated from distribution of elevation increments presented in Figure 8a. (B) Distribution of Kolmogorov elevation events, $\delta h_e(t)$, and resulting bed thicknesses, D^e_{st}. (C) PDF of τ_d and τ_e shown in semi-log space and generated from distribution of elevation increments presented in Figure 8.3(C). (D) Distribution of Kolmogorov elevation events, $\delta h_e(t)$, and resulting bed thicknesses, D^e_{st}.

8.2 Effect of extremes on the stratigraphic bed thicknesses

As was shown in the previous section, the heavy-tailed statistics of surface evolution do not always get preserved in the bed thickness statistics. In this section, we will probe further into how the interplay between the probabilistic structure (i.e., thin-tailed versus heavy-tailed) of the magnitudes of deposition and erosion and the durations of depositional and erosional events effect the distribution of preserved bed thickness. In the remainder of the chapter, for the simplicity of notation, we denote any two random variables to have a symmetric distribution if they have the same nature of decay in their tails (i.e., exponential, thin- tailed versus power law, heavy-tailed).

8.2.1 Influence of Symmetry of the Topographic PDF

An interesting characteristic of both the experimental data and the stochastic surface elevation models described so far is the symmetrical nature of the distributions of the erosional and depositional events, $\delta h_e(t)$, and the durations of depositional and erosional events, τ_d and τ_e. To analyze the importance of this symmetry for the resulting distributions of bed thicknesses, we compare distributions of bed thickness that result from symmetrical and asymmetrical parent distributions of magnitudes of deposition and erosion. In this exercise, rather than constructing synthetic stratigraphic columns from random-walk models of surface elevation increments, we directly generate beds using the difference between the two random variables, depositional events (D_e) and erosional events (E_e), which are in effect random sums of elevation increments, D_i and E_i:

$$\hat{D}^e_{st} = \sum_{i=1}^{\tau_d} D_i - \sum_{i=1}^{\tau_e} E_i \tag{8.3}$$

It is worth noting that the bed thicknesses calculated using equation (8.3) are an approximation of the bed thicknesses constructed from the surface evolution, as this equation takes into account only the erosional thinning of depositional events by the next subsequent erosional event, and not the erosional thinning that could possibly occur due to large magnitude events that could have occurred later in a time series. While equation (8.3) produces only an approximation of bed thickness distributions resulting from a random-walk model of surface elevation evolution, the advantage of using it is that it

allows independent control of the distributions of D_i, E_i, τ_d, and τ_e. In this subsection, we investigate the influence of the symmetric versus asymmetric nature of the distribution of elevation increments and the distributions of the durations of depositional and erosional events on the resulting bed thickness distribution. First, we use equation (8.3) to generate distributions of bed thickness for scenarios in which both elevation increments, $\delta h_i(t)$, and the durations of depositional and erosional events, τ_d and τ_e, have symmetrical distributions, as has been the case for our experimental data and the numerical simulations. Our simulation results demonstrate that, regardless of the shape of the input distributions for $\delta h_i(t)$ and τ_d, τ_e (i.e., thin-tailed versus heavy-tailed), the bed thickness distributions computed using equation (8.3) are exponentially distributed so long as the parent distributions are symmetrical. An example of this is shown in Figure 8.5(B) where we generated the random variables D_i and E_i from symmetric Pareto distributions and generated the random variables τ_d and τ_e from symmetrical exponential distributions.

Next we examine the influence of asymmetry in the distributions of D_i and E_i on the resulting distribution of bed thickness while keeping the τ_d and τ_e distributions symmetrical. Interestingly, as the asymmetry of the D_i to E_i distributions increases, the resulting distribution of bed thickness becomes increasingly weighted toward extremes (approaches a power law in shape). An extreme example of this finding is shown in Figure 8.5(C) where we generated magnitudes of deposition, D_i, from a Pareto distribution with a tail index of 0.75 (very heavy-tail) while generating magnitudes of erosion, E_i, values from an exponential distribution with a scale parameter equal to 5 and the durations of depositional and erosional events from exponential distributions with a scale parameter of 10. The result is a heavy-tailed bed thickness distribution. We assert that this observation represents an important clue as to why bed thickness distributions generated from heavy-tailed surface increments are often exponentially distributed. In systems with heavy-tailed surface increments that have a symmetric distribution, the heavy-tails from one side of the distribution (erosional events) effectively cancel out the heavy-tails from the other side of the distribution (depositional events), thus resulting in a derived distribution that is thin-tailed. Alternatively, increasing the asymmetry of the parent distribution reduces the ability for large magnitude but infrequent erosional increments to balance out large magnitude but infrequent depositional increments,

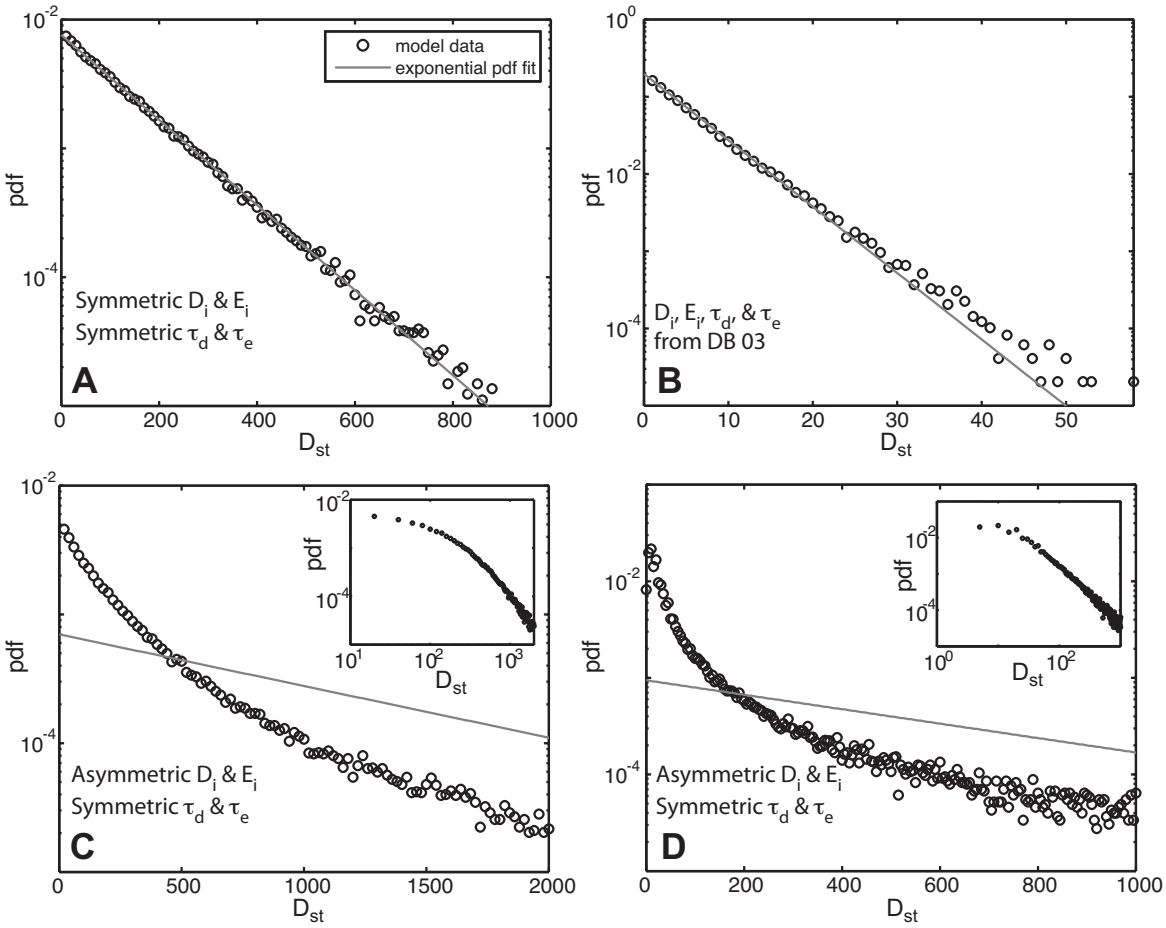

Figure 8.5: Bed thickness distributions generated from individual bed thicknesses calculated using equation (8.3). (A) PDF of bed thicknesses generated using equation (8.3) with input parameters for D_i, E_i, τ_d and τ_e set to equal estimated parameters from DB-03 experiment. (B) PDF of bed thicknesses generated from symmetric distributions of both D_i/E_i and τ_d/τ_e. Random values of D_i and E_i are described by a Pareto distribution with tail-index of 1.5. Mean of combined distribution of depositional and erosional increments, $\delta h_i(t)$ is 10. Random values of τ_d and τ_e are described by an exponential distribution with mean of 10. (C) PDF of bed thicknesses generated from asymmetric distribution of D_i/E_i and symmetric distribution of τ_d/τ_e. Random values of D_i are described by a Pareto distribution with tail-index of 0.75 while values of E_i are described by an exponential distribution with $1/\lambda = 5$. Mean of combined distribution of depositional and erosional increments, $\delta h_i(t)$ is 10. Random values of τ_d and τ_e are described by an exponential distribution with $1/\lambda$ of 10. (D) PDF of bed thicknesses generated from symmetric distribution of D_i/E_i and asymmetric distribution of τ_d/τ_e. Random values of D_i and E_i are described by a Pareto distribution with tail-index of 1.5. Mean of combined distribution of depositional and erosional increments, $\delta h_i(t)$ is 10. Random values of τ_d are described by a Pareto distribution with tail-index of 1.75 while values of τ_e are described by an exponential distribution with μ of 10.

therefore leading to heavy-tailed bed thickness distributions.

In both the experimental data set and the stochastic surface elevation models we find that the durations of depositional and erosional events are well described by thin-tailed distributions. We do not prescribe τ_d and τ_e in our 1D stochastic surface elevation models, but rather they are determined by our assumption of independence between magnitudes of deposition and erosion $\delta h_i(t)$ (can be shown theoretically to follow a negative Binomial distribution). With this information in mind, we explore the implications of asymmetry in the distributions of τ_d and τ_e. Similar to the effect of increasing the asymmetry of the $\delta h_i(t)$ distribution, we find that as the asymmetry of τ_d to τ_e distributions increases, the resulting distribution of bed thicknesses has more weight in the extremes (approaches power law in shape). An extreme example of this is shown in Figure 8.5(D) where we sampled durations of depositional events, τ_d, from a Pareto distribution with a tail index of 1.75 while sampling the durations of erosional events, τ_e, from an exponential distribution with a scale parameter equal to 10 and magnitudes of deposition and erosion from symmetrical Pareto distributions with a tail index of 1.5. In Table 8.1 we summarize our observations on the link between symmetry in the distributions that describe the surface dynamics and the resulting shape of the bed thickness distribution.

Finally, to test the accuracy of the approximation used in equation 8.3 to describe the preserved bed thicknesses, we generated random variables D_i, E_i, τ_d, and τ_e using distributions that described the surface evolution in the DB-03 experiment. We used Pareto distributions for D_i and E_i with tail indexes α_1 and α_2 equal to 2.6 and 1.1, respectively and exponential distributions for τ_d and τ_e with $\langle \tau_d \rangle = 2.6$ min and $\langle \tau_e \rangle = 2.2$ min. The bed thicknesses calculated using these parameters was found to be well approximated by an exponential distribution, with $\langle \hat{D}^e_{st} \rangle$ of 6.2 mm, slightly less than the value we estimated for the DB-03 experiment (Figure 8.5(A)). This agreement confirms the validity of our stochastic simulations for the purpose of studying how the interplay between depositional and erosional events gets recorded in the preserved stratigraphy.

		Asymmetric D_i and E_i Distributions		
	Symmetric D_i and E_i distributions	Both Distributions are Thin-tailed	Both Distributions are Heavy-Tailed	D_i Distributions Heavy-Tailed, E_i Distribution Thin-Tailed
Symmetric τ_d and τ_e Distributions	D_{st}: Thin-tailed	D_{st}: Thin-tailed	D_{st}: Between thin and heavy-tailed	D_{st}: Heavy-tailed
Asymmetric τ_d and τ_e Distributions. Both distributions are thin-tailed	D_{st}: Thin-tailed	D_{st}: Thin-tailed	D_{st}: Between thin and heavy-tailed	D_{st}: Heavy-tailed
Asymmetric τ_d and τ_e Distributions. Both distributions are heavy-tailed	D_{st}: Between thin and heavy-tailed	D_{st}: Between thin and heavy-tailed	D_{st}: Between thin and heavy-tailed	D_{st}: Heavy-tailed
Asymmetric τ_d and τ_e Distributions. τ_d distribution heavy-tailed, τ_e distribution thin-tailed	D_{st}: Heavy-tailed	D_{st}: Heavy-tailed	D_{st}: Heavy-tailed	D_{st}: Heavy-tailed

Table 8.1: Regime Matrix Illustrating Relationship Between Shape of D_i, E_i, τ_d, and τ_e Distributions and Resulting D_{st} Distribution

8.2.2 Mapping Surface Variability to Bed-Thickness Statistics

In previous sections and chapter 7, we presented data from physical and numerical experiments that indicate that the statistics describing the preserved bed thicknesses generally do not record the signature of heavy-tailed surface evolution statistics. While information on the nature of the distributions tail (thin-tailed versus heavy-tailed) of surface evolution events may be filtered from the stratigraphic record, in this section we demonstrate variability of elevation increments, δh_i, relative to the mean deposition, $\langle \delta h_i \rangle$, influences the mean of preserved bed thicknesses, $\langle D_{st} \rangle$. This was demonstrated analytically by Paola and Borgman [13] for the case of zero net deposition and thin-tailed elevation statistics; here we generalize that result. Specifically, we are interested in relating the variability and mean of elevation increment distributions to the statistics describing the preserved bed thicknesses. One common measure of a distribution's variability is the interquartile range, IQR, which is equal to the difference between the third and first quartiles of the distribution. To compare the spread of the parent distribution to its mean we examine the nondimensional interquartile range coefficient, $\Phi_{\delta h_i}$:

$$\Phi_{\delta h_i} = \frac{IQR_{\delta h_i}}{\langle \delta h_i \rangle} = \frac{F^{-1}_{\delta h_i}(0.75) - F^{-1}_{\delta h_i}(0.25)}{\langle \delta h_i \rangle} \tag{8.4}$$

An additional metric that compares a distributions variability to its mean is the coefficient of variation, $CV_{\delta h_i}$, defined as:

$$CV_{\delta h_i} = \frac{\langle (\delta h_i - \langle \delta h_i \rangle)^2 \rangle^{1/2}}{\langle \delta h_i \rangle} \tag{8.5}$$

An advantage of the interquartile range over the coefficient of variation is that the interquartile range of all thin-tailed and heavy-tailed distributions formally exists, while the standard deviation, σ, does not formally exist for heavy-tailed distributions with a tail index less than 2. We note, though, that for any finite sequence of random numbers generated from a thin or heavy-tailed distribution, a standard deviation can always be calculated. However, for thin-tailed random variables, the calculated standard deviation converges to a fixed value with an increase in the sample size while, for heavy- tailed random variables with tail index less than 2, the calculated standard deviation diverges with increasing sample size, casting uncertainty in inferences from finite size data sets.

With this in mind, we generated a sequence of synthetic stratigraphic columns, as outlined in section 8.2.1, constructed from elevation increments that span a range of values of the non-dimensional interquartile range ($\Phi_{\delta h_i}$). For each constructed stratigraphic column we tracked the interquartile range of the distribution of elevation increments, the mean of the elevation increments $\langle \delta h_i \rangle$, and the estimated mean of the preserved bed thicknesses, D_{st}, which fully characterizes the distribution of bed thicknesses since they are well described by an exponential distribution.

Figure 8.6 shows how the non-dimensional bed thickness (calculated by taking the ratio of the estimated mean bed thickness to the background net depositional rate, $\langle D_{st} \rangle / \langle \delta h_i \rangle$) varies as a function of the non-dimensional interquartile range of the distribution of elevation increments ($\Phi_{\delta h_i}$) for synthetic stratigraphic columns created by both thin-tailed (exponential) and heavy-tailed (power law) elevation increment distributions. Note that since both axes of Figure 8.6 are non-dimensional, one can compare systems of different absolute scale, but similar in their ratio of surface variability to mean background deposition rate. Each data point on Figure 8.6 represents the outcome of a single 1D stochastic model of sedimentation as outlined in section 8.1. Utilizing symmetrical distributions and user specified values of the non-dimensional interquartile range of the distribution of elevation increments, we constructed the preserved bed thickness distributions from which we estimated the mean preserved bed thickness, $\langle D_{st} \rangle$. For time series constructed with up to $100,000$ increments (the maximum time series length generated in this analysis) we noted no difference in the shape of the relationship between the non-dimensional bed thickness and the non-dimensional interquartile range of the distribution of elevation increments. Interestingly, we found that the data from the DB-03 experiment nicely plot on the curve computed from the 1D stochastic models. As the coefficient of variation (CV) is a more commonly used metric to compare a distribution's variability to its mean we also checked for the dependence of the non-dimensional bed thickness versus the coefficient of variation of the surface elevation increments, while acknowledging that the coefficient of variation would not formally exist for heavy-tailed distribution of elevation increments.

As the non-dimensional interquartile range of the distribution of elevation increments increases from a minimum possible value of zero, the non-dimensional bed thickness decreases until it reaches a global minimum of approximately 7 at a value of $\Phi_{\delta h_i} \sim 1.4$.

Further increases in the non-dimensional interquartile range of the distribution of elevation increments result in an increase of the non-dimensional bed thickness with the rate of increase characterized by a slope equal to ~ 1.4. In summary, Figure 8.6 illustrates that a large value for the mean of a bed thickness distribution relative to the background deposition rate can result from either extremely low or extremely high variability in elevation increments relative to the background drift. On the left-hand side of this relationship in Figure 8.6 ($\Phi_{\delta h_i} < 1.4$), increasing the variability of elevation increments, for a given background drift, decreases the mean bed thickness in the resulting stratigraphic column. On this side of the plot the variability of elevation increments is small relative to the mean background drift, thus erosional events are rare and the stratigraphic column is constructed from a broad distribution of thick deposits. In other words, increasing the surface variability tends to break thick deposits into smaller units reducing thus the mean of the preserved bed thicknesses. On the right-hand side of this relationship in Figure 8.6 ($\Phi_{\delta h_i} > 1.4$) increasing the variability of elevation increments, for a given background drift, increases the mean bed thickness in the resulting stratigraphic column. On this side of the plot the variability of elevation increments is large relative to the mean, thus most sediment that is deposited is eventually removed by future erosional events and the stratigraphic column is constructed from sediment that is reworked by a broad distribution of erosional events.

Analysis of the Kolmogorov event, $\delta h_e(t)$, distributions provides additional insight into the processes responsible for the shape of the relationship between the non-dimensional interquartile range of the distribution of elevation increments and the non-dimensional bed thickness. All model runs for Figure 8.6 had symmetrical distributions of elevation increments. Insert plots within Figure 8.6 define the shape of the Kolmogorov event's distributions for three values of the non-dimensional interquartile range of the distribution of elevation increments. For conditions where $\Phi_{\delta h_i} > 1.4$ the resulting distribution of Kolmogorov events is approximately symmetrical in form. As the value of non-dimensional interquartile range of the distribution of elevation increments, $\Phi_{\delta h_i}$, decreases below a value of 1.4, the distribution of the Kolmogorov events becomes increasingly asymmetric with more weight on the positive (D_e) side of the distribution than the negative end (E_e) of the distribution.

For all conditions analyzed, the mapping of elevation increments to Kolmogorov

events is associated with a significant thinning of the tail of the distribution. This results in depositional and erosional events (D_e and E_e) that are well described by thin-tailed, exponential distributions. This allows us to compare the estimated scale parameters of the depositional and erosional events, $\hat{\mu}_{D_e}$ and $\hat{\mu}_{E_e}$, respectively. For conditions where $\Phi_{\delta h_i} < 1.4$, we find that the estimated mean of the depositional events is much larger than the estimated mean of the erosional events ($\hat{\mu}_{D_e} \gg \hat{\mu}_{E_e}$) and thus the distribution of the Kolmogorov events is asymmetric. However, as the value of the non-dimensional interquartile range of the distribution of elevation increments increases, the difference between the estimated means of the depositional and erosional events decreases and as a result the mean of the preserved bed thicknesses ($\hat{\mu}_{D_{st}}$) decreases. This is summarized in the following scaling relationship:

$$\hat{\mu}_{D_{st}} \sim \hat{\mu}_{D_e} - \hat{\mu}_{E_e} \tag{8.6}$$

The decrease in the estimated mean of the preserved bed thicknesses continues until the distributions of the depositional and erosional events are roughly symmetrical. At this location, the $\delta h_e(t)$ distribution can be approximated as a Laplace distribution. We note that the interquartile range of a Laplace distribution (see equation 8.1) is equal to $2bln(2)$ or approximately $1.4b$, where b is the scale parameter of the Laplace distribution. We observe that the global minimum in the values of non-dimensional bed thickness occurs at a value where the background net depositional rate ($\langle \delta h_i \rangle$) is equal to the scale parameter (b) of the best fit Laplace distribution of the Kolmogorov events suggesting that the filtering of information contained within the tails of an elevation increments distribution also strongly influences the relationship shown in Figure 8.6. Above the value of $\Phi_{\delta h_i} \sim 1.4$ the Kolmogorov events' distribution is well described by a Laplace distribution (i.e., symmetrical distribution of depositional and erosional events), and increasing the value of the non-dimensional interquartile range of the distribution of elevation increments results in an increase of the non-dimensional bed thickness at a rate characterized by a slope approximately equal to 1.4 (or approximately equal to $2ln(2)$). In essence, for symmetrical elevation events, an increase in the variability of elevation events always causes an increase in the mean bed thickness, similar to the finding by Paola and Borgman [13].

Finally, to test the sampling interval scale-dependence of the trend observed in

Figure 8.6, we generated elevation time series as discussed above and calculated the non-dimensional interquartile range of the distribution of the elevation increments and the non-dimensional bed thickness at the finest resolution. We then subsampled the elevation time series, extracting every n^{th} elevation measurement, and recalculated the non-dimensional interquartile range of the distribution of the elevation increments and the non-dimensional bed thickness of the new subsampled elevation time series. We find that the non-dimensional interquartile range of the distribution of the elevation increments and the non-dimensional bed thickness from the subsampled elevation time series plots on the trend that was generated from the elevation time series considered at the finest resolution. In other words, we find that the relationship established in Figure 8.6 is robust to changes in scales of measurement of the surface elevation increments.

8.2.3 Implications for Stratigraphy

Analysis of the DB-03 experimental data and the1D stochastic models that generated synthetic stratigraphy suggests a predictable relationship between the variability in topography and the mean bed thickness of a stratigraphic column. Environments with near-symmetric distributions of elevation increments (both thin- and heavy-tailed), and near-symmetric distributions of periods of depositional and erosional events produce stratigraphic columns composed of exponentially distributed beds. The fact that most reported unconformity-bounded bed thickness distributions are exponential suggests that field scale distributions of elevation increments and periods of depositional and erosional events are in fact often symmetrical. While yet untested, the relationship presented in Figure 8.6 might also aid in the analysis and identification of paleo-environments. For example, suppose for the sake of argument that, for a given background deposition rate the appropriately scaled variability in surface evolution of braided rivers were greater than in meandering rivers. Then the preserved bed thickness distributions generated from braided rivers would plot more toward the right-hand side of Figure 8.6 compared to bed distributions resulting from meandering rivers. We believe these questions pose an interesting line of investigation for future experimental studies. Further questions which remain to be addressed include 1) the relationship between the Kolmogorov definition of beds, defined as strata deposited between successive preserved erosional surfaces, and beds defined in outcrops as strata bounded above

and below by distinct textural horizons. This might be achieved in controlled laboratory experiments where time series of elevation can be compared to spatially referenced images of preserved physical stratigraphy. 2) What is the relationship between surface variability and resulting bed-thickness statistics for systems with nested distributions of surface topography. For instance, how do the PDFs of topographic fluctuations relate to bed thicknesses in avulsive river systems with river channel bottoms covered by depth-limited dunes?

Finally, in our previous study on the statistics of surface dynamics in depositional braided fluvial systems, Ganti et al.[263] found that several distributions associated with surface dynamics follow truncated Pareto distributions. They reported that the truncation scales for these distributions are set by the depths of channels constructing a package of sediment and the time scale of avulsion associated with these channels. This finding also has implications for the conversion of elevation increments to stratigraphic beds thickness. The truncation at a scale associated with the roughness of the surface topography essentially makes the tails of the distribution of elevation increments thinner than the case where the distribution is not truncated. As a result, the distributions of the Kolmogorov events and the preserved bed thickness that result from a truncated parent distribution will have tails that exhibit faster decay (lesser weight in extremes) than distributions arising from non- truncated parent distributions, adding to the prevalence of exponential-like bed thickness distributions in the stratigraphic record.

All in all, then, we see two broad categories of bed creation in the stratigraphic record. The first, which we believe is the most common, involves reworking of the surface by a combination of upward and downward increments (deposition and erosion, or "cut-and-fill"). We have shown here that this case is expected to produce exponential-type (thin-tailed) bed thickness distributions regardless of whether the distributions of the associated sediment surface dynamics are thin- or heavy-tailed. The second case is that in which there is strong asymmetry between deposition and erosion. This could mean that the depositional events are heavy-tailed and the erosional events thin-tailed, for which we are not aware of any field examples; or more simply that the erosional events are absent or negligible, for example at the distal end of the depositional system. With no erosional modification, the beds are then a faithful record of the events that produced them. This is the case studied, for example, by Rothman et al. [249], and

here if the events have a heavy-tailed distribution then so will the deposits.

8.3 Conclusions

This study presents an extensive analysis of experimental and stochastically generated surface morphology to quantitatively examine the relation between surface elevation evolution and the resulting stratigraphy. The main results are summarized as follows:

1. Thin-tailed (e.g., exponential) bed thickness distributions result from heavy-tailed surface evolution statistics, as evidenced from both the laboratory experimental data and numerical simulations. We showed that this thinning of the tail of the distribution occurs in environments where the distributions of the surface elevation increments and periods of depositional and erosional events (τ_d and τ_e) have positive means and are symmetric in shape.

2. Asymmetry in parent topographic PDFs results in bed thickness distributions that carry some of the heavy-tailed statistics present in their parent distributions. Truncation of the parent distribution tails due to depositional processes further reduces the chance of occurrence of extremes in preserved bed thicknesses compared to their parent distributions. The implication of this result adds to the prevalence of exponential bed thicknesses as heavy-tailed distributions in nature are often truncated at some scale.

3. The interquartile range (difference between the 75^{th} and 25^{th} quartiles) of the surface elevation increments can serve as a predictor of mean bed thickness of the stratigraphic deposit. This relationship holds for both thin and heavy-tailed surface statistics and demonstrates that information related to the variability of surface fluctuations is stored in the stratigraphic record.

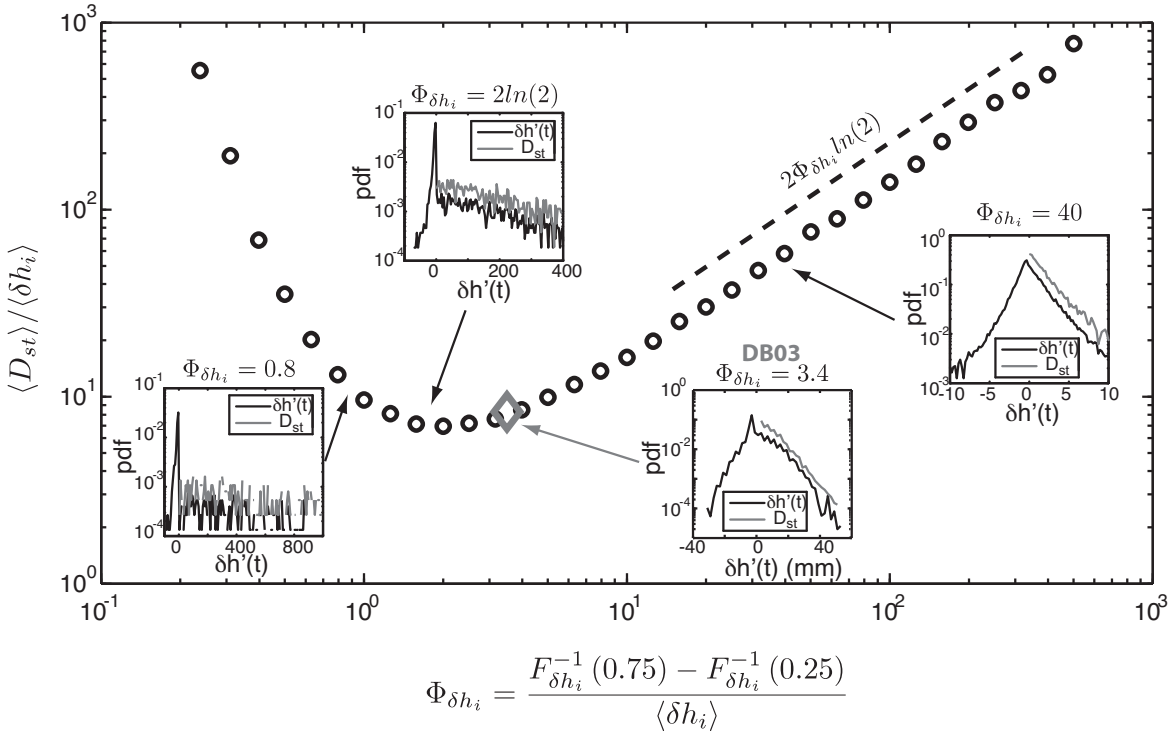

Figure 8.6: Model results documenting relationship between (A) $\Phi_{\delta h_i}$ and (B) $CV_{\delta h_i}$ for surface elevation fluctuations and $\langle D_{st}\rangle/\langle\delta h_i\rangle$ generated from 1D synthetic stratigraphy models with input PDF of $\delta h_i(t)$ generated from exponential distribution with $\lambda = 1.0$ are shown with black open circles, while 1D models with input PDF of $\delta h_i(t)$ generated from Pareto distribution with $\alpha = 1.75$ are shown with gray crosses. Gray open triangle indicates relationship between data from DB-03 experiment. Insert plots illustrate shape of Kolmogorov increments, $\delta h_e(t)$, and resulting bed thickness, D^e_{st}, distributions for 1D models with three $\Phi_{\delta h_i}$ values. Distributions displayed in insert plots resulted from elevation increments, $\delta h_i(t)$ generated from Pareto distributions with $\alpha = 1.75$.

Chapter 9

Kinematic controls on the geometrical structure of the preserved cross-sets

The architecture of stratigraphy is a function of three characteristics of depositional systems: 1) the topography of an actively evolving surface, 2) surface kinematics of topographic evolution, and 3) the rate of net deposition [216, 55, 217, 62]. As all three of these properties are influenced by environmental conditions (e.g., climate and tectonics), the architecture of stratigraphy contains information that could be used to quantitatively reconstruct paleolandscape dynamics across many time scales [218, 54, 219]. Quantitative analysis of stratigraphy exposed in outcrops or imaged in seismic data coupled to numerical models relating Earth-surface dynamics to the preserved stratigraphy has blossomed in the last fifty years, initiating with the pioneering works by [231], [56] and [63]. The general goal for many of these studies was to develop tools to invert stratigraphic records for deciphering paleo-environmental conditions.

Of the structures present in the stratigraphic record, the cross-stratified units formed by migrating ripples and dunes are amongst the most commonly observed. Dunes and ripples migrating on a bed leave a distinct signature in the stratigraphic record owing to the size sorting of particles on the lee faces of the bed forms [264, 265, 266] and because scouring produces erosional surfaces that are preserved in the stratigraphic deposits

[267, 266]. The deposit that is preserved between two successive erosional surfaces is called a set. The cross-stratification patterns depend on the movement of the bed forms, the change in shape, and any change in the direction of travel of the bed forms [e.g., 268]. Since, the geometrical structure of cross-stratified units (e.g., set thicknesses) can be related to the water depth existing at the time of bed form migration [e.g., 269, 270], data of stratigraphic deposits can be used to reconstruct paleochannel depth and width [271].

The relationship between the geometry of bed forms and associated cross-stratification has been a subject of qualitative [e.g., 270, 268] and quantitative analysis for many years [e.g., 272, 13, 273, 274, 247, 267, 246]. The architecture of cross-stratified units comprises of the distribution of set thicknesses, and the length, slope and curvature of the cross-sets. Of these, the most studied variable in the literature is the set thickness. [13] developed an exact theory that relates the variability in bed form heights to the distribution of the set thicknesses under zero net depositional conditions. This theory was modified to the case where net deposition occurs and an empirical relationship between the mean set thickness and the bed form geometry and net aggradation rate was proposed [273]. Several experimental studies validated the Paola-Borgman and the modified Paola-Borgman theories and quantified the role of net aggradation rate and variability in bed form heights in controlling the set thicknesses [274, 275, 247, 267]. Further, via a numerical model for bed form evolution, [246] highlighted the importance of the competition between net aggradation rate and bed form migration rate on the resulting distribution of set thicknesses. The controls on the length of the cross-sets were studied qualitatively [268] and quantitatively using experimental data [267]. [268] stated that the length of bounding surfaces of cross-sets formed by current ripples is about half the bed form wavelength, which was later experimentally validated by [267].

Almost all studies to date have focused on the effect that migration and aggradation rates have on the geometry of the cross-sets. Although the change in shape of the bed forms has been thought to have an effect on the geometry of the cross-sets as early as the work of [268], very little quantitative or experimental insight has been gained in this respect. In a recent study [276], the change in shape of the evolving bed forms was quantified by a vertical speed called deformation rate. The focus of our study is to understand the effect of deformation on the architecture of stratigraphy and to develop

theoretical relationships between the surface kinematics of bed form evolution and the geometrical structure of the cross-sets (in particular, the curvature of the cross-sets).

This chapter is structured as follows. In the next section, we develop the theoretical relationships between the slope and curvature of the bounding surfaces of the preserved cross-sets in terms of the surface kinematics of bed form evolution. In Section 9.2, we describe the experimental setup and data of bed form evolution used in this study. The analyses for characterizing the surface kinematics of bed form evolution and the geometrical structure of the preserved stratigraphy for the experimental data are presented in Sections 9.3 and 9.4, respectively. In Section 9.5, we validate the proposed theoretical relationships between surface kinematics of bed form evolution and the geometrical structure of the preserved stratigraphy using the experimental data collected under zero net depositional conditions. Finally, discussion and conclusions are presented in Sections 9.6 and 9.7, respectively.

9.1 Theoretical development

Consider a train of bed forms whose 1D elevation in the stream wise direction x as it evolves over time t is given by $\eta(x,t)$. The surface kinematics of the evolution of this train of bed forms can be characterized in terms of the rate of migration of the bed forms and the change in shape of the bed forms as they migrate (see Figure 9.1). [276] proposed a unifying theoretical framework to investigate the evolution of sandy bed rivers. They proposed that the bed is appropriately described by a kinematic wave with a source term given by:

$$\frac{\partial \eta(x,t)}{\partial t} + V_c \frac{\partial \eta(x,t)}{\partial x} = \Pi(x,t) \tag{9.1}$$

where V_c is the characteristic bed form migration rate, and Π is the deformation rate, which is a vertical speed. When $\Pi = 0$, the above equation describes the case of evolving bed forms that are translationally invariant whereas $\Pi > 0$ describes the case of locally aggrading bed and $\Pi < 0$ describes the case of locally eroding bed. Dynamic equilibrium for a bed corresponds to the case when the deformation rate averages to zero over a certain time scale. [276] noted that the dynamic bed evolution, as defined by equation (9.1), can be used to infer the features preserved in the stratigraphic record. Namely, this equation can be used to quantify the effect that deformation of the bed

forms has on the geometry of the preserved stratigraphy.

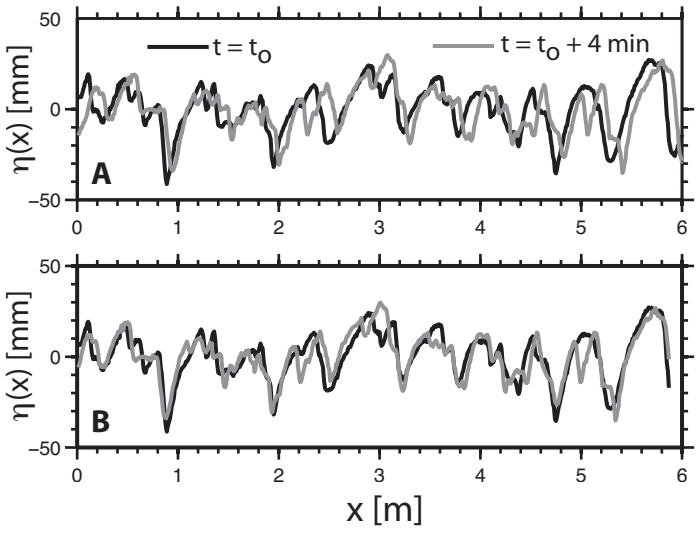

Figure 9.1: (Top panel) Two superimposed streambed profiles from the experimental data set corresponding to the 80 lps water discharge. The gray profile is from 4 mins after the black profile. Notice that the initial streambed profile has translated and deformed over time. This deformation becomes more evident after accounting for the mean migration component by shifting the gray profile backward along the longitudinal axis (bottom panel).

The deformation rate, as defined above, includes bed form state change due to changing flow conditions as well the changes of mean bed elevation that are both short-time variations around an equilibrium profile (as in Figure 9.1(B)) and that are larger excursions like climbing bed forms. Thus, the deformation rate, as defined by McElroy and Mohrig [276], has the ability to produce stratigraphy that encompasses the whole range of behaviors between the steady aggradation of Rubin and Hunter [272] to the bed form variability described by Paola and Borgman [13]. Our interest here is to use the above definition of dynamic bed evolution to understand the effect that the change in shape of the bed forms has on the geometrical structure of preserved cross-sets. For this purpose, we can decompose the deformation rate into two components: (a) a mean aggradation rate that quantifies any large excursions like climbing bed forms ($\bar{r}$), and (b) change in shape of the bed forms that is quantified by the short-time variations around an equilibrium profile (π). Under this decomposition, the short-time variations around

an equilibrium profile will average out to be zero over some time scale (i.e., $\langle \pi \rangle_t = 0$).

Since, the deformation rate is a vertical speed that describes the rate of vertical change in the elevation, the slopes of the bounding surfaces of the cross-sets will be given by:

$$S_{st} = \frac{\Pi}{V_c} = \frac{\bar{r}}{V_c} + \frac{\pi}{V_c} \tag{9.2}$$

This relationship was established as early as the works by Allen [270] and Rubin and Hunter [272], where the angle of climb of the bed forms was defined as the ratio of the vertical speed to the horizontal, stream wise speed. The above definition gives us further insight in that the first component of the slope of the bounding surfaces results from the constant net aggradation present in the system, which results in a constant slope of the bounding surfaces. The second component in the above equation is a stochastic entity which on an average is zero but results in local changes of the slope of the bounding surface. Any changes in the local slope of the bounding surfaces will result in curved bounding surfaces.

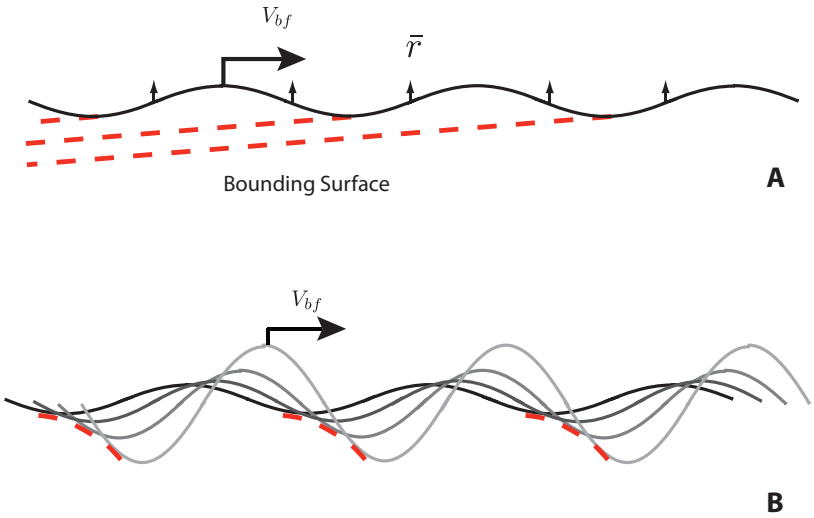

Figure 9.2: Schematic highlighting the role of deformation of bed forms in the formation of stratigraphic bounding surfaces. (A) Translationally invariant bed forms under constant net deposition ($\bar{r}$) and migration rates (V_{bf}) produce straight set boundaries. (B) However, when the bed forms change in shape during their evolution then the resulting stratigraphic boundaries have a curvature owing to the local changes in the slope of the bounding surface.

The spatial rate of change of the slope of the bounding surface is defined as the curvature of the bounding surfaces. Thus, we can derive the curvature of the bounding surfaces from equation (9.2) as:

$$C_{st} = \frac{\partial S_{st}}{\partial x} = \frac{\partial}{\partial x}\left(\frac{\Pi}{V_c}\right) = \frac{\partial}{\partial x}\left(\frac{\bar{r}}{V_c} + \frac{\pi}{V_c}\right) \tag{9.3}$$

where C_{st} is the curvature of the bounding surfaces of the cross-sets. From the above equation, we note that curved bounding surfaces can result from changes in net aggradation rate, migration rate and bed form deformation rate. In the case when the characteristic migration rate and the net aggradation rate are constant, the curvature of the bounding surfaces of the preserved cross-sets is given by:

$$C_{st} = \frac{1}{V_c}\frac{\partial \pi}{\partial x} \tag{9.4}$$

where π corresponds to the short-time variations around an equilibrium bed profile and quantifies the change in shape of the bed forms. Further, equation (9.3) implies that translationally invariant bed forms do not produce curved bounding surfaces under constant net aggradation rate. Inherent to the above derivation is the time scale of applicability of these relationships. The bounding surfaces of the cross-sets are formed over a time scale that corresponds to the time it takes for a single bed form to translate a distance equal to its bed form length and thus the migration and deformation rate need to be computed over that time scale. In the next section, we describe the experimental data of bed form evolution collected under zero net deposition, in which case the deformation rate comprises only the short-time variations that correspond to the change in the shape of the bed forms ($\Pi = \pi$).

9.2 Experimental arrangement and data collected

Experiments were conducted during the summer of 2011 on the Tilting Bed Flume at the Saint Anthony Falls Laboratory (SAFL) at the University of Minnesota in Minneapolis, MN. The flume is a rectangular channel with length, width, and depth of 15.0, 0.92, and 0.65 meters, respectively. The bed of the flume was adjusted to zero slope ($\pm 10^{-4}$). Sand grain sizes used in the experiments, measured using a Retsch Camsizer, were roughly lognormal, with median diameter, $D_{50} = 0.37$ mm, and range $D_{10} = 0.25$ mm

to $D_{90} = 0.58$ mm, representing the 10^{th} and 90^{th} percentiles of grain size, respectively. Measured sand density was $\rho_s = 2.60$ g/mL, and measured surface bed sediment volume fraction was $\phi = 0.58$.

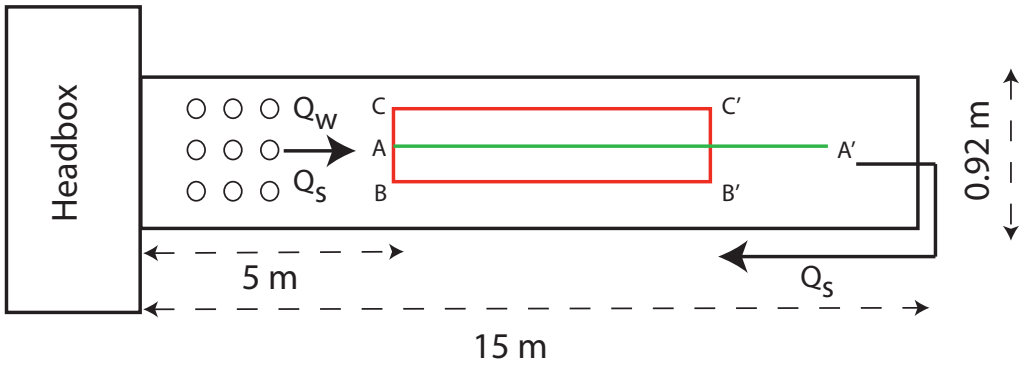

Figure 9.3: Schematic of the plan view of the experiment. For the water discharge of 40 lps, data of bed elevation evolution were collected along the transect $A - A'$ at an approximate temporal resolution of 17 s (green line). For the water discharge of 80 lps, data of bed elevation evolution were collected along two parallel longitudinal transects ($B - B'$ and $C - C'$) and two parallel lateral transects ($B - C$ and $B' - C'$) at an approximate resolution of 45 s (red lines).

Water from the Mississippi River entered the flume through a large pipe submerged in an upstream headbox and exited the flume into a discharge channel by a free overfall. Head gradient between the Mississippi River inlet channel and water height in the headbox naturally propelled the water flow into the flume. Water discharge was controlled manually by a hydraulically actuated valve. Water discharge was determined by a linear calibration curve relating valve pressure to water discharge. The discharge calibration curve was determined by filling large weigh tanks for known durations of time for a range of six discharges. Uncertainty of the discharge values based on the magnitude of residuals to the fit calibration curve was 1.75 lps. Additional uncertainty in the water discharge may have also been introduced by changes in hydrostatic pressure due to variability in water level in the inlet channel. The head difference varied among experiments from about $4.0 - 4.4$ m, producing an additional discharge uncertainty of $\pm 2.4\%$.

The flume contained a roughly constant volume of sand, which was retained in the flume by a recirculating pump. Downstream of the test section, a 20 cm high wall

helped to ensure a minimum depth of sediment in the flume. Downstream sand flux overtopping the wall settled into a submerged funnel located roughly 14 m downstream of the headbox. After settling to the bottom, a water jet carried the sediment back to the upstream end of the flume, releasing it back to the flow evenly across the channel cross-section through a manifold. The discharge of the pump measured by a broad-crested weir was 13.3 ± 1.1 lps. Water for the eductor jet was drawn directly from the headbox of the flume, thus the only addition of water discharge generated by the flume was that created by suction of water into the settling funnel, which we could not measure. Downstream of the collection funnel, a 26 cm high gate maintained a minimum flow depth within the flume, preventing the formation of lateral instabilities and braiding.

Unsteadiness in water from the headbox was smoothed as it flowed through a mesh of cobbles. A matrix of upright PVC pipes downstream of the recirculation manifold helped to straighten water flow (see Figure 9.3), and a piece of foam floating on the water surface smoothed out water surface disturbances. Nonetheless, a zone of sediment scour formed downstream of the flow straightener, extending to about 3 m from the headbox. To ensure flow and bed form uniformity, we thus limited our bed form analyses to the zone from $5 - 13$ m downstream of the flume headbox. Detailed description of the experimental arrangement can be found in [277].

We measured bed topography during the experiments by successive sonar scans using a JSR Ultrasonic DPR300 Pulser / Receiver. The sonar, which was minimally submerged about 1 cm below the water surface (to reduce flow disturbances), swept up and down the length of the observation section along longitudinal transect(s), recording bed elevation at 1 cm intervals. The sonar recorded bed topography with sub-millimeter resolution, although uncertainty in picking out the sonar waveform peak suggests vertical accuracy on the order of 1 mm.

We collected experimental data of bed topographic evolution for two flows: 40 lps and 80 lps. Data were collected after the bed had reached a dynamic steady-state, which was determined by no change in the standard deviation of the bed topography in time. For a water discharge of 40 lps, data of topographic evolution were collected at a temporal resolution of approximately 17 s along the 8 m longitudinal transect $A - A'$ (shown in Figure 9.3). Figure 9.4(A) shows the streambed profiles at 1 hr intervals

for a water discharge of 40 lps and the space-time plot of the sequential streambed profiles for the same discharge are shown at every 17 s in Figure 9.4(C). For a water discharge of 80 lps, data of topographic evolution were collected at a temporal resolution of approximately 41 s along two 6 m longitudinal transects ($B - B'$ and $C - C'$ in Figure 9.3) and along two 30 cm lateral transects ($B - C$ and $B' - C'$ in Figure 9.3). Figure 9.4(B) shows the streambed profiles at 1.5 hr intervals for a water discharge of 80 lps and the space-time plot of the sequential streambed profiles for the same discharge are shown at every 45 s in Figure 9.4(D). In the next section, we use the experimental data of bed form evolution to characterize the surface kinematics of surface evolution for both the flows.

9.3 Characteristics of surface kinematics

In this section, our goal is to characterize the surface kinematics of bed form evolution using the experimental data described in Section 9.2. As discussed in Section 9.1, the surface kinematics of bed form evolution is completely characterized by migration and deformation of the bed forms [276]. In equation (9.1), the characteristic migration rate V_c can be estimated by performing a cross-correlation analysis of the bed elevations along the streambed profiles at various time instances [276]. However, this approach quantifies the bulk migration rate of all the bed forms present along a streamed profile. Our goal here is to clearly demarcate the translational component of surface kinematics from the deformation component, which is purely associated with the change in shape of the bed forms rather than the differential migration rates of various bed forms along a streambed profile. To achieve this goal, we first detrended the streambed profiles by removing the mean bed elevation and a slight downstream shallowing and then computed the instantaneous migration rate at each point of the streambed profile as:

$$V(x,t) = -\frac{\Delta\eta(x,t)/\Delta t}{\Delta\eta(x,t)/\Delta x} \tag{9.5}$$

where $\Delta\eta(x,t)/\Delta t$ denotes the rate of temporal change in elevation and $\Delta\eta(x,t)/\Delta x$ denotes the local slope, both computed via central differencing. In order to avoid singularities in the computed instantaneous migration rates, we neglected the data points that had the absolute value of the local slope less than 0.01, which comprised less than

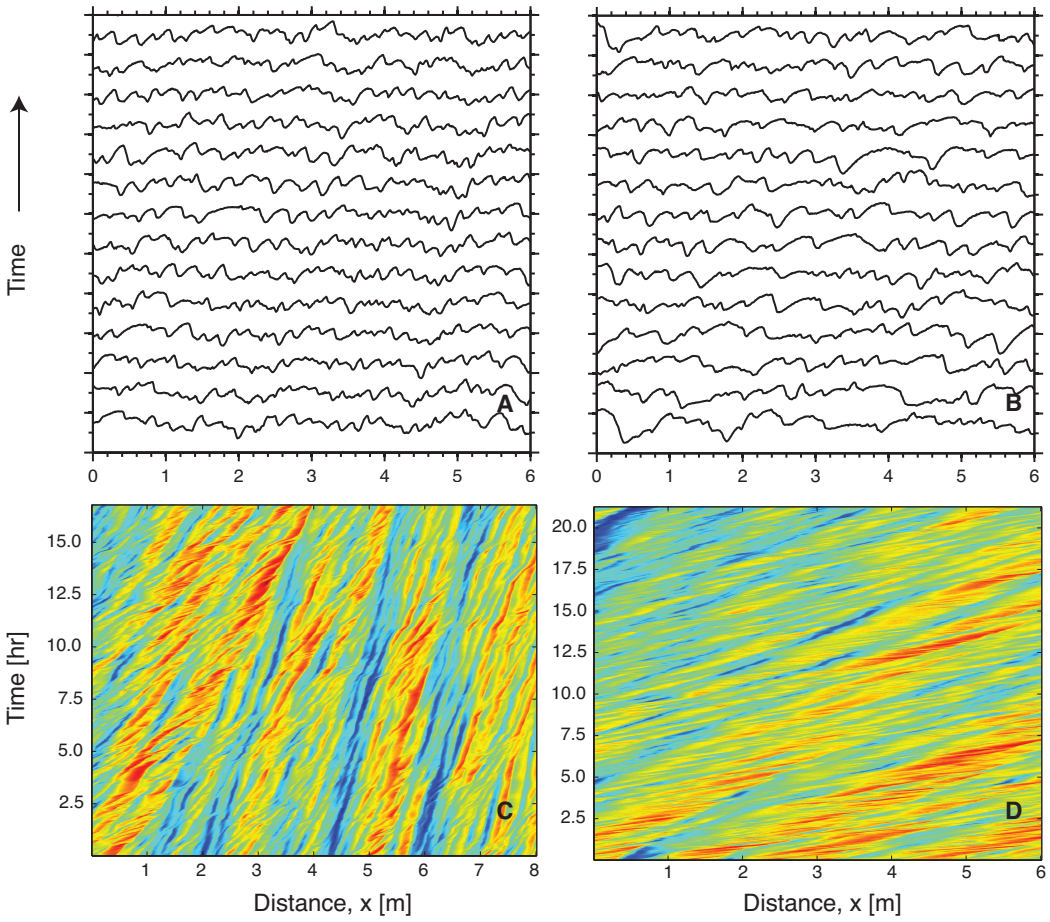

Figure 9.4: Sequential streambed profiles, shown every 1 hr and 1.5 hr for water discharge of (A) 40 lps and (B) 80 lps, respectively, with vertical offset to allow visualization. Space-time plot of sequential streambed profiles shown every 17 s and 45 s for water discharge of 40 lps (C) and 80 lps (D), respectively. Bed form crests and troughs are blue and red in color, respectively.

10% of the data set.

Once we gained access to the instantaneous migration rates at each point in space and time of the bed form evolution, we extracted the bed forms along all the time snap shots of the streambed profile. We used a simple peak detection algorithm to identify the crests and troughs of each of the bed forms. The bed elevation at each point along the streambed profile was compared to the bed elevation of its immediate neighbors (upstream and downstream). A point along the streambed profile was chosen to be a crest (or trough) of a bed form if the bed elevation at that point was greater (or lower) than the bed elevation of its immediate neighbors by a fixed value. This fixed value was arbitrarily chosen to be one-fourth of the standard deviation of the bed elevations along a streambed profile to avoid noisy observations from contaminating our extraction data. Figure 9.5 shows a sample streambed profile along with the extracted bed form crests and troughs for the experimental run with a water discharge of 80 lps. The length of a bed form, l_{bf}, was defined as the longitudinal stream wise distance between two consecutive troughs of a bed form and the bed form height, h_{bf}, was defined as the difference between bed elevations of consecutive crests and troughs of a bed form.

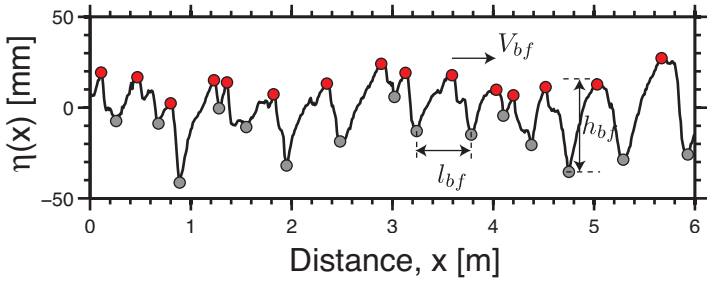

Figure 9.5: A sample detrended, mean-removed streambed profile during the experimental run with a water discharge of 80 lps. The extracted bed form crests and troughs are indicated by red and grey circles, respectively. Also defined in the above plot are the length and height of a bed form.

We then defined the time scale of migration, T_m, as the ratio of the average bed form length to the space-time average of the instantaneous migration rate, i.e.,

$$T_m = \frac{\langle l_{bf} \rangle}{\langle \langle V(x,t) \rangle_t \rangle_x} \tag{9.6}$$

where $\langle . \rangle$ denotes the average of the quantity within the angled brackets. The time

scale of migration quantifies the average time it takes for a bed form to translate by a distance equal to the average bed form length. We then computed the bed form-averaged migration rate, $V_{bf}(x,t)$, by averaging the instantaneous migration rate, $V(x,t)$ (estimated using equation (9.5)), over the bed form length at each time instant and then performing a time averaging over a non-overlapping time window equal to the migration time scale, T_m, i.e., $V_{bf}(x,t) = \langle\langle V(x,t)\rangle_{l_{bf}}\rangle_{T_m}$. This exercise yielded the bed form averaged migration rate at each point in space and time.

The instantaneous deformation rate was subsequently estimated using a discrete form of equation (9.1) given by:

$$\Pi(x,t) = \frac{\Delta\eta(x,t)}{\Delta t} + V_{bf}(x,t)\frac{\Delta\eta(x,t)}{\Delta x} \tag{9.7}$$

This quantity $\Pi(x,t)$ denotes the instantaneous deformation rate corresponding to the spatial and temporal resolution at which the above equation is applied, i.e., the spatial and temporal resolution at which experimental data were collected. In order to quantify the amount of deformation that a bed form experienced in the time that the bed form translated by one wavelength $\langle l_{bf}\rangle$, we computed the net deformation rate at each point along a bed form by averaging the instantaneous deformation rate over the migration time scale, T_m, i.e., $\Pi_{bf} = \langle\Pi(x,t)\rangle_{T_m}$. In essence, if we were to treat a single bed form as an object, the bed form averaged migration rate V_{bf} describes the rate at which this object translates (which is a constant) and the net deformation rate Π_{bf} describes the rate at which each point on this object changes its shape in the time this object translated by its own length. Figure 9.6 shows the empirical distributions of the estimated deformation rates Π_{bf} for the experimental runs with a water discharge of 40 lps (black circles) and 80 lps (grey diamonds). The estimated means of the deformation rates for both flows were approximately zero, confirming that the bed was at dynamic steady-state (see Table 9.1 for a summary of the estimated statistics of surface kinematics). The probability density functions (pdfs) of the estimated deformation rates exhibit exponential tails for both the flows (see Figure 9.6).

In order to compare deformation and migration of bed forms, we computed a deformation time scale, which was defined as:

$$T_d = \frac{\langle h_{bf}\rangle}{\langle\langle|\Pi(x,t)|\rangle_x\rangle_t} \tag{9.8}$$

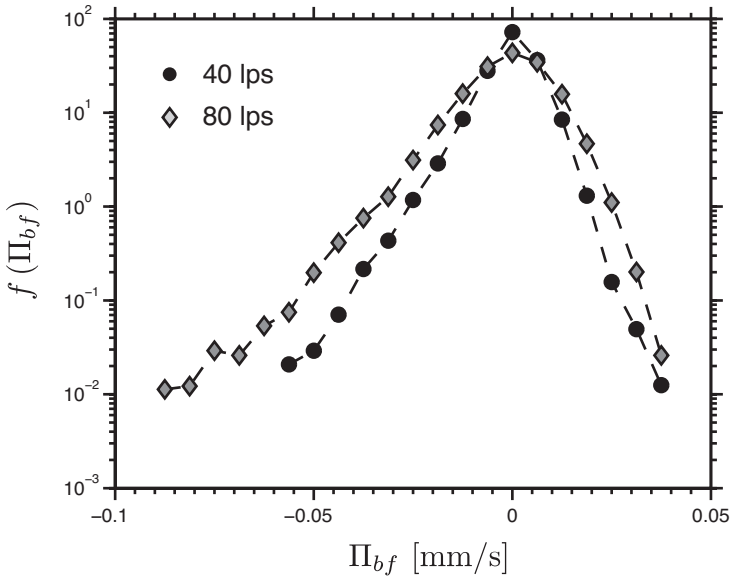

Figure 9.6: Relative frequency of the computed deformation rates Π_{bf} in semi-log scale for water discharge of 40 lps (black circles) and 80 lps (grey diamonds). Notice the linear nature of the tails in this semi-log plot, which correspond to an exponential decay.

where T_d is the deformation time scale, and h_{bf} is the bed form height. This time scale quantifies the average time it takes for a bed form to lose complete memory of its shape. If the deformation time scale and the migration time scale are comparable then it implies that the bed form loses the memory of its shape when it translates by one bed form wavelength. Table 9.1 summarizes the computed migration and deformation time scales for both the experimental runs. In the next section, we construct the stratigraphic deposits for both the experimental runs and extract the statistics of the geometrical structure of the stratigraphic boundaries.

9.4 Geometrical structure of the preserved stratigraphy

The preserved stratigraphic column can be built from the elevation time series (see Figure 9.7) and in this section we construct and analyze the geometrical structure of the bounding surfaces of the preserved cross-sets. We constructed the stratigraphic columns at each point along the streambed profile using the data of elevation time series collected during the experimental runs (see [263] and [278] for examples where this

Quantity	Water discharge, 40 lps	Water Discharge, 80 lps
V_{bf} [mm/s]	0.092 ± 0.013	0.26 ± 0.01
Π_{bf} [mm/s]	$1.67 \times 10^{-4} \pm 0.019$	$1.2 \times 10^{-3} \pm 0.011$
$\lvert\Pi_{bf}\rvert$ [mm/s]	0.005 ± 0.0014	0.008 ± 0.0072
l_{bf} [cm]	22.7 ± 8.9	32.5 ± 15.0
h_{bf} [mm]	19.7 ± 10.0	22.7 ± 13.0
T_m [mins]	41.2	20.8
T_d [mins]	65.7	47.3

Table 9.1: Estimated statistics of the surface kinematics of bed form evolution. The temporal resolution of the data is approximately 17 s and 45 s for 40 lps and 80 lps flows, respectively.

method was applied). This exercise provided us with the 2-D structure of the preserved stratigraphy. Figure 9.8 shows the 2-D structure of the preserved stratigraphy for a 40 cm longitudinal section for the experiment with water discharge of 40 lps. Two distinct features were identified in the 2-D structure of the preserved stratigraphy, namely, the constructed boundaries (solid lines in Figure 9.8) and the sampled topography (dashed lines in Figure 9.8). Constructed boundaries are the surfaces that are preserved in the stratigraphic record, which never existed in the topographic evolution. On the other hand, sampled topography here refers to the record of the migrating lee faces in the preserved stratigraphy. Our first goal in this section is to delineate these two features in the stratigraphic record.

Sampled topographic surfaces in the preserved stratigraphy have relatively steep slopes (corresponding to the angle of repose) and a near-zero curvature as they represent the migrating lee faces of the bed forms. Also of importance is the time of preservation of these surfaces. A single bed form migrating downstream results in the formation of the sampled topographic surfaces in the stratigraphic record within the migration time scale T_m as they represent the record of the migrating lee faces of the bed form. The surfaces that correspond to the sampled topography are sandwiched between the constructed boundaries in the preserved stratigraphy. Thus, on an average, the constructed boundaries are created over a time scale that corresponds to the time scale of migration. We used the time of preservation to delineate the constructed boundaries from the sampled topography in the 2-D stratigraphy. From the constructed 2-D stratigraphy (for example, see Figure 9.9(A)), we kept the surfaces that were T_m

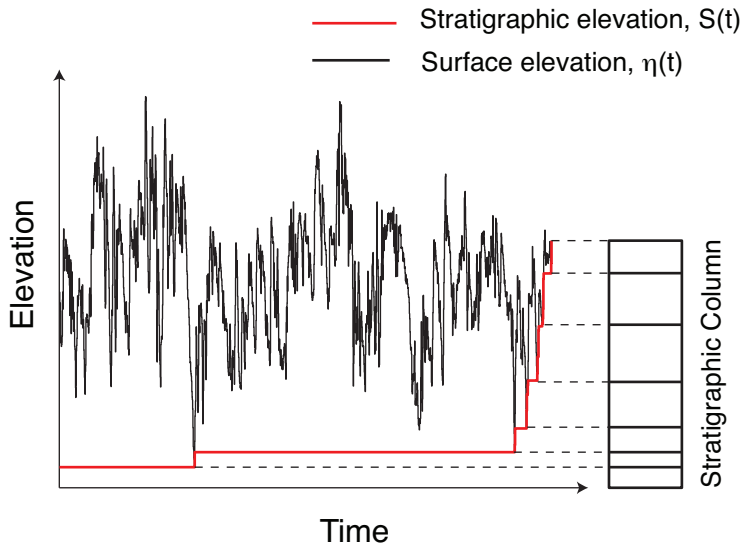

Figure 9.7: A schematic showing the building of a stratigraphic column ($S(t)$, red line) from the elevation time series ($\eta(t)$, black line). Stratigraphic deposits are depositional bodies bound between two erosional events.

mins apart in their preservation and eliminated the rest. As seen from visual inspection in Figure 9.9(B), this exercise yielded the constructed boundaries and removed almost all of the preserved lee faces of the migrating bed forms.

Further, notice that the constructed boundaries of the preserved stratigraphy are noisy with millimeter scale fluctuations (Figure 9.9(B)), which are seldom found in field observations. In order to remove this noise, we need to perform some smoothing operation on the constructed stratigraphy. The most common way of performing this smoothing is to use a moving average filter. However, this operator would have the undesirable effect of not preserving (instead it will result in dilation) the local features in the stratigraphic boundaries as equal weight is given to both the point of interest and the points around it. We used a Gaussian window filter, $G(L)$, in this study to remove the noise in the constructed stratigraphic boundaries as this filter gives maximum weight to the point of interest and progressively lower weights to the surrounding points. Since the average length of the preserved cross-sets was documented to be half of the mean bed form length [268, 267], we chose the length scale of our filtering to be a quarter of the mean bed form lengths, i.e., $L = \langle l_{bf} \rangle / 4$ (which will correspond to half the average

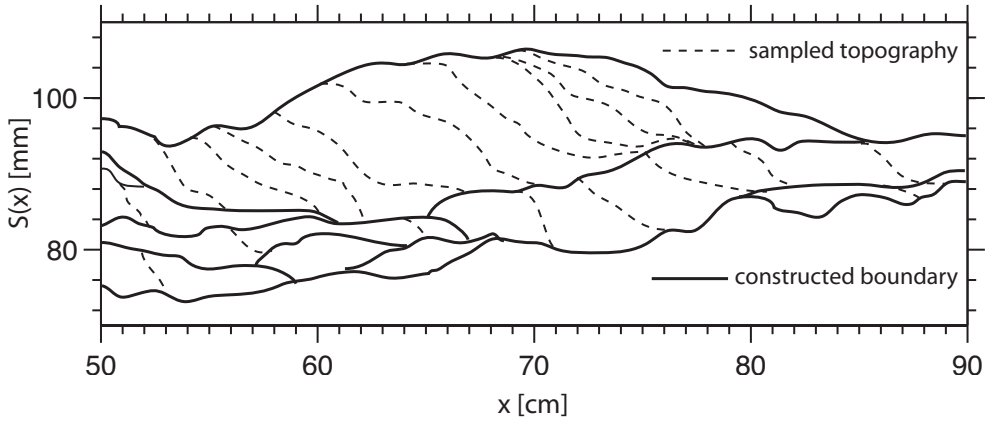

Figure 9.8: Constructed preserved stratigraphy for a 40 cm longitudinal section from the 40 lps experimental run. Two distinct features can be observed in the preserved stratigraphy, namely, the constructed boundaries (solid lines) and the sampled topography (dashed lines). Constructed boundaries are surfaces that are preserved, which are not present during the topographic evolution, whereas the sampled topography corresponds to the record of migrating lee faces of the bed forms.

length of the cross-sets). Further, we can take advantage of the well-known property of the convolution product,

$$\frac{\partial\,(S \star G)}{\partial x} = G \star \frac{\partial S}{\partial x} = \frac{\partial G}{\partial x} \star S \tag{9.9}$$

which implies that smoothing the stratigraphic boundary S with a kernel G and then taking the derivative (left most term) is equivalent to taking derivatives of the stratigraphic boundary and smoothing these derivatives with the kernel G (middle term) or equivalent to smoothing the stratigraphic boundary directly with the derivative of the kernel G (right most term), in computing the slope and curvature of bounding surfaces of the cross-sets. Since the derivatives of Gaussian filter are proper wavelets, we can use wavelet filtering techniques to compute the slope and curvature of the stratigraphic boundaries at the given scale [e.g., 9].

In this study, we delineated the constructed boundaries from the preserved stratigraphy corresponding to the experimental bed form evolution and smoothed them with a Gaussian window filter. We then computed the first and second derivatives of the smoothed data to get the local slope and curvature of these surfaces, respectively (first term of equation (9.9)). Figure 9.10 shows the empirical densities (gray bars) of the

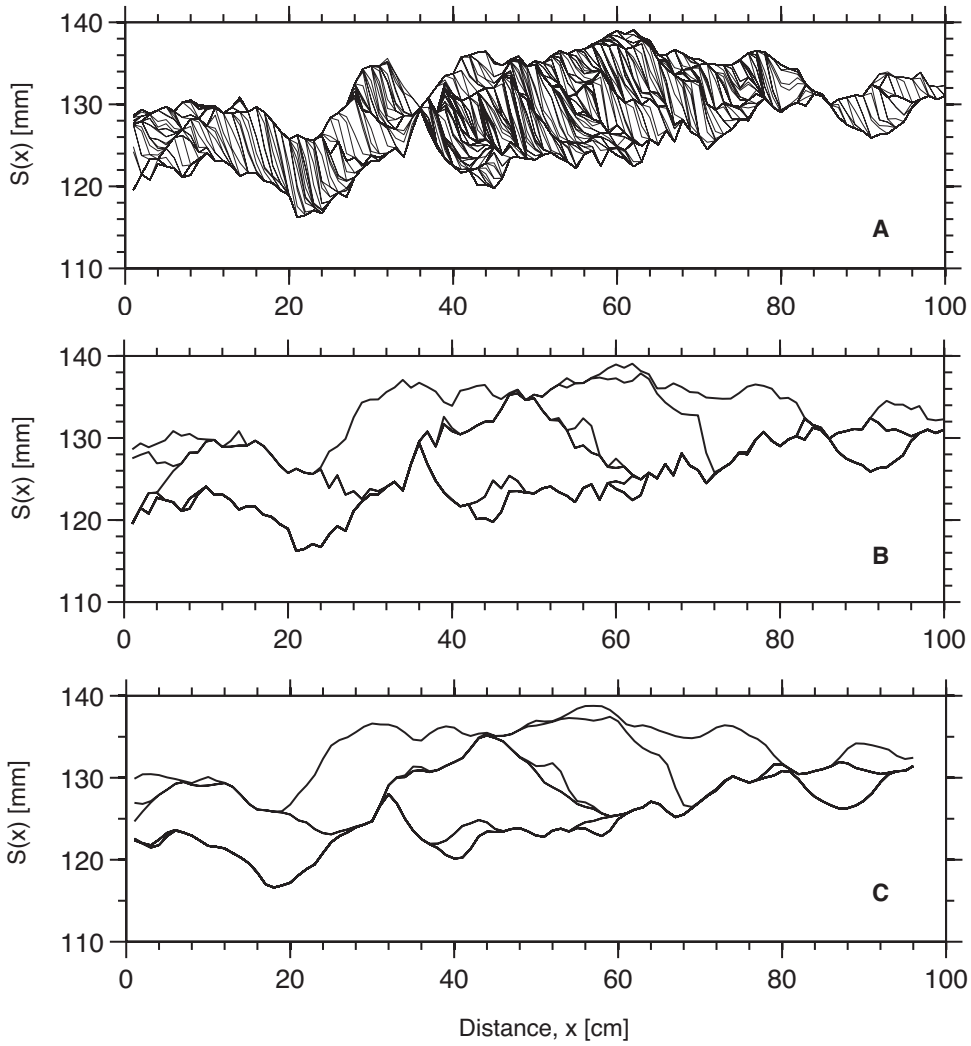

Figure 9.9: (A) Constructed 2-D structure of preserved stratigraphy for a one meter section of the longitudinal transect $B - B'$ (see Figure 9.3) for the experimental run with a water discharge of 40 lps. (B) The constructed boundaries, delineated using the time separation between the preserved surfaces corresponding to the average time of migration of the bed forms, in the 2-D structure of the preserved stratigraphy. (C) Constructed boundaries smoothed using a local Gaussian filter of length equal to a quarter of the mean bed form length. Notice that the smoothing operation removes the millimeter scale noise present in the constructed boundaries.

observed slopes (S_{st}) and curvatures (C_{st}) of the constructed boundaries in the preserved stratigraphy for both 40 lps and 80 lps. In the next section, we compare the observed statistics of the geometrical structure of the stratigraphic boundaries with the theoretical predictions presented in Section 9.1.

9.5 Results

As stated in Section 9.1, the local slope of the stratigraphic boundary is equal to the ratio of the vertical speed to the horizontal speed at a point on the bed form. Thus, the prediction of the local slope of the stratigraphic boundary at each point under no net deposition condition (like the experimental case) is:

$$S_{st} = \frac{\Pi_{bf}}{V_{bf}} \tag{9.10}$$

We computed the predicted slope of the bounding surfaces of the preserved cross-sets by evaluating the above equation using the experimental data collected for both flows. Further, the predicted local curvature of the bounding surfaces can be obtained by taking the first spatial derivative of equation (9.10):

$$C_{st} = \frac{\partial S_{st}}{\partial x} = \frac{1}{V_{bf}} \frac{\partial \Pi_{bf}}{\partial x} \tag{9.11}$$

For this purpose, we computed the spatial gradients of the net deformation rate (Π_{bf}) via central differencing. We then computed the predicted curvature of the stratigraphic boundaries using equation (9.11).

Figure 9.10 shows the empirical densities of the predicted slope and curvature of the bounding surfaces of the preserved cross-sets for both the 40 lps and 80 lps experimental runs. It is visually evident that equations (9.10) and (9.11) provide a very good approximation of the observed slope and curvature of the stratigraphic boundaries. We performed the Kolmogorov-Smirnov two-sample test to check if both the samples of the observed and predicted quantities of slope and curvature of the stratigraphic boundaries came from the same underlying continuous distribution [279]. The test statistic in the Kolmogorov-Smirnov test is the maximum of the absolute value of the distance between the two sample cumulative distribution functions (cdfs). The null hypothesis is that both the samples come from the same underlying continuous distribution and the null

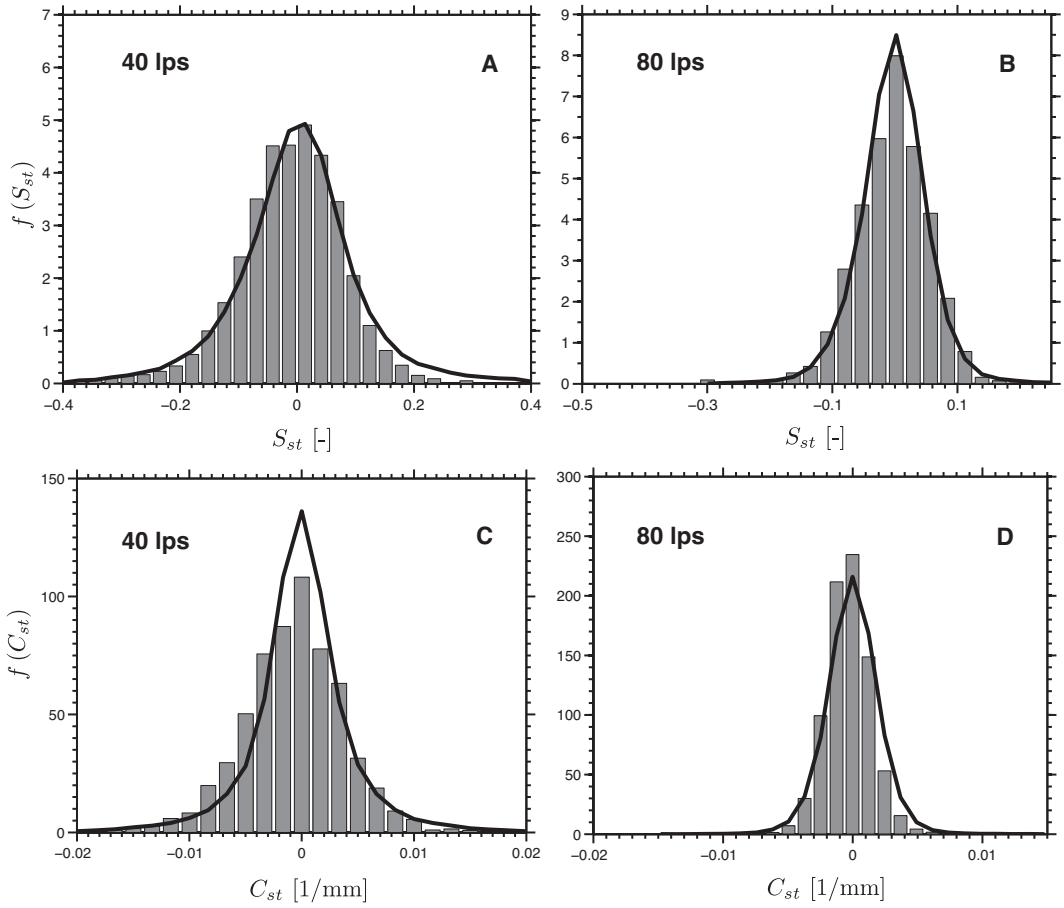

Figure 9.10: Plot showing the empirical (gray bars) and the theoretically predicted (solid line) densities of the local slopes (A, B) and curvatures (C, D) of the stratigraphic boundaries for both the 40 lps and 80 lps experimental runs. The observed slopes and curvatures were computed as the first and second derivatives of the smoothed stratigraphic boundaries, respectively. The predicted slopes and curvatures of the stratigraphic boundaries were computed using equations (9.10) and (9.11), respectively.

hypothesis is rejected if the maximum of the absolute value of the distance between the two sample cdfs (D_{CDF}) is greater than some threshold value (D_{α_1}). This threshold value, for large sample sizes, is given by:

$$D_{\alpha_1} = c(\alpha_1)\sqrt{\frac{n_1 + n_2}{n_1 \times n_2}} \tag{9.12}$$

where α_1 is the significance level, n_1 and n_2 are the sample sizes and $c(\alpha_1)$ is a coefficient, which comes from the Kolmogorov distribution tables. Figure 9.11 shows the absolute values of the distance between the observed and predicted cdfs of the slope and curvature of the stratigraphic boundaries along with the threshold of acceptance of the null hypothesis in the Kolmogorov-Smirnov test at a significance level of 5%. From Figures 9.11(A) and (B), we conclude that the observed and predicted slopes of the stratigraphic boundaries have the same underlying continuous distribution as $D_{CDF} < D_{\alpha_1}$ indicating, thus, that equation (9.10) provides a means of relating the characteristics of the surface kinematics of bed form evolution to the slope of the stratigraphic boundaries. Figures 9.11(C) and (D) indicate that the distance between the sample cdfs of the observed and predicted curvature of the stratigraphic boundaries exceeds the threshold value at a significance level of 5%, which prompts us to reject the null hypothesis. However, we note that the values of D_{CDF} exceed the threshold D_{α_1} at curvatures that are very close to zero. We believe that this is a direct effect of the resolution of the data collected. The vertical and the stream wise resolution of the data collected were 1 mm and 1 cm, respectively, thus, indicating that the local curvature values very close to zero are not resolved very well in this dataset. Except at the values of local curvature very close to zero, the distance between the two sample cdfs of the observed and predicted curvatures of the stratigraphic boundaries is well within the threshold value of D_{α_1}, indicating that the predicted curvature of the stratigraphic boundaries computed using equation (9.11) provides a good approximation of the observed pdf of the local slopes of the stratigraphic boundaries.

Further, we compared the statistics (mean and standard deviation) of the absolute values of the observed and predicted slope $|S_{st}|$ and curvature $|C_{st}|$ of the stratigraphic boundaries. Figure 9.12 documents that both and the mean and standard deviation of the geometrical properties of the startigraphic boundaries are well described by equations (9.10) and (9.11). All in all, we conclude that deformation of bed forms plays

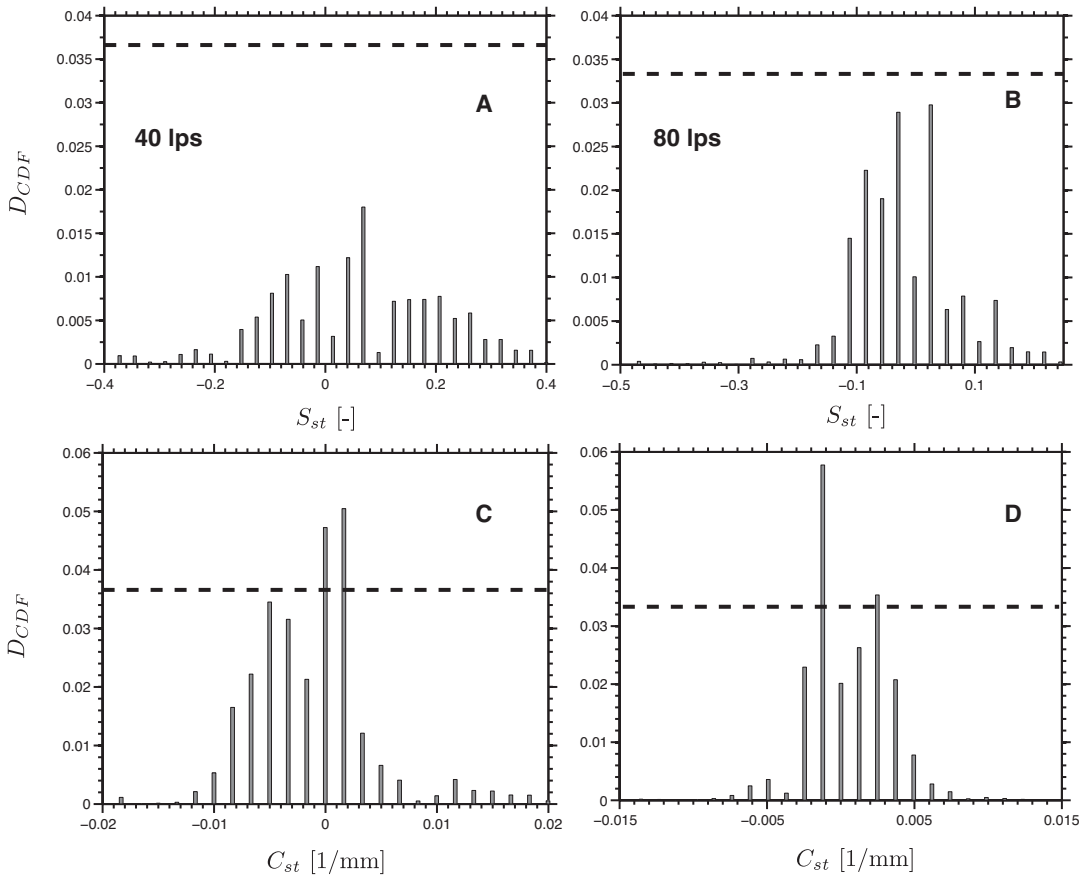

Figure 9.11: The absolute value of the distance between the two sample cdfs of slopes ((A) and (B)) and curvatures ((C) and (D)) of the stratigraphic boundaries along with the threshold value (dashed line) of acceptance for the Kolmogorov-Smirnov test at a significance level of 5%.

an important role in setting the geometrical structure of the stratigraphic boundaries with the ratio of deformation rate and the migration rate setting the slope of the stratigraphic boundary and the ratio of the spatial gradient of the deformation rate and the migration rate setting the curvature of the stratigraphic boundary.

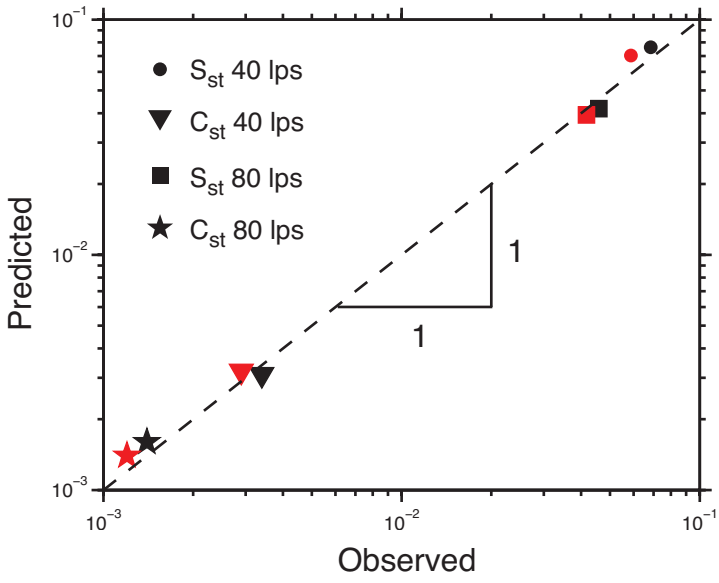

Figure 9.12: Plot showing the comparison of the mean (black markers) and standard deviation (red markers) of the absolute value of the observed and predicted slope and curvature of the stratigraphic boundaries for both 40 lps and 80 lps experimental runs.

9.6 Discussion

As was shown in the previous section, the surface kinematics of the bed form evolution can be statistically mapped into the geometrical structure of the bounding surfaces of the preserved cross-sets. The set thickness distribution $f(D_{st})$, along with the length, slope and curvature of the stratigraphic boundaries completely describe the geometrical structure of the preserved stratigraphy. Under zero net deposition, Paola and Borgman [13] derived an analytical relationship between the variability of the bed form heights h_{bf} and the distribution of set thickness D_{st}. They used a two-parameter Gamma

distribution given by,

$$f\left(h_{bf}\right) = \frac{h_{bf}^{\alpha-1} exp\left(-h_{bf}/\beta\right)}{\beta^{\alpha}\Gamma(\alpha)} \tag{9.13}$$

where α is the power-law parameter and β is the exponential parameter of the Gamma distribution, to describe the pdf of the bed form heights. (Note that the purpose of using the Gamma distribution was to capture the exponential tail of the pdf of the bed form heights). They analytically derived set thickness distribution for $D_{st} > 0$ to be:

$$f\left(D_{st}\right) = \frac{ae^{-aD_{st}}\left(e^{-aD_{st}} + aD_{st} - 1\right)}{\left(1 - e^{-aD_{st}}\right)^2} \tag{9.14}$$

and zero for $D_{st} \leq 0$. The parameter of the set thickness distribution a was related to the exponential parameter of the bed form heights as $a = 2/\beta$ [13]. Figure 9.13 shows that our experimental data is in very good agreement with the theory of Paola and Borgman [13]. The bed form heights were well described by a two-parameter Gamma distribution and equation (9.14) provides a very good description of the resulting set thickness distribution. Thus, this result states that the bed form heights together with the length of the bed forms act as the control on the set thickness distribution and the length of the cross-sets [e.g., 267].

Our results in the previous section state that the slope and curvature of the stratigraphic boundaries record the competition between the deformation and migration of the bed forms. We note that the mean and standard deviation of the deformation rate changes at a much slower rate with the flow when compared to the migration rate (see Table 9.1). Thus, the numerator in the right hand side (deformation rate and gradient of deformation rate) of equations (9.10) and (9.11) does not change at the same rate with the flow as the denominator (migration rate). This results in higher variability in slope and curvature of the stratigraphic boundaries at lower flows when compared to the higher flows (see Figure 9.10). This is also reflected in the higher values of the mean and standard deviation of the absolute values of the slope and curvature of the stratigraphic boundaries at low flow when compared to the higher flow (see Figure 9.12).

Further, gradual changes in the migration rate and the aggradation rate of the bed forms are also recorded in the geometrical structure of the stratigraphic boundaries (see equations (9.2) and (9.3)). We note that a large-scale curvature (corresponding to a scale much larger than the length scale of the bed forms) can be imposed on

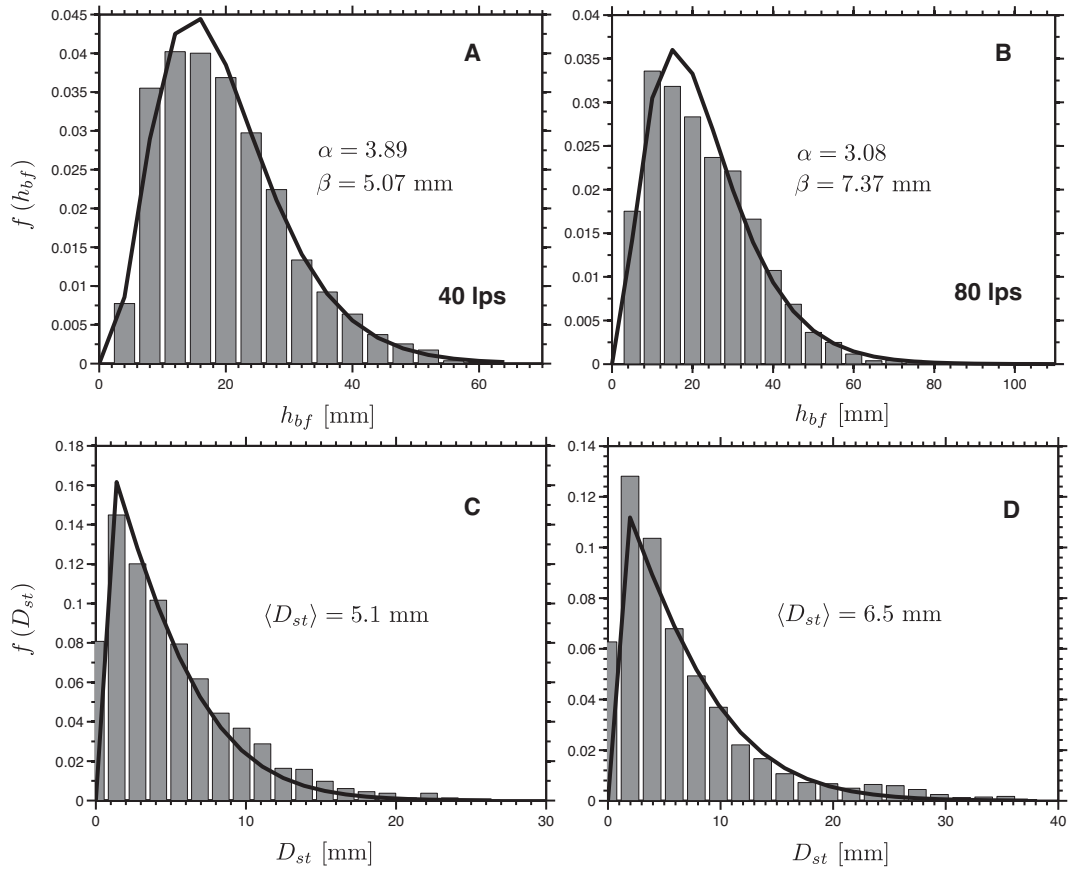

Figure 9.13: (Top panels) Plots showing the empirical densities (gray bars) of the extracted bed form heights along with the best fit two parameter Gamma distribution (solid line) for 40 lps and 80 lps experimental runs. (Bottom panels) Observed empirical densities (gray bars) of the set thicknesses computed from the constructed preserved stratigraphy for the experimental runs. Also shown is the predicted set thickness distribution (solid line) based on the variability of bed form heights computed using equation (9.14) with $a = 2/\beta$ [13].

the stratigraphic boundaries if there is a gradual change in the migration rate or the net aggradation rate in the system. According to equation (9.3), this effect should be recorded in the curvature of the stratigraphic boundaries and multi-scale analysis of curvature of the stratigraphic boundaries has the potential to delineate not only the effect of bed form deformation, but also the changes in migration speed and aggradation rate that might result from some climatic changes in the system. Quantitative relationships between preserved stratigraphy and surface kinematics together with the information of the environmental conditions that result in a given set of surface kinematics have the potential of unlocking the paleoenvironmental conditions from the vast amount of available stratigraphic data.

9.7 Conclusion

In this study, we used experimental data of bed form evolution collected from a Tilting Flume experiment conducted at St. Anthony Falls Laboratory, University of Minnesota to develop and validate quantitative relationships between the surface kinematics of bed form evolution and the geometrical structure of the bounding surfaces of the preserved cross-sets. The following conclusions were drawn from the present study.

1. The local slope of the stratigraphic boundaries S_{st} was shown to be equal to the ratio of the deformation rate of bed forms Π_{bf} and the migration rate of the bed forms V_{bf}, under no net deposition condition. The deformation rate quantifies the change in shape of the bed forms, while the migration rate quantifies the rate of translation of the bed forms.

2. We showed that the curvature of the stratigraphic boundaries C_{st}, defined as the first spatial derivative of the local slopes of the stratigraphic boundaries, was equal to the ratio of the spatial gradient of the deformation rate and the migration rate of the evolving bed forms.

3. We concluded that the deformation rate increases at a slower rate with flow when compared to the migration rate, thus, implying that under low flow conditions the slope and curvature of the stratigraphic boundaries exhibit higher variability when compared to the case of higher flows.

4. Further, the theoretical predictor of the curvature of the stratigraphic boundaries (equation (9.3)) suggests that a multi-scale analysis of the curvature of the stratigraphic boundaries has the potential to give us information not only about the deformation, but also about any gradual changes in the migration rate or aggradation rate in the system.

5. Finally, we showed that the experimental data of set thickness distribution was consistent with the theory of Paola and Borgman [13], with the bed form heights being well described by a two-parameter Gamma distribution and the set thickness distribution was well approximated with the theoretical pdf of equation (9.14).

Chapter 10

Conclusions and Future Prospects

In this thesis research, sediment transport in diverse environments was studied from a unique point of view, placing special emphasis on the role of the spatial heterogeneity and temporal variability across a wide range of scales: from particle to hillslope to a river system. Sediment flux was treated as resulting from the movement of an ensemble of sediment particles, which alternate between states of rest and motion. It was shown that the existing physical models of sediment flux have inherent assumptions of the statistical nature of rest and motion of the sediment particles. In particular, they assume a thin-tailed distribution for the waiting times and the sediment travel distances, or in other words, the existence of a characteristic space and time scale of transport. When no characteristic space and/or time scale of transport exists in a system, due to, for example, a finite chance of large waiting times or sediment travel distances, then we move into the realm of non-local theories for sediment transport. This thesis research presents the first comprehensive treatment of the notion of non-local transport on the Earth's surface.

The non-local theories of sediment transport presented in this thesis account for the heavy-tailed nature of the waiting times and/or the sediment travel distances in a system, thus, shedding new light on the role of extremes in geomorphic systems. Specifically, the non-local transport theories are concise, continuum models that have the ability to capture the role of the extremes in geomorphic systems. The heavy-tailed nature of the resulting states of motion and rest of sediment particles can be the effect of

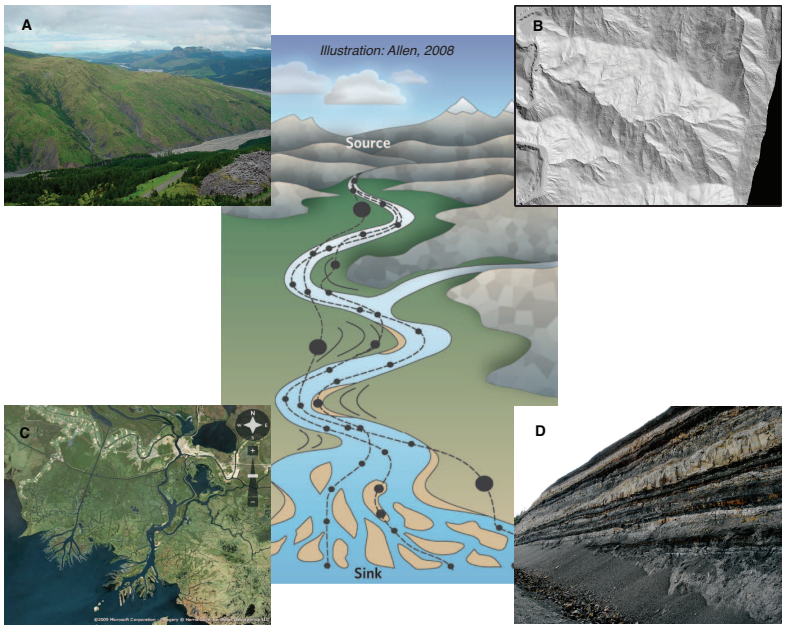

Figure 10.1: An illustration of the Earth's sediment routing system. The transport processes studied here are highlighted with pictures, which range from sediment transport on hillslopes (A), to catchment scale dynamics (B), to deposition of sediment in deltaic systems (C) and their implications for the preserved stratigraphic record (D) (Photographs courtesy: CSMDS and NCED).

the nature of extremes of the driving forces of sediment transport (e.g., extreme fluctuations in runoff and streamflow) or they could be a manifestation of the heterogeneity of the system under consideration (e.g., multiple reasons for sudden sediment production on a hillslope). Further, this thesis research raises important questions and highlights the practical implications in the application of the local, nonlinear sediment transport models. The main messages of this thesis research are as follows:

1. The non-local, linear sediment transport model and the local, nonlinear sediment transport model for hillslopes present themselves as competing models that could give rise to the same sediment flux and steady-state properties of landscapes, but the underlying assumptions behind these models have important practical implications. The application of the local, nonlinear sediment transport model can result in scale-dependence of model parameters and also does not explain the observed variability in the sediment flux in natural environments.

2. The heavy-tailed nature of the states of motion and rest of the sediment particles, which is a manifestation of the extremes, results in the observed steady-state properties of landscapes, thus, shedding new light in interpreting the link between geomorphic process and form.

3. In deltaic systems, the heavy-tailed nature of the space-time dynamics of surface evolution is preferentially preserved in the stratigraphic record. Specifically, the extremes of the erosional and depositional events cancel themselves out in the stratigraphic record, resulting in thin-tailed statistics of the 1D stratigraphy. However, the heavy-tailed nature of the waiting times manifests itself as the Sadler effect (i.e., the apparent dependence of deposition rate on time), which can give us insight into the avulsion dynamics of the deltaic system.

This thesis research also raises many important questions and opens new directions for future research. These include:

1. Extensive and thorough experimental and field studies that establish the particle scale dynamics that form the basis for the non-local sediment transport models are rare at present [43] and are essential in relating the physics of the processes involved to the model parameters of the non-local transport models.

2. Nonlinear and non-local sediment transport hypotheses are seen as mutually exclusive approaches at present. However it is understood that if we consider only nonlinearity and neglect non-locality in the sediment flux modeling then we overestimate the strength of nonlinearity and similarly if we neglect nonlinearity and only consider non-locality then we overestimate the degree of non-locality in the system, thus, highlighting the need for a combined nonlinear, non-local approach to sediment flux modeling. Future work should involve a combined nonlinear, non-local approach to describing sediment transport. Preliminary efforts in this direction [e.g., 280] seem fruitful.

3. The statistical approach of characterizing the surface dynamics of deltaic systems has the potential to explore many other questions pertaining to surface-to-subsurface characterization of these systems, for example, how does the deltaic system self-organize into a dynamic structure capable of maintaining the subaerial

delta over different time scales? It is envisioned that the physical controls on the spatial distribution of depositional and erosional events across the system can provide information on how the geometrical parameters of the deltaic system (e.g., channel depth, width, etc.) control the dynamics of the evolving and reorganizing deltaic surface, and this is a topic of future study.

4. Moving sediment particles carry with them the attached pollutants and biological agents. Several stream processes, such as, nutrient or dissolved oxygen uptakes, are largely influenced by the tremendous heterogeneity of the sediment-water interface, which can introduce non-local effects manifested in very long inactivity times or very fast sediment velocities. Extension of the ideas presented herein to biological or non-reactive chemical transport on the Earth's surface, such as, modeling dissolved oxygen concentration and nutrient uptake is an area of future study.

References

[1] D.A. Benson. *The Fractional Advection-Dispersion Equation: Development and Application, PhD thesis*. University of Nevada, Reno, 1998.

[2] E. Foufoula-Georgiou and P. Passalacqua. Nonlocal transport theories in geomorphology: mathematical modeling of broad scales of motion. In *Treatise on Geomorphology (edited by Shroder, J., Jr., and Baas, A.)*, page vol. 2. Academic Press, San Diego, CA, 2012.

[3] R. Schumer, M. M. Meerschaert, and B. Baeumer. Fractional advection-dispersion equations for modeling transport at the earth surface. *J. Geophys. Res.*, 114:F00A07, 2009. doi:10.1029/2008JF001246.

[4] I. M. Sokolov and J. Klafter. From diffusion to anomalous diffusion: A century after einstein's brownian motion. *Chaos*, 15:026103, 2005.

[5] J.J. Roering, J. T. Perron, and J.W. Kirchner. Functional relationships between denudation and hillslope form and relief. *Earth and Planetary Science Letters*, 264:245–258, 2007.

[6] V. R. Voller and C. Paola. Can anomalous diffusion describe depositional fluvial profiles? *J. Geophys. Res.*, 115:F00A13, 2010. doi:10.1029/2009JF001278.

[7] J.J. Roering, J.W. Kirchner, and W.E. Dietrich. Evidence for nonlinear, diffusive sediment transport on hillslopes and implications for landscape morphology. *Water Resour. Res.*, 35:853–870, 1999.

[8] J. A. McKean, W. E. Dietrich, R. C. Finkel, J. R. Southon, and M. W. Caffee. Quantification of soil production and downslope creep rates from cosmogenic 10be

accumulations on a hillslope profile. *Geology*, 21:343–346, 1993. doi:10.1130/0091-7613(1993)021¡0343:QOSPAD¿2.3.CO;2.

[9] B. Lashermes, E. Foufoula-Georgiou, and W. E. Dietrich. Channel network extraction from high resolution topography using wavelets. *Geophys. Res. Lett.*, 34:L23S04, doi:10.1029/2007GL031140, 2007.

[10] R. A. DiBiase, K. X. Whipple, A. M. Heimsath, and W. B. Ouimet. Landscape form and millennial erosion rates in the san gabriel mountains, ca. *Earth and Planetary Science Lett.*, 289:134–144, 2010.

[11] E. Foufoula-Georgiou, V. Ganti, and W. E. Dietrich. A non-local theory for sediment transport on hillslopes. *J. Geophys. Res.*, 115:F00A16, 2010. doi:10.1029/2009JF001280.

[12] P. R. Wilcock and J. B. Southard. Bed-load transport of a mixed-size sediment: Fractional transport rates, bed forms, and the development of a coarse bed-surface layer. *Water Resour. Res.*, 25(7):1629–1641, 1989.

[13] C. Paola and L. Borgman. Reconstructing random topography from preserved stratification. *Sedimentology*, 38:553–565, 1991.

[14] F. M. Exner. Zur physik der dunen. *Akad. Wiss. Wien Math. Naturwiss. Klasse*, 129(2a):929–952, 1920.

[15] F. M. Exner. Uber die wechselwirkung zwischen wasser und geschiebe in flussen. *Akad. Wiss. Wien Math. Naturwiss. Klasse*, 134(2a):165–204, 1925.

[16] C. Paola and V. R. Voller. A generalized exner equation for sediment mass balance. *J. Geophys. Res.*, 110:F04014, 2005. doi:10.1029/2004JF000274.

[17] W.E. Dietrich, D. Bellugi, A.M. Heimsath, J.J. Roering, L. Sklar, and J.D. Stock. Geomorphic transport laws for predicting landscape form and dynamics. In *Prediction in Geomorphology, Geophysical Monograph Series (edited by P. Wilcock and R. Iverson)*, pages 103–123. AGU, Washington D.C., 2003.

[18] H. Schey. *Div Grad Curl and All That: An Informal Text on Vector Calculus.* 2nd ed., W. W. Norton, New York, 1992.

[19] E. Foufoula-Georgiou, V. Ganti, and P. Passalacqua. Geomorphic transport laws: Non-local flux with classical mass balance. *University of Minnesota Supercomputing Institute Research Report*, UMSI 2008/27, May 2008.

[20] W. Feller. *Introduction to Probability Theory and Its Applications*. Wiley, New York, 1971.

[21] M. M. Meerschaert, D. A. Benson, and B. Baeumer. Multidimensional advection and fractional dispersion. *Phys. Rev. E*, 35:L17403, 1999. doi:10.1029/2008GL034899.

[22] J. H. Cushman and T. R. Ginn. Fractional advection-dispersion equation: a classical mass balance with convolution-fickian flux. *Water Resour. Res.*, 36:3763–3766, 2000.

[23] R. Metzler and A. Compte. Generalized diffusion-advection schemes and dispersive sedimentation: A fractional approach. *J. Phys. Chem. B*, 104(16):3858–3865, 2000. doi:10.1021/jp993698f.

[24] J.-P. Bouchaud and A. Georges. Anomalous diffusion in disordered media: Statistical mechanisms, models and physical applications. *Phys. Rep.*, 195(4–5):127–293, 1990. doi:10.1016/0370-1573(90)90099-N.

[25] M. F. Shlesinger, G. M. Zaslavsky, and U. Frisch. *Lévy Flights and Related Topics in Physics, Lect. Notes in Phys.* vol. 450, Springer, Berlin, 1995. doi:10.1007/3-540-59222-9.

[26] A. Pekalski and K. Sznajid-Weron. *Anomalous Diffusion: From Basics to Applications, Lect. Notes in Phys.* vol. 519, Springer, Berlin, 1999. doi:10.1007/BFb0106828.

[27] B. Berkowitz, J. Klafter, R. Metzler, and H. Scher. Physical pictures of transport in heterogeneous media: Advection-dispersion, random-walk, and fractional derivative formulations. *Water Resour. Res.*, 38(10):1191, 2002. doi:10.1029/2001WR001030.

[28] E. J. Gabet, D. J. Reichman, and E. W. Seabloom. The effects of bioturbation on soil processes and sediment transport. *Annu. Rev. Earth Planet. Sci.*, 31:249–273, 2003. doi:10.1146/annurev.earth.31.100901.141314.

[29] A. M. Heimsath, W. E. Dietrich, K. Nishiizumi, and R. C. Finkel. Cosmogenics nuclides, topography, and spatial variation of soil depth. *Geomorphology*, 27:151–172, 1999. doi:10.1016/S0169-555X(98)00095-6.

[30] A. M. Heimsath, W. E. Dietrich, K. Nishiizumi, and R. C. Finkel. Stochastic processes of soil production and transport: erosion rates, topographic variation and cosmogenic nuclides in oregon coast range. *Ear. Surf. Proc. and Landforms*, 26(5):531–552, 2001.

[31] G. Parker, C. Paola, and S. Leclair. Probabilistic exner sediment continuity equation for mixtures with no active layer. *J. Hydrual. Engg.*, 126(11):818–826, 2000.

[32] W. E. H. Culling. Analytical theory of erosion. *J. Geol.*, 68:336–344, 1960.

[33] W. E. H. Culling. Soil creep and the development of hillside slopes. *J. Geol.*, 71:127–161, 1963.

[34] W. E. H. Culling. Theory of erosion on soil-covered slopes. *J. Geol.*, 73:230–254, 1965.

[35] D. J. Andrews and R. C. Bucknam. Fitting degradation of shoreline scarps by a nonlinear diffusion model. *J. Geophys. Res.*, 92 (12):857–867, 1987.

[36] J. T. Hack and J. C. Goodlett. Geomorphology and forest ecology of a mountain region in the central appalachians. *U. S. Geol. Surv. Prof. Pap.*, 347:66 pp., 1960.

[37] W. Sayre and D. Hubbell. Transport and dispersion of labeled bed material, north loup river, nebraska. *U.S. Geological Survey Professional Paper*, 433-C:48 pp., 1965.

[38] T. G. Drake, R. L. Shreve, W. E. Dietrich, P. J. Whiting, and L. B. Leopold. Bedload transport of fine gravel observed by motion-picture photography. *J. Flu. Mech.*, 192:193–217, 1988.

[39] M. A. Hassan and M. Church. Distance of movement of coarse particles in gravel bed streams. *Water Resour. Res.*, 27(4):503–511, 1991.

[40] R. I. Ferguson and S. J. Wathen. Tracer-pebble movement along a concave river profile: Virtual velocity in relation to grain size and shear stress. *Water Resour. Res.*, 34:2031–2038, 1998.

[41] V. Nikora, H. Habersack, T. Huber, and I. McEwan. On bed particle diffusion in gravel bed flows under weak bed load transport. *Water Resour. Res.*, 38(6):1081, 2002.

[42] V. Ganti, M. M. Meerschaert, E. Foufoula-Georgiou, E. Viparelli, and G. Parker. Normal and anomalous diffusion of gravel tracer particles in rivers. *J. Geophys. Res.*, 115:F00A12, 2010. doi:10.1029/2008JF001222.

[43] R. L. Martin, D. J. Jerolmack, and R. Schumer. The physical basis for anomalous diffusion in bedload transport. *J. Geophys. Res.*, 117:F01018, 2012. doi:10.1029/2011JF002075.

[44] D. J. Furbish, P. K. Haff, J. C. Roseberry, and M. W. Schmeeckle. A probabilistic description of the bed load sediment flux: 1. theory. *J. Geophys. Res.*, under review, 2012.

[45] D. J. Furbish, J. C. Roseberry, and M. W. Schmeeckle. A probabilistic description of the bed load sediment flux: 3. the particle velocity distribution and the diffusive flux. *J. Geophys. Res.*, under review, 2012.

[46] D. J. Furbish, A. E. Ball, and M. W. Schmeeckle. A probabilistic description of the bed load sediment flux: 4. fickian diffusion at low transport rates. *J. Geophys. Res.*, under review, 2012.

[47] J. C. Roseberry, M. W. Schmeeckle, and D. J. Furbish. A probabilistic description of the bed load sediment flux: 3. particle activity and motions. *J. Geophys. Res.*, under review, 2012.

[48] I. G. Lisle, C. W. Rose, W. L. Hogarth, P. B. Hairsine, G. C. Sander, and J. Y.

Parkange. Stochastic sedimenttransport in soil erosion. *J. Hydrol.*, 204:217–230, 1998.

[49] H. A. Einstein. Formulas for the transportation of bed load. *Transactions*, ASCE Paper No. 2140, 1942.

[50] D. N. Bradley, G. E. Tucker, and D. A. Benson. Fractional dispersion in a sand bed river. *J. Geophys. Res.*, 115:F00A09, 2010. doi:10.1029/2009JF001268.

[51] A. Singh, K. Fienberg, D. J. Jerolmack, J. Marr, and E. Foufoula-Georgiou. Experimental evidence for statistical scaling and intermittency in sediment transport rates. *J. Geophys. Res.*, 114:F01025, 2009. doi:10.1029/2007JF000963.

[52] A. Singh, S. Lanzoni, and E. Foufoula-Georgiou. Nonlinearity and complexity in gravel bed dynamics. In *Stochastic Environmental Research and Risk Assessment*, pages 967–975. 23(7), 2007.

[53] A. Singh, F. Porté-Agel, and E. Foufoula-Georgiou. On the influence of gravel bed dynamics on velocity power spectra. *Water Resour. Res.*, 46:W04509, 2010. doi:10.1029/2009WR008190.

[54] C. Paola. Quantitative models of sedimentary basin filling. *Sedimentology*, 47:121–178, 2000.

[55] B. Sheets, T. A. Hickson, and C. Paola. Assembling the stratigraphic record: depositional patterns and time-scales in an experimental alluvial basin. *Basin Research*, 14:287–301, 2002.

[56] M. R. Leeder. A quantitative stratigraphic model for alluvium, with special reference to channel deposit density and interconnectedness. In *Fluvial Sedimentology, Candadian Society of Petroleum Geologist Memoir 5 (edited by A. D. Miall)*, pages 587–596. Allen and Unwin, Winchester, Mass., 1985.

[57] V. Sapozhnikov and E. Foufoula-Georgiou. Self-affinity in braided rivers. *Water Resour. Res.*, 32:1429–1439, 1996.

[58] V. B. Sapozhnikov and E. Foufoula-Georgiou. Experimental evidence of dynamic scaling and indications of self-organized criticality in braided rivers. *Water Resour. Res.*, 33:1983–1991, 1997.

[59] V. B. Sapozhnikov and E. Foufoula-Georgiou. Horizontal and vertical self-organization of braided rivers toward a critical state. *Water Resour. Res.*, 35 (3):843–851, 1999.

[60] E. Foufoula-Georgiou and V. B. Sapozhnikov. Anisotropic scaling in braided rivers: An integrated theoretical framework and results from application to an experimental river. *Water Resour. Res.*, 34(4):863–867, 1998.

[61] J. M. Martin. *Quantitative sequence stratigraphy, PhD thesis*. Univ. of Minnesota, Minneapolis, 2007.

[62] N. Strong and C. Paola. Valleys that never were: time surfaces versus stratigraphic surfaces. *J. Sed. Res.*, 78:579–593, 2008.

[63] J. R. L. Allen. Studies in fluviatile sedimentation; an exploratory quantitative model for the architecture of avulsion-controlled alluvial sites. *Sedimentary Geology*, 26:617–644, 1978.

[64] P. M. Sadler. Sediment accumulation rates and the completeness of stratigraphic sections. *J. Geol.*, 89(5):569–584, 1981.

[65] R. W. Fleming and A. M. Johnson. Rates of seasonal creep of silty clay soil. *Q. J. Eng. Geol.*, 8:1–29, 1975. doi:10.1144/GSL.QJEG.1975.008.01.01.

[66] M. J. Kirkby. Measurement and theory of soil creep. *J. Geol.*, 75:359–378, 1967. doi:10.1086/627267.

[67] A. L. Washburn. *Periglacial Processes and Environments*. 320 pp., Edward Arnold, London, 1973.

[68] C. Darwin. *The Formation of Vegetable Mould Through the Action of Worms*. John Murray, London, 1881.

[69] S. A. Norman, R. J. Schaetzl, and T. W. Small. Effects of slope angle on mass movements by tree uprooting. *Geomorphology*, 14:19–27, 1995. doi:10.1016/0169-555X(95)00016-X.

[70] J.J. Roering and M. Gerber. Fire and the evolution of steep, soil- mantled landscapes. *Geology*, 33:349–352, 2005. doi:10.1130/G21260.1.

[71] J.J. Roering. How well can hillslope evolution models 'explain' topography? simulating soil transport and production with high-reolution topographic data. *Geol. Soc. Am. Bull.*, 120 (9):1248–1262, 2008.

[72] D. J. Furbish, P. K. Haff, W. E. Dietrich, and A. M. Heimsath. Statistical description of slope-dependent soil transport and diffusion-like coefficient. *J. Geophys. Res.*, 114:F00A05, 2009. doi:10.1029/2009JF001267.

[73] G. E. Tucker and D. N. Bradley. Trouble with diffusion: reassessing hillslope erosion laws with a particle-based model. *J. Geophys. Res.*, 115:F00A10, 2010. doi:10.1029/2009JF001264.

[74] A.D. Howard. A detachment-limited model of drainage basin evolution. *Water Resour. Res.*, 30 (7):2261–2285, 1994.

[75] G. K. Gilbert. The complexity of hilltops. *J. Geol.*, 17:344–350, 1909.

[76] J. T. Hack. Interpretation of erosional topography in humid temperate regions. *Am. J. Sci.*, 258 A:80–97, 1960.

[77] P. O. Koons. The topographic evolution of collisional mountain belts: A numerical look at the southern alps, new zealand. *Am. J. Sci.*, 288:1041–1069, 1989.

[78] J. H. Cushman. On diffusion in fractal porous media. *Water Resour. Res.*, 27(4):643–644, 1991. doi:10.1029/91WR00162.

[79] J. H. Cushman. *The Physics of Fluids in Hierarchical Porous Media: Angstroms to Miles*. Kluwer Acad., Norwell, Mass., 1997.

[80] M. M. Meerschaert and H. P. Scheffler. *Limit Distributions for Sums of Independent Random Vectors: Heavy Tails in Theory and Practice*. Wiley, New York, U.S.A., 2001.

[81] R. Schumer, D. A. Benson, M. M. Meerschaert, and S. W. Wheatcraft. Eulerian derivation of the fractional advection-dispersion equation. *J. Contaminant Hydrol.*, 48:69–88, 2001.

[82] J. Lamperti. Semi-stable stochastic processes. *Trans. Am. Math. Soc.*, 104:62–78, 1962.

[83] D. A. Benson, S. W. Wheatcraft, and M. M. Meerschaert. Application of a fractional advection-dispersion equation. *Water Resour. Res.*, 36(6):1403–1412, 2000.

[84] Z. Q. Deng, J. L. M. P. de Lima, and V. P. Singh. Fractional kinetic model for first flush of stormwater pollutants. *J. Environ. Eng.*, 131(2):232–241, 2005. DOI:10.1061/(ASCE)0733-9372(2005)131:2.

[85] Z. Q. Deng, J. L. M. P. de Lima, M. I. P. de Lima, and V. P. Singh. A fractional dispersion model for overland solute transport. *Water Resour. Res.*, 42:W03416, 2006. doi:10.1029/2005WR004146.

[86] D. Campos, J. Fort, and V. Mendez. Transport on fractal river networks: Application to migration fronts. *Theor. Popul. Biol.*, 69:88–93, 2006. doi:10.1016/j.tpb.2005.09.001.

[87] P. Biler, T. Funaki, and W. Woyczynski. Fractal burgers equations. *J. Diff. Eqs.*, 148:9–46, 1998.

[88] W. Woyczynski. *Burgers-KPZ Turbulence: Gottingen Lectures, Lect. Notes in Math.* vol. 1700, Springer, Berlin, 1998.

[89] C.P. Stark, E. Foufoula-Georgiou, and V. Ganti. A nonlocal theory of sediment buffering and bedrock channel evolution. *J. Geophys. Res.*, 114:F01029, 2009. doi:10.1029/2008JF000981.

[90] K. Miller and B. Ross. *Introduction to the Fractional Calculus and Fractional Differential Equations*. John Wiley and Sons, New York, 1993.

[91] K. B. Oldham and J. Spanier. *The Fractional Calculus*. Academic, New York, 1974.

[92] M. M. Meerschaert and C. Tadjeran. Finite difference approximations for fractional advection-dispersion flow equations. *J. Comput. Appl. Math.*, 172(1):65–77, 2004.

[93] A. K. Grünwald. Uber 'begrenzt' derivationen und deren anwendung. *Z. angew. Math. und Phys.*, 12:441–480, 1867.

[94] S. L. Reneau and W. E. Dietrich. Erosion rates in the southern oregon coast range: Evidence for an equilibrium between hillslope erosion and sediment yield. *Earth Surf. Proc. Landforms*, 16:307–322, 1991. doi:10.1002/esp.3290160405.

[95] K. Yoo, R. Amundson, A. M. Heimsath, and W. E. Dietrich. Process-based model linking pocket gopher (thomomys bottae) activity to sediment transport and soil thickness. *Geology*, 33:917–920, 2005. doi:10.1130/G21831.1.

[96] K. Yoo, R. Amundson, A. M. Heimsath, and W. E. Dietrich. Spa- tial patterns of soil organic carbon on hillslopes: Integrating geomorphic processes and the biological c cycle. *Geoderma*, 130:47–65, 2006. doi:10.1016/j.geoderma.2005.01.008.

[97] I. Podlubny. *Fractional Differential Equations, vol. 198.* Academic Press, San Diego, 1999.

[98] P. Passalacqua, F. Porté-Agel, E. Foufoula-Georgiou, and C. Paola. Application of dynamic subgrid-scale concepts from large-eddy simulation to modeling landscape evolution. *Water Resour. Res.*, 42:W06D11, doi:10.1029/2006WR004879, 2006.

[99] L. W. Gelhar and C. L. Axness. Three-dimensional stochastic analysis of macrodispersion in aquifers. *Water Resour. Res.*, 19(1):161–180, 1983. doi:10.1029/WR019i001p00161.

[100] G. Dagan. *Subsurface Flow and Transport: A Stochastic Approach.* Cambridge Univ. Press, Cambridge, Mass., 1997.

[101] N. Su. Development of the fokker-planck equation and its solutions for modeling transport of conservative and reactive solutes in physically heterogeneous media. *Water Resour. Res.*, 31(12):3025–3032, 1995. doi:10.1029/95WR02765.

[102] D. A. Benson, S. W. Wheatcraft, and M. M. Meerschaert. The fractional-order governing equation of lévy motion. *Water Resour. Res.*, 36(6):1413–1423, 2000.

[103] B. Baeumer, D. A. Benson, M. M. Meerschaert, and S. W. Wheatcraft. Subordinated advection-dispersion equation for contaminant transport. *Water Resour. Res.*, 37(6):1543–1550, 2001.

[104] G. K. Gilbert. Report on the geology of henry mountains. *U. S. Geographical and Geological Survey of the Rocky Mountain region*, 2nd edition:160 pp., 1877.

[105] Y. Martin and M. Church. Diffusion in landscape development models: On the nature of basic transport relations. *Ear. Surf. Proc. Landforms*, 22:273–279, 1997.

[106] N. F. Fernandes and W. E. Dietrich. Hillslope evolution by diffusive processes: The timescale for equilibrium adjustments. *Water Resour. Res.*, 33(6):1307–1318, 1997.

[107] M. J. Kirkby. Hillslope process-response models based on the continuity equation. *Inst. Brit. Geogr., Spec. Publ.*, 3:15–30, 1971.

[108] E. J. Gabet. Gopher bioturbation: Field evidence for non-linear hillslope diffusion. *Ear. Surf. Proc. and Landforms*, 25:1419–1428, 2000.

[109] D. J. Furbish, K. K. Hammer, M. Schmeeckle, M. N. Borosund, and S. M. Mudd. Rain splash of dry sand revealed by high-speed imaging and sticky paper splash targets. *J. Geophys. Res.*, 112, 2007. doi:10.1029/2006JF000498.

[110] G. E. Tucker and G. R. Hancock. Modeling landscape evolution. *Ear. Surf. Proc. and Landforms*, 35(1):28–50, 2010.

[111] A. E. Scheidegger. Mathematical models of slope development. *Bull. Geol. Soc. Ameri.*, 72(1):37–49, 1961.

[112] J. DePloey and J. Savat. Contribution a letude de lerosion par le splash. *Zeitschrift fur Geomorphologie*, 12:174–193, 1968.

[113] M. J. Kirkby. Modeling cliff development in south wales: Savigear re-reviewed. *Z. Geomorphol.*, 28:405–426, 1984.

[114] D. J. Andrews and T. C. Hanks. Scarp degraded by linear diffusion: Inverse solution for age. *J. Geophys. Res.*, 90 (B12):193–208, 1985.

[115] K. L. Pierce and S. M. Colman. Effect of height and orientation (microclimate) on geomorphic degradation rates and processes, late-glacial terrace scarps in central idaho. *Geol. Soc. Ameri. Bull.*, 97(7):869–885, 1986.

[116] R.S. Anderson and N.F. Humphrey. Interaction of weathering and transport processes in the evolution of arid landscapes. In *Quantitative Dynamic Stratigraphy (edited by T.A. Cross)*, pages 349–361. Prentice-Hall, Englewood Cliffs, N.J., 1990.

[117] R. S. Anderson. Evolution of the santa cruz mountains, california, through tectonic growth and geomorphic decay. *J. Geophys. Res.*, 99 (20):161–174, 1994.

[118] J.J. Roering, J.W. Kirchner, and W.E. Dietrich. Hillslope evolution by nonlinear slope-dependent transport: Steady-state morphology and equilibrium adjustment timescales. *J. Geophys. Res.*, 106 (B8):499–513, 2001.

[119] D. J. Furbish and P. K. Haff. From divots to swales: Hillslope sediment transport across divers length scales. *J. Geophys. Res.*, 115, 2010. doi:10.1029/2009JF001576.

[120] D. R. Montgomery and E. Foufoula-Georgiou. Channel network source representation for digital elevation models,. *Water Resour. Res.*, 29(12):3925–3934, 1993.

[121] W. Zhang and D. R. Montgomery. Digital elevation model grid size, landscape representation, and hydrologic simulations. *Water Resour. Res.*, 30(4):1019–1028, 1994.

[122] J. P. Walker and G. R. Willgoose. On the effect of digital elevation model accuracy on hydrology and geomorphology. *Water Resour. Res.*, 35(7):2259–2268, 1999.

[123] X. Zhang, N. A. Drake, J. Wainwright, and M. Mulligan. Comparison of slope estimates from low resolution dems: Scaling issues and a fractal method for their solution. *Earth Surf. Process. Landforms*, 24:763–779, 1999.

[124] K. G. Evans and G. R. Willgoose. Post-mining landform evolution modelling: 2. effects of vegetation and surface ripping. *Earth Surf. Process. Landforms*, 25:803–823, 2000.

[125] C.P. Stark and G.J. Stark. A channelizataion model of landscape evolution. *Am. J. Sci.*, 301:486–512, 2001.

[126] X. Zhang, N. A. Drake, and J. Wainwright. Scaling land surface parameters for global-scale soil erosion estimation. *Water Resour. Res.*, 38(9):1180, 2002. doi:10.1029/2001ER000356.

[127] J. Boardman. Soil erosion science: Reflections on the limitations of current approaches. *Catena*, 68:73–86, 2006.

[128] R. Sorensen and J. Seibert. Effects of dem resolution on the calculation of topographical indices: Twi and its components. *J. Hydrology*, 347:79–89, 2007.

[129] G.R. Hancock. The use of digital elevation models in the identification and characterization of catchments over different grid scales. *Hydrol. Process.*, 19:1727–1749, 2005.

[130] G.R. Hancock. The impact of different grid ding methods on catchment geomorphology and soil erosion over long timescales using landscape evolution model. *Earth Surf. Process. Landforms*, 31:1035–1050, 2006.

[131] J.J. Roering, J. Marshall, A. Booth, M. Mort, and Q. Jin. Functional relationships between denudation and hillslope form and relief. *Earth and Planetary Science Letters*, 298:183–190, 2010.

[132] P. Passalacqua, T. Do Trung, E. Foufoula-Georgiou, G. Sapiro, and W. E. Dietrich. A geometric framework for channel network extraction from lidar: nonlinear diffusion and geodesic paths. *J. Geophys. Res.*, 115:F01002, 2009. doi:10.1029/2009JF001254.

[133] P. Passalacqua, P. Tarolli, and E. Foufoula-Georgiou. Testing space-scale methodologies for automatic geomorphic feature extraction from liar in a

complex mountainous landscape. *Water Resour. Res.*, 46:W11535, 2010. doi:10.1029/2009WR008812.

[134] M. Germano, U. Piomelli, P. Moin, and W. H. Cabot. A dynamic subgrid-scale eddy viscosity model. *Phys. Fluids*, 3:1760–1765, 1991.

[135] P. Moin, K. D. Squires, and S. Lee. A dynamic subgrid-scale model for compressible turbulence and scalar transport. *Phys. Fluids*, 3:2746–2757, 1991.

[136] C. Meneveau and J. Katz. Scale invariance and turbulence models for large-eddy simulation. *Annu. Rev. Fluid Mech.*, 32:1–32, 2000.

[137] S. B. Pope. *Turbulent Flows*. Cambridge University Press, New York, 2000.

[138] F. Porté-Agel, C. Meneveau, and M. B. Parlange. A scale- dependent dynamic model for large-eddy simulation: Application to a neutral atmospheric boundary layer. *J. Flu. Mech.*, 415:261–284, 2000.

[139] P. Sagaut. *Large Eddy Simulation for Incompressible Flows: An Introduction*. Springer, New York, 2002.

[140] B. J. Geurts. *Elements of Direct and Large Eddy Simulations*. 388 pp., R. T. Edwards, Flourtown, Pa, 2004.

[141] S. B. Pope. Ten questions concerning the large-eddy simulation of turbulent flows. *New J. Phys.*, 6:35, 2004.

[142] F. Porté-Agel. A scale-dependent dynamic model for scalar transport in the atmospheric boundary layer. *Bound. Layer Meteor.*, 112:81–105, 2004.

[143] D. Harris and E. Foufoula-Georgiou. Subgrid variability and stochastic downscaling of modeled precipitation and its effects on radiative transfer computations. *J. Geophys. Res.*, 106(D10):10349–10362, 2001.

[144] D. Nykanen and E. Foufoula-Georgiou. Soil moisture variability and its effect on scale-dependency of nonlinear parameterizations in coupled land-atmosphere models. *Adv. Water Res.*, 24(9–10):1143–1157, 2001.

[145] M. Chruch and M. A. Hassan. Size and distance of travel of unconstrained clasts on a streambed. *Water Resour. Res.*, 28:299–303, 1992.

[146] P. R. Wilcock. Entrainment, displacement and transport of tracer gravels. *Earth Surf. Proc. Land.*, 22:1125–1138, 1997.

[147] R. I. Ferguson and T. B. Hoey. Long-term slowdown of river tracer pebbles: Generic models and implications for interpreting short-term tracer studies. *Water Resour. Res.*, 38(8):1142, 2002.

[148] R. S. Pyrce and P. E. Ashmore. Particle path length distributions in meandering gravel-bed streams: Results from physical models. *Earth Surf. Proc. Land.*, 28:951–966, 2003.

[149] H. A. Einstein. Geschiebetrieb als wahrscheinlichkeitsproblem, in *Mitteilung der Versuchsanstalt für Wasserbau an der Eidgenössische Technische Hochschule Zürich*, verlag rascher, zurich, switzerland. *Sedimentation (edited by H. W. Shen)*, Colo. State Univ., Fort Collins:C1–C105, 1937.

[150] H. A. Einstein and E. A. El-Sammi. Hydrodynamic forces on a rough wall. *Rev. Mod. Phys.*, 21:520–524, 1949.

[151] A. S. Paintal. A stochastic model for bed load transport. *J. Hydraulic Res.*, 9(4):527–554, 1971.

[152] J. Nelson, R. L. Shreve, S. R. McLean, and T. G. Drake. Role of near-bed turbulence structure in bed load transport and bed form mechanics. *Water Resour. Res.*, 31(8):2071–2086, 1995.

[153] N. Cheng and Y. Chiew. Pickup probability for sediment entrainment. *J. Hydraul. Eng.*, 124(2):232–235, 1998.

[154] F. Lopez and M. H. Garcia. Risk of sediment erosion and suspension in turbulent flows. *J. Hydraul. Res.*, 127(3):231–235, 2001.

[155] M. G. Kleinhans and L. C. van Rijn. Stochastic prediction of sediment transport in sand-gravel bed rivers. *J. Hydraul. Res.*, 128(4):412–425, 2002.

[156] N. Cheng. Analysis of bedload transport in laminar flows. *Adv. Water Resour.*, 27:937–942, 2004.

[157] N. S. Cheng, T. Tang, and L. Zhu. Evaluation of bedload transport subject to high sheer stress fluctuations. *Water Resour. Res.*, 40:W05601, 2004. doi:10.1029/2003WR00300.

[158] F. Charru, H. Mouilleron, and O. Eiff. Erosion and deposition of particles on a bed sheared by viscous flow. *J. Fluid Mech.*, 519:55–80, 2004.

[159] C. Ancey, T. Bohm, M. Jodeau, and P. Frey. Statistical description of sediment transport experiments. *Phys. Rev. E*, 74:011302, 2006.

[160] C. Ancey, A. C. Davidson, T. Bohm, M. Jodeau, and P. Frey. Entrainment and motion of coarse particles in a shallow water stream down a steep slope. *J. Fluid Mech.*, 595:83–114, 2008.

[161] C. Ancey. Stochastic approximation of the exner equation under lower-regime conditions. *J. Geophys. Res.*, 114:xx–xx–xx, 2010.

[162] V. Ganti, A. Singh, P. Passalacqua, and E. Foufoula-Georgiou. Subordinated brownian motion model for sediment transport. *Phys. Rev. E.*, 80:011111, 2009.

[163] Y. Nino and M. Garcia. Experiments on saltation of sand in water. *J. Hydraulic Engg.*, 124(10):1014–1025, 1998.

[164] H. A. Einstein. The bed-load function for sediment transportation in open channel flows. *Tech. Bull.*, 1026., Soil Conserv. Serv., U. S. Dept. of Agric., Washington, D. C.:78 pp., 1950.

[165] T. Tsujimoto. *Probabilistic model of the process of bedload transport and its application to mobile-bed problems, Ph.D. Thesis.* Kyoto University, Yoshida, 1978.

[166] M. Wong, G. Parker, P. DeVries, T. M. Brown, and S. J. Burges. Experiments on dispersion of tracer stones under lower-regime plane-bed equilibrium bed load transport. *Water Resour. Res.*, 43:W03440, 2002. doi:10.1029/2006WR005172.

[167] M. A. Hassan and M. Church. Vertical mixing of coarse particles in gravel bed rivers: A kinematic model. *Water Resour. Res.*, 30:1173–1186, 1994.

[168] A. Blom, G. Parker, J. S. Ribberink, and H. J. de Vriend. Vertical sorting and the morphodynamics of bed-form-dominated rivers: An equilibrium sorting model. *J. Geophys. Res.*, 111, 2006. doi:10.1029/2004JF000175.

[169] W. C. Bradley. Effect of weathering on abrasion of granitic gravel, colorado river, texas. *Geol. Soc. of Am. Bull.*, 81:61–80, 1970.

[170] J. W. Lauer and G. Parker. Modeling framework for sediment deposition, storage, and evacuation in the floodplain of a meandering river: Theory. *Water Resour. Res.*, 44:W04425, 2008.

[171] J. W. Lauer and G. Parker. Modeling framework for sediment deposition, storage, and evacuation in the floodplain of a meandering river: Application to the clark fork river, montana. *Water Resour. Res.*, 44:W08404, 2008.

[172] R. Schumer, D. A. Benson, M. M. Meerschaert, and B. Baeumer. Fractal mobile/immobile solute transport. *Water Resour. Res.*, 39(10):1296, 2003. doi:10.1029/2003WR002141.

[173] M. H. Garcia. Sedimentation engineering processes, measurements, modeling and practice. *ASCE Manual No. 110*, page 1050 pp., 2008.

[174] T. B. Hoey and R. I. Ferguson. Numerical simulation of downstream fining by selective transport in gravel bed rivers: Model development and illustration. *Water Resour. Res.*, 30:2251–2260, 1994.

[175] C. M. Toro-Escobar, G. Parker, and C. Paola. Transfer function for the deposition of poorly sorted gravel in response to streambed aggradation. *J. Hydraulic Res.*, 34(1):35–53, 1996.

[176] A. Papoulis and S. Pillai. *Probability, random variables and stochastic processes.* McGraw Hill, xx-xx, 2002.

[177] Z. M. Odibat and N. T. Shawagfeh. Generalized taylor's formula. *Appl. Math. Comput.*, 186:286–293, 2007.

[178] S. W. Wheatcraft and M. M. Meerschaert. Fractional conservation of mass. *Adv. Water Resour.*, 31:1377–1381, 2008.

[179] G. Parker. Transport of gravel and sediment mixtures. In *Chapter 3, Sedimentation Engineering Processes, Measurements, Modeling and Practice (edited by M. Garcia)*. ASCE Manual and Reports on Engineering Practice 110, xx-xx, 2008.

[180] H. Nakagawa and T. Tsujimoto. On probabilistic characteristics of motion of individual sediment particles on stream beds. *Proceedings of the 2nd IAHR International Symposium on Stochastic Hydraulics, Madrid*, Int. Assoc. of Hydraul. Eng. and Res.:293–316, 1976.

[181] H. Nakagawa and T. Tsujimoto. Sand bed instability due to bed load motion. *J. Hydraul. Div. Am. Soc. Civ. Eng.*, 106(HY12):2029–2051, 1980.

[182] M. A. Hassan and M. Church. Size and distance of travel of unconstrained clasts on a streambed. *Water Resour. Res.*, 28(1):299–303, 1992.

[183] S. Lanzoni and M. Tubino. Grain sorting and bar instability. *J. Flu. Mech.*, 393:149–174, 1999.

[184] J. R. M. Hosking and J. R. Wallace. Parameter and quantile estimation for the generalized pareto distribution. *Technometrics*, 29(3):339–349, 1987.

[185] K. M. Hill, L. DellAngelo, and M. M. Meerschaert. Heavy-tailed travel distance in gravel bed transport: An exploratory enquiry. *J. Geophys. Res.*, 115:F00A14, 2010. doi: 10.1029/2009JF001276.

[186] E. W. Montroll and G.H. Weiss. Random walks on lattices. ii. *J. Mathematical Phys.*, 6:167–181, 1965.

[187] H. Scher and M. Lax. Stochastic transport in a disordered solid. i. theory. *Phys. Rev. B*, 7:4491–4502, 1973.

[188] M. M. Meerschaert and H. P. Scheffler. Limit theorems for continuous time random walks with infinite mean waiting times. *J. Applied Probab.*, 3:623–638, 2004.

[189] E. Scalas, R. Gorenflo, and F. Mainardi. Uncoupled continuous-time random walks: Solution and limiting behavior of the master equation. *Phys. Rev. E*, 69:011107(1–8), 2004.

[190] D. Fulger, E. Scalas, and G. German. Monte carlo simulation of uncoupled continuous-time random walks yielding a stochastic solution of the space-time fractional diffusion. *Phys. Rev. E*, 77:021122, 2008.

[191] J. P. Nolan. Numerical calculation of stable densities and distribution functions. *Commun. Statist.-Stochastic Models*, 13(4):759–774, 1997.

[192] V. M. Zolotarev. One-dimensional stable distributions. *Translations of Mathematical Monographs*, 65:American Mathematical Society, Providence, RI. Translated from Russian by H. H. McFaden, Translation edited by Ben Silver., 1986.

[193] R. Schumer and D. J. Jerolmack. Real and apparent changes in sediment deposition rates through time. *J. Geophys. Res.*, 114:F00A06, 2009. doi:10.1029/2009JF001266.

[194] A. Einstein. *Investigations of the theory of Brownian movement.* Dover, New York, 1956.

[195] J. Gessler. *The beginning of bedload movement of mixtures investigated as natural armoring channels, PhD Thesis.* Swiss Federal Institute of Technology, Zurich, 1967.

[196] A. Papanicolaou, P. Diplas, N. Evangelopoulos, and S. Fotopoulos. Stochastic incipient motion criterion for spheres under various bed packing conditions. *J. Hydraul. Engg.*, 128:369, 2002.

[197] C. Paola, S. M. Weile, and M. A. Reinhart. Upper-regime parallel lamination as the result of turbulent sediment transport and low-amplitude bedforms. *Sedimentology*, 36:47–70, 1989.

[198] X. Zhang and B. Xie. Incipient velocity and incipient probability of particles. *J. Hydraul. Eng.*, 10:53–59, 1995.

[199] A. Papanicolaou. *The role of turbulence on the initiation of sediment motion, PhD thesis*. Virginia Institute of Technology, Blacksburg, 1997.

[200] A. Papanicolaou, P. Diplas, C. Dancey, and M. Balakrishnan. surface roughness effects in near-bed turbulence: Implications to sediment entrainment. *J. Eng. Mech.*, 127(3):211–218, 2001.

[201] G. Parisi and U. Frisch. On the singularity structure of fully developed turbulence. In *Turbulence and Predictability in Geophysical Fluid Dynamics (edited by M. Ghil, R. Benzi, and G. Parisi)*, pages 84–88. Elsevier, New York, 1985.

[202] K. Fienberg, A. Singh, D. J. Jerolmack, J. Marr, and E. Foufoula-Georgiou. A theoretical framework for interpreting and quantifying the sampling time dependence of gravel bedload transport rates. *Bedload Research International Cooperative Meeting*, Minneapolis, MN.:11–14 April, 2008.

[203] B. Castaing, Y. Gagne, and E. J. Hopfinger. Velocity probability density-functions of high reynolds-number turbulence. *Physica D*, 46:177–200, 1990. doi:10.1016/0167-2789(90)90035-N.

[204] V. Venugopal, S. G. Roux, E. Foufoula-Georgiou, and A. Arneodo. Revisiting multifractality of high-resolution temporal rainfall using a wavelet-based formalism. *Water Resour. Res.*, 42:W06D14, 2006. doi:10.1029/2005WR004489.

[205] K. Bunte and S. R. Abt. Effect of sampling time on measured gravel bed load transport rates in a coarse-bedded stream. *Water Resour. Res.*, 41:W11405, 2005. doi:10.1029/2004WR003880.

[206] V. V. Novikov. Physical properties of fractal structures. In *Fractals, diffusion and relaxation in disordered complex systems (edited by W. T. Coffey and Y. P. Kalmykov)*, page pp. 203. Advances in Chemical Physics, Part B, Vol. 133, New York, 2006.

[207] M. Dentz, A. Cortis, H. Scher, and B. Berkowitz. Time behavior of solute transport in heterogeneous media: Transition from anomalous to normal transport,. *Adv. Water Resour.*, 27:155–173, 2004.

[208] A. Cortis, Y. Chen, H. Scher, and B. Berkowitz. Quantitative characterization of pore-scale disorder effects on transport in "homogeneous" granular media. *Phys. Rev. E*, 70 (10):041108, 2004. doi:10.1103/PhysRevE.70.041108.

[209] S. Bochner. Diffusion equations and stochastic processes. *Proc. Natl. Acad. Sci. U.S.A.*, 48:2039–2043, 1962.

[210] R. Gorenflo, F. Mainardi, and A. Vivoli. Continuous-time random walk and parametric subordination in fractional diffusion. *Chaos, Solitons, and Fractals*, 34(1):87–103, 2007.

[211] T. J. Kozubowski, M. M. Meerschaert, and K. Podgrórski. Fractional laplace motion. *Adv. in Appl. Probab.*, 38(2):451–464, 2006.

[212] S. Kotz, T. J. Kozubowski, and K. Podgórski. *The Laplace Dis- tribution and Generalizations: A Revisit with Applications to Communications, Economics, Engineering and Finance*. Birkhauser, Boston, 2001.

[213] B. Berkowitz and H. Scher. Anomalous transport in random fracture networks. *Phys Rev. Lett.*, 79(20):4038–4041, 1997.

[214] F. J. Molz, M. M. Meerschaert, T. J. Kozubowski, and P. D. Hyden. Do heterogeneous sediment properties and turbulent velocity fluctuations have something in common? some history and a new stochastic process. In *Dynamics of Fluids and Transport in Fractured Rock (edited by B. Faybishenko, P. A. Witherspoon, and J. Gale, Geophysical Monograph No. 162)*, pages 13–22. American Geophysical Union, Washington D. C., 2005.

[215] E. S. Ching and Y. Tu. Passive scalar fluctuations with and with- out a mean gradient: A numerical study. *Phys. Rev. E*, 49:1278–1282, 1994.

[216] C. Paola, K. M. Straub, D. Mohrig, and L. Reinhardt. The "unreasonable effectiveness" of stratigraphic and geomorphic experiments. *Earth Science Reviews*, 97:1–43, 2009.

[217] B. Sheets, C. Paola, and J. M. Kelberer. Creation and preservation of channelform sand bodies in an experimental alluvial basin. In *Sedimentary Processes,*

Environments and Basins (edited by G. Nichols, E. Williams, and C. Paola), pages 555–567. Blackwell Publishing, Oxford, U.K., 2007.

[218] D. V. Ager. *The Nature of the Stratigraphic Record*. Wiley, New York, 1973.

[219] P. A. Allen. Time scales of tectonic landscapes and their sediment routing systems. In *Landscape Evolution: Denudation, Climate and Tectonics Over Different Time and Space Scales (edited by Gallager, K., S. J. Jones, and J. Wainwright)*, pages 7–28. Prentice-Hall, Englewood Cliffs, N.J., 2008.

[220] J. Alexander and M. R. Leeder. Active tectonic control on alluvial architecture. In *Recent Developments in Fluvial Sedimentology (edited by Ethridge, F. G., R. M., Flores, and M. D. Harvey)*, pages 243–252. Prentice-Hall, Englewood Cliffs, N.J., 1987.

[221] S. D. Mackey and J. S. Bridge. 3-dimensional model for alluvial stratigraphy - theory and application. *J. Sed. Res. Section B - Stratigraphy and Global Studies*, 65:7–31, 1995.

[222] M. J. Pyrcz, O. Catuneanu, and C. V. Deutsch. Stochastic surface-based modeling of turbidite lobes. *AAPG Bulletin*, 89:177–191, 2005.

[223] E. A. Hajek, P. L. Heller, and B. A. Sheets. Significance of channel-belt clustering in alluvial basins. *Geology*, 38:535–538, 2010.

[224] K. M. Straub, C. Paola, D. Mohrig, M. A. Wolinsky, and T. George. Compensational stacking of channelized sedimentary deposits. *J. Sed. Res.*, 79:673–688, 2009.

[225] J. D. Pelletier and D. L. Turcotte. Synthetic stratigraphy with a stochastic diffusion model of fluvial sedimentation. *J. Sediment. Res.*, 67(6):1060–1067, 1997.

[226] R. Le B. Hooke. Model geology: prototype and laboratory streams: discussion. *Bull. geol. Soc. Am.*, 79:391–394, 1968.

[227] R. Bruno, L. Sorriso-Valvo, V. Carbone, and B. Bavassano. A possible truncated-lévy-flight statistics recovered from interplanetary solar-wind velocity and magnetic-field fluctuations. *Europhys. Lett.*, 66(1):146–152, 2004.

[228] Y. Zhang, D. A. Benson, and B. Baeumer. Predicting the tails of breakthrough curves in regional-scale alluvial systems. *Ground Water*, 45 (4):473–484, 2007.

[229] A. Clauset, C. R. Shalizi, and M. E. J. Newman. Power law distributions in empirical data. *SIAM Review*, 51(4):661–703, 2009.

[230] I. B. Aban, M. M. Meerschaert, and A. K. Panorska. Parameter estimation for the truncated pareto distribution. *Journal of American Statistical Association*, 101(473):270–277, 2006.

[231] A. N. Kolmogorov. Solution of a problem in probability theory connected with the problem of the mechanism of stratification. *American Mathematical Society Translation*, 53:171–177, 1951.

[232] D. L. Turcotte. *Fractals and chaos in Geology and Geophysics*. Cambridge University Press, New York, U.S.A., 1992.

[233] A. Arneodo, E. Bacry, and J. F. Muzy. Towards log-normal statistics in high reynolds number turbulence. *Eur. Phys. J. B*, 1:129–140, 1998.

[234] D. Mohrig, P. L. Heller, C. Paola, and W. J. Lyons. Interpreting avulsion process from ancient alluvial sequences: Gaudalope-matarranya system (northern spain) and wasatch formation (western colorado). *GSA Bulletin*, 112(12):1787–1803, 2000.

[235] E. Foufoula-Georgiou and C. P. Stark. Introduction to special section on stochastic transport and emergent scaling on earth's surface: Rethinking geomorphic transport-stochastic theories, broad scales of motion and nonlocality. *J. Geophys. Res.*, 115:F00A01, 2010. doi:10.1029/2010JF001661.

[236] C. J. Harman, D. M. Reeves, B. Baeumer, and M. Sivapalan. A subordinated kinematic wave equation for heavy-tailed flow responses from heterogeneous hillslopes. *J. Geophys. Res.*, 115:F00A08, 2010. doi:10.1029/2009JF001273.

[237] C. Paola, P. L. Heller, and C. L. Angevine. The large-scale dynamics of grain-size variation in alluvial basins, 1: Theory. *Basin Research*, 4:73–90, 1992.

[238] M. M. Meerschaert, Y. Zhang, and B. Baeumer. Tempered anomalous diffusion in heterogeneous systems. *JGeophys. Res. Lett.*, 35:5026–5028, 2008.

[239] A. Cartea and D. del Castillo-Negrete. Fluid limit of the continuous time random walk with general lévy jump distribution functions. *Phys. Rev. E*, 76:041105, 2007.

[240] J. Rosiński. Tempering stable processes. *Stochastic Processes Appl.*, 117:677–707, 2007.

[241] T. W. Gardner, D. W. Jorgensen, C. Shuan, and C. R. Lemieux. Geomorphic and tectonic process rates: Effects of measured time interval. *Geology*, pages 259–261, 1987. doi:10.1130/0091-7613(1987)15¡259: GATPRE¿2.0.CO;2.

[242] D. J. Jerolmack and P. Sadler. Transience and persistence in the depositional record of continental margins. *J. Geophys. Res.*, 112:F03S13, 2007. doi:10.1029/2006JF000555.

[243] D. Strauss and P. M. Sadler. Stochastic-models for the completeness of stratigraphic sections. *Math. Geol.*, 21(1):37–59, 1989. doi:10.1007/ BF00897239.

[244] J. C. Tipper. Rates of sedimentation, and stratigraphical completeness. *Nature*, 302 (5910):696–698, 1983. doi:10.1038/302696a0.

[245] N. Endo. Inverse problem and solution of the kolmogorov model for bed thickness distribution. *Math. Geosci.*, 42(8):955–968, 2010. doi:10.1007/s11004-010-9300-y.

[246] D. J. Jerolmack and D. Mohrig. Frozen dynamics of migrating bedforms. *Geology*, 33(1):57–60, 2005.

[247] S. F. Leclair and J. S. Bridge. Quantitative interpretation of sedimentary structures formed by river dunes. *J. Sed. Res.*, 71:713–716, 2001.

[248] M. F. Dacey. Models of bed formation. *J. Int. Assoc. Math. Geol.*, 11 (6):655–668, 1979. doi:10.1007/BF01031890.

[249] D. H. Rothman, J. P. Grotzinger, and P. Flemings. Scaling in turbidite deposition. *J. Sed. Res.*, 64(1):59–67, 1994.

[250] P. J. Talling. On the frequency distribution of turbidite thicknesses. *Sedimentology*, 48:1297–1329, 2001. doi:10.1046/j.1365-3091.2001.00423.x.

[251] Z. Sylvester. Turbidite bed thickness distributions: Methods and pitfalls of analysis and modelling. *Sedimentology*, 54:847–870, 2007. doi:10.1111/j.1365-3091.2007.00863.x.

[252] R. J. Bailey and D. G. Smith. Scaling in stratigraphic data series: Implications for practical stratigraphy. *First Break*, 28:57–66, 2010.

[253] J. Carlson and J. P. Grotzinger. Submarine fan environment inferred from turbidite thickness distributions. *Sedimentology*, 48(6):1331–1351, 2001. doi:10.1046/j.1365-3091.2001.00426.x.

[254] C. Pirmez, R. N. Hiscott, and J. D. Kronen. Sandy turbidite successions at the base of channel-levee systems of the amazon fan revealed by fms logs and cores: Unraveling the facies architecture of large submarine fans. In *Proceedings of the Ocean Drilling Program, Scientific Results (edited by R. D. Flood et al.)*, pages 7–33. Ocean Drill. Prog., College Station, Texas, 1997.

[255] H. D. Sinclair and P. A. Cowie. Basin-floor topography and the scaling of turbidites. *J. Geol.*, 111:277–299, 2003. doi:10.1086/373969.

[256] C. N. Drummond and P. J. Dugan. Self-organizing models of shallow-water carbonate accumulation. *J. Sed. Res.*, 69(4):939–946, 1999.

[257] R. D. Beeden. *Sedimentology of some turbidites and related rocks from the Cloridorme Group, Ordovician, Quebec, MS thesis*. McMaster Univ., Hamilton, Ontario, Canada, 1983.

[258] C. N. Drummond and B. H. Wilkinson. Stratal thickness frequen- cies and the prevalence of orderedness in stratigraphic sequences. *J. Geol.*, 104:1–18, 1996. doi:10.1086/629798.

[259] S. Mizutani and I. Hattori. Stochastic analysis of bed-thickness distribution of sediments. *Math. Geol.*, 4:123–146, 1972. doi:10.1007/ BF02080298.

[260] T. Muto. The kolmogorov model of bed-thickness distribution: An assessment based on numerical simulation and field-data analysis. *Terra Nova*, 7:417–423, 1995. doi:10.1111/j.1365-3121.1995.tb00537.x.

[261] G. M. Molchan and D. L. Turcotte. A stochastic model of sedimentation: Probabilities and multifractality. *Eur. J. Appl. Math.*, 13:371–383, 2002. doi:10.1017/S0956792502004850.

[262] W. Schwarzacher. *Sedimentation Models and Quantitative Stratigraphy*. 382 pp., Elsevier, Amsterdam, 1975.

[263] V. Ganti, K. M. Straub, E. Foufoula-Georgiou, and C. Paola. Space-time dynamics of depositional systems: Experimental evidence and theoretical modeling of heavy-tailed statistics. *J. Geophys. Res.*, 116:F02011, 2011. doi:10.1029/2010JF001893.

[264] R. S. Anderson and K. L. Bunas. Grain size segregation and stratigraphy in aeolian ripples modelled with a cellular automaton. *Nature*, 365:740–743, 1993.

[265] H. A. Makse. Grain segregation mechanism in aeolian sand ripples. *European Physical Journal E*, 1:127–135, 2000.

[266] A. Blom, J. S. Ribberink, and H. J. de Vriend. Vertical sorting in bedforms: Flume experi- ments with a natural and trimodal sediment mixture. *Water Resour. Res.*, 39(2), 2003. doi: 10.1029/2001WR001088.

[267] S. F. Leclair. Preservation of cross-strata due to the migration of subaqueous dunes: An experimental investigation. *Sedimentology*, 49:1157–1180, 2002.

[268] J. R. L. Allen. Features of cross-stratified units due to random and other changes in bed forms. *Sedimentology*, 20:189–202, 1973.

[269] M. S. Yalin. Geometrical properties of sand waves. *J. Hydraul. Eng.*, 90:105–119, 1964.

[270] J. R. L. Allen. A quantitative model of climbing ripples and their cross-laminated deposits. *Sedimentology*, 14:5–26, 1970.

[271] J. S. Bridge and R. S. Tye. Interpreting the dimension of ancient channel bars, channels, and channel belts from wireline-logs and cores. *AAPG Bull.*, 84:1205–1228, 2000.

[272] D. M. Rubin and R. E. Hunter. Bedform climbing in theory and nature. *Sedimentology*, 29:121–138, 1982.

[273] J. S. Bridge and J. L. Best. Preservation of planar lam- inae due to migration of low-relief bad waves over aggrading upper-stage plane beds: Comparison of experimental data with theory. *Sedimentology*, 44:253–262, 1997.

[274] S. F. Leclair, J. S. Bridge, and F. Wang. Preservation of cross-strata due to migration of subaqueous dunes over aggrading and non-aggrading beds: comparison of experimental data with theory. *Geosci. Can.*, 24:55–66, 1997.

[275] J. E. A. Storms, R. L. Van Dam, and S. F. Leclair. Preservation of cross-strata due to migration of current ripples over aggrading and non-aggrading beds: Comparison of experimental data with theory. *Sedimentology*, 46:189–200, 1999.

[276] B. McElroy and D. Mohrig. Nature of deformation of sandy bed forms. *J. Geophys. Res.*, 114:F00A04, 2009. doi:10.1029/2008JF001220.

[277] R. L. Martin, D. J. Jerolmack, and R. Schumer. Origin of hysteresis in bedform response to unsteady flows. *Water Resour. Res.*, 2012. under review.

[278] K. M. Straub, V. Ganti, C. Paola, and E. Foufoula-Georgiou. Prevalence of exponential bed thickness distributions in the stratigraphic record: Experiments and theory. *J. Geophys. Res.*, 117:F2, 2012. doi:10.1029/2011JF002034.

[279] F. J. Massey. The kolmogorov-smirnov test for goodness of fit. *J. Am. Stat. Assoc.*, 46(253):68–78, 1951.

[280] F. Falcini, V. Ganti, C. Paola, E. Foufoula-Georgiou, and V. R. Voller. A combined non-linear and non-local model for sediment transport in depositional systems. *J. Geophys. Res.*, under review, 2012.

[281] J. F. Muzy, E. Bacry, and A. Arneodo. The multifractal formalism revisited with wavelets. *Int. J. Bifurcation Chaos*, 4:245–302, 1994.

[282] E. Bacry, J. F. Muzy, and A. Arneodo. Singularity spectrum of fractal signals from wavelet analysis: Exact analysis. *J. Stat. Phys.*, 70:635–674, 1993.

[283] S. Jaffard. Multifractal formalism for functions: 1. results valid for all functions. *SIAM J. Math. Anal.*, 28:944–970, 1997.

[284] A. Stuart and J. K. Ord. *Kendall's Advanced Theory of Statistics, Vol. 1.* Oxford University Press, New York, 1987.

[285] P. Kumar and E. Foufoula-Georgiou. A multicomponent decomposition of spatial rainfall fields, 2. self-similarity in fluctuations. *Water Resour. Res.*, 29(8):2533–2544, 1993.

[286] B. Dodov and E. Foufoula-Georgiou. Generalized hydraulic geometry: Derivation based on multiscaling formalism. *Water Resour. Res.*, 40:W06302, doi:10.1029/2003WR002082, 2004.

[287] Z. Q. Deng, V. P. Singh, and L. Bengtsson. Numerical solution of fractional advection-dispersion equation. *J. Hydraul. Eng.*, 130(5):422–431, 2004.

Appendix A

Geometrical interpretation of multifractal analysis

The local singularity of a function at location t_0 is quantified using the so-called Hölder exponent defined as:

$$|f(t_0) - f(t_0 + \epsilon)| \sim C|\epsilon|^{\mathcal{H}(t_0)} \tag{A.1}$$

where $0 < \mathcal{H}(t_0) < 1$ is the Hölder exponent of the function f at a location t_0 [281]. As seen in the above equation, the limit of $\mathcal{H} = 0$ corresponds to discontinuity in the signal and $\mathcal{H} = 1$ corresponds to discontinuity in the derivative of the signal. As $\mathcal{H} \to 0$ the signal is said to be more irregular or "rougher". The spectrum of Hölder exponents (also called the spectrum of singularities), $D(\mathcal{H})$, is defined as the Hausdorff dimension of all the points t in the signal which have the same Hölder exponent [201, 282, 283], i.e.,

$$D(\mathcal{H}) = d_{\mathcal{H}}\{t : \mathcal{H}(t) = \mathcal{H}\} \tag{A.2}$$

The scaling exponent function, $\zeta(q)$, and the spectrum of Hölder exponents, $D(\mathcal{H})$, are related through the Legendre transform given as [281, 204]:

$$D(\mathcal{H}) = \min_q\{q\mathcal{H} - \zeta(q) + D_f\} \tag{A.3}$$

where D_f is the fractal dimension of the support of singularities of the function $f(t)$. For the case of a continuously differentiable $\zeta(q)$, the following relations hold:

$$\mathcal{H} = \frac{d\zeta(q)}{dq} \tag{A.4a}$$

$$D(\mathcal{H}) = q\mathcal{H} - \zeta(q) + 1 \tag{A.4b}$$

thus providing a means of computing the spectrum of Hölder exponents from the scaling exponent function $\zeta(q)$. (Equation (A.4b) is consistent with equation (A.3) and, in fact, in view of equation (7.14), $D_f = 1 - c_0$). Notice that when $\zeta(q)$ has a linear dependence on q (monofractality) the value of the Hölder exponent is a constant for all locations t (and $D(\mathcal{H})$ is a spike) indicating a homogeneous arrangement of local singularities in the signal. However, when $\zeta(q)$ has a nonlinear dependence on q (multifractality), more than one singularity is present in the signal which is characterized by a whole $D(\mathcal{H})$ spectrum of Hölder exponents, thus indicating a heterogeneous spread of various degrees of singularities across the signal. This heterogeneity of singularity arrangement manifests itself, visually, as spikes of varied strength heterogeneously arranged in the signal (as seen in Figure 7.3).

In this study we used the higher-order structure function analysis to estimate the scaling exponent function and, by taking the Legendre transform, equation (A.4), estimate the spectrum of Hölder exponents (as shown in Figure 7.15(C)). More sophisticated methods for the computation of the spectrum of Hölder exponents from the data are available via Wavelet Transform Modulus Maxima (WTMM) and Cumulant analysis (see [204] for a detailed description of these methods). For example, the WTMM method (applied to the maxima of the wavelet coefficients only and not to the whole signal) allows computation of statistical moments of negative order and thus it has direct access to the right part of the spectrum of singularities. However, in our case the quadratic approximation of the spectrum of scaling exponents curve provides an excellent approximation to the empirically computed spectrum (see Figure 7.15(B)) allowing thus an accurate approximation of the right part of the spectrum of singularities due to its parabolic symmetric shape.

Appendix B

Stable distributions

If $X, X_1, X_2, \ldots$ are mutually independent random variables with a common distribution F_s, then the distribution F_s is said to be stable if for each $n \in \mathbb{Z}$, there exists constants C_n and r_n such that [82, 20]:

$$S_n \stackrel{d}{=} C_n X + r_n \tag{B.1}$$

where $S_n = X_1 + X_2 + \cdots + X_n$ and $\stackrel{d}{=}$ means identical in distribution. In other words, stable distributions are aggregation invariant up to a scale parameter, C_n, and location parameter, r_n. The normalizing constant C_n is of the form $n^{\frac{1}{\alpha}}$ for $0 < \alpha \leq 2$, where α is called the characteristic exponent of the distribution F_s. The distribution F_s is said to be strictly stable when $r_n = 0$. Closed-form expressions of the density functions of stable distributions exist for values of α equal to $2, 1$ and 0.5. In general, the stable pdf is defined by its Fourier transform [284]:

$$\hat{\rho}(k) = \{-i\delta k - |\gamma k|^{\alpha} \left(1 + i\beta \mathrm{sgn}(k) \tan\left(\frac{\pi\alpha}{2}\right)\right)\} \tag{B.2}$$

for $0 < \alpha \leq 2$ and $\alpha \neq 1$. In the above equation $\mathrm{sgn}(\cdot)$ denotes the signum function. The remaining parameters of the distribution are the location parameter ($-\infty < \delta < \infty$), scale parameter ($\gamma > 0$) and the skewness parameter ($-1 \leq \beta \leq 1$). The distribution is symmetric for $\beta = 0$ and is said to be completely skewed for $\beta = -1$ and $\beta = 1$. For $\alpha = 2$, $\hat{\rho}(k)$ gives the Fourier transform of a Gaussian density with mean δ and variance $2\gamma^2$. For the special case $\alpha = 1$, the Fourier transform is expressed in a slightly different way. When $\alpha = 1$ and $\beta = 0$, the stable distribution is also called a Cauchy distribution.

If a random variable X has an α-stable distribution, then its theoretical statistical moments exist only up to order α. The mean of the distribution exists when $1 < \alpha \leq 2$, but when $0 < \alpha < 1$ both the mean and variance of the distribution are undefined. Thus, the Gaussian distribution is the only stable distribution with finite mean and variance. Stable distributions provide good approximations for spatial rainfall fluctuations in convective storms [285], daily discharges in river flows [286], spatial snapshots of tracer plumes in underground aquifers [83] and river flows [287].

Appendix C

Numerical simulation of heavy-tailed random variables

C.1 Symmetric α-stable random numbers

The most convenient way of generating symmetric α-stable random variables is by using the following transformation method [190]:

$$\xi_\alpha = \gamma_x \left(\frac{-cos\phi lnu}{cos\left((1-\alpha)\phi\right)} \right)^{1-1/\alpha} \frac{sin\left(\alpha\phi\right)}{cos\phi} \tag{C.1}$$

where $\phi = \pi\left(v - 1/2\right)$, $u, v \in (0,1)$ are independent uniform random numbers, γ_x is the scale parameter and ξ_α is a symmetric α-stable random number. For $\alpha = 2$, the above equation reduces to $\xi_2 = 2\gamma_x\sqrt{-lnu}sin\phi$, which is the Box-Muller method for Gaussian deviates. The other two notable limit cases are the Cauchy distribution, with $\alpha = 1$ and $\xi_1 = \gamma_x tan\phi$, and the Lévy distribution, with $\alpha = 1/2$ and $\xi_{1/2} = -\gamma_x tan\phi/\left(2cos\phi lnu\right)$. Using the above relation we can simulate not only the heavy-tailed step lengths of a CTRW process, but we can use the above relationship to plot stable distributions of various tail-indices.

C.2 One parameter Mittag-Leffler random numbers

The probability density of the heavy-tailed waiting times can be described by a Mittag-Leffler probability distribution. The most convenient way of generating random variables from a Mittag-Leffler distribution is as follows [190]:

$$\tau_\beta = -\gamma_t lnu \left(\frac{sin(\beta\pi)}{tan(\beta\pi v)} - cos(\beta\pi) \right)^{1/\beta} \tag{C.2}$$

where $u, v \in (0, 1)$ are independent uniform random numbers, γ_t is the scale parameter, and τ_β is a Mittag-Leffler random number. For $\beta = 1$, the above equation reduces to the inversion formula for the exponential distribution: $\tau_1 = -\gamma_t lnu$.

C.3 Truncated and Tempered Pareto random numbers

Truncated and Tempered Pareto random variables can be simulated by generating the Pareto random variables and imposing on them the a priori known upper bound. Let us denote a Pareto random variable by x_p. The easiest way of generating a Pareto random variable with a tail index α is by raising a uniform random variable, u, to a power of $-\alpha$, i.e., $x_p = u^{-\alpha}$. A truncated Pareto random variable (x_{tp}) with a tail index α and upper bound ν can then be iteratively generated by retaining the Pareto random variables lesser than ν and by discarding the values greater than ν, i.e., $x_{tp} = \{x_p \leq \nu\}$. Further, an exponential random variable (x_e) with a rate parameter β can be simulated from a uniform random variable by using the following relationship: $x_e = -(1/\beta)ln(u)$. A tempered Pareto random variable (x_{temp}) with a tail index α and rate of exponential tempering β can then be iteratively generated by retaining the Pareto random variables lesser than x_e and by discarding the values greater than x_e in each iteration, i.e., $x_{temp} = \{x_p \leq x_e\}$. It is easy to see that unlike the truncated Pareto random variables, the random numbers sampled from a tempered Pareto distribution have a stochastic truncation as the extremes are governed by the exponential random variable x_e.

Appendix D

Fractional Calculus

D.1 Definitions

The two most common definitions of a fractional derivative are its Riemann-Liouville form and the Caputo form. Both these definitions are fundamentally based on the definition of a fractional integral. Fractional integration of order α is defined as the convolution with a power-law "memory" kernel, which can be written as:

$$I_x^{\alpha}\{f\} = \frac{1}{\Gamma(\alpha)} \int_0^x \frac{f(\zeta)}{(x-\zeta)^{1-\alpha}} d\zeta \tag{D.1}$$

where $I^{\alpha}\{.\}$ denotes the fractional integral of order α. The α^{th} derivative of a function $f(x)$ in its Riemann-Liouville form is then defined as the n^{th} derivative of the $(n-\alpha)^{th}$ integral, i.e.,

$$D^{\alpha} f(x) = D^n I^{n-\alpha} f(x) = \frac{1}{\Gamma(n-\alpha)} \frac{d^n}{dx^n} \int_0^x (x-\zeta)^{n-1-\alpha} f(\zeta)\, d\zeta \tag{D.2}$$

where $n-1 < \alpha < n, n \in \mathbb{Z}$ and $D^{\alpha}\{.\}$ denotes the fractional differentiation operator of order α.

The alternate is the Caputo fractional derivative, which is defined as the $(n-\alpha)^{th}$ integral of the n^{th} derivative of $f(x)$:

$$D^{\alpha} f(x) = I^{n-\alpha} D^n f(x) = \frac{1}{\Gamma(n-\alpha)} \int_0^x (x-\zeta)^{n-1-\alpha} \frac{d^n}{d\zeta^n} (f(\zeta))\, d\zeta \tag{D.3}$$

Application of the fractional integral operator of order $1-\alpha$ to a power function of order β gives:

$$I_x^{1-\alpha}\{x^\beta\} = \frac{\Gamma(\beta+1)}{\Gamma(\beta-\alpha)x^{\beta-\alpha+1}} \tag{D.4}$$

and the fractional derivative of the same function is:

$$D_x^{1-\alpha}\{x^\beta\} = \frac{\Gamma(\beta+1)}{\Gamma(\beta+\alpha)x^{\beta+\alpha-1}} \tag{D.5}$$

One of the key differences in the functional forms of the two definitions is that, the Caputo derivative of a constant is zero, whereas the Riemann-Liouville definition of a constant is given by:

$$D_x^{1-\alpha}\{c\} = \frac{c}{\Gamma(\alpha)}x^{\alpha-1} \tag{D.6}$$

D.2 Discretization of fractional derivatives

The one-shift Grünwald weights have been shown to be stable in numerical computations and approximations of the fractional derivatives. The discretized approximation of a fractional derivative of order $1 < \alpha \leq 2$ of some function $f(x)$ is given by:

$$\frac{\partial^\alpha f(x)}{\partial x^\alpha} = \frac{1}{\Gamma(-\alpha)} \lim_{N\to\infty} \frac{1}{\Delta x^\alpha} \sum_{k=0}^{N} \frac{\Gamma(k-\alpha)}{\Gamma(k+1)} f\left(x-(k-1)\Delta x\right) \tag{D.7}$$

where Δx is the spatial grid size of the discretization and N is the number of grid points. Further, the one-shift Grünwald discretization of the fractional derivative has been shown to be consistent and unconditionally stable in the implicit Euler and Crank-Nicholson schemes.